Roma Tre

Fisica

CORSO DI DOTTORATO DI RICERCA IN

XXXVIII

CICLO DEL CORSO DI DOTTORATO

Laboratory Measurements and Simulations Supporting the Search for Liquid Water in the Solar System Using Radar Sounders

---

Titolo della Tesi

Gabriele Turchetti

Nome e Cognome del dottorando — Firma

Elena Pettinelli

Docente Guida/Tutor: Prof.ssa — Firma

Giorgio Matt

Coordinatore: Prof. — Firma

Contents

0.1 Search for Liquid Water in the Solar System . . . 1
0.1.1 Two Case Studies . . . 2
0.2 Purpose of the Thesis . . . 2

1 Water on Mars **3**
1.1 The Past of the Red Planet . . . 3
1.2 The Present . . . 3
1.3 The Missions . . . 4
1.3.1 Mars Express . . . 4

2 Jovian Icy Moons **9**
2.1 Ganymede . . . 9
2.1.1 Atmosphere . . . 10
2.1.2 Surface . . . 10
2.1.3 Interior . . . 11
2.1.4 Ocean . . . 12
2.2 Europa . . . 12
2.2.1 Atmosphere . . . 13
2.2.2 Surface . . . 13
2.2.3 Interior . . . 14
2.2.4 Ocean . . . 15
2.3 Callisto . . . 15
2.3.1 Atmosphere . . . 16
2.3.2 Surface . . . 16
2.3.3 Interior . . . 17
2.3.4 Ocean . . . 17
2.4 The Missions . . . 18
2.4.1 JUICE . . . 19
2.4.2 Europa Clipper . . . 20

3 Electromagnetic Theory **22**
3.1 Maxwell Equations . . . 22
3.1.1 Maxwell Equations in the Frequency Domain . . . 24
3.2 The Wave Equation . . . 24
3.3 Electromagnetic Properties . . . 27
3.3.1 Polarization Phenomena . . . 27
3.3.2 Electric Susceptibility and Relative Permittivity . . . 29
3.3.3 Complex Effective Permittivity and Conductivity . . . 30
3.3.4 Circuital Approach . . . 30
3.3.5 Magnetic Permeability . . . 32
3.3.6 Permittivity vs Frequency . . . 32
3.3.7 Permittivity vs Temperature . . . 34

4 Geomaterials Electromagnetic Properties **36**
4.1 Rocks . . . 36
4.2 Soils . . . 36
4.3 Meteorites . . . 37
4.4 Water . . . 37
4.4.1 Liquid Water . . . 38
4.4.2 Saline Water Dielectric Properties . . . 39
4.5 Moisture . . . 39

4.6 Water Ice . . . 39
4.6.1 Dielectric Models: Jaccard Theory and Wait-and-Switch . . . 41
4.6.2 Effects of Dopants . . . 43
4.6.3 Effects of Anisotropy and Density . . . 43
4.6.4 Ice Formation and Growth Processes . . . 44
4.7 Ice Doped with Sodium Chloride . . . 47
4.8 Dirty Ice . . . 48
4.9 Mixing Models . . . 50
4.9.1 Maxwell-Garnett Model . . . 50
4.9.2 The Bruggeman Model . . . 53
4.9.3 The Looyenga-Landau-Lifshitz Model . . . 53
4.9.4 The Complex Refractive Index Model . . . 53
4.9.5 The Lichtenecker Model . . . 53
4.9.6 Power-Law Mixing Models . . . 53
4.9.7 Permittivity Bounds for Binary Mixtures . . . 54
4.9.8 The Archie Model . . . 55

5 Radio Echo Sounding 56
5.1 Antenna Systems . . . 56
5.2 Fundamental Radar Equation . . . 57
5.3 System Parameters . . . 58
5.3.1 Frequency . . . 59
5.3.2 Radar Signals . . . 59
5.4 Radar Signals Propagation in Geological Media . . . 61
5.4.1 Reflection Coefficient . . . 62
5.4.2 Energy Dissipation Mechanisms . . . 62
5.4.3 Surface Roughness . . . 63
5.4.4 Subsurface Clutter . . . 64
5.5 Resolution . . . 64
5.5.1 Vertical Resolution . . . 64
5.5.2 Horizontal Resolution . . . 65
5.5.3 Radar Footprint . . . 66
5.6 Interference Phenomena . . . 66
5.7 Radargrams . . . 67

6 Laboratory Instruments and Setup 68
6.1 Introduction to Transmission Line Theory . . . 68
6.1.1 Electromagnetic Description . . . 68
6.1.2 Circuital Approach . . . 70
6.2 Networks . . . 72
6.2.1 Impedance and Admittance Matrices . . . 73
6.2.2 Scattering Matrix . . . 73
6.2.3 The Transmission Matrix . . . 74
6.3 Coaxial Transmission Line . . . 74
6.3.1 Modified Nicholson-Ross-Weir Algorithm . . . 75
6.4 Experimental Setup . . . 76
6.4.1 Coaxial Probe Architecture . . . 76
6.4.2 Calibration . . . 77
6.5 Uncertainty Quantification . . . 78
6.5.1 Measurement Procedures . . . 79

7 Measurements 81
7.1 Martian Subglacial Brines . . . 81
7.1.1 Magnesium Perchlorate Solutions . . . 82
7.1.2 Calcium Perchlorate Solutions . . . 88
7.1.3 Previous Studies . . . 90
7.2 Icy Moons . . . 93
7.2.1 Europa: Ice Doped with Sodium Chloride . . . 93
7.2.2 Ganymede and Callisto: Dirty Ice . . . 97

8 Simulations 103

8.1 Simulations Framework . . . 103
8.2 Europa . . . 104
8.2.1 Temperature Profiles . . . 105
8.2.2 Concentration Profiles . . . 106
8.2.3 Targets . . . 108
8.2.4 Results . . . 109
8.3 Ganymede and Callisto . . . 113
8.3.1 Attenuation . . . 113
8.3.2 Interference Phenomena . . . 113

9 Conclusion **119**

Bibliography **I**

List of Figures

1.1 Illustration of Mars Express spacecraft . . . 5
1.2 Map of the Martian Planum Australe . . . 7

2.1 Picture of Ganymede terrains . . . 11
2.2 Illustration of Ganymede's interior . . . 12
2.3 Chaotic terrain on Europa . . . 14
2.4 Illustration of Europa's interior . . . 15
2.5 Picture of the heavily cratered surface of Callisto . . . 17
2.6 Illustration of Callisto's interior . . . 18

3.1 Transverse EM wave scheme . . . 27
3.2 Simplified scheme of the atom polarization . . . 28
3.3 Diagram of polarization phenomena . . . 29
3.4 Polarization in a parallel-plate capacitor filled with homogeneous dielectric material 29
3.5 Equivalent circuit system and phase shift between voltage and current . . . 31
3.6 Diagram of the currents I_l, I_{tot}, I_c . . . 31
3.7 The behavior of the relative permittivity with frequency . . . 34
3.8 The Cole-Cole or Argand diagram for a Debye model with one relaxation frequency 34
3.9 Temperature dependence of dielectric parameters σ and ϵ. . . . 35

4.1 Real permittivity values for different rocks . . . 37
4.2 Dielectric permittivity spectra of pure water at two distinct temperatures . . . 38
4.3 Microwave spectra of complex permittivity for pure water and saline water . . . 39
4.4 Dielectric permittivity and loss tangent of both solid and powder granite . . . 40
4.5 Ih pure water ice crystal . . . 40
4.6 Dielectric properties of HF doped ice for different concentrations and temperature ranges . . . 43
4.7 Scheme of the different types of terrestrial ices and their location . . . 44
4.8 Real and imaginary parts of the dielectric permittivity of artificial sea ice as a function of frequency . . . 46
4.9 Conductivity as a function of chloride concentration for samples of terrestrial ices: 47
4.10 Idealized phase diagram for a water salt solution . . . 48
4.11 Eutectic diagram of sodium chloride . . . 49
4.12 Relative dielectric permittivity at different temperatures as a function of dust mass-fraction in the LL5 chondritic dust sample mixed with ice . . . 50
4.13 Model-based curves and experimental values of the bulk real and imaginary parts of permittivity of dirty ice mixtures . . . 51
4.14 Scheme of the two-phase mixture described by Maxwell-Garnett formula . . . 51
4.15 Two limit cases of randomly distributed ellipsoidal inclusions in dirty ice samples 52

4.16 Power-law models for the effective permittivity of a mixture with high dielectric contrast . . . 54
4.17 Wiener and Hashin-Shtrikman boundaries for the relative effective permittivity of mixture . . . 55

5.1 Diagram of radar investigation . . . 58
5.2 Frequency bands used in geophysical methods . . . 60
5.3 Representation of a chirp signal . . . 61
5.4 Effects of roughness on radar signals . . . 64
5.5 Simplified illustration to define vertical and horizontal resolution . . . 64
5.6 Scheme vertical resolution in radar systems . . . 65
5.7 Scheme lateral resolution in radar systems . . . 66
5.8 Examples of radargrams . . . 67

6.1 Transmission line and lumped element equivalent circuit . . . 70
6.2 Transmission line representation . . . 72
6.3 Block diagram of a two-port Vector Network Analyzer . . . 73
6.4 The transmission matrix in a two-port network. . . . 74
6.5 Transmission and reflection of EM waves caused by a sample inside and the transmission line . . . 74
6.6 Transmission line with a dielectric . . . 76
6.7 Picture of the measurement setup . . . 77
6.8 Coaxial probes . . . 77
6.9 The connector calibrator . . . 78
6.10 Air and glass beads calibration . . . 79
6.11 The mixing procedure . . . 80
6.12 Setup of the measurement box . . . 80

7.1 Real permittivity as a function of the temperature of a magnesium perchlorate and a sodium chloride solution . . . 82
7.2 Temperature of magnesium perchlorate solutions in the heating phase . . . 83
7.3 Spectra of real permittivity and conductivity of a magnesium perchlorate sample 84
7.4 All the measurements of ε' and σ of magnesium perchlorate solutions at 4 MHz . 84
7.5 Apparent permittivity ε_a as a function of temperature in the range 195 K - 240 K 85
7.6 Apparent permittivity ε_a as a function of temperature with different cell length . 85
7.7 Apparent permittivity ε_a as a function of temperature with different residence time in the ultra-freezer . . . 86
7.8 Apparent permittivity ε_a as a function of temperature with different residence time in the ultra-freezer . . . 87
7.9 Pictures of two magnesium perchlorate solutions samples (mush and frozen) immediately after the extraction from the ultra-freezer . . . 87
7.10 Permittivity values of two measurements with one that underwent freezing due to mechanical stress . . . 88
7.11 Pictures of the sample subjected to mechanical stress during cable tightening . . 89
7.12 Temperature of calcium perchlorate solutions in the heating phase . . . 90
7.13 Spectra of real permittivity and conductivity of a calcium perchlorate sample . . 90
7.14 All the measurements of ε' and σ of calcium perchlorate solutions at 4 MHz . . . 91
7.15 Apparent permittivity ε_a as a function of temperature in the range 195 K - 240 K of all the measurements of calcium perchlorate solutions . . . 91
7.16 Pictures of the calcium perchlorate solutions immediately after the removal from the ultra-freezer . . . 92
7.17 Perchlorate solution measurements from a previous study . . . 92
7.18 LCR meter measurements at 1 MHz of the apparent permittivity of a calcium perchlorate solution . . . 93
7.19 Permittivity and conductivity of all $NaCl$ solutions . . . 95
7.20 Permittivity and conductivity of all $NaCl$ solutions in the frozen phase . . . 95
7.21 Real part of the permittivity at 240 K as a function of $NaCl$ concentration measure with the VNA, together with the three different mixing formulas employed for the fit . . . 96
7.22 Real part of the permittivity of the 20 mM $NaCl$ doped ice sample as a function of temperature at 1 MHz . . . 96

7.23 Conductivity at 240 K as a function of the concentration in a log-scale 97
7.24 Activation energy in eV as a function of $NaCl$ concentration at 9 MHz 98
7.25 Conductivity of 20 mM doped ice sample as a function of temperature measured with the LCR meter 98
7.26 Powdered dry samples dielectric permittivity as a function of temperature 100
7.27 A powdered frozen saturated sample dielectric permittivity as a function of temperature 100
7.28 Magnetic permeability spectra of the three powdered dry samples 101
7.29 Maps of complex dielectric permittivity of dirty ice contaminated with CI carbonaceous chondrite as functions of porosity and temperature 101
7.30 Maps of complex dielectric permittivity of dirty ice contaminated with L5 ordinary chondrite as functions of porosity and temperature 102

8.1 Scheme of the stratigraphy structure of the simulations 105
8.2 Numerical simulations of solid-state convection within Europa's ice shell, covering ice shell thicknesses from 5 to 45 km 106
8.3 Diagram of different temperature profiles within Europa's ice shell 107
8.4 Temperature and salinity profiles according to top-down solidification model . . . 107
8.5 ε' and σ as a function of depth of an icy crust formed with top-down solidification 108
8.6 An overview of the possible radar targets in the icy crust of Europa 108
8.7 Simplified scheme of the simulations 109
8.8 Reflection coefficient, as a function of depth, caused by a target of liquid water at different depths 110
8.9 Reflection coefficient in the case of a 3 km icy crust, with a mushy layer as a target situated at the end of the crust 110
8.10 Reflection coefficient, expressed in dB, of target of different permittivities in a 5 km icy crust with a linear temperature profile 111
8.11 Reflection coefficient, expressed in dB, of target of 4 different permittivities in a 6 km, 9 km and 12 km conductive icy crust 112
8.12 Reflection coefficient, expressed in dB, of target of different permittivities in a 6 km icy crust before the mushy layer with different temperature profiles 112
8.13 Maps of the parametric attenuation in a dirty ice layer with L5 ordinary chondrite and CI simulant as contaminant computed at 9 MHz 113
8.14 Illustration of the scenarios investigated by the simulations for Ganymede 114
8.15 Results of simulations of the attenuation, expressed in decibels, corresponding to the scenario illustrated hypothesized for Ganymede 115
8.16 Reflection coefficients in case of interference phenomena 115
8.17 Reflection coefficient of the surface given by a dirty ice layer with carbonaceous chondrite CI inclusions and the permittivity computed by the coefficient 116
8.18 Reflection coefficient of a surface characterized by dirty ice layer with carbonaceous chondrites inclusions including the magnetic properties 116
8.19 Reflection coefficient of a surface characterized by dirty ice layer with carbonaceous chondrites inclusions including the magnetic properties with a larger bandwidth 117
8.20 Maps of the reflection coefficient, expressed in dB, of the surface signal in case of dirty ice with carbonaceous chondrite CI simulants inclusions 118
8.21 Reflection coefficient of the surface discontinuity in the case of a gradient of inclusions with different percentage at the surface level 118

List of Tables

1.1 MARSIS subsurface sounder parameters 6

2.1 Physical parameters of Ganymede 10

2.2 Physical parameters of Europa 13
2.3 Physical parameters of Callisto 16
2.4 RIME main parameters 20
2.5 REASON main parameters 21

4.1 Dielectric properties of representative meteorite samples 37

7.1 Table of the magnesium perchlorate solutions measurements 83
7.2 Table of calcium perchlorate solutions measurements 88
7.3 List of $NaCl$ concentrations of the solutions examined by our previous studies . 94
7.4 Activation Energies for different concentrations and temperature intervals 97
7.5 Temperature fitting functions at 9 MHz for the EM properties of the grains of the L5 ordinary chondrite and CI carbonaceous chondrite simulant 101

Introduction

The search for extraterrestrial life and possible new habitable worlds has always been of great interest to the scientific community.
Taking inspiration from the development of life on Earth, one of the most commonly used approaches in this field is the search for liquid water, as it is considered a fundamental ingredient. The presence of liquid water can be investigated using a multidisciplinary analytical framework combining remote observational techniques with computational modeling, or, if possible, direct sampling methodologies depending on many factors - for example on whether the targets are in our Solar System or in other star systems. The most direct observation is in situ, employing landers and rovers, sampling the soil and analyzing the content of rocks and regolith. Other techniques involve geophysics measurements like the propagation of seismic waves, multiwavelength spectroscopy to investigate the composition of the atmosphere and the surface, or gravity and magnetic field measurements that allow us to infer the composition of the interior of celestial bodies. In this thesis we will address a technique that has proven to be very effective in recent years in the Solar System, the Radio Echo Sounding (RES), discussed in detail in Chapter 5. Radar sounders, working simultaneously as transmitting and receiving antennas, send radio waves towards the surface of the target and use the reflections of these signals (echoes) to reconstruct the stratigraphy of the soil. The propagation of the signals and the characteristics of the echoes depend significantly on the electromagnetic properties of the materials involved in the investigation. Therefore, a deep knowledge of electromagnetic properties of surface and interior of celestial bodies is essential for a correct radar analysis. RES techniques have already been used on Earth, on the Moon, on Mars, and will be employed in the future on other celestial bodies of the Solar System.

0.1 Search for Liquid Water in the Solar System

In a stellar system, the habitable zone is defined as the region where environmental conditions could allow the presence of liquid water on the surface of a planet. In our Solar System, the only planet in this region is the Earth, but other celestial bodies could have the right conditions to host liquid water beneath the surface. For instance, in 2018, radar observations revealed signatures consistent with the presence of liquid water beneath the Martian South Pole. These findings added to the body of morphological evidence indicating that Mars once hosted liquid water on its surface in the distant past. In the outer Solar System there are many celestial bodies that are likely to host liquid water oceans in their interior [148], the so-called *Ocean Worlds*.
Geophysics measurements and modeling suggest the presence of liquid water in the interior of the Jovian icy moons (Europa, Ganymede, and Callisto), the Saturn's moons (Enceladus, Titan, Mimas, and Dione), the dwarf planets (Pluto and Ceres), the Neptune's moon Triton, and other smaller celestial bodies. All of these bodies could be investigated with radar sounders to evaluate the habitability of their subsurface and to detect possible liquid water reservoirs. To date, there are two missions, the JUpiter ICy moons Explorer (JUICE) and Europa Clipper, traveling toward the Jovian icy moons, and the upcoming mission Envision, whose target is Venus, that will use radar technology - among other tools - to probe the interior of these celestial bodies searching for liquid water evidence.
The analysis of radar data allows the correct reconstruction of the stratigraphy of the target thanks to the electromagnetic discontinuities of the subsurface. The electromagnetic properties, in particular the dielectric permittivity ϵ and the magnetic permeability μ, influence the attenuation of the signals and the characteristics of the echoes, and depend on materials, temperature and frequency.

0.1.1 Two Case Studies

In this manuscript, we will focus on two main topics: the subglacial lake under the Martian South Pole and the Jovian icy moons.
After the detection in 2018, one of the most critical questions, also related to the potential habitability, concerns the physical state of the lake in terms of temperature and composition. It is well known that perchlorate solutions can remain in a liquid or partially liquid state at temperatures significantly lower than 273 K. In this work, we present the electromagnetic properties of potential analogues of the lake as a function of temperature, and we discuss possible techniques that could be employed in further studies of this kind.
With regard to the icy satellites, we investigated the properties of the icy shell under different scenarios, integrating laboratory measurements with radar simulations.

0.2 Purpose of the Thesis

This thesis project aims at presenting laboratory and simulation results concerning radar analysis and electromagnetic properties of planetary analogues. It proceeds along two distinct lines of investigation: the study of laboratory data of salty ice as implication of the conditions of the subglacial water on Mars, and simulations of radar signals propagation through the Jovian moons icy crusts to allow a better comprehension of future radar data.
The first part of the manuscript is focused on an introduction about the two targets, Mars (Chapter 1) and Jovian icy moons (Chapter 2). The second part is about the electromagnetic theory (Chapter 3), the characteristics of geomaterials (Chapter 4), radar analysis basic principles (Chapter 5), and our laboratory setup (Chapter 6). In the last part, we discuss the results of the laboratory measurements about Mars subglacial water and Jovian icy moons (Chapter 7) and the simulations of radar signals propagation (Chapter 8).

Both Mars and the icy satellites are characterized by the presence of brines - water-salt solutions (such as perchlorates or sodium chloride) - occurring in both solid and liquid states. These components are likely to be widespread in planetary environments. Consequently, studying the electromagnetic behavior of brines is of great importance for the search for liquid water and potentially habitable environments in the Solar System, as well as for the interpretation of radar sounder observations.

Chapter 1

Water on Mars

1.1 The Past of the Red Planet

Mars appears today inhospitable to life at the surface. The low mean atmospheric pressure (~600 Pa), cold mean surface temperatures (~215 K), and negligible water vapor content, render the planet not suitable to host stable surface liquid water under current environmental parameters. However, multidisciplinary studies employing orbital remote sensing, in-situ geochemical analysis, and comparative planetology, have established a robust scientific consensus regarding the planet's aqueous history.
Evidence indicates that Mars experienced substantial hydrological activity during the Noachian and Hesperian Era (4.1 billion to 3.0 billion years ago [40]) with elevated atmospheric pressure, enhanced greenhouse warming, and large surface water reservoirs that fundamentally altered the planet's geological and geochemical evolution. During the Noachian, conditions may have been warm enough to allow the presence of stable bodies of surface water, as indicated by the formation of valley networks, lake beds, and possibly oceans ([68]).
Some evidence comes from Martian clay minerals that suggest interactions between water and rock, forming deposits that imply past warmer and wetter conditions ([61]).
Other studies have shown that Martian meteorites exhibit signs of aqueous alteration consistent with a wet environment meaning that a large quantity of water might have interacted with the Martian surface and subsurface ([12]).
Recently, the rover Perseverance identified mineralogical evidence consistent with aqueous processes, such as iron oxides, clays, and carbonates, essential indicators of past presence of water ([20]). Also, the rover has revealed evidence of sedimentary structures characteristic of deltaic environments that suggest that Jezero Crater was once the site of a lake where water was stable enough to allow the deposition of sedimentary rocks ([129]).

1.2 The Present

In the present day the amount of water on the red planet is modest. Considerable quantities are in the form of ice and potentially as liquid water near the surface. Liquid water has escaped through several mechanisms of atmospheric loss, leading to significant transformations of climate and surface conditions over geologic time. These escape processes are mainly influenced by solar and environmental phenomena. The major escape mechanisms are:

- **Thermal escape**, in which solar radiation heats the atmosphere and lighter hydrogen atoms, reaching the escape velocity to break free from Mars gravitational potential, escape into space at considerable rates ([69]);
- **Photochemical escape** which involves the dissociation of water vapor into hydrogen and oxygen molecules under the influence of ultraviolet light from the Sun ([123]);
- **Atmospheric escape**, due to the lack of the magnetic field protection, in which solar wind enhances the ion escape rates ([169]).

Seasonal variations could also have contributed to and accelerated water loss ([66]). The main reservoirs of water on Mars today are stored in the Polar Ice Caps, and in the subsurface ice. Beyond ice, there is evidence of water locked within hydrated minerals throughout the Martian regolith and crust ([179]). Concerning water in its liquid form, in addition to the

detected subglacial lake, which is discussed later, recent analyses of seismic data collected from the InSight mission, including measurements of seismic waves generated by natural quakes and impacts ([14]), suggest the possible presence of reservoirs at the base of the upper Martian crust at a depth between 5.4 and 8 km ([194]).
Many missions have aimed at detecting liquid water on Mars in order to understand whether it had been there and where it had gone, and many missions are still dedicated to this task.

1.3 The Missions

Key missions that made significant contributions to understand the liquid water issue on Mars are:

- **Past orbiters** Viking 1-2 (1976), Mars Global Surveyor (1997-2006), and the ongoing orbiting missions Mars Odyssey, Mars Express, Mars Reconnaissance Orbiter (MRO), Mars Atmosphere and Volatile Evolution (MAVEN);
- **The landers** Viking 1-2 (1976), Phoenix (2008), and InSight (2018–2022);
- **The rovers** Spirit and Opportunity (2004-2018), Curiosity (2012), and Perseverance (2021).

In the following sections, we focus on the Mars Express mission and, in particular, on the Mars Advanced Radar for Subsurface and Ionosphere Sounding (MARSIS) because it is strictly related to this thesis project.

1.3.1 Mars Express

Mars Express (Fig. 1.1) mission was launched on 2 June 2003 and entered the Martian orbit on 25 December 2003 ([43]). The mission purpose was to significantly enhance our understanding of the Martian environment, geology, and atmosphere. The primary scientific objectives included:

- The **geological mapping** of the surface and the identification of peculiar features to understand the geological history;
- The **study of the atmosphere** in terms of composition, structure, and dynamics to understand its evolutions and possible implications for the past habitability;
- The **exploration of the subsurface**, employing the radar instrument, to detect water ice and potentially liquid water reservoirs.

Mars Express is equipped with 7 scientific instruments:

- MARSIS (Mars Advanced Radar for Subsurface and Ionosphere Sounding) designed to probe Martian subsurface, particularly to identify liquid water beneath polar ice deposits ([163]);
- OMEGA (Observatoire pour la Minéralogie, l'Eau, les Glaces et l'Activité), a visible and infrared imaging spectrometer that increases knowledge about the geology and hydrology ([21]);
- PFS (Planetary Fourier Spectrometer) that investigates the thermal emissions from the surface and contributed to the atmospheric analysis ([67]);
- SPICAM (Spectroscopy for the Investigation of the Characteristics of the Atmosphere of Mars), an UV and infrared spectrometer designed to study the Martian atmosphere, particularly its structure, composition, and spatial distribution ([19]);
- ASPERA (Analyzer of Space Plasmas and Energetic Atoms) that measures the composition and dynamics of the atmospheric escape processes and its interaction with the solar wind ([16]);
- VMC (Visual Monitoring Camera) developed to monitor the Beagle 2 lander lost during the entry, captures images of the Martian surface, monitoring dust storms and atmospheric changes ([151]);

- HRSC (High Resolution Stereo Camera) creates 3D topographic maps of the Martian surface and provide high-resolution images ([146]).

Finally, MaRs, the Mars Radio Science experiment, uses the radio communication system to investigate the atmosphere, ionosphere, gravity field, and interior structure of Mars ([157]).

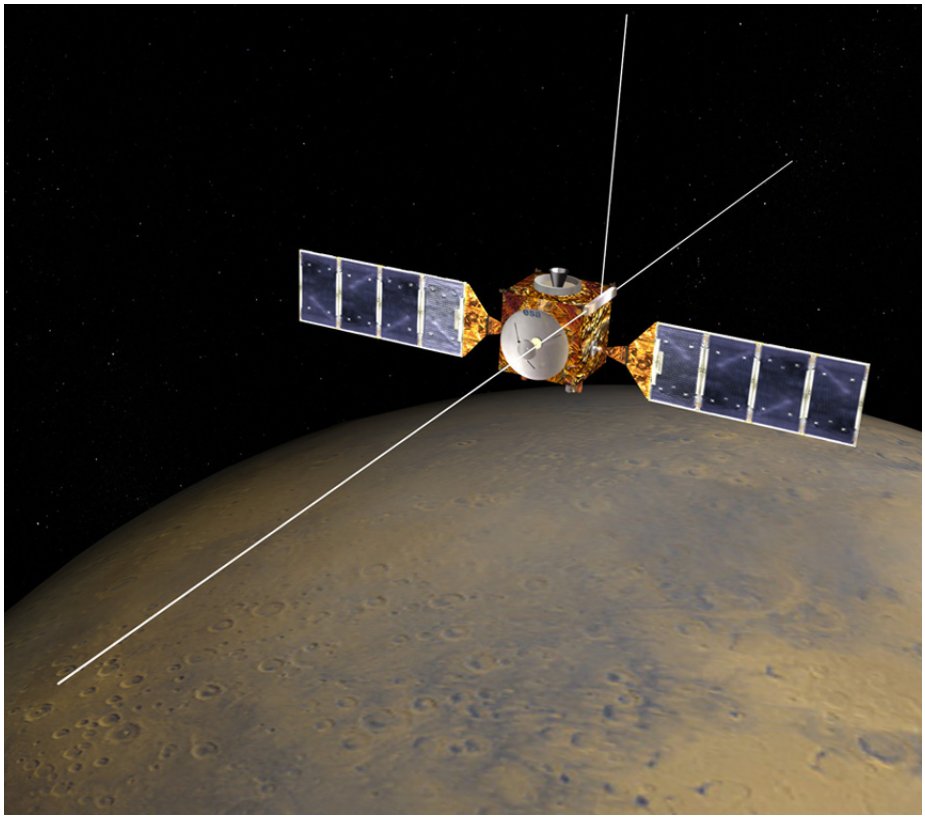

Figure 1.1: Illustration of Mars Express spacecraft.

Mars Advanced Radar for Subsurface and Ionosphere Sounding

MARSIS is a nadir-looking, low frequency radar sounder with dipole antenna of 40 m developed by Italian and US researchers that operates during high elliptical orbital phases of the spacecraft. It requires nighttime conditions to sound surface and subsurface to avoid interference from the Martian ionosphere, which is significantly high in daytime.
MARSIS started its operations in July 2005 with the primary scientific objective of detecting subsurface ice deposits and liquid water reservoirs within the Martian regolith, while simultaneously investigating potential biosignatures within the planetary subsurface. Secondary objectives are the surface topography, composition characterization, and the investigation of subsurface geology and ionospheric behavior. It operates in two modes:

- **Subsurface sounding mode** generates a swept frequency high power radio pulses and collects the echoes reflected by electromagnetic discontinuities in the subsurface; it employs a chirp signal for transmission to acquire data of high enough signal-to-noise ratio and uses 1 MHz bandwidth pulses centered at 3, 4 or 5 MHz. It can use at the same time two frequencies to reduce the ionospheric distortions, as well as to investigate frequency dependent effects in data analysis.

- **Active ionosphere sounding mode** measures the dispersion effects of the ionosphere and studies the characteristics of the ionosphere itself. It operates above the altitude of about 900 km, or when subsurface sounding is not working, with the entire range of frequencies of the radar, 0.1-5.5 MHz, using simple low bandwidth pulses radiated through the dipole antenna.

In this work we focus on the results of the subsurface sounding mode whose parameters are shown in Tab. 1.1 ([97]). In free space, the vertical resolution is of 150 m (approximately 210 m after the correlation between the transmitted and received waveform called range compression).

Parameter	Description
Subsurface sounding altitude range	250–900 km
Dipole antenna length	40 m tip to tip
Monopole antenna length	7 m
Subsurface sounder frequency range	1.3–5.5 MHz (4 Bands)
Peak radiated power	1.5–5 W
Subsurface sounder pulse repetition rate	127 Hz
Subsurface sounder transmit pulse length	250 ms
Subsurface sounder wavelength	60–160 m
Bandwidth per band	1 MHz
Sounder free space depth resolution	150 m
Sounder dynamic range	40–50 dB
Nominal depth window	15 km
Number of processed channels	2 or 4
Number of simultaneous frequencies	1 or 2
Data quantization	8 bits per sample
Data quantization rate	2.8 megasamples per second
Data window duration	350 ms
Data rate output	18–75 Kbps
Data volume	285 Mbit per day
Dc operation power	60W
Total mass	20 kg

Table 1.1: MARSIS subsurface sounder parameters [97].

The resolution for the subsurface is proportional to the square root of the permittivity of the material of the medium. The horizontal resolution is influenced by the altitude of the satellite, the frequency of the pulse transmitted, and the surface roughness; it usually ranges from 10 to 30 km. After the onboard correction for the vertical motion and Synthetic Aperture Radar (SAR) processing (coherent summation of consecutive pulses), horizontal resolution along the track improves up to 5-10 km. MARSIS explored a large part of the Martian surface and subsurface, but, in this project, we focused on the South Pole region and, in particular, on the South Polar Layered Deposit (SPLD).

Evidence of Subglacial Liquid Water

In 2018, the analysis of MARSIS data led to the detection of liquid water evidence in *Ultimi Scopuli* ([152]), a region located in the SPLD (Fig. 1.2). The main subglacial liquid water body detected is located at the depth of 1.5 km and covers an area 20 km wide. This detection was made using 29 profiles, acquired by MARSIS, considering the differences in echo power (then in electromagnetic properties) between the surface and the basal unit in the area of the bright reflection anomalies.

The Debate

The detection of anomalous radar reflections compatible with the presence of subglacial liquid water in *Ultimi Scopuli* has been followed by numerous studies fueling an ongoing and lively scientific debate; some of these supported the thesis using additional methods that confirm the detection, others proposed alternative interpretations to that of liquid water, while still others highlighted critical issues that subglacial lake hypothesis must address. Here we report some of these studies:

- In 2019, [188] examining the conditions required for the stability of the subglacial lake, highlighted that the concentration of perchlorate salts detected on Mars would not be sufficient to maintain water in a liquid state and the geothermal heat flux required would

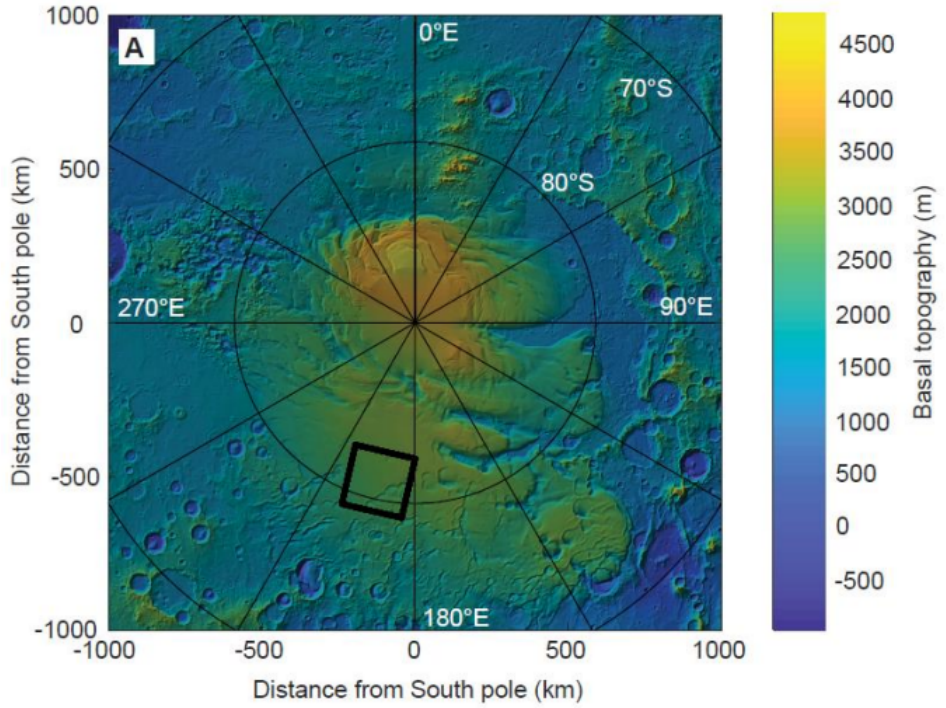

Figure 1.2: Planum Australe map 75° S latitude produced using the Mars Orbiter Laser Altimeter (MOLA) topographic dataset ([186]). The black square identifies the area studied by ([152]).

be greater than 72 mW/m^2, significantly higher than the values measured of approximately 25 mW/m^2. Such conditions would imply the presence of a magmatic chamber, or alternatively, other explanations that do not involve liquid water.

- In 2021, [118] confirmed the subglacial lake thesis by analyzing a larger dataset (134 radar tracks). This study considers additional parameters beyond those previously investigated, such as the variability of the signal in the transition from rocky to wet regions. Moreover, the presence of other smaller water bodies adjacent to the main lake has been identified.
- In 2021, [22] hypothesized that the bright reflections were caused by highly conductive materials and proposed alternative explanations such as highly saline ice or conductive minerals including clays, hydrated minerals like jarosite, and metallic minerals such as hematite, without considering the presence of liquid water as necessary to reproduce observed data.
- In 2021, [187] highlighted the challenges associated with the liquid water interpretation, the presence of salts, and the requirement for unrealistically high temperatures, and instead invokes smectites clays as a possible explanation for the MARSIS data.
- In 2021, [102], analyzing a larger dataset than [152], noted that the phenomenon of basal reflection anomalies appears to be more widespread and not confined to the *Ultimi Scopuli* region; therefore, the authors attributed their origin to explanations less exceptional than the presence of liquid water. One possible interpretation is the occurrence of subsurface dry ice, which could induce distortions in the radar data.
- In 2022, [114] tried to explain MARSIS data through interference phenomena between more layers of H_2O ice and CO_2 ice.
- In 2022, [72] suggested that dry volcanic terrains could provide an alternative explanation for the bright echoes.
- In 2022, [117] provided further confirmations by introducing new approaches computing signal attenuation as an additional diagnostic parameter.
- In 2022, [133] carried out measurements to refute the hydrated salts and clays hypothesis of [187], indicating metastable perchlorate solutions as the most plausible explanation.

- In 2022, [153], by analyzing simulations that include the presence of dry ice, concludes that interference phenomena cannot account for MARSIS data, for which the most robust interpretation remains the presence of liquid water, most likely in hypersaline solutions.
- In 2022, [6] supported the subglacial lake thesis by analyzing data from the Mars Orbiter Laser Altimeter ([186]), onboard the Mars Global Surveyor, identifying morphological analogies between surface topographic anomalies associated with terrestrial subglacial lakes and those observed in the *Ultimi Scopuli* region. This latter evidence is of particular scientific significance as it is independent of MARSIS data.
- In 2023, [50] showed additional measurements on clays to demonstrate that they cannot reproduce the data of *Ultimi Scopuli*.
- In 2023, [119] demonstrated that the anomalies observed by MARSIS cannot be the result of the interference phenomena described by [114], since data exhibit similar behavior across all frequencies, a feature not reproduced in the simulations. Furthermore, scenarios presented by [114] are based on an inaccurate geological context.
- In 2024, [113] once again invoked interference phenomena, employing ice-dust stratigraphies to explain MARSIS data.
- In 2024, [73] demonstrated that a thin surface dust layer, previously neglected, could fundamentally alter the interpretation of radar data. Before drawing conclusions about the presence of liquid water on Mars, it is essential to better characterize this surface layer through future missions and more detailed observations.

One of the open questions remains the capability of liquid water to persist under the subglacial conditions at the Martian South Pole. The surface temperature at *Ultimi Scopuli* is estimated to be around 160 K ([118]), while at the depth of the putative lake it may reach approximately 170 K ([152]) or higher, neglecting the possibility of thermal anomalies or magmatic chambers ([188]). The proposed solutions are the presence of hypersaline perchlorate brines. In Chapter 7, we present rigorous methodologies through which we investigated the potential stability of calcium and magnesium perchlorate solutions at Martian temperatures, and we analyzed their electromagnetic properties to assess whether they can reproduce MARSIS data, thus serving as plausible analogues for the putative subglacial lake at *Ultimi Scopuli*.

Chapter 2

Jovian Icy Moons

The Jovian system represents one of the most complex and scientifically fascinating planetary environments in our Solar System: it harbors a diverse collection of natural satellites that have fundamentally reshaped our understanding of planetary formation, astrobiology, and the potential distribution of life throughout the cosmos. Jupiter, with its 95 confirmed moons as of recent astronomical surveys ([56]), operates as a miniature Solar System whose gravitational influence has captured and shaped an extraordinary array of celestial bodies ranging from small, irregular asteroids to large, geologically active worlds. This extensive satellite system provides a natural laboratory for studying planetary processes across a broad spectrum of environmental conditions, from the sulfur-rich volcanic landscapes of Io to the ice-covered oceans of Europa, Ganymede, and Callisto. Among these, the four Galilean moons hold particular scientific significance. Discovered by Galileo Galilei in 1610, their observation provided key evidence for the heliocentric model, demonstrating that celestial bodies could orbit an object other than Earth. These satellites remain central to planetary science, both as laboratories for studying geological and geophysical processes and as potential habitats beyond Earth.
Each of the Galilean moons exhibits unique characteristics. Io is the most geologically active body in the Solar System, with sulfurous plumes and lava lakes reshaping its landscape. This activity is driven by tidal heating resulting from gravitational interactions mainly with Jupiter, but also with the other Galilean moons. The other three, the icy moons Europa, Ganymede, and Callisto are characterized by water icy surfaces, and geophysical evidence strongly support the presence of subsurface oceans ([178], [108], [106], [212], [103]). These so-called *Ocean Worlds* are of particular interest for astrobiology, as liquid water, in combination with internal heat sources and chemical gradients, provides a potential environment for life. The Jovian icy moons have already been investigated by six missions Pioneer 10 and 11 (1973 and 1974, respectively), Voyager 1 and 2 (1979), Galileo (1995-2003), and Juno (2016-ongoing); their surfaces appear shaped by both endogenic and exogenic geological processes such as tectonism, cryovolcanism, and impact cratering. In this work we focus on the icy moons to support the two missions, JUICE and Europa Clipper, that will enter the Jovian system in 2030-2031.

2.1 Ganymede

Ganymede is the largest moon of Jupiter and in the entire Solar System. Its unique features, due to its size, composition, magnetosphere, and subsurface ocean made it a very captivating subject of study. Ganymede orbits Jupiter at a mean distance of 1070400 km with an orbital period of 7.15 Earth days, locked in a 1:2:4 Laplace resonance with Europa and Io ([158]) and tidally locked to Jupiter. This gravitational configuration with the same hemisphere facing Jupiter throughout its orbit has profound implications for the satellite's thermal evolution and internal dynamics, as tidal heating from orbital eccentricity variations provides a continuous energy source for geological activity ([181]). The two hemispheres are called leading (facing Jupiter) and trailing (opposite side to Jupiter) and they have different characteristics in many aspects. Ganymede represents an intermediate case between the low-density, ice-rich satellites of the outer Solar System and the higher-density, rock-rich bodies of the inner Solar System ([2]) suggesting a significant differentiation into distinct compositional layers. Also being the only moon known to possess an intrinsic magnetic field, it has significant implications for understanding its internal structure and evolutionary history. The magnetospheric coupling due to the interaction with Jupiter's powerful magnetosphere ([108], [178]) provides a natural

laboratory for studying plasma physics processes on scales impossible to replicate in terrestrial experiments. The Tab. 2.1 reports the main parameter of this satellite.

Mean radius	2634.1 ± 0.3 km
Mass	1.482 $\times 10^{23}$ kg
Density	1.936 g/cm^3
Intrinsic magnetic field at equatorial surface	750 nT
Ambient Jovian magnetic field	120 nT
$\frac{C}{MR^2}$	0.3105 ± 0.0028
Mean Surface Temperature	100 - 150 K
Rotational Period	7.154 days

Table 2.1: Physical parameters of Ganymede ([181],[196]).

2.1.1 Atmosphere

The exosphere of Ganymede is dominated by the presence of O_2, H, H_2O detected through UV emission and absorption measurements ([196]). The dissociation of O_2 and H_2 by mostly auroral electrons causes the presence of atomic O and H observed in the UV spectra. The O_2 is globally abundant near the surface, since it does not condense at surface temperatures and is heavy enough to be gravitationally bound. At higher altitudes, lighter H_2 molecules are the primary compound. Asymmetries in the presence of molecular oxygen are observed in the atmosphere between the two hemispheres. The trailing one is shielded by the intrinsic magnetic field, whereas, in the leading one the energetic ions from Jupiter can access the surface producing molecular oxygen through the sputtering process. The presence of water vapor, supported by spectral observations, could be caused by sublimation processes at the surface ([175]). Atomic oxygen results from the photo-dissociation of O_2 by solar radiation and energetic particles ([138]). Ganymede's atmosphere exhibits spatial and temporal variability influenced by its interaction with Jupiter's magnetosphere including auroral phenomena that further affect the atmospheric composition.

2.1.2 Surface

Ganymede's surface is characterized by a combination of cratered terrains, indicative of an ancient, heavily bombarded history, and younger, tectonically active regions that suggest ongoing geological processes. The three main components of its crust are water ice, hydrated salts, and darkening agents consisting probably in silicates and carbonaceous materials. The surface is inhomogeneous, but differentiated in two main types of terrains, bright and dark (Fig. 2.1). Bright terrains are younger, with larger percentages of water ice due to endogenous phenomena like tectonic resurfacing, and dark terrain are older with larger percentage of the darkening agents. The distribution of these terrains is also correlated with orbit since trailing hemisphere appears brighter and leading hemisphere darker ([104]); this correlation could be explained by considering the larger amount of darkening agents in the region of the higher exposure to energetic particles of Jovian plasma identified by the Jovian Infra-Red Auroral Mapper (JIRAM) onboard Juno spacecraft ([145]), and the brighter trailing hemisphere shielded by the magnetosphere ([164]). The origin of the darkening agents identified as meteoric rocks, like chondrites, could be endogenous or exogenous or both, and it is still under debate ([34]). The composition of the dirty ice mixture of the surface (water ice and the darkening agent) and the distribution of the impurities of the ice along the crust are crucial to the comprehension of future radar data and they are addressed deeply in Chapter 8. In summary the main compounds detected on the surface are:

- **Water ice**, the most abundant component of Ganymede's surface dominates both the bright and dark terrains. Its detection has been facilitated by several instruments, including the Near-Infrared Mapping Spectrometer (NIMS) onboard the Galileo spacecraft and by ground based observation ([105]).
- **Carbon dioxide** detected by HST and JWST measuring specific spectral lines corresponding to CO_2 absorption features ([27]).

- **Frost sulfur dioxide** identified in the trailing hemisphere with the space-based telescope International Ultraviolet Explorer (IUE) ([58]).
- **Silicates** primarily in the dark regions contributing to the coloration and albedo differences across various surface areas detected through the identification of absorption features ([141]).
- **Hydrogen peroxide**, believed to exist in small quantities on the surface of Ganymede, potentially formed through photolytic processes under ultraviolet light from the Sun. Its detection occurs through remote sensing techniques by HST and JWST ([27]).
- **Tholins** formed through chemical reactions involving carbon-rich materials under ultraviolet light, detected through spectral analyses associated with organic materials ([141]).
- **Sulfuric acid hydrates** indicated by specific absorption features. These compounds are of particular interest because they may indicate geochemical complexity relating to Ganymede's potential subsurface ocean ([27]).
- **Mixtures** of $NaCl{\cdot}H_2O$, NH_4Cl, $NaHCO_3$ or $(NH_4)_2CO_2$ and $Na_2Mg(SO_4)_2{\cdot}4H_2O$ detected through high spatial resolution infrared spectra observed with JIRAM in the trailing hemisphere.

From a morphologic point of view older dark terrains exhibit a rugged appearance, characterized by concentric furrows and various geological structures formed through processes such as impact gardening and the thermal segregation of materials and ancient tectonic activities ([11]). The presence of heavier materials and sedimentation processes over time may have contributed to the accumulation of these darker materials. The younger bright grooved terrain, primarily composed of clean, crystalline water ice, exhibits a high albedo, resulting in its bright appearance. They are characterized by smooth surfaces, often exhibiting parallel ridges and troughs known as *sulci*. These features indicate tectonic and cryovolcanic resurfacing processes driven by tidal heating that have significantly modified the surface over time ([34]). The relative youth of grooved terrain, inferred from low crater densities, indicates ongoing or recent geological activity.

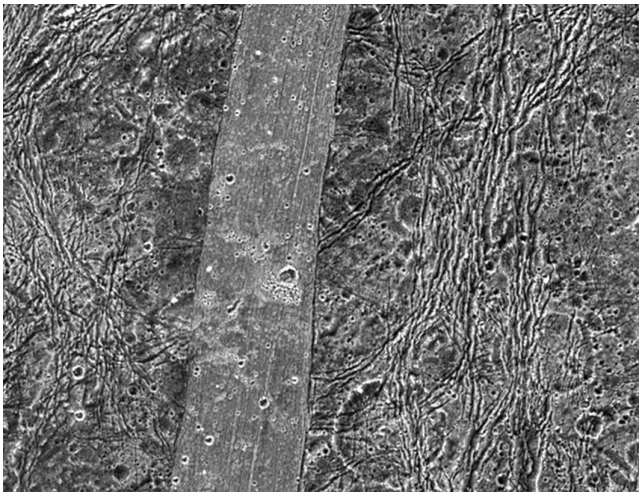

Figure 2.1: The picture of the region of *Nicholson Regio/Arbela Sulcus*, taken by NASA's Galileo spacecraft, shows the contrast between the smooth bright terrain and the surrounding highly fractured dark terrain. Credit: *NASA/JPL/Brown University*.

2.1.3 Interior

Ganymede's internal structure, as revealed by gravitational field measurements from the Galileo spacecraft, consists of a differentiated three-layer system (Fig. 2.2): a metallic iron core, a rocky silicate mantle, and an outer shell of water ice and liquid water. The iron core, with a radius estimated at 700-900 km, generates the satellite's magnetic field through dynamo action, requiring the presence of liquid metal and sufficient convective motion ([108]). Surrounding the core the mantle is composed of various silicate materials and may contain significant amounts

of sulfur and other volatile compounds, affecting both the thermal evolution and potential geochemistry of the satellite. The outermost ice shell represents perhaps the most complex and scientifically intriguing component of Ganymede's structure. Theoretical models and observational evidence suggest a multi-layered ice shell with a thickness of 100 or more kilometers, potentially containing a subsurface ocean.

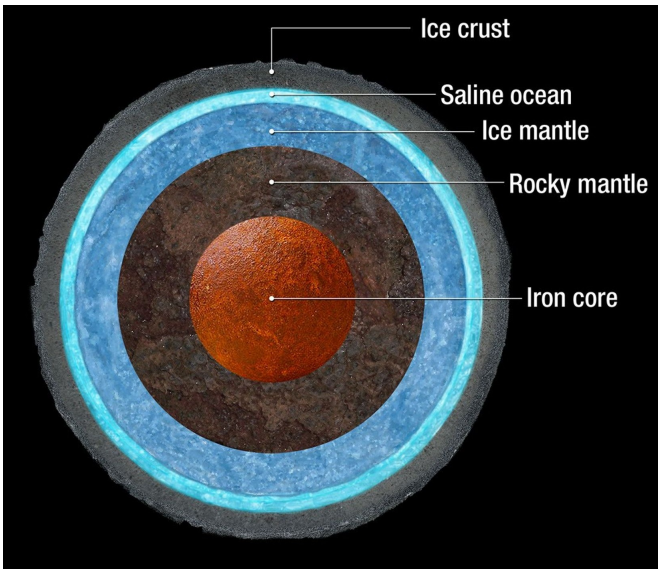

Figure 2.2: Illustration of Ganymede's interior based on theoretical models and on observations by NASA's Galileo orbiter, and HST. Credit: *NASA, ESA, and A. Feild (STScI).*

2.1.4 Ocean

The presence of an interior ocean makes Ganymede a very interesting target also for the search for habitability conditions. Its presence has been inferred by many factors:

- **Magnetic field measurements** suggest the presence of a conductive layer beneath the surface. The Galileo magnetometer data indicate an ocean of electrically conductive liquid, likely salty water ([109]).
- HST data of Ganymede's **auroral patterns** show variations that could be explained with interactions between its magnetic field and a subsurface ocean. The oscillation patterns of these auroras provide indirect evidence for the presence of a conductive layer beneath the ice, consistent with a subsurface ocean ([178]).
- **Thermal models** predict that Ganymede must harbor a subsurface ocean if the moon has experienced sufficient tidal heating from gravitational interactions with Jupiter and other Galilean moons.

The ocean is thought to exist in a *water sandwich* ([148]) configuration between two layer of ices in different pressure phases: a lower pressure phase above (Ice I) and a higher pressure phase below (Ice V and VI). Other models predict instead an alternation of liquid water layers and different ice phases in a *club sandwich* configuration. The ocean is probably highly saline since it has to be very conductive according to the observations. It contains various ions, like sodium or sulfate, coming from interactions between the ocean and the rocky mantle and dissolved salts like $Mg(SO_4)_2$ ([203]).

2.2 Europa

Europa is the fourth largest moon of Jupiter and the smallest of the four Galilean satellites; it is slightly smaller than the Earth's Moon, but its ocean is probably the most extensive liquid water ocean in the Solar System, harboring more than twice the volume of all Earth's oceans. Europa represents one of the most compelling targets for astrobiological investigation not only because of the presence of the subsurface ocean, but for its dynamic interaction with the thin icy shell. The moon's subsurface ocean, maintained in liquid state through tidal heating generated

by Jupiter's gravitational influence, represents a stable aquatic environment that has likely persisted for billions of years. The detection of plume event by HST ([173]) confirmed the dynamic interactions between the ocean and the icy shell that facilitate the possible circulation of organic compounds and the availability of energy sources necessary to support biological processes. The intense activity of this satellite is also proven by the lack of craters probably due to cyclical resurfacing phenomena and plates tectonic activities ([202]). Since it is tidally locked, also Europa has a trailing and a leading hemisphere. The main physical parameters of Europa are shown in Tab. 2.2.

Mean radius	1560.7 ± 0.7 km
Mass	0.480 $\times 10^{23}$ kg
Density	3.014 g/cm^3
Intrinsic magnetic field at equatorial surface	-
Ambient Jovian magnetic field	420 nT
$\frac{C}{MR^2}$	0.346 ± 0.005
Mean Surface Temperature	90 K
Rotational Period	3.551 days

Table 2.2: Physical parameters of Europa ([181], [8]).

2.2.1 Atmosphere

Europa has a tenuous atmosphere predominantly characterized by molecular oxygen O_2, along with smaller amounts of other gases such as hydrogen H_2 and water vapor H_2O. O_2, the most abundant component is produced via radiolysis of water ice on its surface caused by high-energy particles from Jupiter's magnetosphere ([195]). It has been detected by HST through specific far-ultraviolet emissions ([174]). H_2, present in smaller quantities, is generated through the photodissociation of water ice and it is more abundant at higher altitude. The water vapor is associated with active geological processes and may periodically escape into the atmosphere, possibly through geysers or plumes originating from the subsurface ocean ([173]). It is more abundant at poles. In addition to molecular oxygen, atomic oxygen has been identified, probably produced by the dissociation of O_2 ([76]) from the magnetosphere electrons. The interaction between Europa's atmosphere and its environment is significantly influenced by Jupiter's intense magnetosphere.

2.2.2 Surface

Europa presents a distinctive and varied surface characterized by several types of terrain, each reflecting its complex geological history and ongoing processes. The main features are:

- **Chaos terrains** is characterized by disrupted and chaotic ice blocks, thought to form due to subsurface processes, such as the upward movement of warmer ice or liquid water from the ocean below, causing the overlying ice to fracture and become chaotic ([200]).
- **Lineae**, linear cracks and ridges, provide evidence of tectonic activity and are believed to be the result of tidal forces exerted by Jupiter.
- **Ridged plains** are expansive areas marked by a series of parallel ridges and grooves that likely formed from tectonic stresses across the ice shell, less disrupted than chaos terrains, indicating that they may be older.
- **Lenticulae, pits, and domes** are circular features which are believed to form from beneath the ice shell due to thermal-induced processes. Pits often result from the collapse of surface layers due to subsurface activities, while domes may form as a result of upwellings from the ocean below, creating topographic uplift as materials intrude into the overlying ice layer ([154], [184]).
- **Bright and dark regions** are present also on Europa with pure water ice regions and areas characterized by a larger amount of impurities, such as salts.

Figure 2.3: Chaotic terrain on Europa, an evidence of some of the most recent geologic activity. Credit: *NASA/JPL, Caltech*.

The interactions with the inner ocean, the highly dynamic activity of the satellite, its proximity to Jupiter, the lack of shielding due to the absence of an intrinsic magnetic field, and the presence of a tenuous atmosphere all cause the accumulation of numerous compounds on Europa's surface, of both exogenous and endogenous origin. The main compounds detected on the surface are:

- **Water ice** covers most of the moon's surface; it is purer in the bright terrain and with impurities in the darker terrain ([94]).
- **Hydrated sulfate minerals** such as magnesium sulfate detected through analyses conducted by the Near-Infrared Mapping Spectrograph (NIMS) onboard the Galileo spacecraft. These sulfates are a possible indication of the interaction of the ocean with the surface and could be a hint for the ocean's composition ([180]).
- **Sodium chloride** has been observed by HST. This finding suggests that $NaCl$ could be a significant component of the subsurface ocean ([199]).
- **Hydrogen peroxide** is present primarily in its leading hemisphere. Its presence is attributed to radiolytic processes, wherein energetic particles from Jupiter's magnetic field interact with water ice, generating H_2O_2 as a product ([94]).
- **Carbon dioxide** has been mapped using data from various studies, indicating potential internal sources of carbon. Understanding CO_2's origins is essential, as it may derive from subsurface ocean chemistry, impact delivery, or radiation processing of surface materials ([198]).

From a radar point of view it is very important to know the composition of the crust and the discrimination from endogenous and exogenous compounds to evaluate the instrument performances, therefore this topic is addressed more in depth in Chapter 8.

2.2.3 Interior

According to some current models, Europa's internal structure consists of four distinct layers (Fig. 2.4): a metallic core, a silicate mantle, a subsurface ocean, and an outer icy crust extending to the surface. The origin, structure, composition, and size of the core are still under debate. Even the thickness of the shell is not well characterized, since it changes significantly depending on the study. For instance, the differentiated layers model of Fig. 2.4 with a metallic core, supported by Galileo mission measurements, has been proposed by [3]. However, recent studies, such as those by [197], have considered the possibility of a core smaller than previously assumed, impacting the moon's ability to generate a dynamo and indicating a more complex evolution. Surrounding the core the rocky mantle is probably composed of silicate minerals. The interaction between the ocean and the rocky mantle could produce hydrothermal activity and enrich the ocean chemically creating habitable environments ([176]). Regarding the icy

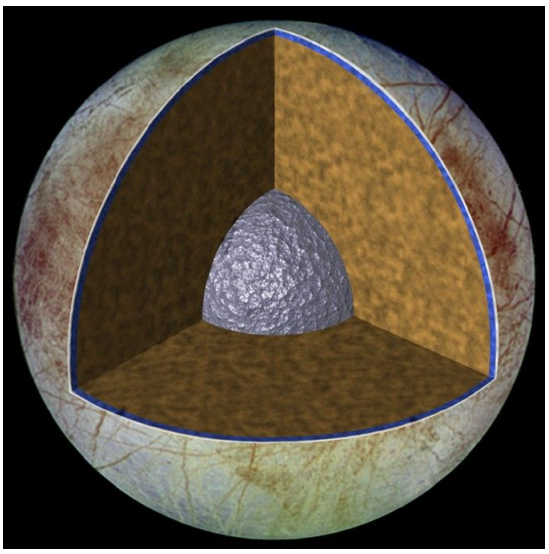

Figure 2.4: Illustration of a possible internal structure of Europa formed by a metallic (iron and nickel) core (shown in gray), surrounded by a rock shell (shown in brown), surrounded by a shell of liquid water (shown in blue) and an ice shell (shown in white). Credit: *NASA/JPL*.

shell, [23], basing on the previous literature, reported several possible methods to model its thickness going from few km to more than 40 km. Recently, [207] explores the effects of tidal heating by Jupiter and geophysical processes could change the ice thickness. The dimension of the icy shell also influences thermal dynamics; the heat transfer could be through conduction, convection or both. In the case of a thin shell the main regime is conduction, and, for a thicker one, the convection could be the major heat transfer regime ([140]).

2.2.4 Ocean

The interior ocean is probably characterized by a dynamic convection and frequent interactions with the icy shell ([9]). Its composition remains under debate: according to some studies, the dominant salt is $MgSO_4$, while others suggest that the ocean is primarily composed of water and $NaCl$. The salinity of the ocean is significant, as it affects the freezing point and the density of the water, which could influence the ocean's temperature and chemistry. The evidence for the presence of a subsurface ocean on Europa is:

- **Magnetic field** data from Galileo magnetometer implied the presence of a conductive layer in the moon's interior. The conductive salty liquid water ocean creates an induced magnetic field as Europa moves through Jupiter's magnetic field ([103]).
- **Surface geological evidence** such as chaos terrain and resurfacing features as mentioned above.
- **Water vapor plume events** observed by HST ([173]).
- **Gravitational measurements** by Galileo show that Europa's internal structure is consistent with a differentiated body containing a liquid layer.

The possibility of detecting directly the ocean with radar instruments due to the likely thin icy crust is very exciting for the future missions and is discussed deeply in Chapter 8.

2.3 Callisto

Callisto is the second largest moon of Jupiter and the most distant of the Galilean satellites. Because of its position, Callisto is less influenced by the planet's intense gravitational and tidal forces, leading to a remarkably stable environment. This stability has allowed the preservation of ancient surface features, making Callisto a prime candidate for studying the evolution of icy moons. Its heavily cratered ice-rich surface may represent an example of what the Jovian system, and also the Solar System was like in its early stages. The combination of its ancient, stable environment, substantial water inventory, and relative accessibility for spacecraft exploration positions Callisto at the forefront of astrobiology research and Solar System exploration.

Like the other Galilean moons it is tidally locked with Jupiter, meaning that it is characterized by a leading and a trailing hemispheres. Tab. 2.3 shows the main physical parameters of Callisto.

Mean radius	2408.4 ± 0.3 km
Mass	1.076 $\times 10^{23}$ kg
Density	1.839 g/cm^3
Intrinsic magnetic field at equatorial surface	-
Ambient Jovian magnetic field	35 nT
$\frac{C}{MR^2}$	0.359 ± 0.005
Mean Surface Temperature	150 ± 50 K
Rotational Period	16.689 days

Table 2.3: Physical parameters of Callisto ([181],[121]).

2.3.1 Atmosphere

Callisto's atmosphere is thin and exhibits seasonal variability as well, influenced mainly by changes in solar radiation and its spatial distribution across the moon's surface ([41]). It is significantly shaped by its interaction with Jupiter's magnetosphere, which creates electromagnetic effects that can lead to the sputtering of surface materials. Callisto's atmosphere is primarily composed of several gases with varying origins, which are affected by interactions with Jupiter's intense magnetosphere. One of the main constituents is carbon dioxide, detected by JWST through absorption spectra features associated with solid-state carbon-dioxide ice. This indicates that potential sources of CO_2, are the sublimation processes of surface ice ([41]). The atmospheric CO_2 is distributed heterogeneously across the surface. Other compounds detected are the same of the other icy moons like molecular hydrogen, probably originated from the dissociation of water ice on the surface, due to radiation processing and radiolysis of resulting from energetic particle bombardment from Jupiter's magnetosphere ([124], [39]). Also brief emissions of water vapor might arise during sublimation events, especially under conditions of surface heating ([65]).

2.3.2 Surface

Callisto's surface is dominated by a significant number of impact craters (Fig. 2.5), displaying some of the oldest geological features in the Solar System. Its craters change in size exhibiting features like secondary craters, indicating a complex history of impact events. The surface displays a combination of dark and bright regions, often associated with varying compositions. The dark areas contain a higher concentration of non-ice materials, likely due to processes such as impact gardening and the retention of impact ejecta. In contrast, the brighter areas predominantly consist of water ice. Some regions are similar to the chaotic terrains of the other moons, but less common. The main impact feature is the Valhalla crater, the largest multi-ring basin of the satellite, with a bright central region of 600 km in diameter, surrounded by an extensive ring system. It is located on the leading hemisphere of Callisto ([185]). The compounds detected on the surface could be indicative of the interior characteristics of Callisto or caused by space weathering events:

- **Water ice** is the dominant component of Callisto's surface confirmed through spectroscopic observations ([161]).
- **Carbon dioxide** in significant quantities especially around impact craters and in various surface features. Their concentrations indicate that it might play a role in Callisto's surface processes and potential geochemistry ([85]).
- **Sulfur dioxide** detected through spectral analyses may be linked to the processes of surface modification driven by radiation from Jupiter's magnetosphere ([85]).
- Some studies suggested the presence of **organic materials**, like tholins and other carbon-rich compounds ([137]).

- **Hydrated sulfates and other mineral compounds** have also been identified on the surface of Callisto, indicating possible interactions between the icy shell and the underlying rocky structure.

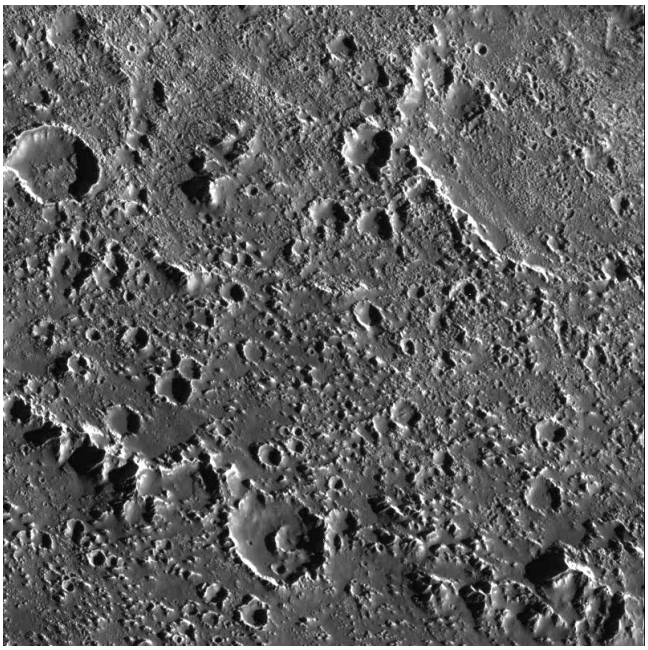

Figure 2.5: An example of the heavily cratered surface of Callisto, the textured terrain in the Asgard basin. Credits: *NASA/JPL*.

2.3.3 Interior

The structure of the interior of Callisto is still under debate. Unlike Europa and Ganymede, which show evidence of significant internal differentiation, Callisto appears to have experienced only partial differentiation, potentially retaining a primordial structure (Fig. 2.6). Some models suggest that it has a uniform composition where dense materials have not completely separated from the ice. This is supported by evidence suggesting that Callisto has a relatively low degree of internal heating, resulting in little geological activity compared to more active moons. Its interior is primarily composed of a mixture of water ice and rocky materials. It is generally believed to have a bulk composition similar to that of carbonaceous chondrites, with a significant fraction of water ice mixed with silicate rock ([112]). This ice-rich nature suggests the possibility of a subsurface ocean interacting with the rocky mantle underneath. This incomplete differentiation may be key to understanding how Callisto could maintain a subsurface ocean despite its distance from Jupiter and the correspondingly weak tidal heating. Considering the hypothesis of differentiation, various models suggest a possible internal structure consisting of a thin ice shell overlaying a mixed ice-rock mantle and a dense core ([144]) indicated the existence of two and three-layer models, reflecting hydrostatic equilibrium and considering different degrees of differentiation. The core is hypothesized to be composed of a rocky-iron mixture consisting mainly of silicates with possibly some metallic content.

2.3.4 Ocean

Even though it is the least active and the most distant of the Jovian icy moons, Callisto shows evidence of the presence of a subsurface liquid ocean beneath its thick crust (100-300 km) similar to the other satellites:

- **Magnetic field data** collected by Galileo mission suggest the existence of a subsurface layer that conducts electricity, possibly corresponding to a salty ocean. The observed induced currents and magnetic phenomena from Jupiter's magnetosphere could be linked to a subsurface ocean rather than being solely attributed to magnetospheric plasma interactions ([125], [47]).

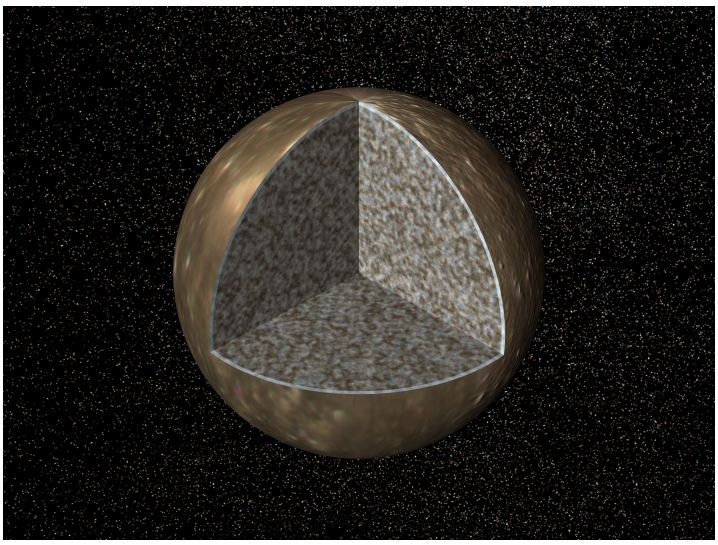

Figure 2.6: Possible interior structure of Callisto. Credits *NASA/JPL*

- Some regions present **surface features** of chaos terrain and substantial modification due to possible internal processes coherent with the presence of a liquid water ocean.

The possible composition of the subsurface ocean include the presence of salts such as $MgSO_4$ and $NaCl$ (like in the other moons) influencing the temperature of the liquid water lowering its freezing point. These salts may be derived from chemical interactions between the ocean, the crust and the rocky mantle below.

2.4 The Missions

Due to the considerable scientific interest it has aroused and its distinctive characteristics, the Jovian system has been the target of multiple space missions, which have carried out both flybys and extended orbital investigations.

- **Pioneer program (10 and 11)** launched in the early 1970s provided the first close-up images of Jupiter and crucial data regarding its atmospheric characteristics, magnetic field, and radiation belts.
- **Voyager missions (1 and 2)** in 1979 conducted detailed flybys of Jupiter and its Galilean moons discovering volcanic activity on Io and Jupiter's faint ring system ([185]).
- **Ulysses** made two flybys in 1992 and 2004 measuring Jovian magnetosphere and solar wind properties in Jovian environment.
- **Galileo** mission ([95]) from 1995 to 2003 is the first Jupiter orbiter. It conducted numerous flybys of the Galilean satellites leading to groundbreaking discoveries such as the subsurface ocean on Europa and the intrinsic magnetic field of Ganymede. Its data continue to influence ongoing research regarding Jovian dynamics and magnetospheric phenomena.
- **Cassini** ([165]) mission captured high-resolution images during its flyby on its way to Saturn.
- **New Horizon** used Jupiter for a gravity assist providing observation of Io's volcanic activity and of Jovian atmosphere and magnetosphere in 2007.
- **Juno mission** ([28]) entered the orbit in 2016 and is to date orbiting around Jupiter using advanced imaging techniques and spectroscopic instruments to provide insights into the chemistry and dynamics of the Jovian atmosphere. It also conducted close flybys of Ganymede (2021), Europa (2022), and Io (2023–2024).

This thesis project aims at supporting the missions to the Jovian System (JUICE and Europa Clipper) and especially the radar instruments (RIME and REASON) that are going to probe the interior of the icy moons.

2.4.1 JUICE

The JUpiter ICy moons Explorer (JUICE) ([71]) mission has been launched on April 14, 2023 by the European Space Agency. Its primary objective is to characterize the possibility of habitable environments on Europa, Ganymede, and Callisto. The mission plans to enter the Jovian System in July 2031, will undertake a series of flybys of the Jovian moons during the four-year Jupiter orbital phase, followed by an orbital phase around Ganymede being the first spacecraft orbiting around a moon other than Earth's Moon. The mission is designed to conduct a comprehensive assessment of these moons icy shells, internal oceans, and potential geophysical activity, utilizing a suite of 10 advanced instruments:

- **JANUS** (Jovis, Amorum ac Natorum Undique Scrutator) is a high-resolution optical camera designed to capture detailed images of the icy moons providing critical surface and geological information ([54])
- **GALA** (GAnymede Laser Altimeter) is a laser altimeter capable of measuring the surface of Ganymede with high precision. It will help map the topography of the moon, analyze its surface features, and investigate the ice shell's thickness ([63]).
- **RIME** (Radar for Icy Moon Exploration) is a radar sounder that will penetrate the icy crusts of the moons to investigate subsurface structures, providing insights into the thickness of the ice layers and the presence of any liquid water beneath ([36]).
- **MAJIS** (Moons And Jupiter Imaging Spectrometer) is a visible-infrared hyperspectral imaging spectrometer that will observe cloud features and atmospheric constituents on Jupiter, and characterize ices and minerals on the icy moon surfaces ([166]).
- **3GM** (Gravity and Geophysics of Jupiter and the Galilean Moons) will measure gravity fields of the moons (and Jupiter), atmospheric structure and will infer internal density distributions ([38]).
- **PEP** (Particle Environment Package) consists in several sensors studying the plasma environment around Jupiter and its moons measuring energetic particles, including ions and electrons ([17]).
- **J-MAG** is the JUICE Magnetometer equipped with sensors to characterize the Jovian magnetic field and its interaction with that of Ganymede ([59]).
- **RPWI** (Radio and Plasma Wave Investigation) will characterize the radio emission, plasma environment and electric and magnetic fluctuations of Jovian system using a suite of sensors and probes ([205]).
- **UVS** (UltraViolet imaging Spectrograph) will characterize the composition and dynamics of the exospheres of the icy moons, studying the Jovian aurorae, the structure of the planet's upper atmosphere ([53]).
- **SWI** (Sub-millimeter Wave Instrument) is a Sub-millimeter Radiometer that is designed to investigate the temperature structure, composition and dynamics of Jupiter's atmosphere, and the exospheres and surfaces of the icy moons ([77]).

RIME

RIME is a low-frequency radar sounder designed to penetrate the icy crusts, to investigate the relationship between the distribution of non-ice material, geological features, and subsurface processes, and to explore the recently active zones. Radar main parameters are shown in Tab. 2.4. Some parameters will change during the circular orbiting phase and the flybys. The pulse repetition frequency varies from 200-400 Hz during the circular orbital phase to 500 Hz during flybys; so do the receiver window length (117-226 μs during orbits, 226 μs during flybys), and the data rate (216-250 kbps during Ganymede orbital phase, 2400 kbps during flyby phases). The penetration of the radar depends on its altitude and the composition of the subsurface. Under optimal conditions (pure cold ice) it is expected to probe as deep as 9 km below the surface or even more, but it is very sensitive to temperature gradient and to composition, therefore high temperatures and impurities in the ice would limit significantly the penetration. These topics are addressed deeply in Chapter 8.

Parameter	Description
Operating altitude range	200–1000 km
Antenna length	Dipole of 16 m
Central frequency	9 MHz
Bandwidth	1 and 3 MHz
Peak radiated power	10 W
Chirp length	50-100 μs
Radar mass (includes Harness)	9.7 kg
Vertical resolution in ice	30 - 90 m
Cross-track resolution	2 - 10 km
Along-track resolution	0.3 - 1 .0 km
Spatial resolution	0.3-1 km (with ground processing)
Expected SNR	55 dB

Table 2.4: RIME main parameters ([36]).

2.4.2 Europa Clipper

The mission Europa Clipper has been launched on October 24, 2024 and will approach the Jovian System in 2030. It will not orbit around any of the icy satellites, but it will conduct several flybys around the icy moons focusing on Europa. Planned flybys of Europa are indeed 49 ([155]). Its primary objective is to examine the icy moons seeking potential environments suitable for life as we know it. To achieve this goal it carries 9 science instruments onboard:

- **Europa-UVS**, Europa Ultraviolet Spectrograph, investigates the atmosphere, detecting any active plumes. It explores the surface composition providing information about the relationship between Europa and Jovian magnetosphere ([170]).
- **EIS**, Europa Imaging System, designed to perform a global high-resolution coverage, three-dimensional digital terrain models, and meter-scale imaging to characterize the surface of Europa ([201]).
- **MISE**, Mapping Imaging Spectrometer for Europa, maps the surface composition at the spatial scales relevant to analyze geologic processes through infrared reflectance spectroscopy ([25]).
- **E-THEMIS**, Europa Thermal Emission Imaging System, a three-band thermal infrared imager, designed to map temperatures focusing on any heat flow anomalies and detect passive thermal signatures of geologically recent activities ([45]).
- **REASON**, Radar for Europa Assessment and Sounding: Ocean to Near-surface, uses radar echo sounding to probe Europa's subsurface, looking for any evidence of the liquid water to determine possible habitability condition and to investigate the relationship between the crust and the inner ocean ([26]).
- **MASPEX**, MAss Spectrometer for Planetary EXploration - Europa, is a spectrometer that aim at analyzing the exosphere through the detection of atomic, molecular, and isotopic composition of neutral volatiles in the exosphere ([206]).
- **SUDA**, SUrface Dust Analyzer, a reflectron-type impact ionization mass spectrometer that analyzes the elemental and molecular constituents of ice and dust in the exosphere ([100]).
- **ECM**, Europa Clipper Magnetometer, measures the magnetic inductive response at multiple natural frequencies, associated with Jupiter's rotation period and with Europa's orbital period, and the harmonics and beat frequencies of these two fundamental cycles ([107]).
- **PIMS**, Plasma Instrument for Magnetic Sounding, measures the plasma distributions perturbing the magnetic field around Europa ([209]).

REASON

REASON is a dual-frequency ice-penetrating radar designed to probe the interior and characterize the surface and the exosphere of Europa. It will be the first ice-penetrating radar to explore the outer Solar System followed by RIME. The two radar instruments will observe the same targets and operate in the same period and at the same frequency and will therefore work in conjunction to provide a comprehensive overview of the crust of the icy satellites, particularly Europa. REASON is able to work in two main operational modes, High Frequency mode (HF) and Very High Frequency mode (VHF) with different parameters. Main parameters are shown in Tab. 2.5. REASON will operate using a combination of radar measurement techniques: sounding, reflectometry, altimetry, interferometery, and plasma characterization. The combination of 9 MHz and 60 MHz allows a complete analysis of the crust in terms of high penetration (9 MHz) and high surface resolution (60 MHz). The capability to identify traces of brines in the upper part of the crust, and the possibility to infer the composition analyzing the attenuation of radar waves, for RIME and REASON, is addressed in Chapter 8.

Parameter	**Description**
Operating altitude range	25 km to 1000 km from Europa
Antenna length	Two 8.8m monopoles (HF) and a dipole of 2.76 m (VHF).
Central frequency	9 MHz (HF) and 60 MHz (VHF)
Bandwidth	1 MHz and 10 MHz
Radiated Power	10 W - 30 W
Pulse Length	30 μs - 100 μs
Radar mass	32 kg
Pulse Repetition Frequency (PRF)	50 Hz–3 kHz
Vertical resolution in ice	30 m (VHF) - 300 m (HF)
Along-track resolution	2 km (VHF) - 5.5 km (HF)

Table 2.5: REASON main parameters ([26]).

Chapter 3

Electromagnetic Theory

This chapter introduces the fundamental concepts of electromagnetic (EM) theory, starting from Maxwell's equations, to establish the theoretical basis of electromagnetic methods and their useful techniques for the investigation of celestial bodies interior. These methods work by transmitting EM energy through the surface, into the subsurface and measuring how the constituent materials respond to this excitation, thereby revealing essential information about subsurface structures and compositions. The propagation of EM energy is governed by three fundamental physical quantities: **electrical conductivity**, **dielectric permittivity**, and **magnetic permeability**. These electromagnetic properties are themselves dependent on various physical parameters, including the frequency of the applied EM field, temperature, rock mineralogy, and water content. Here we introduce the EM properties measured in the Chapter 7 and how they are connected with the radio echo sounding technique (Chap. 5).

3.1 Maxwell Equations

The unification of electric and magnetic phenomena was accomplished by Maxwell in his historical work [135]. Maxwell's equations provide a complete mathematical description of electromagnetic radiation propagation through space by establishing the relationships between electric and magnetic fields through a system of differential equations. This set of equations embodies Faraday's law of induction (Eq. 3.1), Ampere's law (Eq. 3.2), Gauss laws of electric (Eq. 3.3) and magnetic field (Eq. 3.4) and describes and relates field vectors, current densities, and charge densities in both space and time. Maxwell equations in time-domain are shown here below:

$$\nabla \times \vec{E}(\vec{r},t) = -\frac{\partial \vec{B}(\vec{r},t)}{\partial t} \tag{3.1}$$

$$\nabla \times \vec{H}(\vec{r},t) = \vec{J}(\vec{r},t) + \frac{\partial \vec{D}(\vec{r},t)}{\partial t} \tag{3.2}$$

$$\nabla \cdot \vec{D}(\vec{r},t) = \rho_q(\vec{r},t) \tag{3.3}$$

$$\nabla \cdot \vec{B}(\vec{r},t) = 0 \tag{3.4}$$

where:
$\vec{E}(\vec{r},t)$ is the electric field intensity in V/m;
$\vec{B}(\vec{r},t)$ is the magnetic flux density in Wb/m^2;
$\vec{H}(\vec{r},t)$ is the magnetic field density in A/m;
$\vec{D}(\vec{r},t)$ is the electric flux density in C/m^2;
$\vec{J}(\vec{r},t)$ is the current density A/m^2;
$\rho_q(\vec{r},t)$ is the electric charge density in C/m^3.

All of these quantities are dependent on the spatial $\vec{r}$ and t temporal coordinates.
The current density could be expressed as the sum of $\vec{J_s}(\vec{r},t)$ and $\vec{J_c}(\vec{r},t)$, respectively the source electric current density and the conduction electric current density. In order to describe the interaction between EM field and the matter it is useful to introduce macroscopic quantities with the following constitutive relations:

$$\vec{J_c}(\vec{r},t) = \sigma * \vec{E}(\vec{r},t) \tag{3.5}$$

$$\vec{D}(\vec{r},t) = \varepsilon * \vec{E}(\vec{r},t) \tag{3.6}$$

$$\vec{B}(\vec{r},t) = \mu * \vec{H}(\vec{r},t) \tag{3.7}$$

where:
σ is the conductivity in S/m;
ε is the dielectric permittivity of the medium in F/m;
μ is the magnetic permeability of the medium in H/m;
$*$ is the convolution product.
These three quantities depend on the medium in which EM field propagates. ε and μ indeed could be written as:

$$\varepsilon = \varepsilon_r \varepsilon_0 \tag{3.8}$$

$$\mu = \mu_r \mu_0 \tag{3.9}$$

in which ε_r and μ_r are the relative (material-dependent) parts, while ε_0 and μ_0 are the permittivity and permeability of the free space and their values are:

$$\varepsilon_0 = 8.854 \times 10^{-12} F/m \tag{3.10}$$

$$\mu_0 = 4\pi \times 10^{-7} H/m \tag{3.11}$$

The conductivity σ in free space is zero.
However, Eq. 3.5, 3.6, 3.7 are not the most general cases, in fact they contain the assumptions of **homogeneity**, **linearity**, **isotropy** and **non-dispersion** of the materials involved.

- In the case of **inhomogeneity**, ε, μ, σ are position-dependent $\vec{r}$ and the equations become:

$$\vec{J_c}(\vec{r},t) = \sigma(\vec{r}) * \vec{E}(\vec{r},t) \tag{3.12}$$

$$\vec{D}(\vec{r},t) = \varepsilon(\vec{r}) * \vec{E}(\vec{r},t) \tag{3.13}$$

$$\vec{B}(\vec{r},t) = \mu(\vec{r}) * \vec{H}(\vec{r},t) \tag{3.14}$$

- In the case of **non-linearity** ε, μ, σ depend on the EM field applied and the equations become:

$$\vec{J_c}(\vec{r},t) = \sigma(E) * \vec{E}(\vec{r},t) \tag{3.15}$$

$$\vec{D}(\vec{r},t) = \varepsilon(E) * \vec{E}(\vec{r},t) \tag{3.16}$$

$$\vec{B}(\vec{r},t) = \mu(H) * \vec{H}(\vec{r},t) \tag{3.17}$$

- In the case of **anisotropy** ε, μ, σ depend on the direction of the applied EM field and could be expressed as a tensor relation, for example Eq. 3.7 in case of anisotropy becomes:

$$\begin{pmatrix} B_x \\ B_y \\ B_z \end{pmatrix} = \begin{pmatrix} \mu_{xx} & \mu_{xy} & \mu_{xz} \\ \mu_{yx} & \mu_{yy} & \mu_{yz} \\ \mu_{zx} & \mu_{zy} & \mu_{zz} \end{pmatrix} \begin{pmatrix} H_x \\ H_y \\ H_z \end{pmatrix} \tag{3.18}$$

- In cases of **dispersive materials**, which is very common in practical application the response to the EM field is time-dependent and the equations become:

$$\vec{J_c}(\vec{r},t) = \sigma(t) * \vec{E}(\vec{r},t) \tag{3.19}$$

$$\vec{D}(\vec{r},t) = \varepsilon(t) * \vec{E}(\vec{r},t) \tag{3.20}$$

$$\vec{B}(\vec{r},t) = \mu(t) * \vec{H}(\vec{r},t) \tag{3.21}$$

3.1.1 Maxwell Equations in the Frequency Domain

Since the constitutive relations (Eq. 3.5, 3.6 and 3.7) contain the convolution product, it could be convenient to switch to frequency domain applying Fourier transform pair. For a function $a(t)$ the relation with the Fourier transform $A(\omega)$ is given by:

$$\mathcal{F}\{a(t)\} = A(\omega) = \int_{-\infty}^{+\infty} a(t)\, e^{-i\omega t}\, dt, \tag{3.22}$$

$$a(t) = \frac{1}{2\pi} \int_{-\infty}^{+\infty} A(\omega)\, e^{i\omega t}\, d\omega. \tag{3.23}$$

in which ω is the angular frequency defined as $2\pi f$ where f is the frequency. Maxwell equations in the frequency domain are given by the Eq. 3.24 -3.27.

$$\nabla \times \vec{E}(\vec{r},\omega) = -i\omega \vec{B}(\vec{r},\omega) \tag{3.24}$$

$$\nabla \times \vec{H}(\vec{r},\omega) = \vec{J}(\vec{r},\omega) + i\omega \vec{D}(\vec{r},\omega) \tag{3.25}$$

$$\nabla \cdot \vec{D}(\vec{r},\omega) = \rho(\vec{r},\omega) \tag{3.26}$$

$$\nabla \cdot \vec{B}(\vec{r},\omega) = 0 \tag{3.27}$$

The advantage of operating in the Fourier domain lies in the fact that the Fourier transform of a convolution product between two functions a, b reduces to a simple product, as expressed in Eq. 3.28.

$$\mathcal{F}\{a(t) * b(t)\} = A(\omega)B(\omega) \tag{3.28}$$

Then, the constitutive relations in Eq. 3.19, 3.20, 3.21 become:

$$\vec{J}_c(\vec{r},\omega) = \sigma(\omega)\vec{E}(\vec{r},\omega) \tag{3.29}$$

$$\vec{D}(\vec{r},\omega) = \varepsilon(\omega)\vec{E}(\vec{r},\omega) \tag{3.30}$$

$$\vec{B}(\vec{r},\omega) = \mu(\omega)\vec{H}(\vec{r},\omega) \tag{3.31}$$

The constitutive relations in the case of dispersive material and frequency domain are fundamental to understand the results in Chap. 7, and studying the variation of ε, μ, σ with temperature, frequency and composition is crucial to perform correct analyses of radar data. To establish a rigorous understanding of the relationship between the radar data analysis and the electromagnetic properties of materials, the following section derives the wave equation and defines the propagation parameters governing electromagnetic wave transmission through lossy media.

3.2 The Wave Equation

To derive the equations that describe the propagation of EM waves the first step is the combination of Maxwell equations (3.1 -3.4) and constitutive equations (3.5 - 3.7) obtaining Eq. 3.32 - 3.35.

$$\nabla \times \vec{E} = -\mu \frac{\partial \vec{H}}{\partial t} \tag{3.32}$$

$$\nabla \times \vec{H} = \vec{J}_s + \sigma \vec{E} + \varepsilon \frac{\partial \vec{E}}{\partial t} \tag{3.33}$$

$$\nabla \cdot \vec{E} = \rho_q / \varepsilon \tag{3.34}$$

$$\nabla \cdot \vec{H} = 0 \tag{3.35}$$

Applying the curl to the left member of 3.32 and 3.33 and using the property of the curl for a generic vector $\vec{V}$ in 3.36, we obtain 3.37 and 3.38.

$$\nabla \times \nabla \times \vec{V} = \nabla(\nabla \cdot \vec{V}) - \nabla^2 \vec{V} \tag{3.36}$$

$$\nabla(\nabla \cdot \vec{E}) - \nabla^2 \vec{E} = -\mu \nabla \times \frac{\partial \vec{H}}{\partial t} \tag{3.37}$$

$$\nabla(\nabla \cdot \vec{H}) - \nabla^2 \vec{H} = \nabla \times (\sigma \vec{E} + \varepsilon \frac{\partial \vec{E}}{\partial t}) \tag{3.38}$$

Assuming the absence of external sources ($\vec{J}_s = 0$ and $\rho_q = 0$) and combining 3.34 and 3.35, with 3.37 and 3.38 the relations become:

$$\nabla^2 \vec{E} = \mu\varepsilon \frac{\partial^2 \vec{E}}{\partial t^2} + \mu\sigma \frac{\partial \vec{E}}{\partial t} \tag{3.39}$$

$$\nabla^2 \vec{H} = \mu\varepsilon \frac{\partial^2 \vec{H}}{\partial t^2} + \mu\sigma \frac{\partial \vec{H}}{\partial t} \tag{3.40}$$

Applying the Fourier transform, same results in the frequency domain have the form of:

$$\nabla^2 \vec{E} = -\omega^2 \mu\varepsilon \vec{E} + i\omega\mu\sigma \vec{E} \tag{3.41}$$

$$\nabla^2 \vec{H} = -\omega^2 \mu\varepsilon \vec{H} + i\omega\mu\sigma \vec{H} \tag{3.42}$$

We can now define the complex propagation constant as

$$\gamma = \sqrt{\omega^2 \mu\varepsilon - i\omega\mu\sigma} \tag{3.43}$$

and rewrite the equations as follows:

$$\nabla^2 \vec{E} + \gamma^2 \vec{E} = 0 \tag{3.44}$$

$$\nabla^2 \vec{H} + \gamma^2 \vec{H} = 0 \tag{3.45}$$

At this point, it is possible to examine two different cases, depending on whether the term $\omega^2\mu\varepsilon$ or the term $\omega\mu\sigma$ dominates. If $\omega^2\mu\varepsilon >> \omega\mu\sigma$, then displacement currents are larger than conduction currents, and the equations become:

$$\nabla^2 \vec{E} + \omega^2 \mu\varepsilon \vec{E} = 0 \tag{3.46}$$

$$\nabla^2 \vec{H} + \omega^2 \mu\varepsilon \vec{H} = 0 \tag{3.47}$$

On the contrary, if the term $\omega^2\mu\varepsilon$ is significantly smaller the case is that of diffusion equations:

$$\nabla^2 \vec{E} - i\omega\mu\sigma \vec{E} = 0 \tag{3.48}$$

$$\nabla^2 \vec{H} - i\omega\mu\sigma \vec{H} = 0 \tag{3.49}$$

To better characterize the propagation of electromagnetic waves through a medium and to understand their dependence on the material parameters, it is useful to express the complex propagation constant as:

$$\gamma = \beta - i\alpha \tag{3.50}$$

in which the term α represents the attenuation in Np/m and the term β represents the phase in rad/m. Defining the complex dielectric permittivity ε, the complex effective dielectric permittivity ε_e and the complex magnetic permeability μ as:

$$\varepsilon = \varepsilon' - i\varepsilon'' \tag{3.51}$$

$$\varepsilon_e = \varepsilon'_e - i\varepsilon''_e = \varepsilon' - i(\varepsilon'' + \sigma/\omega) \tag{3.52}$$

$$\mu = \mu' - i\mu'' \tag{3.53}$$

and combining Eqs. 3.43, 3.50, 3.52 and 3.53 we can derive the attenuation and the phase terms as a function of the matter EM properties explicitly as follows:

$$\alpha = \frac{\omega}{\sqrt{2}} \left[\sqrt{\mu'^2 + \mu''^2} \sqrt{\varepsilon'^2_e + \varepsilon''^2_e} - \varepsilon'_e \mu' + \varepsilon''_e \mu'' \right]^{1/2} [\text{Np/m}] \tag{3.54}$$

$$\beta = \frac{\omega}{\sqrt{2}} \left[\sqrt{\mu'^2 + \mu''^2} \sqrt{\varepsilon'^2_e + \varepsilon''^2_e} + \varepsilon'_e \mu' - \varepsilon''_e \mu'' \right]^{1/2} [rad/m] \tag{3.55}$$

or implicitly ([13]):

$$\alpha = \omega \sqrt{\frac{\mu\varepsilon}{2} \left(\sqrt{1 + \left(\frac{\sigma}{\omega\varepsilon} \right)^2} - 1 \right)} \tag{3.56}$$

$$\beta = \omega \sqrt{\frac{\mu\varepsilon}{2}\left(\sqrt{1+\left(\frac{\sigma}{\omega\varepsilon}\right)^2}+1\right)} \tag{3.57}$$

It is also possible to express the attenuation constant α in dB/m using the relation below:

$$\alpha_{\mathrm{dB}} = 20\log_{10}(e^{\alpha}) = 8.686\alpha \text{ (Np/m)} \tag{3.58}$$

Equations 3.44 and 3.45, define the propagation of EM waves. In the one-dimensional case:

$$\begin{gathered}\vec{E} = \vec{E}(\vec{x},t)\\ \vec{H} = \vec{H}(\vec{x},t)\\ \frac{\partial\vec{E}}{\partial\vec{z}} = \frac{\partial\vec{E}}{\partial\vec{y}} = \frac{\partial\vec{H}}{\partial\vec{z}} = \frac{\partial\vec{H}}{\partial\vec{y}} = 0\end{gathered} \tag{3.59}$$

One solution of the wave equations is the uniform plane wave in which the propagation of the EM field is given by:

$$\vec{E} = E_0 e^{i\omega t-\gamma x} \tag{3.60}$$

$$\vec{H} = H_0 e^{i\omega t-\gamma x} \tag{3.61}$$

that in terms of the α and β coefficients are:

$$\vec{E} = E_0 e^{-\alpha x} e^{2\pi i(vt-\beta x/2\pi)} \tag{3.62}$$

$$\vec{H} = H_0 e^{-\alpha x} e^{2\pi i(vt-\beta x/2\pi)} \tag{3.63}$$

with:

- The period $T = 1/f$.
- The wavelength $\lambda = 2\pi/\beta$.
- The phase velocity $v = \lambda/T = \omega/\beta$.

Maintaining the assumption of plane wave, the coupling of vectors $\vec{E}$ and $\vec{H}$ is evident looking to the field equations writing the field components explicitly:

$$\frac{\partial E_x}{\partial t} = \frac{\partial H_x}{\partial t} = 0 \tag{3.64}$$

$$-\frac{\partial H_z}{\partial x} = \varepsilon_e\frac{\partial E_y}{\partial t}, \quad -\frac{\partial E_z}{\partial x} = -\mu\frac{\partial H_y}{\partial t} \tag{3.65}$$

$$\frac{\partial H_y}{\partial x} = \varepsilon_e\frac{\partial E_z}{\partial t}, \quad \frac{\partial E_y}{\partial x} = -\mu\frac{\partial H_z}{\partial t} \tag{3.66}$$

Furthermore, since the divergences are zero, longitudinal field components of electromagnetic waves are independent of space and time and can therefore be considered null:

$$\frac{\partial E_x}{\partial x} = \frac{\partial H_x}{\partial x} = 0 \tag{3.67}$$

The waves, in this case, are transverse electromagnetic (TEM) plane waves; TEM waves are characterized by the fact that the electric field, the magnetic field, and the direction of propagation are mutually perpendicular. The $\vec{E}$, the $\vec{H}$, and the propagation direction form a right-handed coordinate system (Fig. 3.1). The solution for vectors $\vec{E}$ and $\vec{H}$ into one of the scalar field equations for example is:

$$-\frac{\partial E_y}{\partial x} = \mu\frac{\partial H_z}{\partial t} \tag{3.68}$$

that using the plane wave solution becomes:

$$H_z = \frac{\gamma}{i\omega\mu} E_y \tag{3.69}$$

This relation highlights the coupling of E_y and H_z components. Another useful parameter in geophysical analysis is the *intrinsic impedance* Z of the medium:

$$Z = \frac{|\vec{E}|}{|\vec{H}|} = \frac{\gamma}{i\omega\varepsilon_e} \equiv \frac{i\omega\mu}{\gamma} \tag{3.70}$$

which, using Eq. 3.43 can also be written as:

$$Z = \sqrt{\frac{\mu}{\varepsilon_e}} \tag{3.71}$$

This quantity in the case of the vacuum is:

$$Z_0 = \sqrt{\frac{\mu_0}{\varepsilon_0}} = 376.6\,\Omega \tag{3.72}$$

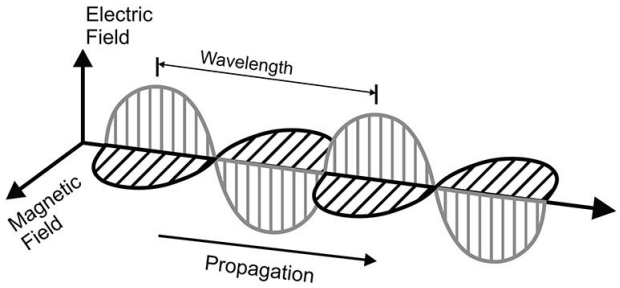

Figure 3.1: Transverse EM wave scheme.

3.3 Electromagnetic Properties

With the constitutive equations (3.5 - 3.7), we introduced ε, μ, σ properties of the matter; in this section we describe these fundamental quantities, providing the framework for characterizing electromagnetic field interactions with dielectric media.

3.3.1 Polarization Phenomena

The dielectric materials function as insulators due to tightly bound electrons within their atomic structure, preventing electrical conduction. In dielectric materials the charges associated with atoms and molecules remain localized under the influence of interatomic and intermolecular forces, in contrast to conductors, where charges can move freely. Despite their macroscopic electrical neutrality, dielectrics exhibit distinctive behavior when subjected to external electromagnetic fields. The applied electric field induces slight displacement of charge centers, creating electric dipoles through the separation of positive and negative charge distributions at the microscopic level (Fig. 3.2). When exposed to an external field, dielectrics experience polarization as the field distorts atomic and molecular structures, forming electrical dipoles leading to a local redistribution of bound charges and resulting in both energy storage and dissipation mechanisms. Under the EM field influence, molecules acquire a non-zero mean electric dipole moment and align themselves along the field direction $\langle p \rangle$. The electric polarization vector $\vec{P}$ is defined as the dipole moment per unit volume:

$$\vec{P} = \lim_{\Delta V \to 0} \frac{1}{\Delta V} \sum_{i=1}^{N_e \Delta V} d\vec{p}_i = N_e \langle \vec{p} \rangle \tag{3.73}$$

where:
ΔV is an infinitesimal volume element;

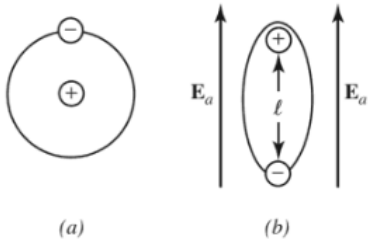

Figure 3.2: A simplified atom before (a) and after (b) the application of an external EM field ([13]).

N_e denotes the number of dipoles per unit volume;
$d\vec{p}_i$ represents the induced dipole moments within the volume.
The dielectric response of a material to an EM field arises from several distinct polarization mechanisms, each associated with characteristic spatial scales and temporal dynamics depending on the frequency of the applied field ([98]). These mechanisms are typically classified in:

Electronic Polarization
f up to $10^{24}Hz$, τ approximately $10^{-15}s$.
This mechanism involves distortion of the electron cloud surrounding atomic nuclei by the external electric field. The induced displacement creates dipoles oriented opposite to the field direction. Electronic polarization establishes rapidly and persists at extremely high frequencies. This process exhibits the shortest relaxation time. A direct correlation exists between material density and the real part of dielectric permittivity ε', as higher densities correspond to greater dipole concentrations per unit volume, and thus larger ε'.

Ionic or Molecular Polarization
f up to $10^{14}Hz$, τ from 10^{-13} to $10^{-12}s$.
The applied electromagnetic field induces a slight separation between positive and negative charges, with the formation of dipoles and distortions of the molecular structure. Materials containing positive and negative ions, which experience mutual displacement under the influence of the external field, exhibit a pronounced susceptibility to this mechanism (sodium chloride for example). At radar frequencies, ionic polarization generally remains the dominant contribution over purely electronic effects.

Orientational (Dipolar) Polarization
f below $10^{12}Hz$, τ depends on viscosity (from $10^{-11}s$ to $10^{-10}s$ for low-viscosity liquids, $10^{-6}s$ for high-viscosity liquids.)
This mechanism occurs in materials possessing permanent dipole moments with random orientations, rendering them macroscopically neutral, for example water. Upon EM field application, dipoles tend to align parallel to the field. This process exhibits strong temperature dependence, as thermal agitation opposes field-induced alignment. Frictional forces counterbalance the alignment leading to shorter relaxation times for low-viscosity liquids with small molecules, and longer ones for viscous liquids.

Hopping or Spontaneous Polarization
This mechanism originates from localized charge-carriers such as electrons, holes, ions, or vacancies transitioning between adjacent sites. Since these charges remain trapped at specific sites for extended periods, they possess limited mobility but occasionally overcome the potential barriers through quantum tunneling or thermal activation. This behavior characterizes glasses and amorphous semiconductors.

Maxwell-Wagner (Space-Charge or Interface) Polarization
f below $10^{6}Hz$, τ from seconds to minutes.
This process involves localized charge migration. The mechanism is particularly significant in heterogeneous materials such as water-saturated rocks, where it depends sensitively on the structural and mineralogical composition. Charge accumulation occurs at interfaces between materials with contrasting dielectric properties. This mechanism is frequently observed in experimental measurements at the electrode sample interface, particularly in parallel-plate capacitor configurations.

The scheme of this classification is represented in Fig. 3.3

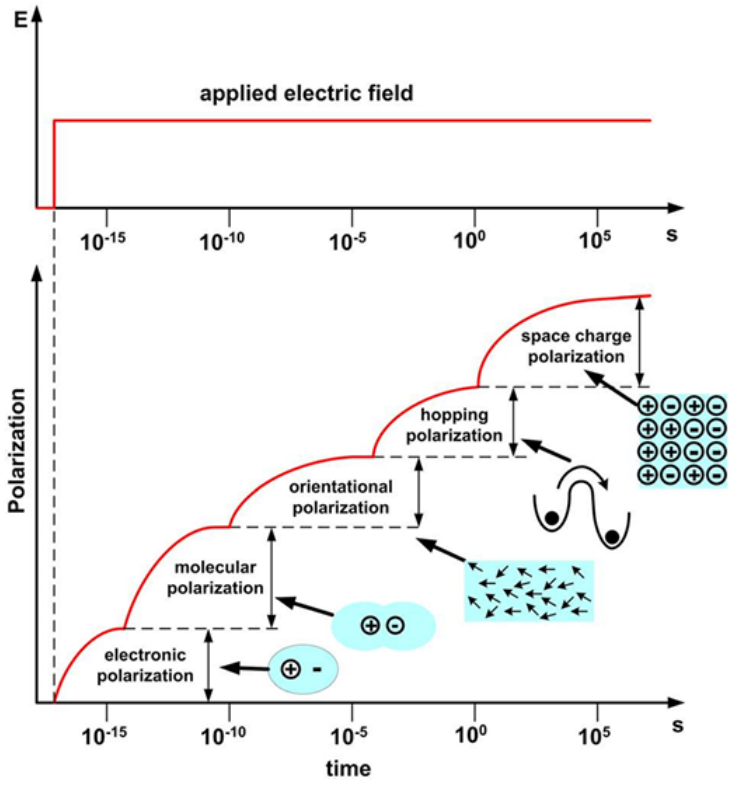

Figure 3.3: Scheme of the different types of polarization phenomena.

3.3.2 Electric Susceptibility and Relative Permittivity

The polarization response induced by the external EM field is measured by the *electric susceptibility*, χ_e. Considering a parallel-plate capacitor filled with homogeneous dielectric material under external EM field influence (Fig. 3.4), the electric flux density comprises two contributions:

$$\vec{D} = \varepsilon_0 \vec{E} + \vec{P} \tag{3.74}$$

where the first part is due to the propagation of the EM field in vacuum and the second one to the presence of the dielectric material between the plates. The polarization relates linearly to

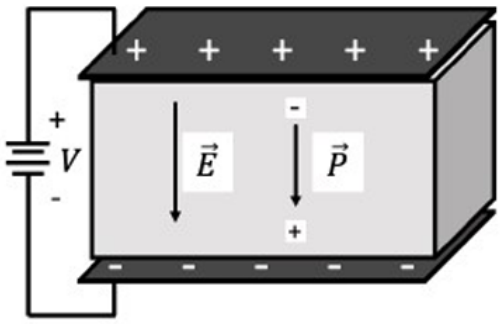

Figure 3.4: A parallel-plate capacitor filled with homogeneous dielectric material under the influence of an external electric field $\vec{E}$. $\vec{P}$ is the polarization vector of the dielectric material, proportional to the external electric field $\vec{E}$.

the applied field through the electric susceptibility:

$$\vec{P} = \varepsilon_0 \chi_e \vec{E} \tag{3.75}$$

Combining Eqs. 3.74 and 3.75, it is possible to relate the electric susceptibility to the dielectric permittivity and to define the relative permittivity as follows:

$$\vec{D} = \varepsilon_0(1+\chi_e)\vec{E} = \varepsilon\vec{E} \tag{3.76}$$

$$\varepsilon_r = \frac{\varepsilon}{\varepsilon_0} = 1 + \chi_e \tag{3.77}$$

Recalling that ε is a complex quantity (Eq. 3.51), the real part describes energy accumulation and the imaginary part accounts for dissipation processes, relaxation losses.

3.3.3 Complex Effective Permittivity and Conductivity

To allow a better comprehension of the electric parameters ε and σ, in this section we explain why we introduced the effective permittivity (Eq. 3.52) and what is its link with the conductivity. Starting with the Ampere's law (Eq. 3.24) we can express the relationship between electric and magnetic fields introducing the complex effective permittivity.

$$\nabla \times \mathbf{H} = \mathbf{J}_s + \mathbf{J}_c + i\omega\varepsilon\mathbf{E} \tag{3.78}$$

$$= \mathbf{J}_s + \sigma\mathbf{E} + i\omega(\varepsilon' - i\varepsilon'')\mathbf{E} \tag{3.79}$$

$$= \mathbf{J}_s + i\omega\left(\varepsilon' - i\varepsilon'' - i\frac{\sigma}{\omega}\right)\mathbf{E} \tag{3.80}$$

$$= \mathbf{J}_s + i\omega\varepsilon_e\mathbf{E} \tag{3.81}$$

and recalling Eq. 3.77 and 3.52 we can formulate the complex relative permittivity normalizing with respect to the free-space permittivity as:

$$\varepsilon_{er} = \frac{\varepsilon_e}{\varepsilon_0} = \frac{\varepsilon'}{\varepsilon_0} - i\left(\frac{\varepsilon''}{\varepsilon_0} + \frac{\sigma}{\omega\varepsilon_0}\right) = \varepsilon'_{er} - i\varepsilon''_{er} \tag{3.82}$$

and the effective conductivity as:

$$\sigma_e = \sigma + \omega\varepsilon'' = \sigma + \sigma_a \tag{3.83}$$

in which the term σ_a, the product of angular frequency and imaginary permittivity, is the dielectric conductivity. The physical interpretation of Eq. 3.83 is that dissipation mechanisms can be divided into frequency, dependent and independent; the static conductivity σ represents the inelastic scattering of free charge carriers during migration, persisting at all frequencies including zero, the dielectric conductivity σ_a encompasses all dissipation mechanisms including ohmic conductivity and charge migration, with frequency dependence. The effective conductivity can be also expressed in terms of static conductivity and high-frequency conductivity ε_∞:

$$\sigma_e = \sigma + (\sigma_\infty - \sigma_s)\frac{\omega^2}{\omega^2 + \omega_{rel}^2} \tag{3.84}$$

where σ_∞ represents the high-frequency conductivity limit and σ represents the low-frequency asymptotic behavior. For notational simplicity, hereafter the complex effective relative permittivity will be indicated as ε, and the effective conductivity as σ, unless explicit distinction is required.

3.3.4 Circuital Approach

An alternative derivation of the parameter of the dielectric permittivity is through circuit analysis ([204]), considering a parallel-plate capacitor connected to an alternating voltage source. The voltage V, the capacitor stored charge Q, and the charging current are respectively:

$$V = V_0 e^{i\omega t} = V_0 e^{i2\pi f t} \tag{3.85}$$

$$Q = C_0 V \tag{3.86}$$

$$I_c = \frac{dQ}{dt} = i\omega C_0 V = I_0 e^{i(\omega t + \pi/2)} \tag{3.87}$$

where C_0 represents the geometric capacitance and the current is 90° phase-shifted with respect to the tension V (Fig. 3.5).

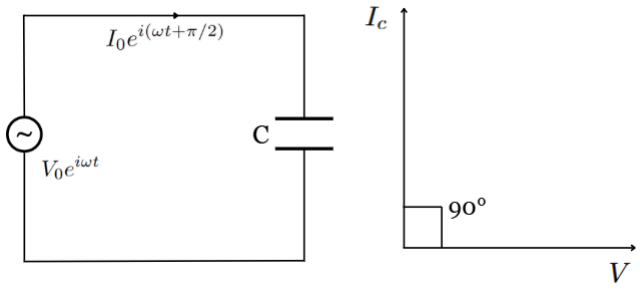

Figure 3.5: Equivalent circuit system of a parallel-plate capacitor connected to an alternating voltage source (left). Phase shift between voltage and current (right).

Introducing a dielectric between the plates of the capacitor, the capacitance and then the I_c become:

$$C = C_0 \frac{\varepsilon'}{\varepsilon_0} = C_0 \varepsilon'_r \tag{3.88}$$

$$I_c = i\omega CV = i\omega C_0 \varepsilon'_r V \tag{3.89}$$

where ε'_r is the real part of the relative permittivity of the dielectric introduced.
In this way the loss current I_l emerges in addition to the charging current. This current is in phase with the applied voltage and proportional to the dielectric conductance G:

$$I_l = GV \tag{3.90}$$

The total current I_{tot} through the capacitor is the combination of both components:

$$I_{tot} = I_c + I_l = V(i\omega C + G) \tag{3.91}$$

The phase angle between charge current I_c and total current I_{tot} defines the loss angle δ, complementary to the power factor angle θ (Fig. 3.6), an indication of the frequency response of the circuit. The behavior of a dielectric could be compared to a RC circuit, the equation of

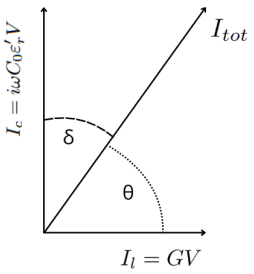

Figure 3.6: Diagram of the currents I_l, I_{tot}, I_c. δ is the loss angle and θ is the power factor angle.

the loss tangent $\tan\delta$ is:

$$\tan\delta = \frac{I_l}{I_c} = \frac{1}{\omega RC} \tag{3.92}$$

Since the dissipation process could also be due to the dielectric properties of the material in the capacitor, for convenience we define G depending on this property as follows:

$$G = \omega \varepsilon'' C_0 / \varepsilon_0 \tag{3.93}$$

The total current can be rewritten as:

$$I_{tot} = V(j\omega\varepsilon' + \omega\varepsilon'')\frac{C_0}{\varepsilon_0} = j\omega C_0 \varepsilon_r V \tag{3.94}$$

This relation leads to a loss tangent definition linked to the permittivity of the dielectric:

$$\tan\delta = \frac{I_l}{I_c} = \frac{\varepsilon''}{\varepsilon'} \tag{3.95}$$

3.3.5 Magnetic Permeability

Similarly to electric polarization, some materials also exhibit magnetic polarization under the influence of an external EM field. These materials are designated as magnetic. The magnetic polarization vector $\vec{M}$ provides the macroscopic description of the alignment of the magnetic dipoles in the material and it is defined as the magnetic dipole moment per unit volume:

$$\vec{M} = \lim_{\Delta V \to 0} \frac{1}{\Delta V} \sum_{i=1}^{N_m \Delta V} d\vec{m}_i \tag{3.96}$$

where:
N_m is the number of magnetic dipoles per unit volume;
$d\vec{m}_i$ is the induced magnetic moments.
In analogy to electric susceptibility, the magnetic susceptibility χ_m is a dimensionless complex quantity that relates the magnetization $\vec{M}$ and the magnetic field $\vec{H}$.

$$\vec{M} = \chi_m \vec{H} \tag{3.97}$$

The magnetic flux density can be written combining the magnetization vector and magnetic field:

$$\vec{B} = \mu_0(\vec{M} + \vec{H}) = \mu_0(1 + \chi_m)\vec{H} = \mu\vec{H} \tag{3.98}$$

In this way, in analogy with the dielectric permittivity we can define magnetic permeability and relative magnetic permeability as:

$$\mu = \mu_0(1 + \chi_m) \tag{3.99}$$

$$\mu_r = \frac{\mu}{\mu_0} = (1 + \chi_m) \tag{3.100}$$

For most of the materials that we analyze in this thesis, the magnetic response to an EM field can be neglected and μ_r is close to or equal 1. For the icy moons simulations in the Sections 8.3.1 and 8.3.2 we address the cases in which the effects of magnetic materials could affect radar performances.

3.3.6 Permittivity vs Frequency

As previously discussed dielectric behavior and polarization mechanisms are characterized by a strong frequency dependence governed by the EM field oscillation. Polarization processes have different phases leading to variations of the dielectric permittivity with the frequency of the applied field.

Dispersion and Relaxation

As the EM field interacts with a dielectric medium, the system does not instantaneously reach equilibrium, instead, a temporal delay precedes the equilibrium. The polarization process occurs in two stages: the instantaneous response due to atomic and molecular distortion, followed by asymptotic approach to equilibrium configuration. The time required for the equilibrium establishment is the relaxation time τ_{rel}, with corresponding relaxation frequency $f_{rel} = (2\pi\tau_{rel})^{-1}$. Geomaterials universally exhibit dielectric losses and dispersion phenomena, highlighting the necessity of frequency-domain characterization. The conversion of potential energy into kinetic energy during dipole alignment, through charge rotation and displacement, results in the decrease of the real permittivity and the increasing imaginary permittivity. The **Kramers-Kronig** relations describe this coupling between the two components ([183]):

$$\varepsilon'(\omega) = \varepsilon_\infty + \frac{2}{\pi}\text{P.V.}\int_0^\infty \frac{x\varepsilon''(x)}{x^2 - \omega^2}dx \tag{3.101}$$

$$\varepsilon''(\omega) = \frac{2\omega}{\pi}\text{P.V.}\int_0^\infty \frac{\varepsilon'(x) - \varepsilon_\infty}{x^2 - \omega^2}dx \tag{3.102}$$

where P.V. denotes the principal value, meaning that in the integration the singular point $x = \omega$ is symmetrically excluded and ε_∞ is the value of dielectric permittivity at very high frequency.

The Debye Model

The *Debye model* provides the most widely adopted mathematical framework for describing frequency-dependent permittivity, originally developed for pure polar molecules and subsequently validated for numerous geomaterials. The model describes a single relaxation process and maintains validity at GHz frequencies:

$$\varepsilon_e(\omega) = \varepsilon_\infty + \frac{\varepsilon_s - \varepsilon_\infty}{1 + i\omega/\omega_{rel}} - i\frac{\sigma_s}{\omega\varepsilon_0} \tag{3.103}$$

and separating real and imaginary components:

$$\varepsilon'_e(\omega) = \varepsilon_\infty + \frac{\varepsilon_s - \varepsilon_\infty}{1 + (\omega/\omega_{rel})^2} \tag{3.104}$$

$$\varepsilon''_e(\omega) = \frac{(\varepsilon_s - \varepsilon_\infty)\omega}{\omega_{rel}(1 + (\omega/\omega_{rel})^2)^2} + \frac{\sigma}{\omega\varepsilon_0} \tag{3.105}$$

where:
$\omega_{rel} = 1/\tau$ represents the relaxation angular frequency;
ε_s is the low-frequency limit permittivity (static permittivity);
σ_s is static conductivity.
Materials with multiple polarization mechanisms manifest multiple relaxation frequencies. The generalized Debye equation including N relaxation frequencies is:

$$\varepsilon_e(\omega) = \varepsilon_\infty + \sum_{n=1}^{N} \frac{\varepsilon_{s,n} - \varepsilon_{\infty,n}}{1 + i\omega/\omega_{rel,n}} - i\frac{\sigma_s}{\omega\varepsilon_0} \tag{3.106}$$

The effective conductivity expressed through relaxation frequency becomes:

$$\sigma_e = \sigma_\infty - \sigma_s \frac{\omega^2}{\omega^2 + \omega_{rel}^2} \tag{3.107}$$

If static conductivity is negligible, the relaxation frequency corresponds to the imaginary permittivity maximum, while the real component exhibits an inflection point:

$$\frac{d\varepsilon''_e(\omega)}{d\omega} = 0 \implies \omega = \omega_{rel} \tag{3.108}$$

$$\varepsilon''_{e,max} = \frac{\varepsilon_s - \varepsilon_\infty}{2} \tag{3.109}$$

$$\varepsilon'_e = \frac{\varepsilon_s + \varepsilon_\infty}{2} \tag{3.110}$$

Cole-Cole Diagram

These relationships can be visualized through the Cole-Cole diagram (Fig. 3.8, [48]), that shows ε'' versus ε' to generate a circle (Eq. 3.111). Only the positive semicircular region possesses physical significance.

$$\left(\varepsilon' - \frac{\varepsilon_s + \varepsilon_\infty}{2}\right)^2 + \varepsilon''^2 = \left(\frac{\varepsilon_s - \varepsilon_\infty}{2}\right)^2 \tag{3.111}$$

Generalized Dispersion Models

As previously mentioned the *Debye model* has limitations for certain materials. In order to develop a model that could adequately represent the behavior of these additional materials, some empirical extensions were incorporated. The first coefficient introduced is α, with $0 < \alpha \leq 1$, in the so-called *Cole-Cole model* ([48]). Further modifications to generalize the model for asymmetry and broadening in dielectric dispersion curves characteristic of polymers have been made in the *Havriliak-Negami model* ([80]).

$$\varepsilon(\omega) = \varepsilon_\infty + \frac{\varepsilon_s - \varepsilon_\infty}{((1 + (i\omega/\omega_{rel})^\alpha)^\beta} \tag{3.112}$$

in which:
if $\beta = 1$ the model reduces to the *Cole-Cole model*;
if $\beta = 1$ and $\alpha = 1$ the model reduces to *Debye model*.

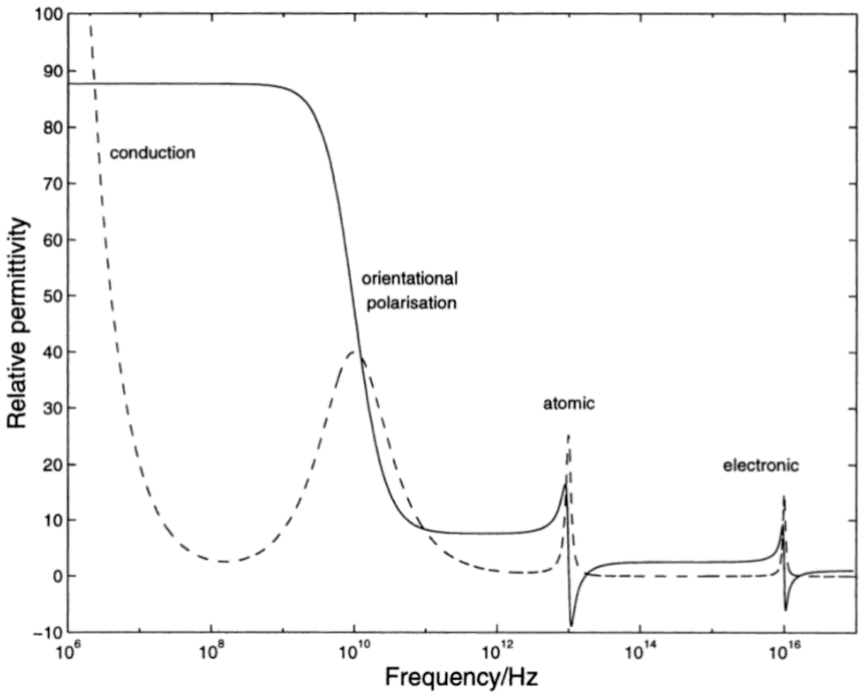

Figure 3.7: The behavior of the relative permittivity with frequency. The solid line represents the real part and the dashed line represents the imaginary part. The variations of both are connected according to Kramers-Kronig equations. In the picture, taken from [183], some of the main polarization mechanisms have been reported.

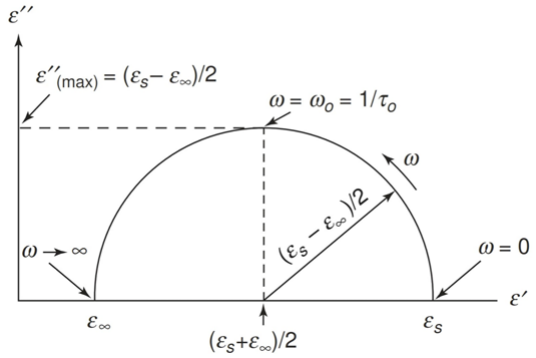

Figure 3.8: The Cole-Cole or Argand diagram for a Debye model with one relaxation frequency. Static conductivity is negligible. Even in this case it is clearly shown how the parts of the complex permittivity are linked.

3.3.7 Permittivity vs Temperature

Dielectric parameters are characterized by a significant temperature sensitivity and for the purposes of this thesis project, this aspect plays a critical role ([204]). The relaxation frequency follows the Arrhenius equation:

$$\omega_{rel} = \omega_0 e^{-\frac{E_a}{k_B T}} \tag{3.113}$$

where:
E_a is the activation energy;
k_B is the Boltzmann's constant;
ω_0 is a proportionality constant;
T is the temperature measured in K.
There is also a relation of the difference between the static permittivity and the high frequency permittivity with temperature:

$$\varepsilon_s - \varepsilon_\infty = \frac{A}{T} \tag{3.114}$$

where A is a material-dependent constant.
Using these equations, the *Debye model*, neglecting static conductivity, could be written as

follows:

$$\varepsilon_e'(\omega) = \varepsilon_\infty + \frac{A/T}{1 + (\omega/\omega_0)^2 e^{2E_a/k_B T}} \tag{3.115}$$

$$\varepsilon_e''(\omega) = \frac{(A/T)\omega e^{E_a/k_B T}}{\omega_0[1 + (\omega/\omega_0)^2 e^{2E_a/k_B T}]} \tag{3.116}$$

Decreasing temperature elevates the real permittivity component and shifts the imaginary permittivity peak toward lower frequencies. Also, the static conductivity exhibits analogous temperature dependence:

$$\sigma_s = \sigma_{s_0} e^{-E_a/k_B T} + \frac{A}{T}\omega_0 e^{-E_a/k_B T} \frac{\omega^2 e^{2E_a/k_B T}}{\omega_0^2 + \omega^2 e^{2E_a/k_B T}} \tag{3.117}$$

where σ_{s_0} represents a proportionality constant. Fig. 3.9 shows the behavior of the dielectric parameters at two different temperatures.

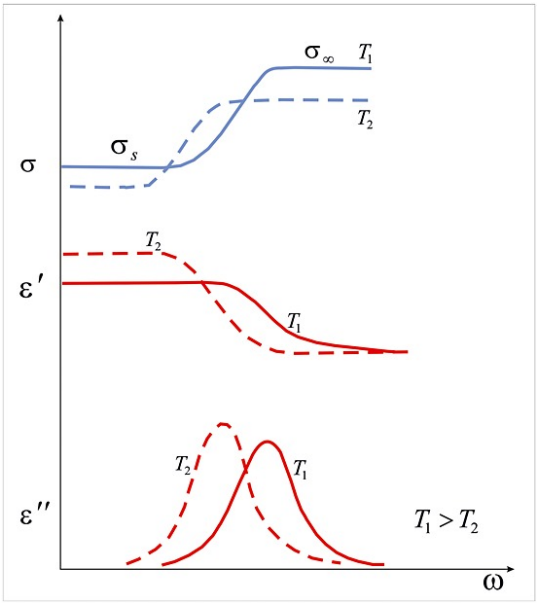

Figure 3.9: Temperature dependence of dielectric parameters σ and ϵ. With decreasing the temperature (T_1 solid line $> T_2$ dashed line) the conductivity decreases (top), the real part of permittivity increases (middle), and the peak of the imaginary part shifts toward lower frequencies (bottom). Taken from [161].

Chapter 4

Geomaterials Electromagnetic Properties

In this chapter we focus on the electromagnetic properties of the geomaterials involved for planetary exploration. Rocks, soils, water and meteorites exhibit peculiar electromagnetic behaviors determined by their composition and structure.

4.1 Rocks

In geological terminology rocks constitute composite materials comprising one or more minerals. The presence of non-mineral components, particularly water, prevents rock EM properties from representing simple summations or averaging of their constituents. Since no systematic correlation with comprehensive chemical and mineralogical composition has been formulated, empirical trends have been identified as functions of silica content. Most rock-forming minerals, particularly silicates and carbonates, exhibit extremely low specific conductivity ($\sigma < 10^{-9}$ S/m), classifying them as insulators. The relative permittivity of abundant rock-forming minerals typically ranges from 4 to 10, though sulfide and oxide groups manifest elevated values. Variations in electrical characteristics arise from impurities and crystalline structure differences, contributing to electrical anisotropy within mineral classes. Comprehensive investigations have documented dielectric properties across diverse rock types and powdered forms at multiple frequencies, providing essential reference data for laboratory measurements and remote sensing interpretation. Fig. 4.1 shows negligible frequency dispersion (at the analyzed frequencies) and indicates minimal relaxation phenomena for common lithologies. Thermal dependence is similarly weak, becoming appreciable only at elevated temperatures ([15]).

4.2 Soils

Soil, or dry particulate material, represents a porous medium comprising mineral grains and interstitial air voids. As a heterogeneous system, its permittivity depends primarily on bulk density ρ_b, which varies from approximately 1 g/cm^3 for highly porous materials to 3.4 g/cm^3 for more dense compositions. The EM properties of soils can be predicted through *mixing formulas*, models used to describe heterogeneous materials based on their constituent components, that will be discussed later in this work. These mixing models take into account the phase of the constituents, their distribution, their shape, and allow to obtain EM properties as functions of porosity. An empirical relationship quantifying the real permittivity dependence on bulk density in the microwave frequencies has been established by [57]:

$$\varepsilon'_{\text{soil}} = (1.01 + 0.44\rho_b)^2 - 0.062 \tag{4.1}$$

Nevertheless, in general it has been shown that, without the presence of liquid water, the real part of permittivity ranges between 2 and 4 and the imaginary part is lower than 0.05. The main contribution is given by variation of bulk density (or porosity).

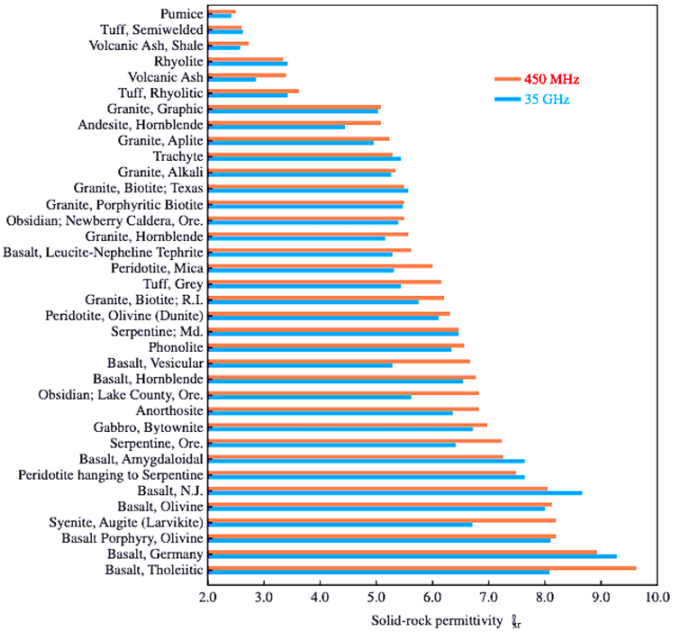

Figure 4.1: Comparison of the real permittivity values for different rocks at two different frequencies 450 MHz - 35 GHz ([126]).

4.3 Meteorites

Meteorites are extraterrestrial solid bodies recovered from planetary surfaces; they are derived from ablation processes of meteoroids, small rocky or metallic bodies in interplanetary space, that enter the atmosphere. Dielectric properties of meteorites are mainly influenced by their metallic content. Since metal distribution is spatially heterogeneous, measurements can show high variability ([49]). The imaginary permittivity component demonstrates pronounced enhancement with increasing metal fraction, consistent with theoretical expectations. The imaginary part generally is proportional to the metallic content. In Tab. 4.1 dielectric properties for various meteorite classifications in both granular and consolidated forms are shown.

Classification	Name	ε'	ε''	Porosity	Metal (vol.%)	Frequency (MHz)
CR2	NWA 801	2.6	—	0.3	5–8	20–1000
CM	NWA 5797	2.9	—	0.3	0.1	20–1000
LL5	MAC 88122	4.7	0.019	0.3	2.0	20–1000
L5	NWA 12857	4.7	0.057	0.3	4.1	10–100
L6	Holbrook	7.8	0.12	Solid	4.1	450
H5	LEW 85320	5.7	0.29	0.3	8.4	20–1000
H5	Plainview	25.4–30.4	2.5–6.1	Solid	8.4	420–1800
EH4	Indarch	130–150	8.5–18.0	Solid	10	450

Table 4.1: Dielectric properties of representative meteorite samples. Classifications: CR2 and CM are carbonaceous chondrites; LL5, L5, L6 are ordinary chondrites with low metal content; H5 and EH4 are high iron-content chondrites (taken from [84]).

In the framework of Jovian icy moons, ordinary and carbonaceous chondrites are of particular importance, as they may be a significant component of the icy crusts of Ganymede and Callisto (Chap. 8).

4.4 Water

The EM properties of liquid and water ice are very peculiar at radar frequencies making radar investigations a very useful tool to explore icy worlds and to search for liquid water: water ice is practically transparent to radio waves allowing radar instruments to probe several kilometers through icy crust, in contrast, liquid water produces strong and easily distinguishable reflections.

However, the presence of other substances (such as salts) in both water and ice significantly alters their EM properties and consequently affects radar performances. We focus on these aspects in Chap. 8.

4.4.1 Liquid Water

The dielectric response of pure water, defined as distilled water without dissolved ionic species, is characterized by well-defined behavior described by a single relaxation Debye formalism below 50GHz ([79]):

$$\varepsilon'(\omega) = \varepsilon_\infty + \frac{\varepsilon_s - \varepsilon_\infty}{1 + (\omega/\omega_{\text{rel}})^2} \tag{4.2}$$

$$\varepsilon''(\omega) = \frac{(\varepsilon_s - \varepsilon_\infty)\omega}{\omega_{\text{rel}}(1 + (\omega/\omega_{\text{rel}})^2)} \tag{4.3}$$

where:
ε_∞ is the high-frequency permittivity limit;
ε_s is the static permittivity;
ω_{rel} is the characteristic relaxation angular frequency.
The high-frequency permittivity has a weak thermal dependence and may be approximated as constant with $\varepsilon_\infty = 4.9$ ([116]). The relaxation time τ_{rel} demonstrates significant temperature sensitivity, described by the empirical relation:

$$2\pi\tau_{\text{rel}}(T) = 1.1109 \times 10^{-10} - 3.824 \times 10^{-12}T + 6.938 \times 10^{-14}T^2 - 5.096 \times 10^{-16}T^3 \tag{4.4}$$

where temperature T is expressed in degrees Celsius. The corresponding relaxation frequency $f_{w,\text{rel}}$ resides within the microwave spectrum (Fig.4.2):

$$\begin{aligned} f_{w,\text{rel}}(0℃) &\approx 8.9 \text{ GHz} \\ f_{w,\text{rel}}(20℃) &\approx 16.7 \text{ GHz} \end{aligned} \tag{4.5}$$

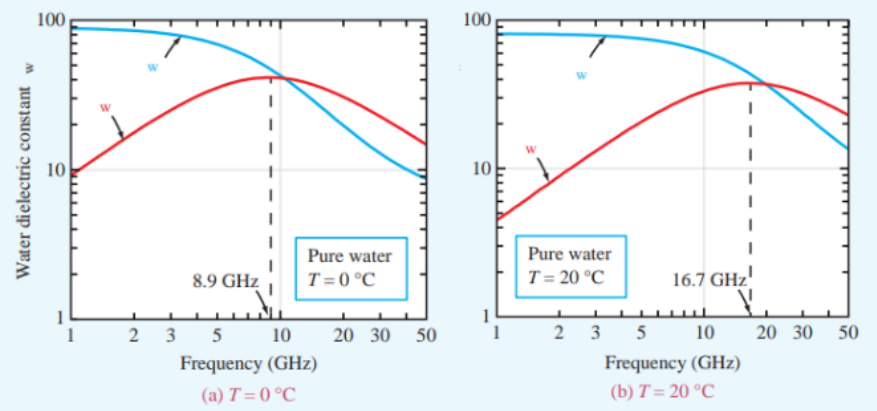

Figure 4.2: Microwave-frequency complex dielectric permittivity spectra of pure water at two distinct temperatures (0℃ and 20℃). The blue line is the real part and the red line is the imaginary part. The dashed line corresponds to the maximum of the imaginary part, therefore to the relaxation frequencies described in the Eq. 4.5 (taken from [126]).

The static permittivity ε_s of pure water likewise exhibits thermal variation according to [110]:

$$\varepsilon_s = 88.045 - 0.4147T + 6.925 \times 10^{-4}T^2 + 1.075 \times 10^{-5}T^3 \tag{4.6}$$

where T is expressed in degrees Celsius. With a relative permittivity of about 80, pure liquid water ranks among the most polarizable natural substances. This high polarizability accounts for its pronounced ability to reflect radio signals (see Chap. 5). Furthermore, due to both its elevated permittivity and its occurrence within pore spaces of soils and rocks, water strongly affects the electromagnetic behavior of natural media.

4.4.2 Saline Water Dielectric Properties

In the case of saline water the electromagnetic response necessitates a more sophisticated formulation with the introduction of a second relaxation in the *Debye model*. Decreasing the amount of salt the model reduces asymptotically to the pure water one ([134]):

$$\varepsilon'(\omega) = \varepsilon_\infty + \frac{\varepsilon_s - \varepsilon_1}{1 + (\omega/\omega_{\text{rel},1})^2} + \frac{\varepsilon_s - \varepsilon_\infty}{1 + (\omega/\omega_{\text{rel},2})^2} \tag{4.7}$$

$$\varepsilon''(\omega) = \frac{(\varepsilon_s - \varepsilon_1)\omega}{\omega_{\text{rel},1}(1 + (\omega/\omega_{\text{rel},1})^2)} + \frac{(\varepsilon_s - \varepsilon_\infty)\omega}{\omega_{\text{rel},2}(1 + (\omega/\omega_{\text{rel},2})^2)} + \frac{\sigma_i}{\omega\varepsilon_0} \tag{4.8}$$

where:
$\omega_{\text{rel},1}/2\pi = f_{\text{rel},1} = 8.9$ GHz is the first relaxation frequency of the system;
$\omega_{\text{rel},2}/2\pi = f_{\text{rel},2} = 201.8$ GHz is the second relaxation frequency of the system;
σ_i represents the ionic conductivity (vanishing for pure water);
ε_1 is the permittivity value at the first relaxation frequency.

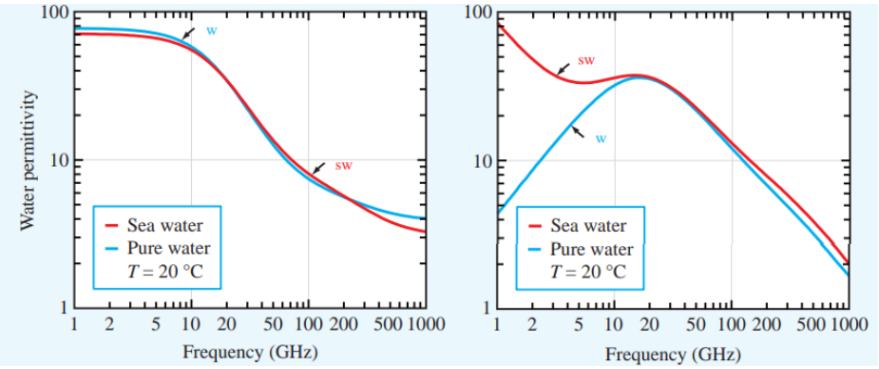

Figure 4.3: Microwave spectra of complex permittivity (real part on the right and imaginary part on the left) for pure water (blue line) and saline water, in particular seawater (red line) at $T = 20$°C (taken from [126]).

4.5 Moisture

The incorporation of water into soils and rocks induces substantial modifications in their dielectric behavior making permittivity and conductivity sensitive to residual water content ([150]). The influence of moisture on electromagnetic properties can be mainly attributed to interfacial space charge polarization mechanisms. The complex interactions between water and the solid matrix typically induce supplementary polarization phenomena and electrode interface effects ([130]).
While monolayer water adsorption on dry material surfaces does not significantly perturb the bulk permittivity, multilayer adsorption induces enhancement in both real and imaginary permittivity components at frequencies below approximately 1 MHz. When water coverage exceeds seven molecular layers, the dielectric signature of water becomes dominant, effectively masking the intrinsic material properties ([150]).
Fig. 4.4 illustrates the effect of moisture content on the real part of the permittivity and on the loss tangent of samples in both intact and powdered forms.

4.6 Water Ice

The analysis of EM properties of water ice is fundamental for the purposes of this thesis, both for Mars and Jovian icy moons. In this section we address the main characteristics of the electric response of ice, the different types of ices on Earth and the influence of chemical dopants. Beyond the *snow line* of the Solar System, the boundary distance from the Sun where temperatures permit the formation and persistence of icy bodies, ice is largely widespread in the surfaces and in the crust of several celestial bodies. Our results about measurements of EM properties could be applied to all of these worlds but also to celestial bodies closer to the Sun that host cold regions in which water ice exists permanently, such as permanently shadowed polar craters on Mercury and the Moon. Ice manifests in twelve distinct crystal structures and

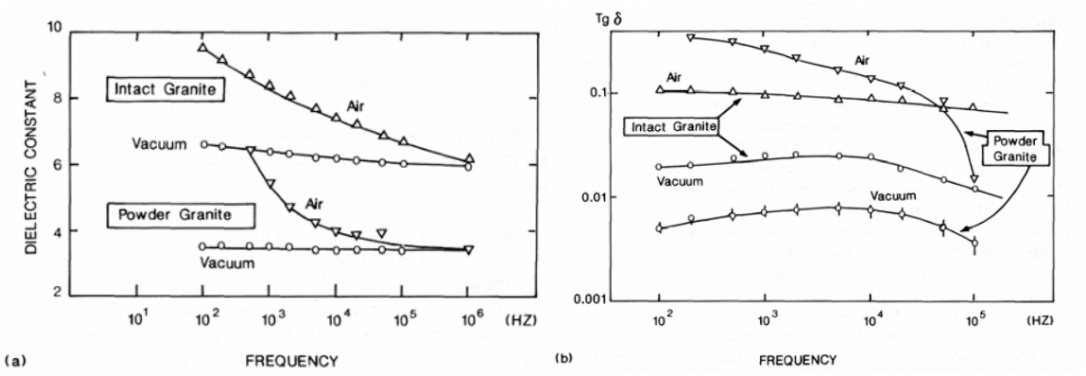

Figure 4.4: Dielectric permittivity (a) and loss tangent (b) of both solid and powder granite measured in vacuum (circles) and air with 30% of humidity conditions (triangles) at ambient temperature (taken from [150]).

.

two amorphous forms. Under low-pressure conditions, the thermodynamically stable phase is designated as ice I, which exists in two variants: ice Ih, commonly termed ordinary ice, with a hexagonal structure, forms when water freezes at standard atmospheric pressure and ice Ic with a cubic structure develops through vapor deposition at around -130℃.
In the first configuration, oxygen atoms are organized in hexagonal layers with alternating vertical displacements. Each water molecule is coordinated like a tetrahedron, surrounded by four nearest-neighbor molecules positioned at the vertices of a regular tetrahedron centered on the molecule, with an inter-oxygen distance of 2.76 Å. Strong covalent O–H bonds hold each molecule together, whereas intermolecular cohesion is maintained through weaker hydrogen bonds (Fig. 4.5 [24]). The arrangement of hydrogen atoms in an ideal ice crystal follows the *Bernal-Fowler* rules ([18]), which establish three fundamental principles:

1. Each water molecule is coordinated like a tetrahedron by four neighboring molecules, with its two hydrogen atoms directed approximately toward two of the four surrounding oxygen atoms.

2. Each oxygen-oxygen linkage contains exactly one hydrogen atom in the intervening space.

3. Each oxygen atom has precisely two nearest-neighbor hydrogen atoms, thereby preserving the molecular structure of water.

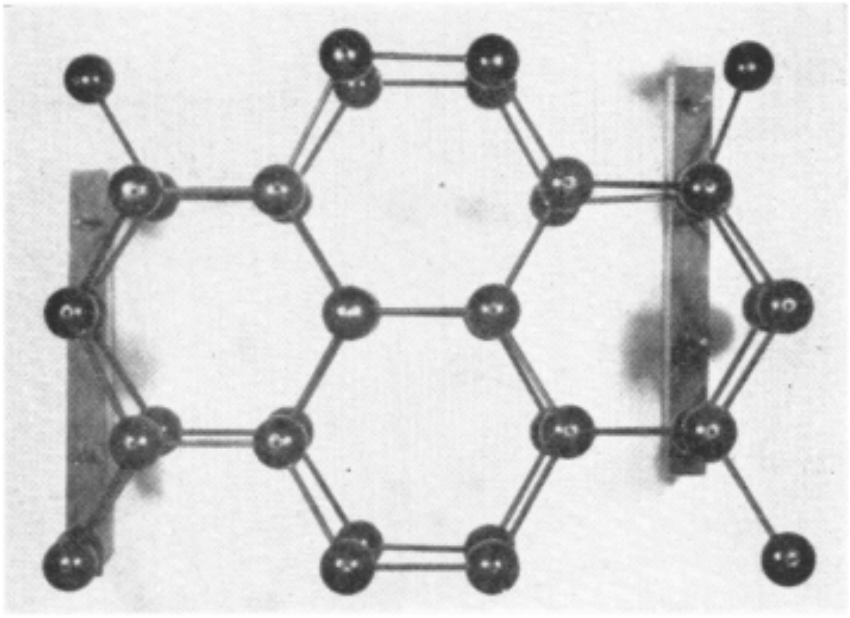

Figure 4.5: Ih pure water ice crystal. Credits [24].

.

Local deviations from these principles generate structural defects within the ice lattice, resulting in different electrical conductivity behavior and relaxation dynamics.

4.6.1 Dielectric Models: Jaccard Theory and Wait-and-Switch

While the Debye model effectively characterizes the dielectric response of pure water ice up to frequencies of several hundred MHz, the Cole–Cole formulation provides a better description, at temperatures up to 250 K ([93]). The **Jaccard theory** ([89], [90]) is the most widely accepted framework for explaining the polarization mechanisms in ice. This theory is based on local violation of the Bernal-Fowler rules in regions called protonic point defects or intrinsic defects, and on their migration through the crystalline lattice, the protonic motion path, that causes molecular reorientation along the defect's trajectory. Jaccard identified two categories of protonic defects:

- **Bjerrum defects** (L and D types) arise from water molecule rotation within the lattice. The L-type represents a proton-deficient site (O$\cdots$O configuration), while the D-type consists of two adjacent protons facing each other (O–H$\cdots$H–O configuration).
- **Ionic defects** result from proton migration along intermolecular bonds, generating ionization states H_3O^+ and OH^-.

Ice is characterized by a strong coupling between polarization and conduction phenomena due to protonic hopping mechanisms. For each defect type, the conductivity is expressed as:

$$\sigma_i = n_i \mu_i |e_i| \tag{4.9}$$

where:
i denotes the defect type;
n_i represents the volumetric defect concentration;
μ_i is the mobility;
e_i signifies the effective charge.
The values of these parameters are reported in [159]. The volumetric concentration n_i of intrinsic defects follows:

$$n_i = N_i \exp\left(-\frac{E_{F_i}}{2k_B T}\right) \tag{4.10}$$

where:
E_{F_i} is the formation energy of defect pairs;
$N_i = \frac{2}{3}N$ for ionic defects;
$N_i = N$ for Bjerrum defects;
N is the number of molecules per unit volume.
Mobility can be expressed as an Arrhenius-type relationship:

$$\mu_i = M_i \frac{1}{T} \exp\left(-\frac{E_{M_i}}{k_B T}\right) \tag{4.11}$$

where:
M_i represents a normalization coefficient;
E_{M_i} is the activation energy for motion.
The ionic and Bjerrum conductivities are respectively defined as:

$$\sigma_{\pm} = \sigma_{H_3O^+} + \sigma_{OH^-} \tag{4.12}$$

$$\sigma_{DL} = \sigma_L + \sigma_D \tag{4.13}$$

At high frequencies ($f \gg f_{rel}$), each defect type activates and migrates independently, yielding a high-frequency conductivity:

$$\sigma_\infty = \sigma_{\pm} + \sigma_{DL} \tag{4.14}$$

The static conductivity σ_s is evaluated from:

$$\frac{e^2}{\sigma_s} = \frac{e_{\pm}^2}{\sigma_{\pm}} + \frac{e_{DL}^2}{\sigma_{DL}} \tag{4.15}$$

Generally, high-frequency conductivity is controlled by defects with higher $n_i \times \mu_i$ products

called majority carriers, while static conductivity is predominantly governed by minority carriers.
The relaxation angular frequency ω_{rel} and static permittivity ε_s can be expressed through Jaccard theory parameters:

$$\omega_{rel} = \Phi \left(\frac{\sigma_{DL}}{e_{DL}^2} + \frac{\sigma_{\pm}}{e_{\pm}^2} \right) \tag{4.16}$$

$$\varepsilon_s = \varepsilon_\infty + \frac{(\sigma_{\pm}/e_{\pm} - \sigma_{DL}/e_{DL})^2}{\varepsilon_0 \Phi (\sigma_{\pm}/e_{\pm}^2 + \sigma_{DL}/e_{DL}^2)^2} \tag{4.17}$$

where Φ represents a temperature-dependent polarizability constant related to the oxygen-oxygen separation distance.
Numerous research groups have investigated the temperature dependence of pure ice relaxation frequency showing a slope change near 230 K. Static permittivity ε_s can also be expressed as:

$$\varepsilon_s = \frac{A}{T} \exp \left[\frac{E_a}{k_B (T - T_0)} \right] \tag{4.18}$$

where:
$A = \sigma_s/(\varepsilon_0 \omega_0)$;
$E_a = E_\tau^a - E_\sigma^a$ is the difference between relaxation time activation energy, E_τ^a, and high-frequency conductivity activation energy, E_σ^a ([7]).
The high-frequency permittivity ε_∞ of pure ice exhibits slight temperature dependence ([70]), expressed as:

$$\varepsilon_\infty = 3.093 \pm 0.003 + (0.72 \pm 0.60) \times 10^{-4} T + (0.11 \pm 0.02) \times 10^{-5} T^2 \tag{4.19}$$

For temperatures above 230 K with one dominant defect type (L defects), conductivity follows:

$$\sigma_\infty - \sigma_s \propto \frac{1}{T} \exp \left(-\frac{E_{\sigma_\infty}}{k_B T} \right) \tag{4.20}$$

The **wait-and-switch** ([159]) model provides an alternative description of pure water ice dielectric behavior alongside the phenomenological Jaccard theory: water dipoles **switch** between different orientational states while adhering to Bernal-Fowler rules. Molecular reorientation occurs exclusively upon encountering lattice defects (Bjerrum or ionic), otherwise, molecules remain in a **waiting** state. At elevated temperature, above 235 K, since Bjerrum defects activation energy (E_{LD}) exceeds that of ionic one, they influence more significantly the polarization. On the contrary, at lower temperatures, the potential barrier for Bjerrum defect motion becomes increasingly difficult to overcome, shifting polarization influence toward ionic defects. Importantly, these two migration types exhibit strong correlation: orientations left by L-D defect migration can impede ionic defect diffusion, and proton hopping generally requires whole-molecule rotation. At higher temperatures, rapid diffusion causes defects to spend relatively brief periods trapped in lattice sites, allowing the two migration types to be considered uncorrelated. In this case the complex permittivity is expressed as:

$$\varepsilon(\omega) = \varepsilon_\infty + \frac{\varepsilon_s - \varepsilon_\infty}{1 + [(i\omega\tau_{LD})^{-1} + (i\omega\tau_{\pm})^{-\alpha_{\pm}}]^{-1}} \tag{4.21}$$

where: τ_{LD} and $\tau_{\pm}^{\alpha_{\pm}}$ represent the relaxation times of orientation defects and ionic defects, respectively.
Above 240 K, $\tau_{LD} \ll \tau_{\pm}$ due to substantial activation energy differences ($E_{LD} > E_{\pm}$), making overall relaxation time predominantly controlled by L-D defects: $\tau \approx \tau_{LD}$.
Below 240 K, the transition from dominant orientation defect motion to dominant ionic defect motion produces an activation energy adjustment, with ionic defects assuming the primary role: $\tau \approx \tau_{\pm}$.
At low temperatures, below 170 K, orientation defect motion substantially decelerates, creating traps for ionic defects. Consequently, proton diffusion becomes correlated with L-D defect movements, and complex permittivity is determined by:

$$\varepsilon(\omega) = \varepsilon_\infty + \frac{\varepsilon_s - \varepsilon_\infty}{1 + [(i\omega\tau_{LD})^{-1} + ((i\omega\tau_{\pm})^{\alpha_{\pm}} + (i\omega\tau_t)^{\alpha_t})^{-1}]^{-1}} \tag{4.22}$$

where: $\tau_t^{\alpha_t}$ refers to the newly created ionic defect traps.
If $\alpha_{\pm}$ and α_t approach unity, this equation reduces to the Cole-Cole model.

4.6.2 Effects of Dopants

The presence of impurities in the ice can change its dielectric properties. For example, HF and HCl acids serve as source of H_3O^+, with the halide ions generating numerous extrinsic Bjerrum defects; these elements are called dopants. The doping phenomenon dramatically alters EM properties leading doped ice to exhibit significantly different behavior compared to pure ice, which could be explained by introducing the eutectic parameters. In a solution the **eutectic concentration** is the specific ratio of components where the lowest melting point occurs, while the **eutectic temperature** is the temperature at which this phase transition happens.
Below the contaminants eutectic concentration, ice forms initially while excluded salts concentrate in *brines* (regions of extremely salty liquid water) that subsequently freeze at the eutectic temperature.
Above the eutectic concentration, hydrates freeze first, followed by ice-hydrate mixture formation at the eutectic temperature.
The variations in dielectric properties depend on the concentration, the temperature, and also on the type of contaminant.
Some salts like $NaCl$ create protonic defects more efficiently while others like $MgSO_4$ are less efficient. Only certain chemical compounds at low concentrations (10^{-3} to 10^{-2} M in solution) can incorporate into the ice lattice, forming solid solutions. Fig. 4.6 summarizes all the effects of concentration and temperature on the high frequencies and static conductivity in the case of HF as impurity. In the case of low concentration and high temperature the high-frequency conductivity is always above the static one as a function of the concentration; σ_∞ is controlled by L-D defects as majority carriers and decreases with decreasing temperature; static conductivity strongly depends on ionic H_3O^+ defects, increasing with impurity concentration, while remaining practically temperature-independent. In the intermediate case, σ_∞ is still above σ_s apart from the *crossover temperature*, T_c, in which ionic and Bjerrum defects almost coincide and then the two conductivities are very close. Below T_c, the situation reverses: L defects become minority carriers controlling σ_s, while ionic defects, now majority carriers, dominate σ_∞. Consequently, the two conductivities exhibit slope interchange. With increasing impurity concentration, and at low temperatures σ_∞ and σ_s magnitudes become comparable proportional to the square root of the concentration.

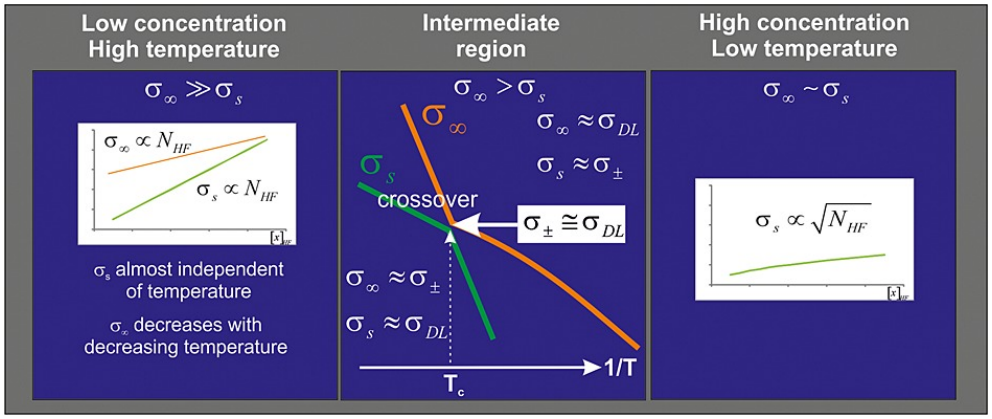

Figure 4.6: Dielectric properties of HF doped ice for different concentrations and temperature ranges. Orange curve and green curves refer to the high-frequency conductivity and static conductivity respectively. In the first panel (low-concentration and high-temperature) σ_∞ is much larger than σ_s; in the intermediate panel σ_∞ is still larger than σ_s , except at the crossover temperature T_c where they almost coincide, and the ice behaves as a pure conductor. In the third panel (high-concentration and low-temperature) σ_∞ and σ_s are of the same order of magnitude and the trend of the static conductivity as a function of the concentration becomes nonlinear (taken from [161]).

4.6.3 Effects of Anisotropy and Density

Dielectric properties are also influenced by possible *anisotropy*, i.e. the difference between the ice crystal orientation and the wave propagation direction; for example in the case of ice Ih crystal, optical axis and crystallographic c-axis coincide and complex permittivity can be

expressed with a tensor ([99]):

$$\varepsilon = \begin{pmatrix} \varepsilon_{\perp c} & 0 & 0 \\ 0 & \varepsilon_{\perp c} & 0 \\ 0 & 0 & \varepsilon_{\parallel c} \end{pmatrix} \tag{4.23}$$

where:
$\varepsilon_{\perp c}$ is the component if the electric field is perpendicular to the c-axis;
$\varepsilon_{\parallel c}$ is the component if the electric field is parallel to the c-axis;
In the case of isotropic polycrystalline ice, complex permittivity is given by a combination of parallel and perpendicular components:

$$\varepsilon = (2\varepsilon_{\perp c} + \varepsilon_{\parallel c})/3 \tag{4.24}$$

The effect of anisotropy on dielectric permittivity is most significant at low frequencies, with approximately a variation of 15% between the two components. At radar frequency, above 1 MHz, this variation could be considered negligible since it reduces to 1%.

4.6.4 Ice Formation and Growth Processes

In this section, we describe how the formation and growth processes influence electrical properties focusing also on the different types of ice present on the Earth and their EM peculiar characteristics. The relaxation times, and consequently the overall complex permittivity behavior, are affected by crystal growth rate: studies demonstrate that relaxation times of pure ice samples formed via rapid crystallization match published values ([177], [92]), while samples obtained through slow crystallization exhibit different relaxation times ([10]). This is due to the fact that a slower growth of the crystal lowers the impurity content and also that different growth speeds can lead to the formation of a different amount of cracks and fractures, air bubbles, and lattice imperfections. The absence of reproducible standard procedures makes the comparison of EM properties of ice samples obtained from different experiments very complex.

Current knowledge indicates that all terrestrial ices consist of polycrystalline hexagonal ice and three distinct typologies exist based on formation mechanism: **meteoric ice**, **sea ice**, and **marine ice** (Fig. 4.7).

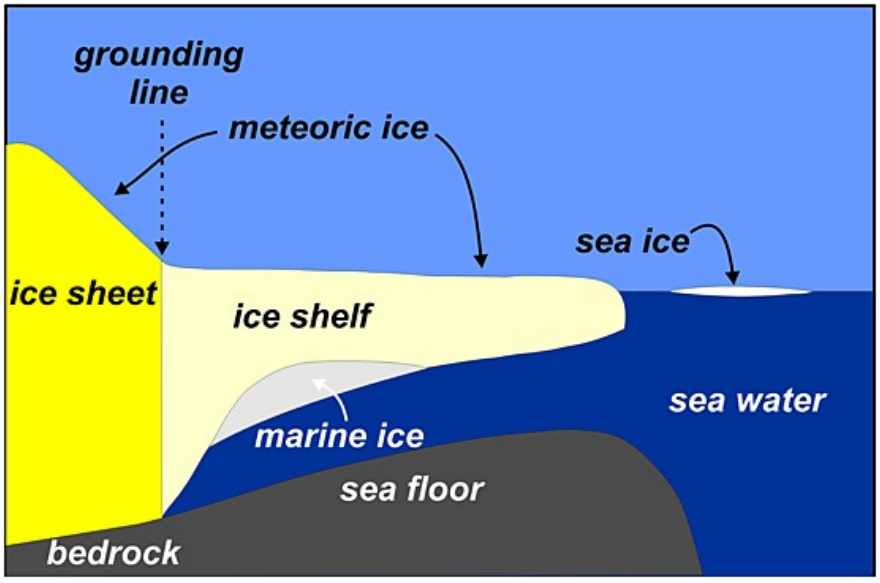

Figure 4.7: Scheme of the different types of terrestrial ices and their location (taken from [161]).

Meteoric Ice

Meteoric ice, present in terrestrial ice caps, forms through densification processes of snow across more stages. First, gravity and accumulating snow compress fresh snow into firn, and continued compression eventually produces solid ice with a density of about 830 kg/m^3. During this process, air or water in pathways between ice grains becomes trapped, creating a polycrystalline

ice containing only isolated air bubbles, while ice crystals gradually grow larger over time. In the upper 500-1000 meters of glacier ice, these trapped bubbles contain either liquid water if temperatures are near melting point, or atmospheric gases if the ice is colder. At greater depths, high pressure increasingly compresses the bubbles until the gas molecules eventually escape and become incorporated into the ice crystal structure itself, forming clathrate hydrates ([161]). The impurities in meteoric ice are deposited as independent aerosols or through the snow, seen as a porous mixture of air, ice crystals, and small amounts of chemical compounds that delivered them to the surface via snowflakes. These aerosols consist mainly of continental dust like silicate minerals $CaCo_3$, $CaSo_4$, sea products like Na^+, Cl^-, Mg^{2+}, and Ca^{2+}, or product of the atmosphere gases like H_2SO_4. In addition, ice can directly absorb several soluble atmospheric gases, such as HCl, NH_3, HNO_3, and H_2O_2. The bulk ionic concentration in meteoric ice is low, typically ranging from 1 to 10 μM, although significantly higher concentrations can occur in basal glacier layers.
Electrical properties of ice cores have been analyzed using different methods:

- Electrical Conductivity Measurements (ECM) revealed that the relationship between the direct-current (DC) conductivity and ion H^+ concentration is nonlinear and possible correlations for other ionic species have not been observed ([75]);
- Dielectric Profiling (DEP) techniques ([143]) have shown a linear variation of the high-frequency conductivity with ionic impurity concentrations in meltwater:

$$\sigma_\infty = \sigma_\infty^{\text{pure}} + \sum_i \hat{\sigma}_i[x_i] \tag{4.25}$$

  where:
  $\sigma_\infty^{\text{pure}}$ is pure ice high-frequency conductivity;
  $[x_i]$ is specific ion concentrations;
  $\hat{\sigma}_i$ represents molar conductivities.

However, the high-frequency conductivity (in μS/m) of meteoric ice can also be expressed as a function of ionic concentration (in μM) using:

$$\sigma_\infty = 9 + 4[H^+] + 1[NH_4^+] + 0.55[Cl^-] \tag{4.26}$$

with a normalization of $-15°C$.
If impurities become highly abundant, there could be Maxwell-Wagner polarization, that, due to high grain conductivity, would enhance interfacial polarization.

Sea Ice

The processes governing the genesis and evolution of sea ice differ markedly from those of meteoric ice. Sea ice is a multiphase structure with classical hexagonal ice, gas, salty water, solid salts and other impurities formed through the freezing of the ocean water. Sea ice formation begins in supercooled and typically turbulent waters, where fine ice crystals, known as frazil ice, nucleate as needles, spicules, or platelets. The continued compression of frazil aggregates by wave motion promotes the formation of so-called *pancake ice* round pieces of ice, 30 cm to 3 m in diameter, which subsequently consolidate and thicken through mechanical processes. Then, under calm hydrodynamic conditions, ice growth beneath the frazil layer proceeds more uniformly. The high salinity of sea ice arises from these brine inclusions, as pure ice Ih excludes most dissolved ions during solidification. Of the total dissolved salt mass in seawater, the main percentage is given by Na^+ and Cl^-, and there are small quantities of SO_4^{2-}, Mg^{2+}, K^+ and Ca^{2+}. Consequently, $Na_2SO_4 \cdot 10H_2O$ (mirabilite) and $NaCl \cdot 2H_2O$ (hydrohalite) constitute the predominant solid salts in sea ice ([161]). Based on its thickness, therefore on its age, sea ice can be classified into three categories: the first two, often unified, are young ice, under 30 cm thickness and first-year ice until 2 m thickness; the third is the multiyear ice, exceeding 2 m thickness that presents a significantly different brine content. The volume fraction of brine is defined as ([126]):

$$f_b = \frac{S_i}{S_b}\frac{\rho_i}{\rho_b} \tag{4.27}$$

where:
S_i represents ice salinity;
S_b is the brine salinity;

ρ_i is pure ice density;
ρ_b is brine density.
Both S_b and ρ_b are temperature-dependent. Sea ice complex dielectric permittivity depends on several parameters: pure ice complex permittivity, brine pocket complex permittivity, brine pocket shape and orientation, and brine volume fraction f_b. The preparation and measurement of both natural and laboratory-grown sea ice samples are very complex since: in natural samples, cutting of ice blocks from a larger mass may lead to brine drainage altering the bulk dielectric response and compromising measurement accuracy, conversely, laboratory-grown ice presents its own uncertainties, particularly concerning its ability to replicate the microstructural and electrical properties of natural sea ice. However, laboratory-grown granular ice obtained by pouring synthetic brines into porous snow samples, and natural columnar sea ice from in situ sampling exhibit similar dielectric behavior with two abrupt permittivity and conductivity changes at the $NaCl$ eutectic temperature of 251 K and below 218 K (when brines completely freeze). Three relaxation phenomena (Fig. 4.8) occur in these sea ice samples:

- At low frequencies, ion migration within brine channels produces **additional static permittivity** and **ion-space charge polarization**.
- At higher frequencies, **Debye-like proton relaxation**.
- In the MHz region, **Maxwell-Wagner relaxation** arising from the contrast between the dielectric properties of brine inclusions and the surrounding ice matrix.

Additional studies of in situ sea ice complex permittivity reveal: (1) brine conductivity increases as temperature decreases to $-8°C$, then decreases; (2) the real part of permittivity strongly depends on brine volume fraction but weakly on brine orientation; conversely, (3) the imaginary part of permittivity strongly depends on brine inclusion orientation but weakly on brine volume fraction.

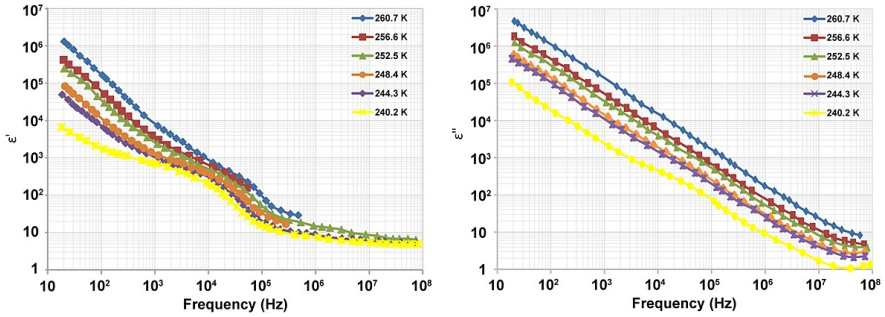

Figure 4.8: Real (left) and imaginary (right) parts of the dielectric permittivity of artificial sea ice as a function of frequency, from about 260 K to 240 K. The three relaxation are visible below 10 kHz (dispersion due to ion migration), between 10 kHz and 100 kHz (Debye relaxation) and above 10 MHz (Maxwell-Wagner relaxation). (taken from [161], modified from[1]).

Marine Ice

The formation of marine ice is governed by thermohaline circulation (circulation due to temperature and saline differences) within the sub-ice-shelf cavity. The melting ice near the base generates a plume of low-salinity, low-density water that ascends along the shelf bottom. This water refreezes, initially forming frazil ice, later compacting into marine ice. As hydrostatic pressure decreases with elevation, the local freezing point rises, favoring the nucleation of frazil ice that, gradually compacting and recrystallizing, forms marine ice. Newly accreted marine ice contains a high concentration of brine inclusions and insoluble particles. Upper layers are impermeable characterized by the lack of air bubbles and the presence of brine pockets. Lower layers are characterized by high porosity and brine drainage channels hydraulically connected with ocean water. The vertical salinity distribution within marine ice remains a matter of debate: some studies reported an increasing salinity with depth ([52]), while other observed the opposite trend ([62]). The electrical characteristics of marine ice remain poorly characterized, with only limited research effectively analyzing conductivity at different depths ([142]). Certain samples align with the linear regression describing the low-salinity (meteoric ice) data suggesting that chloride ions are incorporated into the crystal lattice, generating L-type protonic defects.

Other samples, instead, significantly deviate. In higher-salinity samples, the chloride concentration likely exceeds the solubility limit, resulting in ionic segregation along grain boundaries and a corresponding alteration of the dielectric behavior. Liquid brines persist at temperatures between $-10°C$ and $-30°C$. Fig. 4.9 summarizes conductivity properties of the three type of terrestrial ices.

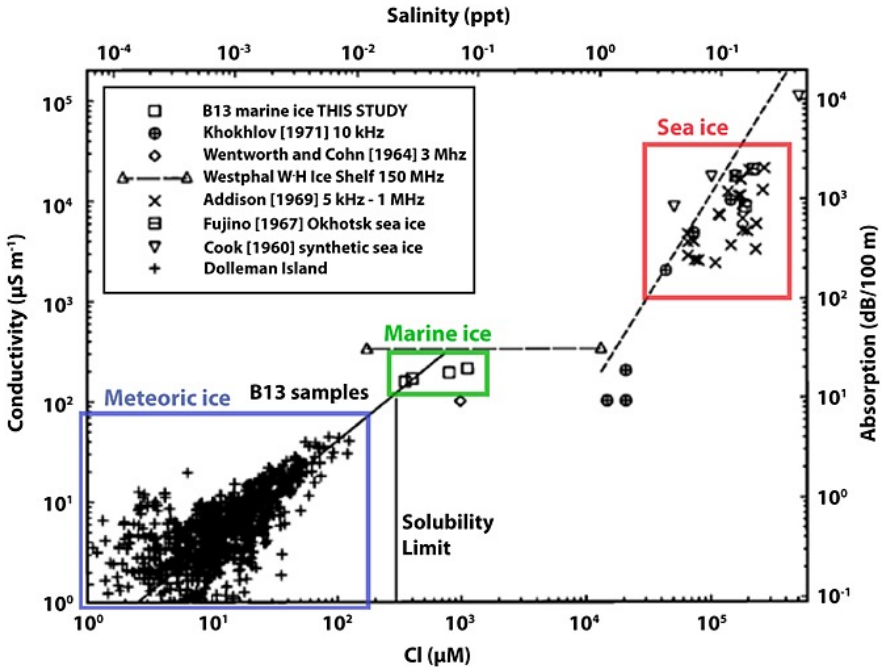

Figure 4.9: Logarithmic conductivity as a function of chloride concentration, or salinity at 251 K for samples of terrestrial ices: meteoric in blue, marine in green, and sea ice in red (taken from [142]).

4.7 Ice Doped with Sodium Chloride

Even if we have already introduced the effects of dopants in the ice, in this section we focus on ice doped with sodium chloride and its dielectric behavior with temperature variations, as it could be a significant component of the icy shell of Europa. As previously mentioned, the introduction of ionic solutes into aqueous solutions fundamentally alters the physicochemical properties of water through a phenomenon commonly referred to as salt doping or impurity doping. When dissolved in water, salts dissociate into their constituent ions, which interact with water molecules, disrupting the hydrogen-bonding network that characterizes pure water. This disruption manifests in several critical modifications to the solution's behavior, including depression of the freezing point, elevation of the boiling point, reduction of vapor pressure, and alteration of dielectric properties. The freezing point depression is particularly significant for planetary science applications. According to colligative theory ([91]), the freezing point depression ΔT_f is proportional to the molal concentration of dissolved particles and is described by:

$$\Delta T_f = K_f \cdot m \tag{4.28}$$

where K_f is the cryoscopic constant of the solvent;
m is the molality of the solution.
For highly concentrated solutions, deviations from ideal behavior necessitate consideration of ion-ion interactions and activity coefficients. Beyond thermodynamic modifications, salt doping profoundly influences the EM properties of aqueous solutions. The presence of mobile ions enhances electrical conductivity and modifies the dielectric response. The imaginary component of the permittivity increases due to enhanced ionic conductivity. The eutectic temperature (T_e) represents a critical parameter in salt-water phase diagrams (Fig. 4.10), corresponding to the lowest temperature at which a liquid phase can exist in equilibrium with solid phases. At the eutectic concentration C_e, the solution and multiple solid phases (typically ice and hydrated salt crystals) coexist at a unique temperature and composition. In the temperature range between the fusion temperature of pure water and the eutectic temperature, the solution exists in a mushy state, a mixture of solid ice and highly concentrated brines. For concentrations and

temperatures beyond the eutectic conditions, metastable states such as supercooled liquids or partially frozen mushy mixtures may persist. In $NaCl$ solutions H_3O^+ and Cl^- ions can be

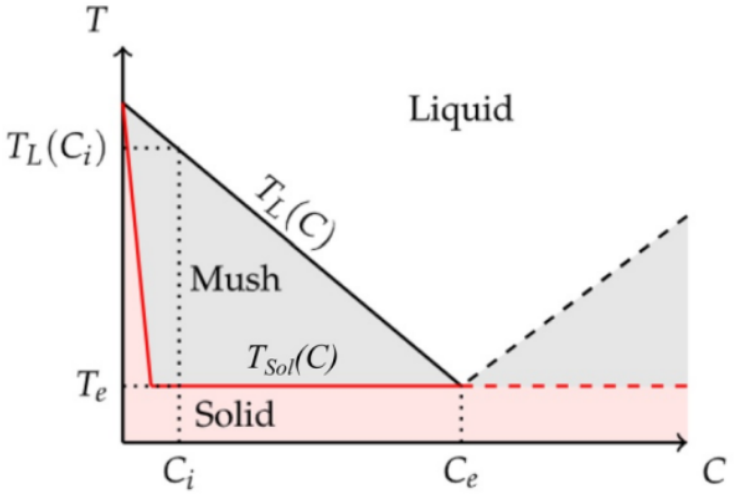

Figure 4.10: Idealized phase diagram for a water salt solution. T_e and C_e are the eutectic parameters. Above the liquidus temperature T_L the solution is a pure fluid and below the solidus temperature T_{sol} it is a mixture of ice and salt. Between these two phases, above the eutectic temperature the solution is in a mushy state: a mixture of solid ice and brines (taken from [156])

incorporated into the ice lattice. The lattice can accommodate these ionic impurities only up to a saturation threshold of approximately 0.1 - 0.3 mM for each species; the unincorporated impurities precipitate as hydrates ([74]). Literature calculations indicate relaxation time saturation at initial $NaCl$ concentrations of approximately 0.3 M. When the composition lies below the eutectic value (23.3 %wt $NaCl$), pure ice is the first phase to crystallize. The excluded salt accumulates in the remaining liquid, leading to progressive brine enrichment. These brines subsequently freeze into an ice-hydrate mixture at the eutectic temperature (approximately 252 K). Instead, exceeding the eutectic concentration, hydrate phases nucleate first, followed by crystallization of ice and hydrate at the same eutectic temperature. The chloride partition coefficient, defined as the equilibrium ratio of Cl^- concentration in the solid phase to that in the liquid is approximately: $k \approx 4 \times 10^{-4}$ for $NaCl$ solutions. As we see also in our measurements (Chap. 7), results demonstrate that an abrupt increase in conductivity and permittivity at the eutectic temperature happens regardless of concentration; it is due to the melting of salty water, and therefore to the appearance of brines in the ice. The real and imaginary part of the permittivity of these brines are described in [193]:

$$\varepsilon'_{\text{brine}} = \varepsilon_{w\infty} + \frac{\varepsilon_{0,\text{brine}} - \varepsilon_{w\infty}}{1 + (2\pi f \tau_{\text{brine}})^2} \tag{4.29}$$

$$\varepsilon''_{\text{brine}} = (2\pi f \tau_{\text{brine}}) \frac{\varepsilon_{0,\text{brine}} - \varepsilon_{w\infty}}{1 + (2\pi f \tau_{\text{brine}})^2} + \frac{\sigma_{\text{brine}}}{2\pi f \varepsilon_0} \tag{4.30}$$

where:
$\varepsilon_{w,\infty} = 4.9$;
τ_{brine} and $\varepsilon_{0,\text{brine}}$ are tabulated in [126]. The eutectic diagram of sodium chloride could be seen in Fig. 4.11. In the case of perchlorate salts, the compound dissociates in solution into its corresponding cation and the perchlorate anion ClO_4^-. The presence of perchlorate likewise contributes to a depression of the freezing point and an increase in the dielectric constant of the solution. This behavior is particularly significant because it may enable the formation of stable or metastable brines within the Martian crust.

4.8 Dirty Ice

In addition to salt-doped ice, the investigation of the EM properties of impurity-rich, or “dirty”, ice is also of considerable relevance for the purposes of this thesis. Such ice, containing contaminants of different origin, may represent a significant component of the outer crust of both Callisto and Ganymede, thereby influencing their bulk dielectric response and radar scattering properties. Dirty ice, relatively rare on Earth (impurity fraction in meteoric ice is typically

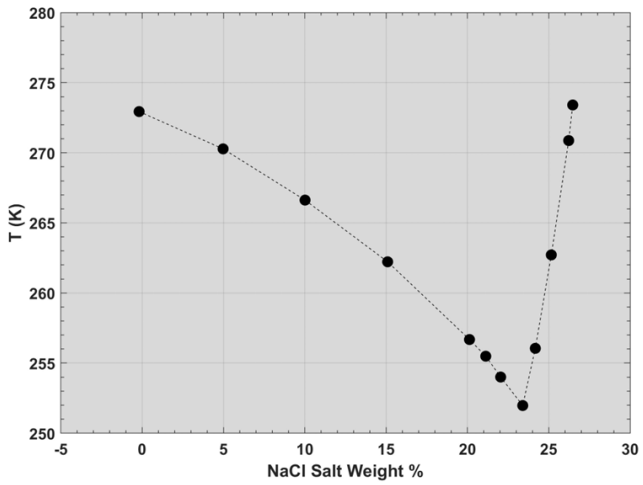

Figure 4.11: Eutectic diagram of sodium chloride, the T_e is 252 K and C_e is 23.3%wt (taken from [31]).

less than 1%), is the term for ice with mechanical inclusions of mineral grains within its polycrystalline structure. Some of the experimental characterizations of the dielectric behavior of planetary dirty ice analogues are relatively recent:

- [83] investigated dirty ice mixtures with dunite, montmorillonite, and kaolinite inclusions at kHz, and extrapolated the results to MHz to estimate radio-wave propagation in comet-like materials. In this case two distinct temperature dependent behaviors have been observed: above the threshold of 200 K, the dielectric response is dominated by the ice matrix with a significant dispersion, while below this temperature, permittivity becomes nearly frequency-independent and primarily governed by grain density and mineral composition.

- [191] examined ice–silicate/salt composites across temperatures of 180–298 K and frequencies between 1 mHz and 1 MHz. In this study the authors identified five relaxation mechanisms: (1) dipolar reorientation of adsorbed water (around 630 kHz), (2) rotation of L-defects (around 200 Hz), (3)-(4) two Maxwell–Wagner effects caused by interfacial polarization within adsorbed water (around 10 Hz) and between salt hydrates and silicates (around 10 mHz), and (5) a low-frequency dispersion in low–water content samples.

- [81] investigated cometary analogs consisting of ice-chondrite mixtures with porosity ranging from 20% to 50%, measured between 1 MHz and 1 GHz and temperatures of 113–298 K. Their findings show that the real part of permittivity increases with temperature and correlates with bulk density. Due to the limited sensitivity to the imaginary component, they employed the Maxwell–Garnett ([183]) formulation to estimate its dependence on dust content.

- [131] analyzed the dielectric properties of ice–basalt mixtures (11% and 43% dust fractions) over 150–250 K and 20 Hz–1 MHz. Real permittivity spectra of the mixtures were comparable to that of pure ice, with high-frequency asymptotic value of $\varepsilon_\infty \approx 5$. In contrast, the imaginary part exhibited a dual behavior: at low frequencies and high temperatures, the contribution of impurities is negligible, whereas at high frequencies and low temperatures, it approached that of dry basalt.

- [32] analyzed the electric responses of dirty ice mixture with carbonaceous chondrite CI simulants and L5 chondrite in the frequency range 1-100 MHz to evaluate radar performances for the study of the crust of Jovian icy moons. The authors measured the EM properties of dry and saturated samples to obtain the behavior of dirty ice depending on the concentration of impurities comparing the results of CI, L5 and Etna basalts.

Some results of these studies are reported in Figs. 4.12 and 4.13. Both pictures show the case of dirty ice mixture with chondrites as contaminants. In the first figure the increase of ε' with temperature and dust content is evident. The second figure shows the values of real and imaginary parts of permittivity as a function of temperature of three dirty ice mixtures, comparing experimental data with best-fitting models at the frequency of 9 MHz.

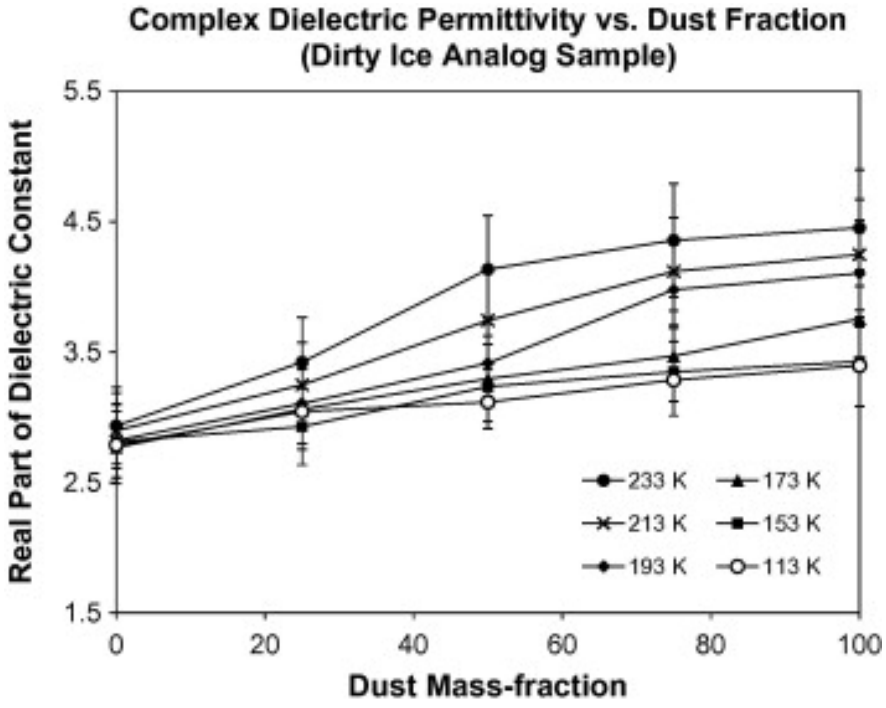

Figure 4.12: The real part of the relative dielectric permittivity at different temperatures as a function of dust mass-fraction in the LL5 chondritic dust sample mixed with ice (taken from [81]).

4.9 Mixing Models

As previously discussed, the EM characterization of planetary surface analogues for radar investigation often involves the analysis of composite multiple phases systems, consisting of ice mixed with mineral grains or rock fragments intermixed with void spaces containing gas or liquid phases. The EM properties of such materials require accounting for the contributions of all constituent phases to derive the bulk or effective permittivity, $\varepsilon_{\text{bulk}}$ or ε_{eff}. The determination of effective electromagnetic properties presents significant challenges due to the complex interplay between phase geometry, volume fractions, inclusions morphology, and the dielectric contrast between constituents. The *mixing models* ([183]) provide mathematical formulations that relate the bulk permittivity to the properties of individual phases, enabling the extraction of intrinsic material parameters from measurements on composite samples. In this section we examine mixing models of two phases: the inclusion phase, characterized by permittivity ε_i and volume fraction of the inclusions ϕ, and the host or matrix phase, with permittivity ε_m and volume fraction $(1-\phi)$. For porous granular systems, ϕ corresponds to porosity when the inclusion phase represents air voids. When describing saturated or frozen samples, the matrix may represent water ice, with solid grains serving as inclusions. The following models are the principal mixing formulations employed in geophysics and planetary science.

4.9.1 Maxwell-Garnett Model

The Maxwell-Garnett (MG) formulas ([136]) represent one of the earliest and most extensively applied mixing theories in electromagnetic characterization. Known as the Lorenz-Lorentz equation, or Clausius-Mossotti formula, it was developed to explain the observed properties of metal spheres embedded in a liquid, and it was later expanded to the broader dielectric situations. This model describes the EM properties of a composite structure with spherical inclusions randomly distributed throughout a continuous host medium (Fig. 4.14). The fundamental MG equation is:

$$\varepsilon_{\text{bulk}} = \varepsilon_m + \frac{3\phi\varepsilon_m(\varepsilon_i - \varepsilon_m)}{\varepsilon_i + 2\varepsilon_m - \phi(\varepsilon_i - \varepsilon_m)} \tag{4.31}$$

This expression derives from consideration of the averaged electric displacement field within the composite. The two limits of this formulation depend on the amount of the inclusions: as $\phi \to 0$, we recover $\varepsilon_{\text{bulk}} \to \varepsilon_m$, while $\phi \to 1$ yields $\varepsilon_{\text{bulk}} \to \varepsilon_i$. However, the functional

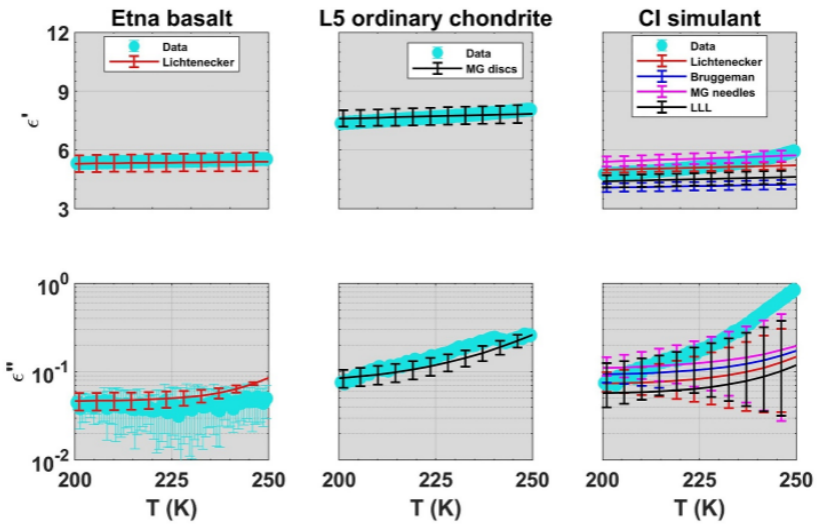

Figure 4.13: Model-based curves and experimental values of the bulk real and imaginary parts of permittivity as a function of temperature at the frequency of 9 MHz: cyan dots indicate experimental data, lines of different colors are the the best fitting models for each sample(taken from [32]).

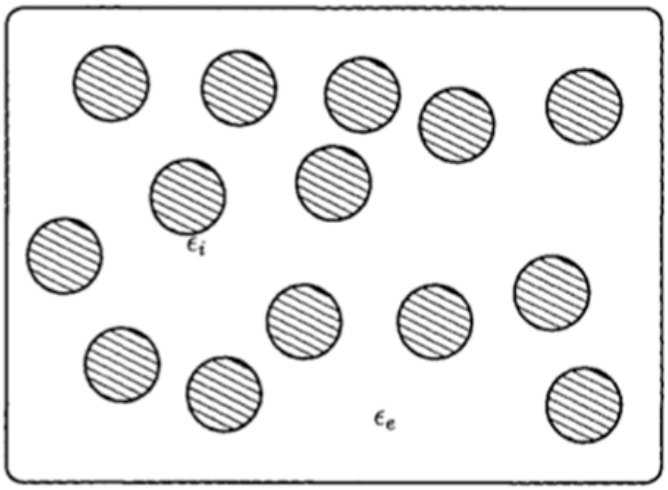

Figure 4.14: Simple scheme of the two-phase mixture described by Maxwell-Garnett formula (taken from [183]).

form changes dramatically upon exchanging phase designations. For a very low concentration of impurities ($\phi \ll 1$), the MG relation simplifies through Taylor expansion:

$$\varepsilon_{\text{bulk}} \approx \varepsilon_m + \frac{3\phi\varepsilon_m(\varepsilon_i - \varepsilon_m)}{\varepsilon_i + 2\varepsilon_m} \tag{4.32}$$

An alternative formulation (*Clausius-Mossotti*) views the inclusions as induced dipole moments contributing to the macroscopic polarization ([183]) and, considering the polarizability α of the spheres the permittivity of a mixture with spherical inclusions as:

$$\frac{\varepsilon_{\text{bulk}} - \varepsilon_m}{\varepsilon_{\text{bulk}} + 2\varepsilon_m} = \frac{\alpha n}{3\varepsilon_m} \tag{4.33}$$

where n is the dipoles number density.
Clausius-Mossotti formula can be found also expressed with the volume fraction of the inclusions, ϕ, and their permittivity, ε_i, in the so called *Rayleigh mixing formula*:

$$\frac{\varepsilon_{\text{bulk}} - \varepsilon_m}{\varepsilon_{\text{bulk}} + 2\varepsilon_m} = \phi\frac{\varepsilon_i - \varepsilon_m}{\varepsilon_i + 2\varepsilon_m} \tag{4.34}$$

The standard MG formulation assumes spherical geometry, but the extension to ellipsoidal

particles incorporates shape-dependent depolarization effects N_i, where i is the direction x, y, z. For an ellipsoid with semi-axes a_x, a_y, a_z, the depolarization factors along principal axes satisfy ([183]):

$$N_x = \frac{a_x a_y a_z}{2} \int_0^\infty \frac{ds}{(s+a_x^2)\sqrt{(s+a_x^2)(s+a_y^2)(s+a_z^2)}} \tag{4.35}$$

with analogous expressions for N_y and N_z (substituting a_x in the first term of the denominator, respectively with a_y and a_z) subject to the constraint $N_x + N_y + N_z = 1$. While in the previous case spheres exhibit isotropic depolarization:

$$(N_x, N_y, N_z) = (1/3, 1/3, 1/3) \tag{4.36}$$

In cases of discs and needles they are respectively (Fig. 4.15):

$$(N_x, N_y, N_z)_{discs} = (1, 0, 0) \tag{4.37}$$

$$(N_x, N_y, N_z)_{needles} = (0, 1/2, 1/2) \tag{4.38}$$

The component of polarizability of the ellipsoids along the x-axis is:

$$\alpha_x = \frac{4\pi a_x a_y a_z}{3} \frac{(\varepsilon_i - \varepsilon_m)\varepsilon_m}{\varepsilon_m + N_x(\varepsilon_i - \varepsilon_m)} \tag{4.39}$$

For randomly oriented ellipsoidal inclusions lacking preferred alignment, the effective permittivity assumes the form:

$$\varepsilon_{\text{bulk}} = \varepsilon_m + \varepsilon_m \frac{\phi}{3} \sum_{j=x,y,z} \frac{\varepsilon_i - \varepsilon_m}{\varepsilon_m + N_j(\varepsilon_i - \varepsilon_m)} \Bigg/ \left[1 - \frac{\phi}{3} \sum_{j=x,y,z} \frac{\varepsilon_i - \varepsilon_m}{\varepsilon_m + N_j(\varepsilon_i - \varepsilon_m)} \right] \tag{4.40}$$

In the two particular limit cases shown in Fig. 4.15 the relation becomes:

$$\varepsilon_{\text{bulk}} = \varepsilon_m + \frac{\phi(\varepsilon_i - \varepsilon_m)(2\varepsilon_i + \varepsilon_m)}{(3-\phi)\varepsilon_i + \phi\varepsilon_m} \tag{4.41}$$

for randomly oriented oblate disks.

$$\varepsilon_{\text{bulk}} = \varepsilon_m + \frac{\phi(\varepsilon_i - \varepsilon_m)(\varepsilon_i + 5\varepsilon_m)}{(3-2\phi)\varepsilon_i + (3+2\phi)\varepsilon_m} \tag{4.42}$$

for randomly oriented needles. Despite its historical significance and widespread adoption, the

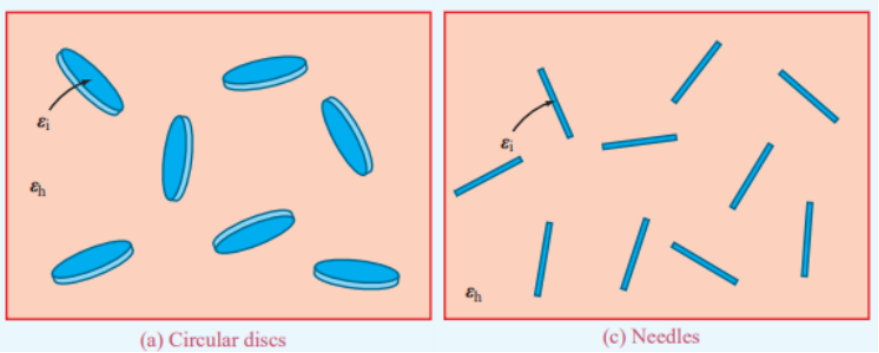

Figure 4.15: Examples of two limit cases of randomly distributed ellipsoidal configurations. On the right panel the inclusion are discs and on the left panel they are needles (modified from [126]).

Maxwell-Garnett approach exhibits reduced accuracy for concentrated mixtures due to its foundational assumption of dilute mixture $\phi << 1$. Previous mixing formulas represent asymmetric configurations, on the contrary the following models consider the mixture systems symmetrically.

Symmetric mixing relations treat both phases equivalently, producing predictions invariant under phase interchange. These formulations typically arise from statistical averaging procedures that homogenize micro-structural details, yielding expressions largely independent of particle morphology.

4.9.2 The Bruggeman Model

The Bruggeman formulation ([35]) addresses limitations of dilute-mixture theories. Considering a mixture of two components with dielectric permittivity ε_1 and ε_2 Bruggeman relations is:

$$(1-\phi)\frac{\varepsilon_2-\varepsilon_{\text{bulk}}}{\varepsilon_2+2\varepsilon_{\text{bulk}}}+\phi\frac{\varepsilon_1-\varepsilon_{\text{bulk}}}{\varepsilon_1+2\varepsilon_{\text{bulk}}}=0 \tag{4.43}$$

This equation must be solved numerically for $\varepsilon_{\text{bulk}}$, but demonstrates improved performance compared to Maxwell-Garnett for systems with comparable phase fractions. Experimental validations across diverse granular materials have confirmed the Bruggeman relation's accuracy, particularly at radio frequencies and microwave bands. Some studies note reduced precision for materials with grain sizes below $30\mu m$ or predicting imaginary components ([60]). The model performs optimally for similar dielectric properties (low dielectric contrast) and similar volume fractions of the component of the mixture ([87]).

4.9.3 The Looyenga-Landau-Lifshitz Model

Independently derived through distinct approaches in the 1960s ([127],[115]), the Looyenga-Landau-Lifshitz (LLL) relation represents mixtures where the constituent permittivities (ε_1, ε_2) deviate slightly from the bulk value ($\varepsilon_{\text{bulk}} \pm \delta\varepsilon$). The formulation is:

$$\varepsilon_{\text{bulk}}^{1/3}=\phi\varepsilon_1^{1/3}+(1-\phi)\varepsilon_2^{1/3} \tag{4.44}$$

This model assumes modest dielectric contrast and makes no explicit reference to particle geometry or spatial arrangement, rendering this expression shape-independent. [127] derivation was obtained examining minerals with real permittivity equal to or greater than 9 with a high percentage of inclusions. Empirical studies such as [139] indicate strong performance for materials with high inclusion fractions and low permittivity contrast. The LLL predictions closely track Bruggeman results.

4.9.4 The Complex Refractive Index Model

The Complex Refractive Index Model (CRIM) has been developed in optical physics to describe the refractive index of non-magnetic gas mixtures ([183]). Its extension to general dielectric composites interprets the effective refractive index as a simple volume average:

$$\sqrt{\varepsilon_{\text{bulk}}}=\phi\sqrt{\varepsilon_1}+(1-\phi)\sqrt{\varepsilon_2} \tag{4.45}$$

This formulation, also known as the time-propagation model, has demonstrated particular success for liquid-saturated systems ([182]). Its performance is worse for brines with elevated ionic strength, likely due to interfacial electrochemical interactions not accounted by the geometric averaging assumption.

4.9.5 The Lichtenecker Model

Originally proposed as an empirical rule and subsequently obtained theoretically, the Lichtenecker relation ([122]) considers the inclusion as randomly oriented spheroids with a uniform shape distribution:

$$\varepsilon_{\text{bulk}}=\varepsilon_1^{\phi}\varepsilon_2^{1-\phi} \tag{4.46}$$

Further work ([211]) established connections to Maxwell's equations and charge conservation principles under random spatial distributions, providing solid theoretical grounding for geological applications. Empirical studies of lunar regolith samples ([149]) from Apollo missions revealed real part of bulk permittivity was well represented by a Lichtenecker model.

4.9.6 Power-Law Mixing Models

The last three models examined all belong to a single family of mixing formulas in which the contributions of the components are averaged on volume weights with variable exponents (Fig. 4.16):

$$\varepsilon_{\text{bulk}}^{\beta}=\phi\varepsilon_1^{\beta}+(1-\phi)\varepsilon_2^{\beta} \tag{4.47}$$

Setting $\beta = 1$ the model is the simple arithmetic averaging also known as the Silberstein formula ([122]), that rarely describes real mixtures accurately due to its oversimplified treatment of field

distribution;
setting $\beta = 1/2$ the model reduces to the CRIM formulation;
setting $\beta = 1/3$ the model reduces to LLL relation;
the limit $\beta \to 0$ corresponds to geometric averaging, producing the Lichtenecker equation.
These formulations generally neglect explicit geometric details such as particle shape or spatial correlations.

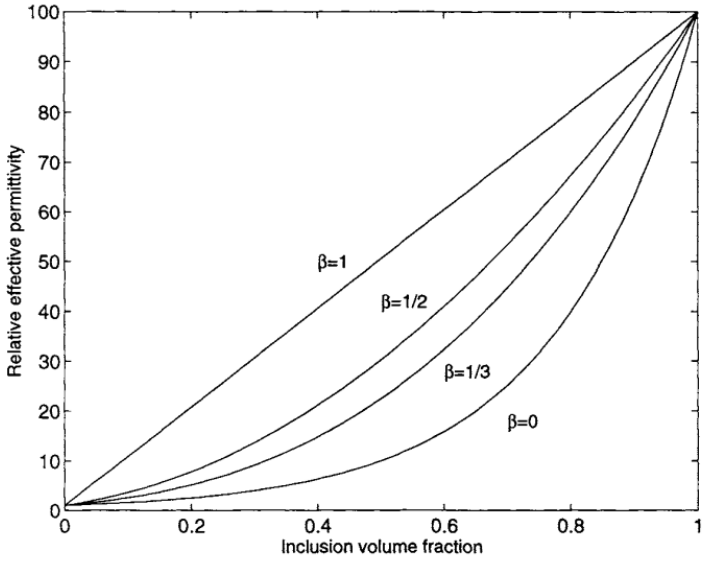

Figure 4.16: Power-law models for the effective permittivity of a mixture with high dielectric contrast ($\varepsilon_1/\varepsilon_2 = 100$)(taken from [183]).

4.9.7 Permittivity Bounds for Binary Mixtures

Regardless of microstructural details, the effective permittivity of any two-phase mixture must satisfy fundamental physical constraints. The most general requirement states:

$$\min\{\varepsilon_1, \varepsilon_2\} \leq \varepsilon_{\text{bulk}} \leq \max\{\varepsilon_1, \varepsilon_2\} \tag{4.48}$$

Two more refined bounds provide tighter constraints under specific conditions: the Wiener bounds and the Hashin-Shtrikman bounds (Fig. 4.17).

Wiener Bounds

The Wiener bounds ([183]) consider, with a circuital approach, the two-phases of the mixture as capacitors in a parallel or series configuration:

$$\varepsilon_{\text{bulk,min}} = \frac{\varepsilon_1 \varepsilon_2}{\phi\varepsilon_2 + (1-\phi)\varepsilon_1} \tag{4.49}$$

$$\varepsilon_{\text{bulk,max}} = \phi\varepsilon_1 + (1-\phi)\varepsilon_2 \tag{4.50}$$

These bounds provide the broadest possible constraints. The minimum corresponds to series connection while the maximum represents parallel connection.

Hashin-Shtrikman Bounds

For isotropic mixtures, tighter constraints are set by the Hashin-Shtrikman bounds ([78]), expressed through the Maxwell-Garnett formulation by systematically switching the phases:

$$\varepsilon_{\text{HS},1} = \varepsilon_2 + \frac{3\phi\varepsilon_2(\varepsilon_1 - \varepsilon_2)}{\varepsilon_1 + 2\varepsilon_2 - \phi(\varepsilon_1 - \varepsilon_2)} \tag{4.51}$$

$$\varepsilon_{\text{HS},2} = \varepsilon_1 + \frac{3(1-\phi)\varepsilon_1(\varepsilon_2 - \varepsilon_1)}{\varepsilon_2 + 2\varepsilon_1 - (1-\phi)(\varepsilon_2 - \varepsilon_1)} \tag{4.52}$$

These expressions provide narrower bounds than Wiener limits for random isotropic microstructures. The choice between Wiener and Hashin-Shtrikman bounds depends on available knowledge regarding mixture isotropy and the desired level of conservatism in interpretation.

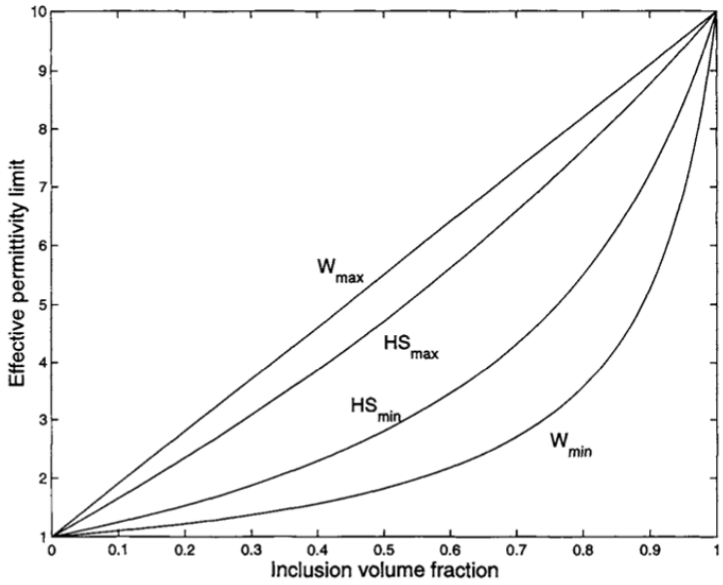

Figure 4.17: Wiener and Hashin-Shtrikman boundaries for the relative effective permittivity of a mixture where components has real permittivities 1 and 10. W_{max} and W_{min} are the Wiener bounds, HS_{max} and HS_{min} are the Hashin-Shtrikman bounds (taken from [183]).

4.9.8 The Archie Model

The Archie law ([5]), empirical in origin, has achieved widespread application for relating conductivity of porous media saturated with conductive fluids:

$$\sigma = \sigma_f \phi^m \tag{4.53}$$

where: σ is conductivity of the medium;
σ_f is the conductivity of the fluid;
ϕ is the porosity;
m is the so-called *cementation exponent*, a curve-fitting parameter. Typical values for m range from 1.3 to 2, with variations depending on lithology and compaction history. Archie originally derived this relationship through bilogarithmic regression analysis, explicitly warning that it represented an approximate empirical trend rather than rigorous theory. Recent analyses [101] have provided a more robust theoretical foundation for Archie's law demonstrating that, despite the inherent scatter observed in brine volume–conductivity data, Archie's relationship yields sufficiently accurate predictions of water saturation. Furthermore, the cementation exponent m must implicitly contain brine geometric characteristics, although the mechanism is not fully understood, since the other two factors do not intrinsically encode this information.

Chapter 5

Radio Echo Sounding

EM remote sensing represents a powerful methodology for subsurface investigation, exploiting the propagation characteristics of radio waves through various media. Among geophysical investigation methods, Radio Echo Sounding (RES) techniques have the advantages of providing high spatial resolution while maintaining non-invasive investigations. RES employs RADAR (Radio Detection and Ranging) instruments, which, although initially developed and primarily employed for military purposes during World War II, began to find scientific applications and underwent significant development between the 1950s and 1970s due to the capability of radio waves to probe deep beneath terrestrial ice sheets ([64]). Over the years, radars have become essential tools in Earth observation, including vegetation mapping, land utilization assessment, and cryospheric monitoring and beyond Earth applications, radar methods play a crucial role in planetary exploration enabling surface characterization, stratigraphic analysis and subsurface features detection ([152]), limiting the necessity for physical sampling or drilling operations. This chapter outlines the fundamental principles of radar systems, with a particular focus on their use in planetary exploration missions.
Radar sounding constitutes a high-resolution geophysical technique employing radio frequency EM waves for subsurface characterization. The standard configuration consists of two antennas (a transmitting antenna and a receiving antenna) maintained in fixed geometric arrangement. The technique involves the emission of EM pulses in the radar frequencies (1 MHz - 100 GHz) that propagate through the investigated medium. Once they encounter EM discontinuities, interfaces between materials exhibiting contrasting electromagnetic properties, they are partially reflected and partially refracted. While the refracted signals penetrate beneath the discontinuity allowing the analysis of the underlying materials, the reflected ones, called echoes, are captured by the receiving antenna and are used to reconstruct the EM properties of the soil. System electronics generate triggering pulses to coordinate transmission and reception sequences, while computational units manage data acquisition and processing.

5.1 Antenna Systems

Antennas constitute critical components in radar sounding applications, serving dual functions as electromagnetic field generators and detectors. The transmitting antenna transforms excitation voltage into spatially and temporally distributed electromagnetic fields, while the receiving antenna performs the inverse operation, converting temporal variations of field vector components into recordable electrical signals. Achieving optimal antenna performance requires addressing several fundamental requirements. Primary among these is precise definition of source and detection locations. Additionally, transmitter and receiver responses must exhibit temporal and spatial invariance to ensure measurement consistency. Finally, antenna bandwidth must align with application-specific requirements. These requirements present significant engineering challenges. EM field generation and detection inherently require finite-dimensional antennas with characteristic sizes comparable to signal wavelengths. Such finite-size antennas exhibit several intrinsic properties: EM field creation and detection occur over spatially distributed regions; this precludes precise point source and detection localization. EM field transit characteristics also vary with the host environment, preventing perfectly invariant antenna response, spatial distribution complicates isolation of individual vector component responses, and bandwidth enhancement through damping necessarily reduces antenna efficiency and environmental

sensitivity.

By analyzing the relationships governing the behavior of both the transmitting and receiving antennas, and subsequently introducing a target into the system, it becomes possible to derive the fundamental radar equation. Indeed, in the transmission case, a generator applied to two terminals excites waves that propagate through space with spherical wavefronts. Conversely, when the antenna operates as a receiving system, the incident wave, produced by a distant source, can be approximated as a portion of a uniform plane wave. This induces an electromagnetic field on the antenna that differs significantly from that associated with the transmitter's generator. The total field on the antenna, which must satisfy the boundary conditions, consequently produces a current distribution substantially different from that of the transmitting antenna. Furthermore, the receiving pattern is identical to the transmission pattern when the antennas are the same. To energetically relate the transmitted power P_t to the power effectively collected in reception P_r, it is convenient to define some parameters like the gain $G(\theta, \phi)$ and the effective area for both transmission and reception ([126]). First we introduce the gain $G(\theta, \phi)$ parameter for a generic antenna through the directivity $D(\theta, \phi)$, a measure of the preferential direction in which electromagnetic energy is radiated:

$$G(\theta, \phi) = D(\theta, \phi)\frac{P_{irr}}{P_g} = \xi D(\theta, \phi) \tag{5.1}$$

where:
P_{irr} is the radiated power;
P_g is the power supplied by the feed;
ξ is the radiation efficiency which, for a lossless antenna, is equal to 1, leading to $G = D$. Usually both gain and directivity of the antenna are defined for the maximum solid angle (θ_M, ϕ_M).
The received power is proportional to the power density incident at the receiver, the *Poynting vector*, S_i:

$$P_r = A_r S_i \tag{5.2}$$

where the *Poynting vector* S_i is related to the peak gain of the transmitting antenna G_t through the following equation:

$$S_i = G_t \frac{P_t}{(4\pi R^2)} \tag{5.3}$$

Therefore, we can determine the received power P_r in terms of the power P_t and the antenna gain G_t:

$$P_r = A_r \frac{G_t}{4\pi R_{tr}^2} P_t \tag{5.4}$$

where R_{tr} is the distance between transmitter and receiver. At this point, we must determine the effective receiving area A_r, which can be computed through the receiving antenna gain G_r and the wavelength λ:

$$A_r = \frac{\lambda^2}{4\pi} G_r \tag{5.5}$$

This relationship is also valid in transmission: $A_t = \lambda^2/(4\pi)G_t$. In conclusion, we have:

$$P_r = \frac{\lambda^2 G_r G_t}{(R_{tr})^2} P_t = \frac{A_r A_t}{(\lambda R_{tr})^2} P_t \tag{5.6}$$

5.2 Fundamental Radar Equation

At this point, we are able to introduce the radar equation derived from Eq. 5.6 in which it is necessary to account for the presence of a reflecting object between the transmitting and receiving antennas. The target illuminated by the EM field emitted by the transmitter is assumed to scatter the incident field, redistributing its energy with a power density that can be expressed through an equivalent scattering area A_s. Consequently, the scattered power P_s, can be written as a function of the incident power density S_t on the target, at a distance R_t:

$$P_s = A_s \frac{G_t}{4\pi R_t^2} P_t \tag{5.7}$$

Now considering that the received power can be evaluated through Eq. 5.2, the incident power density depends on the distance between the scatterer and the receiving antenna, R_r and on the scatterer gain G_s.

$$P_r = A_r \frac{G_s}{4\pi R_r^2} P_s \tag{5.8}$$

Using these last two equations it is possible to define the radar equation that establishes the quantitative relationship between transmitted power, target characteristics, and received signal strength (Fig. 5.1). The general form is ([126]):

$$\frac{P_r}{P_t} = \frac{G_t G_r \lambda^2 \sigma}{(4\pi)^3 R_t^2 R_r^2} e^{-2\alpha(R_t + R_r)} \tag{5.9}$$

where:
P_r = received power (W);
P_t = transmitted power (W);
G_r = receiving antenna gain (dimensionless);
G_t = transmitting antenna gain (dimensionless);
λ = wavelength (m);
σ = radar cross-section of target (m^2) defined as $A_s G_s (1 - a_s)$, considering the target as a transmitting and receiving antenna in which there could be a loss term a_s due to the target material absorption;
R_t = transmitter range to target (m);
R_r = receiver range to target (m);
$\alpha = \omega/c \; Im\sqrt{\varepsilon}$ is the term of attenuation of the radio waves through an attenuating medium. This term is equal to 0 for free space.
In the case of space radar sounders, the receiver and the transmitter antennas coincide, the radar is called monostatic and the equation becomes:

$$\frac{P_r}{P_t} = \frac{G^2 \lambda^2 \sigma}{(4\pi)^3 R^4} e^{-4\alpha R} \tag{5.10}$$

The R^4 dependence reflects the spherical spreading of electromagnetic energy during both propagation paths (transmission and reception), representing one of the fundamental limitations in radar system design [171].

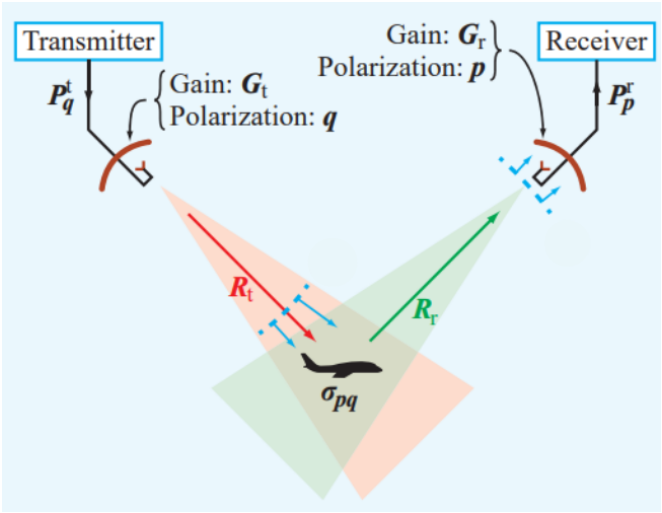

Figure 5.1: A scheme of a radar investigation in a bistatic radar (transmitter and receiver are two different antennas). The P are the powers of the antennas, the G represent the gains, the R are the ranges to the target, σ is the radar cross-section of the target, the superscripts t, r mean transmitter and receiver, and the subscripts p, q represent the different polarization of the signals (modified from [126]).

5.3 System Parameters

The performance characteristics of radar sounding systems are determined by the instrument design parameters that must be optimized for specific target characteristics and the electromagnetic environment. They are also influenced by surface and subsurface conditions and if the

topography is characterized by a pronounced roughness radar analysis could be very challenging. Rugged regions in fact can generate clutter phenomena, back-scattering signals from the surface could mask or be confused or combined with the subsurface echoes causing misinterpretation of basal reflections. Design considerations typically address two critical requirements: achieving adequate spatial and depth resolution for target discrimination, and maintaining sufficient signal-to-noise and signal-to-clutter ratios for reliable detection. System main parameters are the bandwidth B and center frequency f_0, which together determine the temporal width W of the electromagnetic pulse generated by the instrument:

$$W = \frac{1}{B} \tag{5.11}$$

The center frequency wavelength λ_0 relates to propagation velocity v through:

$$\lambda_0 = \frac{v}{f_0} \tag{5.12}$$

The dimensionless ratio $\mathcal{R} = B/f_0$ is a characteristic parameter for system classification. Optimal design philosophy pursues maximization of bandwidth while minimizing center frequency, within the constraint that $\mathcal{R}$ approaches unity as an upper bound.

5.3.1 Frequency

The operating frequency represents a fundamental design choice that balances competing requirements. The choice of frequency depends on the methods employed, the targets, and the environment (Fig. 5.2). In general lower frequencies provide greater penetration depth but sacrifice range resolution, while higher frequencies offer improved resolution at the cost of increased attenuation. The relationship between center frequency f_0 and free-space wavelength is:

$$\lambda_0 = \frac{c}{f_0} \tag{5.13}$$

Typical frequency ranges for subsurface applications include:

- HF band (3 - 30 MHz): deep penetration for ice sheets and dry planetary surfaces;
- VHF band (30 - 300 MHz): moderate penetration with improved resolution;
- UHF band (0.3 - 3 GHz): high resolution for shallow subsurface.

From a scientific perspective, two main types of radar systems can be distinguished: Ground Penetrating Radar (GPR) and Radar Sounders. In general terms, GPR probe the shallow subsurface at higher frequencies offering high spatial resolution, whereas radar sounders operate remotely (from aircraft or satellites) using lower frequencies providing greater penetration depths but lower resolution. The former are radar systems directly coupled to the ground, typically mounted on rovers or towed by an operator. It is primarily used for surveying relatively small areas compared to traditional radar systems installed on aircraft or satellites. Since GPR signals do not propagate through the atmosphere, they achieve very high signal-to-noise ratios and enhanced spatial resolution. However, radar sounders operate below 200 MHz in the case of airborne radars, and even lower frequencies (1 - 10 MHz) for planetary radar sounder, allowing investigations of several kilometers in depth also because they are used on ice, which is a material highly transparent to radio waves.

5.3.2 Radar Signals

Radar instruments use two types of signals: amplitude-modulated (AM) signals and frequency-modulated (FM). Among the AM signals the most common are Gaussian and Ricker, while for the FM signals the typically used in the radars is the chirp.

Gaussian Signal

This signal can be considered an approximation of other signals and has the following characteristics:

$$y(t) = Ae^{-\frac{t^2}{2\sigma_t^2}} \cos(2\pi f_0 t) \tag{5.14}$$

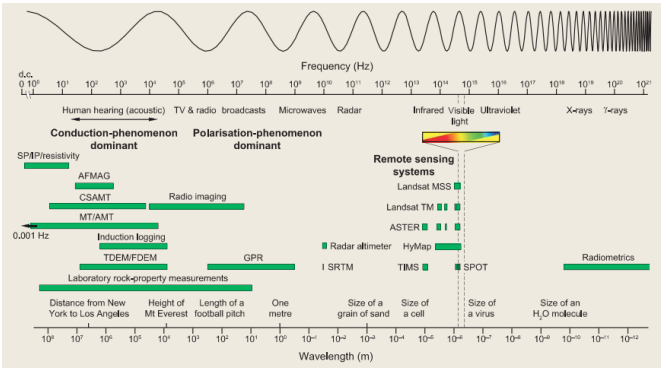

Figure 5.2: Frequency bands used in geophysical methods (taken from [55]).

which has a Gaussian spectrum centered at the carrier frequency $\pm f_0$:

$$Y(f) = \frac{A}{2}\sqrt{2\pi}\sigma_f \left[e^{-\frac{(f-f_0)^2}{2\sigma_f^2}} + e^{-\frac{(f+f_0)^2}{2\sigma_f^2}} \right] \tag{5.15}$$

where:
$\sigma_f = 1/(2\pi\sigma_t)$ is half the signal bandwidth. Defining $B \approx 2\sigma_f$ as the bandwidth and $W \approx 2\sigma_t$ as the pulse width (duration), we have:

$$W = \frac{2}{\pi}\frac{1}{B} \sim \frac{1}{2B} \tag{5.16}$$

Ricker Signal

This signal, typical for Ground Penetrating Radar and also present in seismic data, has the following spectrum:

$$Y(f) = A\frac{f^2}{f_0^2}e^{-\frac{f^2}{f_0^2}} \tag{5.17}$$

that in the time domain is:

$$y(t) = 2Af_0\sqrt{\pi}\left[1 - \frac{1}{2}(2\pi f_0 t)^2\right] e^{-\frac{1}{2}(\pi\sqrt{2}f_0 t)^2} \sim 2Af_0\sqrt{\pi}\cos(2\pi f_0 t)e^{-\frac{t^2}{2\sigma_t^2}} \tag{5.18}$$

where $\sigma_t = 1/(\pi\sqrt{2}f_0)$. This signal is characterized by an asymmetric spectrum with maximum value at frequency $f = f_0$ and mean frequency $\langle f \rangle = \pi/\sqrt{2}f_0$. Its time behavior is that of a modulated signal oscillating at frequency $f = f_0$ with temporal duration $W \sim \sqrt{2}/\pi f_0$.

Chirp Signal

The chirp used in the radar instruments we introduced in Chaps. 1 and 2 is a frequency-modulated (FM) signal typically used in radar sounders (Fig.5.3). It has the characteristic of maximizing the signal-to-noise ratio (SNR) for a given bandwidth B after compression. It is defined as follows:

$$y(t) = \begin{cases} \cos\left(2\pi f_0 t + 2\pi\beta t^2\right), & t \in [-T/2, T/2] \\ 0, & t \notin [-T/2, T/2] \end{cases} \tag{5.19}$$

Its instantaneous frequency, defined as the derivative of the phase, is:

$$f(t) = \frac{1}{2\pi}\frac{d\phi(t)}{dt} = f_0 + 2\beta t \tag{5.20}$$

and varies linearly with time from a minimum value $f_1 = f_0 - \beta T$ to a maximum value $f_2 = f_0 + \beta T$. It can be rewritten as an analytical signal $y_a(t)$:

$$y_a(t) = e^{2\pi i f_0 t + 2\pi i\beta t^2}\mathrm{rect}_T(t) = e^{2\pi i f_0 t}e^{i\alpha t^2}\mathrm{rect}_T(t) \tag{5.21}$$

where $\alpha = 2\pi\beta$.
Chirp duration T is proportional to the bandwidth $B \quad \rightarrow \quad 2\beta T = B$:

$$2\beta T = B \tag{5.22}$$

Range Compression

Usually, the received chirp signal undergoes *range compression* or *dechirping* to obtain a signal of shorter duration. Considering the received signal as the transmitted signal $y_a(t)$ with a delay $\tau = 2R/v$:

$$y_a(t) = e^{i2\pi f_0 t} e^{-i2\pi f_0 \tau} e^{i\alpha(t-\tau)^2} \text{rect}_T(t-\tau) \tag{5.23}$$

Dechirping consists of deconvolving the chirp signal, after removing the carrier from the signal: $y_{\text{de}}(t) = y_a(t)e^{-i2\pi f_0 t}$):

$$y_{\text{de}}(t) = e^{-i2\pi f_0 \tau} e^{i\alpha(t-\tau)^2} \text{rect}_T(t-\tau) \tag{5.24}$$

with its undelayed complex conjugate $y_r^*(t) = e^{-i\alpha t^2} \text{rect}_T(t)$:

$$\begin{aligned} x(t) &= y_{\text{de}}(t) * y_r^*(t) \\ &= e^{-i2\pi f_0 \tau} \int_{-\infty}^{\infty} e^{i\alpha(\xi-\tau)^2} \text{rect}_T(\xi-\tau) e^{-i\alpha(t-\xi)^2} \text{rect}_T(t-\xi) d\xi \\ &= e^{-i2\pi f_0 \tau} e^{-i\alpha(t^2-\tau^2)} \int_{-\infty}^{\infty} e^{i2\alpha(t-\tau)\xi} \text{rect}_T(\xi-\tau) \text{rect}_T(t-\xi) d\xi \end{aligned} \tag{5.25}$$

For $t \approx \tau$, the integral simplifies as follows:

$$\begin{aligned} x(t) &= e^{-i2\pi f_0 \tau} \int_{-T/2}^{T/2} e^{i2\alpha(t-\tau)\xi} d\xi \\ &= e^{-i2\pi f_0 \tau} \mathcal{F}_{\alpha(t-\tau)/\pi}\{\text{rect}_T(\xi)\} \\ &= e^{-i2\pi f_0 \tau} T \text{sinc}[\alpha T(t-\tau)] \\ &= e^{-i2\pi f_0 \tau} T \text{sinc}[\pi B(t-\tau)] \end{aligned} \tag{5.26}$$

The result shows that the signal is phase-shifted by a phase equal to the phase delay at the center frequency f_0 with a reduced duration. For $t = \tau \pm 1/(2B)$ we have $|x(t)| = 2/\pi \approx 0.7$ that is half the signal power, which allows us to define its temporal duration W as:

$$W = \frac{1}{B} \ll T \tag{5.27}$$

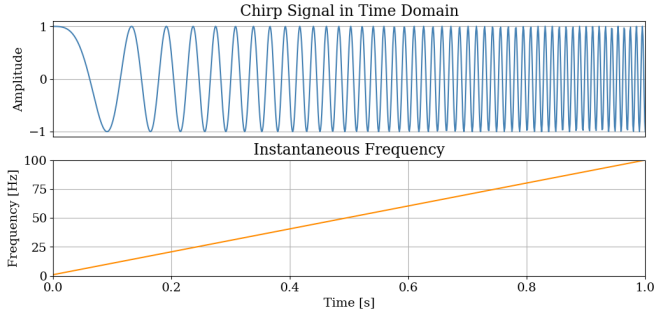

Figure 5.3: Representation of a chirp signal. The upper panel shows the variation of its amplitude over time, highlighting the progressive increase in frequency. The lower panel displays the corresponding frequency variation.

5.4 Radar Signals Propagation in Geological Media

Radar wave propagation through subsurface materials is governed by their EM properties. Considering non-magnetic media ($\mu_r = 1$), the real part of the permittivity ε' controls wave velocity and its imaginary part ε'' determines attenuation. The velocity of propagation in a medium is:

$$v = \frac{c}{\sqrt{\varepsilon'}} \tag{5.28}$$

with c light speed in vacuum.
When a radar pulse is transmitted toward the subsurface, it propagates downward until encountering a dielectric discontinuity (a lithological boundary, ice-rock interface, or fluid contact).

At this interface, a portion of the electromagnetic energy reflects back toward the receiver (the echo). The instrument records the two-way travel time τ, defined as:

$$\tau = \tau_{down} + \tau_{up} \tag{5.29}$$

where τ_{down} represents the propagation time from transmitter to target, and τ_{up} the return time from target to receiver. For monostatic configurations where transmitter and receiver are co-located, and assuming homogeneous media, these times are equal: $\tau_{down} = \tau_{up} = \tau/2$.
In this way radar sounding measurements rely on converting measured time delays into physical depths. For a single homogeneous layer overlying a reflecting interface at depth d, the time delay is linked to the depth according to the following relation:

$$d = \frac{c \cdot \tau}{2\sqrt{\varepsilon'}} \tag{5.30}$$

The accuracy of depth estimates depends critically on knowledge of subsurface dielectric properties. For measurements with time resolution $\Delta\tau$ and permittivity uncertainty $\Delta\varepsilon'$, the depth uncertainty propagates as:

$$\Delta d = \sqrt{\left(\frac{\partial d}{\partial t}\Delta t\right)^2 + \left(\frac{\partial d}{\partial \varepsilon'}\Delta\varepsilon'\right)^2} = \sqrt{\left(\frac{c}{2\sqrt{\varepsilon'}}\Delta t\right)^2 + \left(\frac{c \cdot t}{4(\varepsilon')^{3/2}}\Delta\varepsilon'\right)^2} \tag{5.31}$$

This relationship reveals that depth uncertainty increases with both temporal measurement precision and dielectric property knowledge. For deep targets, the permittivity uncertainty term often dominates, emphasizing the importance of independent dielectric characterization through laboratory measurements, in-situ observations, or inversion techniques.

5.4.1 Reflection Coefficient

Scattering of radar signals occurs at boundaries between materials exhibiting contrasting electromagnetic properties. The presence of this type of interfaces causes reflection, refraction, and diffraction phenomena. These reflections are the echoes collected by the radar. Greater electromagnetic contrast produces proportionally increased reflected energy. The Fresnel reflection coefficient ([126]) of an EM discontinuity between two media $m1$ and $m2$ describes this phenomenon:

$$R_c = \left|\frac{\sqrt{\varepsilon_1/\mu_1} - \sqrt{\varepsilon_2/\mu_2}}{\sqrt{\varepsilon_1/\mu_1} + \sqrt{\varepsilon_2/\mu_2}}\right|^2 \tag{5.32}$$

where:
ε_1 and μ_1 are respectively the dielectric permittivity and the magnetic permeability of $m1$;
ε_2 and μ_2 are respectively the dielectric permittivity and the magnetic permeability of $m2$.
This coefficient assumes sharp boundaries and provides limited accuracy for transitional interfaces and thin-layer structures where thickness approaches signal wavelength dimensions.

5.4.2 Energy Dissipation Mechanisms

The EM signals transmitted by the antenna undergo some energy loss processes due to multiple mechanisms:

- **Antenna losses** due to inefficiencies in energy transmission and reception;
- **Transmission losses** at interfaces, including the air-ground boundary;
- **Geometric spreading** that causes a reduction in energy per unit area following approximately $1/R^2$;
- **Intrinsic absorption**, i.e. conversion of electromagnetic energy to heat through conduction and polarization currents;
- **Scattering attenuation**, i.e. energy dispersed by heterogeneities in the medium.

Intrinsic absorption, related to material EM properties, is described by the loss tangent parameter, $tan\delta$, introduces in Chap. 4. When subjected to time-varying electric fields, dielectric media exhibit characteristic energy dissipation phenomena, commonly referred to as dielectric loss, whereby a portion of the electromagnetic energy is irreversibly converted into thermal energy. These processes are described by the attenuation coefficient α (Eq. 3.56) that can be rewritten in function of the loss tangent parameter $tan\delta$:

$$\alpha = \frac{\omega}{c}\sqrt{\frac{\varepsilon'}{2}}\left[\sqrt{1+\tan^2\delta}-1\right]^{1/2} \tag{5.33}$$

in which the material has been considered non-magnetic.
Volume scattering, instead, results from a subsurface environment generally exhibiting non-uniform characteristics, with heterogeneities functioning as electromagnetic scatterers. Small-scale scatterers generate weak omnidirectional reflections that remain below receiver detection thresholds. This process dissipates electromagnetic energy subsequently absorbed through ohmic mechanisms. The scattering dissipation follows an exponential decay with propagation distance R:

$$E = E_0 \exp(-\alpha_s R) \tag{5.34}$$

where: α_s represents the scattering attenuation coefficient, dependent upon scattering cross-section C_s and scatterer number density N according to the relation:

$$\alpha_s = \frac{NC_s}{2} \tag{5.35}$$

Scattering attenuation exhibits strong frequency dependence. When small-scale scatterers dominate, Rayleigh scattering occurs, characterized by the Rayleigh cross-section:

$$C_s = ca^6 f^4 \tag{5.36}$$

where:
c is a constant with dimensions $[\mathrm{m}^{-4}\,\mathrm{Hz}^{-4}]$;
a represents the characteristic scatterer dimension (sphere radius);
f is radar frequency.
In this framework surface scattering constitutes a distinct phenomenon occurring at continuous interfaces between different media with contrasting dielectric properties.

5.4.3 Surface Roughness

The geometry of the surface has a significant effect in radar contexts and its effects depend on radar working frequencies. In particular, the analysis of surface and subsurface is facilitated by a smooth topography, on the contrary, rugged surfaces could compromise it. The surface roughness can be defined through wavelength-normalized parameters. Considering the root-mean-square height variation s and the wavelength λ the electromagnetic roughness k_S parameter combines these quantities ([126]):

$$k_s = \frac{2\pi}{\lambda}s \tag{5.37}$$

Surface classification employs the Rayleigh criterion, establishing electromagnetic smoothness conditions. Considering Fig. 5.4, for normal incidence a), when a surface exhibits height variation h at point B relative to point A, the reflected ray at B travels a shorter distance by $2h$, creating phase difference $\Delta\phi = 2kh = 4\pi h/\lambda$ where $k = 2\pi/\lambda$. For oblique incidence b) at angle θ, the phase difference becomes $\Delta\phi = 2kh\cos\theta$. The Rayleigh criterion for smoothness requires $\Delta\phi < \pi/2$, or in terms of the root-mean-square height variation s in place of altitude variation h:

$$s < \frac{\lambda}{8\cos\theta} \quad \text{and} \quad k_s < 0.8 \quad \text{for} \quad \theta = 0 \tag{5.38}$$

While this criterion provides first-order roughness classification, more sophisticated analysis employs the Fraunhofer criterion [126], defining far-field distance requirements. For this criterion maximum phase difference between electric field rays from antenna center and edge has to be $\Delta\phi < \pi/8$ leading to:

$$s < \frac{\lambda}{32\cos\theta} \quad \text{or} \quad k_s < 0.2 \quad \text{for} \quad \theta = 0 \tag{5.39}$$

under these conditions a surface could be considered smooth.

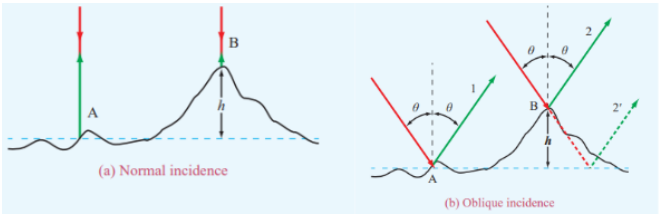

Figure 5.4: Left panel (a) shows the normal incidence in which the phase difference between the rays reflected from A and B is $\Delta\phi = 2kh$. The right panel (b) shows oblique incidence in which it is $\Delta\phi = 2khcos\theta$ (modified from [126]).

5.4.4 Subsurface Clutter

Surface roughness at scales comparable to the wavelength produces volumetric scattering that can obscure or can combine with subsurface returns. The clutter-limited SNR depends on surface statistics and dielectric contrast. Distinguishing geological layering from clutter requires statistical analysis of echo characteristics and SAR focusing to reduce the contributing surface area.

5.5 Resolution

The capability of detecting different targets laterally or vertically is determined by radar resolution.
Considering the echoes coming from two different targets as two delayed signals at times τ_1 and τ_2, we can think of the received signal $y(t)$ as the sum of these two reflections:

$$y(t) \propto x(t-\tau_1) + x(t-\tau_2) \tag{5.40}$$

where $x(t)$ is the transmitted signal, and effects due to amplitude variations are neglected to focus only on resolution. To distinguish the two targets as individual scatterers, the relative delay between the two signals have to follow this relation (Fig. 5.6 in which $\Delta\tau$ is represented by T):

$$\Delta\tau = \tau_2 - \tau_1 \geq W/2 \tag{5.41}$$

Using this relation, it is possible to derive both vertical (or range resolution) and lateral (or horizontal) one.

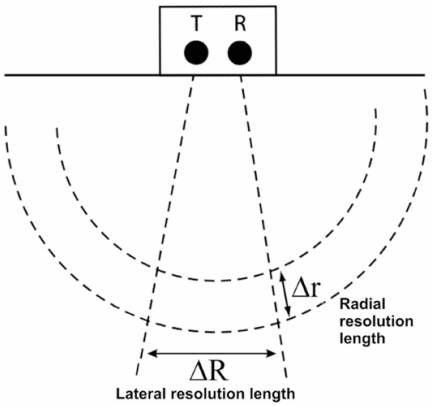

Figure 5.5: Simplified illustration to define vertical Δr and horizontal ΔR resolution (taken from [4]).

5.5.1 Vertical Resolution

Considering two targets at two different depths z_1, z_2, beneath the radar the range resolution is the minimum vertical distance at which we can distinguish the two reflectors: $\Delta z = \min\{z_2 - z_1\}$ (Fig. 5.6). The relative delay between received signals is:

$$\Delta\tau = \tau_2 - \tau_1 = \frac{2z_2}{v} - \frac{2z_1}{v} \tag{5.42}$$

where v is the velocity in the medium between the antennas and the objects.
Using Eq. 5.41 to find the lower limit for Δz it becomes:

$$2\frac{\Delta z}{v} = \frac{W}{2} \tag{5.43}$$

from which we calculate the vertical resolution Δz:

$$\Delta z = \frac{Wv}{4} \tag{5.44}$$

Recalling 5.11, 5.12, and with the assumption that the duration of the transmitted signal is related to the center frequency $W = 1/B \approx 1/f_0$, we obtain the following.

$$\Delta z \sim \frac{\lambda_0}{4} \tag{5.45}$$

This relation is widely used to approximate the range resolution of a radar.

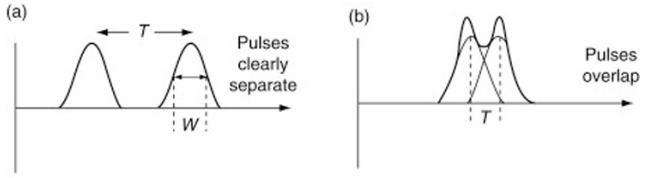

Figure 5.6: Scheme of resolution in radar systems. In the left case a) the difference of the two τ_{twtt} indicated by T is larger than $W/2$ and the two targets are distinguishable; in the right case b) the difference of the two travel time is smaller than $W/2$; the signals reflected from the targets result overlapped in a combined echo that make the radar not capable to identify the reflectors.

5.5.2 Horizontal Resolution

To obtain the horizontal resolution, we consider the two targets at a distance r from each other, but at the same depth z. The minimum horizontal distance at which the two targets can be distinguished ($\Delta r = \min\{r\}$). For simplicity, we consider the case of a radar system located above one of the two objects (Fig.5.7); in this configuration the relative delay between received signals is:

$$\Delta\tau = \tau_2 - \tau_1 = \frac{2\sqrt{r^2 + z^2}}{v} - \frac{2z}{v} \tag{5.46}$$

Hypothesizing the distance between targets much smaller than their depth $r = \Delta r \ll z$, we obtain in the first order:

$$\Delta\tau = \frac{2z}{v}\left(1 + \frac{\Delta r^2}{2z^2}\right) - \frac{2z}{v} = \frac{\Delta r^2}{zv} \tag{5.47}$$

and using Eq. 5.41 we obtain the limit condition:

$$\frac{\Delta r^2}{zv} = \frac{W}{2} \tag{5.48}$$

and lateral resolution Δr is:

$$\Delta r = \sqrt{\frac{zvW}{2}} \tag{5.49}$$

The horizontal resolution depends on velocity, temporal width, and depth; the radar loses resolution for deeper targets. In terms of wavelength, as in the previous case, lateral resolution is:

$$\Delta r = \sqrt{\frac{z\lambda_0}{2}} \tag{5.50}$$

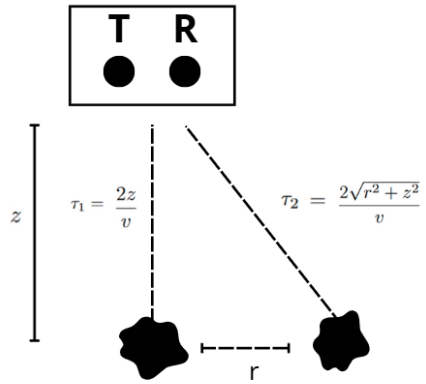

Figure 5.7: Simplified diagram illustrating lateral resolution. The two targets are at the same depth z and they are at a distance r from each other.

5.5.3 Radar Footprint

The lateral resolution is linked to the radar footprint, the area of the surface (or subsurface) that produces coherent signals (interfering and sum constructively with each other), producing a single pulse. Signals sum only when lateral distances are smaller than the lateral resolution. Therefore, recalling Eq. 5.49, radar footprint radius R_f, is defined as:

$$R_f = \sqrt{\frac{\lambda_0 h}{2}} = \sqrt{\frac{hvW}{2}} \tag{5.51}$$

The obtained footprint is valid only for the case of smooth interface with negligible roughness. For irregular and rugged surfaces, this relation is only a lower limit. These considerations are not valid for radars with high directivity like the Synthetic Aperture Radar (SAR).

5.6 Interference Phenomena

Previous equations allow us to introduce the interference phenomenon, which is addressed in Chap. 8 in the particular case of Ganymede.
In the Fourier transform domain, the received spectrum is the sum of spectra generated by two reflectors:

$$Y(f) \propto X_1(f) + X_2(f) = \left(e^{-ik2r_1} + e^{-ik2r_2}\right) X(f) \tag{5.52}$$

where $X(f)$ is the spectrum of the transmitted signal.
Considering the case of two targets at the same depth z, at distance r_1 and r_2 from the radar and at distance Δx from each other

$$r_1 = z \quad \text{and} \quad r_2 = z + \Delta r = \sqrt{z^2 + \Delta x^2} \tag{5.53}$$

the 5.52 becomes:

$$Y(f) \propto e^{-ik2z}\left(1 + e^{-ik2\Delta r}\right) = e^{-ik2z} 2e^{-ik\Delta r}\cos(k\Delta r) \tag{5.54}$$

As previously done, we assume that $\Delta x \ll z$, thus we have $\Delta r \approx \Delta x^2/2z$ and rewrite:

$$Y(f) \propto e^{-ik2z} 2e^{-ik\Delta x^2/z}\cos(k\Delta x^2/2z) \tag{5.55}$$

Analyzing the cosine, in the case of a precise wavelength λ_0, when

$$k\Delta x^2/2z = \pi/2 \quad \rightarrow \quad \Delta x^2 = \lambda_0 z/2 \tag{5.56}$$

there is destructive interference between the two signals: $Y(f) = 0$. For smaller phase values, the interference is constructive.
Same methods can be applied for two target at different depth z. In that case, interference is destructive when:

$$k\Delta r = k\Delta z = 2\pi/\lambda_0 \Delta z = \pi/2 \quad \rightarrow \quad \Delta z = \lambda_0/4 \tag{5.57}$$

For altitudes from the radar much greater than the wavelength ($z \gg \lambda_0$), additional lateral regions of constructive interference occur when:

$$k\Delta r = n\pi \qquad n = 0, 1, 2, \ldots \tag{5.58}$$

which determine the so-called Fresnel zones defined by radii Δx that satisfy the relation $\Delta x^2/\lambda_0 r = n$. These observations of interference phenomena can be applied for one frequency (wavelength λ_0) and have to be considered for each individual spectral component.

5.7 Radargrams

The products of radar instruments are the sums of collected echoes can be visualized as two-dimensional representations termed radargrams (Fig. 5.8), wherein the vertical dimension represents the two-way electromagnetic pulse travel time, the horizontal axis denotes the spatial position of the radar system along the survey trajectory and the color-scale is the intensity of the echoes. In this way, it is possible to represent the different subsurface discontinuities.

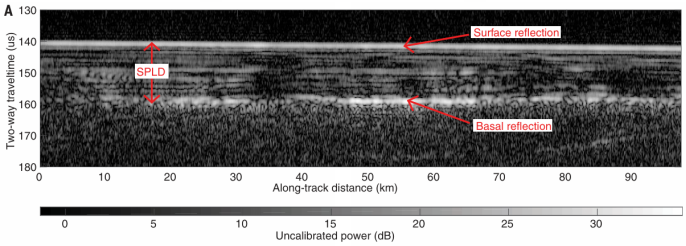

(a) Radargram of MARSIS data (Fig.1.1). Radargrams are bidimensional color-coded maps formed by sequence of echoes collected by the radar along its track. The vertical axis is the two-way travel time of the echo that is related to the depth of the interface that causes the reflection; horizontal axis is the along-track distance of the radar; the color code is function of the echo power. The first visible discontinuity is the interface between the atmosphere and the surface. The bright profiles beneath the superficial one indicate the interfaces that generate the reflections in the subsurface (taken from [152])

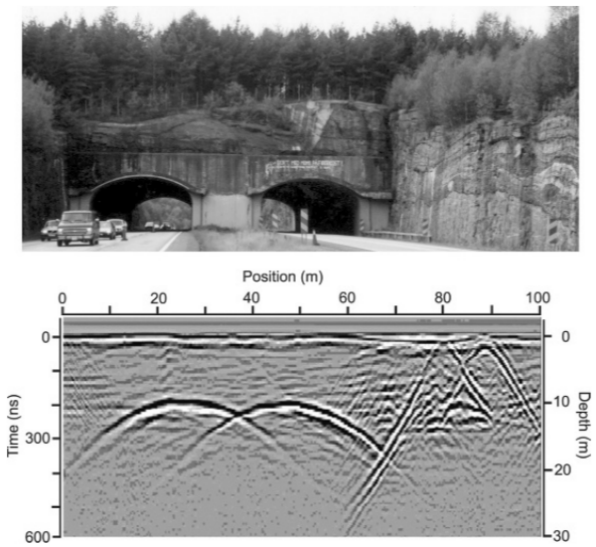

(b) A cross section obtained with Ground Penetrating Radar (GPR) traversing over two road tunnels. The upper panel represents the investigated area, the lower one is the radargram (taken from [96]).

Figure 5.8: Two examples of radargrams. The upper one is about Mars taken by a radar sounder (MARSIS) and the lower one is about the Earth taken by a GPR.

Chapter 6

Laboratory Instruments and Setup

In this chapter, we introduce the instruments and the setup we used to measure the EM properties of materials representative of the subglacial lake beneath Martian South Pole and Jovian icy moons. In order to study the EM properties under conditions similar to those encountered in planetary radar, we use a coaxial transmission line, an ultra-freezer and a Vector Network Analyzer (VNA).

6.1 Introduction to Transmission Line Theory

Transmission lines are specialized physical configurations designed to guide EM radiation between different spatial locations maintaining controlled propagation characteristics. These structures consist of conductors of sufficient longitudinal extent for wave effects to become non-negligible. The material used to confine the field depends on the frequency range in which the electromagnetic wave is intended to propagate. For radio and microwave frequencies, for example, metallic materials are used, sometimes filled with a low-loss dielectric medium, as in the case of coaxial cables. In this study, we employ coaxial transmission line configurations to retrieve the electromagnetic properties of materials across the frequency range of 1 MHz – 1 GHz. There are two complementary theoretical frameworks to describe wave propagation within transmission lines: a rigorous electromagnetic derivation based on Maxwell's formalism, and an alternative circuit-theoretic extension ([120]).

6.1.1 Electromagnetic Description

To provide a rigorous electromagnetic description of the transmission line, we first recall Maxwell's equations in the frequency domain, as presented in Equations 3.24 - 3.27, rewritten in this form:

$$\nabla \times \vec{E}(\vec{r},\omega) = -i\omega\vec{B}(\vec{r},\omega) = -i\omega\mu(\omega)\vec{H}(\vec{r},\omega) \tag{6.1}$$

$$\nabla \times \vec{H}(\vec{r},\omega) = i\omega\vec{D}(\vec{r},\omega) = i\omega\varepsilon(\omega)\vec{E}(\vec{r},\omega) \tag{6.2}$$

Considering TEM propagation, the field polarizations occupy the transverse plane x, y perpendicular to the propagation axis z, the field components satisfy specific partial differential relations:

$$\begin{aligned} &\partial_z E_y = i\omega\mu H_x, \quad \partial_z H_y = -i\omega\varepsilon E_x \\ &\partial_z E_x = -i\omega\mu H_y, \quad \partial_z H_x = i\omega\varepsilon E_y \\ &\partial_x E_y - \partial_y E_x = 0, \quad \partial_x H_y - \partial_y H_x = 0 \end{aligned} \tag{6.3}$$

Factorizing both the electric and magnetic fields as products of vector functions $\vec{t}(x,y)$ and $\vec{p}(x,y)$, and scalar functions $f(z)$ and $g(z)$:

$$\begin{aligned} \vec{E}(\vec{r},\omega) &= [t_x(x,y)\hat{x} + t_y(x,y)\hat{y}]f(z) \\ \vec{H}(\vec{r},\omega) &= [p_x(x,y)\hat{x} + p_y(x,y)\hat{y}]g(z) \end{aligned} \tag{6.4}$$

and assuming:

$$\vec{p}(x,y) = -\hat{z} \times \vec{t}(x,y) \tag{6.5}$$

the dependence on x, y can be expressed as the gradient of a scalar function $\phi(x, y)$ that satisfies the Laplace's equation for a static field:

$$\nabla^2_{x,y}\phi(x, y) = 0 \tag{6.6}$$

We can then express the electric and magnetic fields as follows:

$$\begin{aligned}\vec{E}(\vec{r}, \omega) &= -f(z)\nabla_{x,y}\phi(x, y)\\ \vec{H}(\vec{r}, \omega) &= g(z)\hat{z} \times \nabla_{x,y}\phi(x, y)\end{aligned} \tag{6.7}$$

Substituting these expressions in equation 6.3 and performing differentiation with respect to propagation direction yields one-dimensional wave equations:

$$\frac{\partial^2 g(z, \omega)}{\partial z^2} + \kappa^2 g(z, \omega) = 0 \tag{6.8}$$

$$\frac{\partial^2 f(z, \omega)}{\partial z^2} + \kappa^2 f(z, \omega) = 0 \tag{6.9}$$

where $\kappa = \frac{\omega}{c}\sqrt{\varepsilon(\omega)\mu(\omega)}$ is the magnitude of the wave vector.
These equations have as solutions the sum of two plane waves, one forward $f^+(z)$ and one backward $f^-(z)$:

$$\begin{aligned}f(z) &= f^+(z) + f^-(z) = f^+e^{-i\kappa z} + f^-e^{i\kappa z}\\ g(z) &= \frac{1}{\eta}[f^+(z) - f^-(z)] = \frac{1}{\eta}\left[f^+e^{-i\kappa z} - f^-e^{i\kappa z}\right]\end{aligned} \tag{6.10}$$

where $\eta = \eta_0\sqrt{\mu(\omega)/\varepsilon(\omega)}$ is the wave impedance.
Consequently, the electric and magnetic fields are given by:

$$\begin{aligned}\vec{E}(\vec{r}, \omega) &= -\nabla_{x,y}\phi(x, y)\left[f^+e^{-i\kappa z} + f^-e^{i\kappa z}\right]\\ \eta\vec{H}(\vec{r}, \omega) &= \hat{z} \times \nabla_{x,y}\phi(x, y)\left[f^+e^{-i\kappa z} - f^-e^{i\kappa z}\right]\end{aligned} \tag{6.11}$$

The complete description of the EM field can be obtained by knowing the boundary and initial conditions.

Characteristic Impedance in Coaxial Geometry

In our measurements, we use transmission lines with cylindrical symmetry; this configuration is defined by two conductors that delimit the space in which the wave propagates $r \in [a, b]$ with inner radius a and outer radius b. The scalar potential satisfies Laplace's equation in cylindrical coordinates r, θ:

$$\frac{1}{r}\frac{\partial}{\partial r}\left(r\frac{\partial\phi}{\partial r}\right) + \frac{1}{r^2}\frac{\partial^2\phi}{\partial\theta^2} = 0 \tag{6.12}$$

Considering the boundary conditions $\phi(a, \theta) = \phi_a$ and $\phi(b, \theta) = \phi_b$ and assuming $\phi_b = 0$ and the potential difference between conductors $V_0 = \phi_a - \phi_b$ the potential depends only on r and is given by:

$$\phi(r) = \phi_b + \frac{\phi_a - \phi_b}{\ln(a/b)}\ln(r/b) = \frac{V_0}{\ln(a/b)}\ln(r/b) \tag{6.13}$$

The electric field and the magnetic field are directed respectively in the radial ($\hat{r}$) and azimuthal ($\hat{\theta}$) directions:

$$\begin{aligned}\vec{E}(\vec{r}, \omega) &= \hat{r}\frac{V_0}{\ln(b/a)}\frac{1}{r}\left[f^+e^{-i\kappa z} + f^-e^{i\kappa z}\right]\\ \vec{H}(\vec{r}, \omega) &= \hat{\theta}\frac{V_0}{\eta\ln(b/a)}\frac{1}{r}\left[f^+e^{-i\kappa z} - f^-e^{i\kappa z}\right]\end{aligned} \tag{6.14}$$

The coaxial transmission line is powered by a voltage generator $V_g(t)$, therefore it is convenient to use a circuital approach (addressed in depth in the next section). The voltage $V(z, \omega)$ and current $I(z, \omega)$ along the line, have to satisfy boundary conditions at the beginning and end of the line. The voltage is calculated as the potential difference between the two conductors and the current as the circulation around one of the conductors as follows:

$$\begin{aligned}V(z, \omega) &= \int_a^b \vec{E}(\vec{r}, \omega)\cdot\hat{r}\,dr\\ I(z, \omega) &= \int_0^{2\pi} \vec{H}(\vec{r}, \omega)|_{r=c\in(a,b)}\cdot\hat{\theta}\,c\,d\theta\end{aligned} \tag{6.15}$$

From this, we obtain an expression that is also valid for other transmission lines:

$$\begin{aligned} V(z,\omega) &= V_0[f^+e^{-i\kappa z} + f^-e^{i\kappa z}] \\ I(z,\omega) &= \frac{V_0}{Z_c}\left[f^+e^{-i\kappa z} - f^-e^{i\kappa z}\right] \end{aligned} \tag{6.16}$$

where Z_c is the characteristic impedance, defined as:

$$Z_c = f_g\eta = f_g\eta_0\sqrt{\frac{\mu}{\varepsilon}} = Z_{c0}\sqrt{\frac{\mu}{\varepsilon}} \tag{6.17}$$

where:
Z_{c0} is the characteristic impedance of the line in air;
f_g is a geometric factor determined by the transverse dimensions of the transmission line;
η is the impedance of the wave and η_0 is the impedance of the wave in air.

In our specific case, the coaxial transmission line, we have $f_g = \ln(a/b)/(2\pi)$.

6.1.2 Circuital Approach

Considering the ratio between physical dimensions and the EM wavelength, circuits can be categorized into ordinary circuits (lumped-elements) and transmission lines. In lumped-element circuits, the physical dimensions of the components are much smaller than the wavelength of the signal ($\Delta z \ll \lambda$). Conversely, transmission lines constitute distributed-parameter networks wherein physical dimensions approach or exceed EM wavelengths, propagation effects can no longer be neglected and voltage and current change as continuous functions of position and time along the guiding structure (Fig. 6.1). However, an infinitesimal portion dz of the transmission line can be described as a lumped element circuit ($dz \ll \lambda$) and the circuit can be described by all infinitesimal circuit elements of length dz . The parameters distributed continuously throughout the circuit materials are:

- Series resistance per unit length R [Ω/m];
- Series inductance per unit length L [H/m];
- Shunt conductance per unit length G [S/m];
- Shunt capacitance per unit length C [F/m].

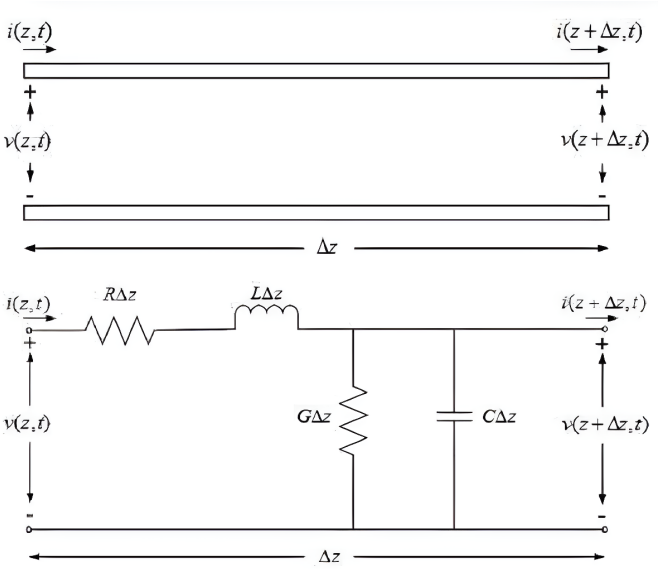

Figure 6.1: Transmission line with the representation of voltage and currents (a); lumped element equivalent circuit (b). Picture taken from [167].

Applying Kirchhoff's circuit laws to differential line segments produces the so-called *telegrapher equations*:

$$\frac{\partial V(z,\omega)}{\partial z} = -(R + i\omega L)I(z,\omega) \tag{6.18}$$

$$\frac{\partial I(z,\omega)}{\partial z} = -(G + i\omega C)V(z,\omega) \tag{6.19}$$

which can be solved by imposing $\kappa = -i\sqrt{(R + i\omega L)(G + i\omega C)}$ to find the current I and voltage V behavior:

$$V(z) = V_0^+ e^{-\kappa z} + V_0^- e^{\kappa z} \tag{6.20}$$

$$I(z) = I_0^+ e^{-\kappa z} + I_0^- e^{\kappa z} \tag{6.21}$$

where the exponential terms $e^{-\kappa z}$ and $e^{\kappa z}$ represent the propagation along the z-axis.
The current can be written as:

$$I(z) = \frac{V_0^+ e^{-\kappa z} + V_0^- e^{\kappa z}}{\eta} = \frac{R + i\omega L}{\kappa} V_0^+ e^{-\kappa z} + V_0^- e^{\kappa z} \tag{6.22}$$

Therefore, we can define the characteristic impedance Z_c as follows:

$$Z_c = \sqrt{\frac{R + i\omega L}{G + i\omega C}} \tag{6.23}$$

Recalling the EM description of the previous section, we obtain the distributed circuit parameters depending on EM properties through the comparison of κ and Z_c:

$$\kappa = \frac{\omega}{c}\sqrt{\varepsilon(\omega)\mu(\omega)} \qquad \kappa = -i\sqrt{(R + i\omega L)(G + i\omega C)} \tag{6.24}$$

$$Z_c = f_g \eta_0 \sqrt{\frac{\mu}{\varepsilon}} \qquad Z_c = \sqrt{\frac{R + i\omega L}{G + i\omega C}} \tag{6.25}$$

$$C = C_0 \varepsilon' = \frac{1}{c Z_{c0}} \varepsilon' \tag{6.26}$$

$$L = L_0 \mu' = \frac{Z_{c0}}{c} \mu' \tag{6.27}$$

$$G = \omega C_0 \varepsilon'' = \omega \frac{1}{c Z_{c0}} \varepsilon'' \tag{6.28}$$

$$R = \omega L_0 \mu'' = \omega \frac{Z_{c0}}{c} \mu'' \tag{6.29}$$

This establishes the equivalence between circuit and field-theoretic descriptions via the geometric factor f_g.

A characteristic parameter is the *input impedance* $Z_{in}(\omega)$ of the equivalent circuit of the transmission line. Assuming a homogeneous (with constant EM parameters along the line) transmission line of length L powered at $z = 0$ by a voltage generator $vg(t)$ and connected to a load of impedance Z_L at $z = L$, the reflection coefficient Γ is defined by:

$$\Gamma(z) = \frac{V^-(z)}{V^+(z)} = \frac{v^-}{v^+} e^{i\kappa 2z} \tag{6.30}$$

where:
v^- is the reflected wave;
v^+ is the transmitted wave.
The Eq. 6.16 can be rewritten as:

$$\begin{aligned} V(z) &= v^+(z)[1 + \Gamma(z)] \\ I(z) &= \frac{1}{Z_c} v^+(z)[1 - \Gamma(z)] \end{aligned} \tag{6.31}$$

in which $v^+ = V_0 f^+$ and $v^- = V_0 f^-$.
Considering the impedance Z as the ratio between V and I and imposing boundary conditions, the load reflection coefficient result:

$$\Gamma_L = \frac{Z_L - Z_c}{Z_L + Z_c} \tag{6.32}$$

and imposing $z = 0$ we obtain the input impedance at the generator interface:

$$Z_{in} = Z_c \frac{1+\Gamma(0)}{1-\Gamma(0)} = Z_c \frac{1+\Gamma_L e^{-i\kappa 2L}}{1-\Gamma_L e^{-i\kappa 2L}} = Z_c \frac{Z_L + iZ_c \tan(\kappa L)}{Z_c + iZ_L \tan(\kappa L)} \tag{6.33}$$

In the general case, in which the impedance of the generator (Z_g) at the beginning of the line ($z = 0$) and the impedance Z_L are different from the characteristic impedance (Z_c) we have two mismatches at the beginning and at the end of the line (6.2). This configuration cause multiple reflections and the back-scattering function, the energy fraction that comes back at the generator is defined as follows:

$$S(\omega) = \frac{Z_{in} - Z_g}{Z_{in} + Z_g} = \frac{\Gamma_g + \Gamma_L e^{-2i\kappa\ell}}{1 + \Gamma_g \Gamma_L e^{-2i\kappa\ell}} \tag{6.34}$$

where $\Gamma_g = (Z_{in} - Z_g)/(Z_{in} + Z_g)$ represents generator mismatch. In the following, three repre-

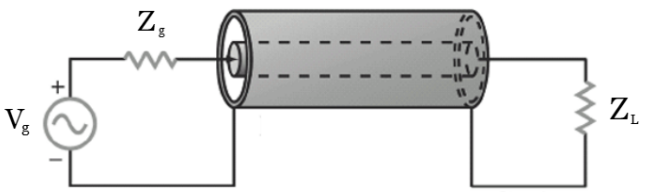

Figure 6.2: Transmission line representation with the generator V_g and the impedances Z_g and Z_L (modified from [120]).

sentative cases are examined, which will provide the conceptual groundwork for the calibration (discussed later) procedure of the Vector Network Analyzer (VNA) instruments that we used to measure the EM properties of planetary analogues.

- **Adapted load**: the load has an impedance equal to the characteristic impedance ($Z_L = Z_c$). In this scenario, no reflection phenomenon occurs at the end of the line (impedance matching), since the reflection coefficient is zero $\Gamma_L = 0$ and the reflection is only due to the mismatch between the generator and the line:

$$S(\omega) = \Gamma_g \tag{6.35}$$

- **Short load**: the load has zero impedance ($Z_L = 0$) and we expect that at the end of the line a total reflection phenomenon occurs with reflection coefficient $\Gamma_L = -1$, the energy is not transmitted to the load and beyond:

$$S(\omega) = \frac{\Gamma_g - e^{-i\kappa 2L}}{1 - \Gamma_g e^{-i\kappa 2L}} \quad Z_{\text{in}} = iZ_c \tan(\kappa L) \tag{6.36}$$

- **Open load**: the impedance of the load is infinite ($Z_L = \infty$). At the end of the line a total reflection phenomenon occurs but with reflection coefficient $\Gamma_L = 1$, the energy is not transmitted to the load and beyond:

$$S(\omega) = \frac{\Gamma_g + e^{-i\kappa 2L}}{1 + \Gamma_g e^{-i\kappa 2L}} \quad Z_{\text{in}} = -i\frac{Z_c}{\tan(\kappa L)} \tag{6.37}$$

6.2 Networks

In order to introduce the instrument, this section presents a brief introduction about microwave networks.

6.2.1 Impedance and Admittance Matrices

We describe the relationship between the different ports of the network in terms of equivalent circuits employing impedance and admittance matrices. Each port of a N-port microwave network has equivalent voltages and currents for the incident (V_n^+, I_n^+) and reflected (V_n^-, I_n^-) waves and the total voltage and current at the terminal plane of that port are given by:

$$V_n = V_n^+ + V_n^- \tag{6.38}$$

$$I_n = I_n^+ + I_n^- \tag{6.39}$$

Considering these voltages and currents at the N-ports the total impedance matrix of the network can be written as:

$$\begin{pmatrix} V_1 \\ V_2 \\ \vdots \\ V_N \end{pmatrix} = \begin{pmatrix} Z_{11} & Z_{12} & \cdots & Z_{1N} \\ Z_{21} & \ddots & & \vdots \\ \vdots & & \ddots & \vdots \\ Z_{N1} & \cdots & \cdots & Z_{NN} \end{pmatrix} \begin{pmatrix} I_1 \\ I_2 \\ \vdots \\ I_N \end{pmatrix} \tag{6.40}$$

or equivalently:

$$[\mathbf{V}] = [\mathbf{Z}][\mathbf{I}] \tag{6.41}$$

The admittance matrix ($\mathbf{Y}$), the inverse of the impedance matrix and is similarly defined by:

$$[\mathbf{I}] = [\mathbf{Y}][\mathbf{V}] \tag{6.42}$$

Each element of the impedance matrix (Z_{ij}) can easily be found with the ratio of the voltage and current correspondent elements ($V_i I_j$):

$$Z_{ij} = \left.\frac{V_i}{I_j}\right|_{I_k=0, k\neq j} \tag{6.43}$$

where the condition that all ports except the jth have been open-circuited is indicated by $I_k = 0$, $k \neq j$.
In the case of reciprocal networks, the impedance and consequently the admittance matrices are symmetric.

6.2.2 Scattering Matrix

However, high-frequency networks are well represented by the scattering matrix that provide a simpler description for the measurements performed by the Vector Network Analyzer. Fig. 6.3 shows a simplified block diagram of a two-port VNA, the instrument used to obtain the results presented in next chapters. For each port, the scattering matrix relates incident and reflected

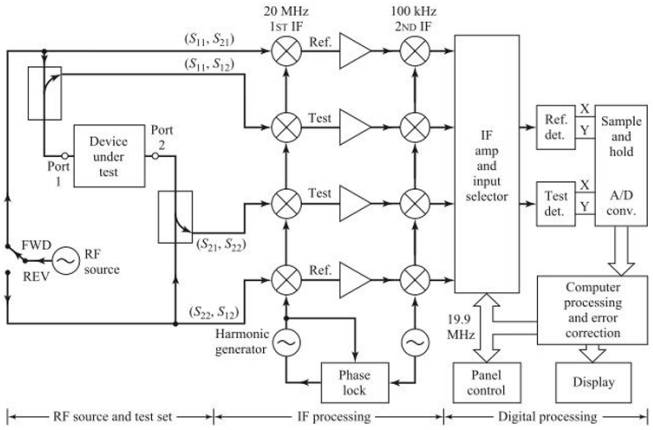

Figure 6.3: Block diagram of a two-port Vector Network Analyzer ([31]).

tension waves. Considering a 2-port network the scattering matrix is defined as

$$\begin{pmatrix} V_1^- \\ V_2^- \end{pmatrix} = \begin{pmatrix} S_{11} & S_{12} \\ S_{21} & S_{22} \end{pmatrix} \begin{pmatrix} V_1^+ \\ V_2^+ \end{pmatrix} \tag{6.44}$$

in which the element S_{ij} can be found as

$$S_{ij} = \left.\frac{V_i^-}{V_j^+}\right|_{V_k^+=0, k\neq j} \tag{6.45}$$

where the fact that all ports terminate in matched loads except the jth one is represented by $V_k^+ = 0$, $k \neq j$. S_{11} and S_{22} are the reflection coefficients, and S_{21} and S_{12} are the transmission coefficients. Also the [**S**] matrix is symmetric for reciprocal networks.

6.2.3 The Transmission Matrix

Another matrix representative of the 2-port network is the transmission (or ABCD) matrix (Fig. 6.4) defined in terms of the total tensions and currents:

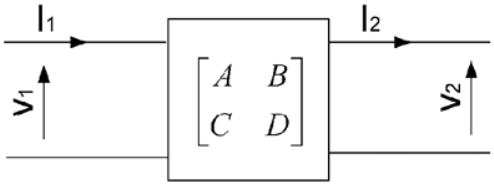

Figure 6.4: The transmission matrix in a two-port network.

$$\begin{pmatrix} V_1 \\ I_1 \end{pmatrix} = \begin{pmatrix} A & B \\ C & D \end{pmatrix} \begin{pmatrix} V_2 \\ I_2 \end{pmatrix} \tag{6.46}$$

6.3 Coaxial Transmission Line

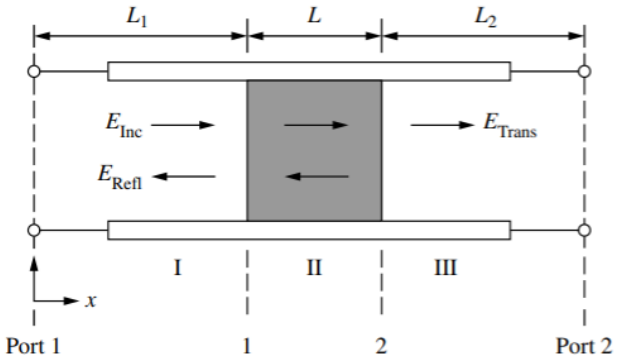

Figure 6.5: Diagram of transmission and reflection of EM waves caused by a sample inside and the transmission line in a two ports network (taken from [42]).

Fig. 6.5 illustrates schematically the configuration of the instruments for our measurements. In the regions I and III are the transmission lines connecting the two ports VNA to the region II in which the transmission line is filled with the sample. Assuming normalized incident waves, the electric field distribution is:

$$E_I = e^{-\kappa_0 x} + C_1 e^{\kappa_0 x} \tag{6.47}$$

$$E_{II} = C_2 e^{-\kappa x} + C_3 e^{\kappa x} \tag{6.48}$$

$$E_{III} = C_4 e^{-\kappa_0 x} \tag{6.49}$$

where κ and κ_0 are the propagation constants with the studied material and in the free space. Using boundary conditions on the EM field at the interfaces allows the determination of the

coefficients C_{1-4}. The scattering matrix in this case is symmetric and the scattering parameters are:

$$S_{11} = R_1^2 \cdot \frac{\Gamma(1-T^2)}{1-\Gamma^2 T^2} \tag{6.50}$$

$$S_{22} = R_2^2 \cdot \frac{\Gamma(1-T^2)}{1-\Gamma^2 T^2} \tag{6.51}$$

$$S_{12} = S_{21} = R_1 R_2 \cdot \frac{T(1-\Gamma^2)}{1-\Gamma^2 T^2} \tag{6.52}$$

with reference plane transformations $R_1 = e^{-\kappa_0 L_1}$ and $R_2 = e^{-\kappa_0 L_2}$ and transmission coefficient $T = e^{-\kappa L}$, and reflection coefficient:

$$\Gamma = \frac{\sqrt{\mu/\varepsilon} - 1}{\sqrt{\mu/\varepsilon} + 1} \tag{6.53}$$

In a two-port Vector Network Analyzer, such as the one employed for this work, by measuring the reflection parameters S_{11}, S_{22} and the transmission parameters S_{12}, S_{21}, it is possible to estimate the complex permittivity and permeability using some algorithms.

6.3.1 Modified Nicholson-Ross-Weir Algorithm

The Nicholson-Ross-Weir (NRW) inversion algorithm allows the extraction of EM properties of the studied sample from scattering parameters measured by the VNA ([147],[208]). In our case, for geometries with impedance mismatch between measurement cell and connecting cables (the cross-section of the measurement cell is larger than those of the cables that connect the probe to the instrument) the algorithm was slightly modified (Fig. 6.6, [132]) with a geometric correction factor $F_g = Z_c/Z_p$ in which Z_c and Z_p are the impedances of the connecting lines and the probe in air respectively. The relations between the reflection and transmission coefficients (Γ, T) with the scattering parameters are:

$$\Gamma = K \pm \sqrt{K^2 - 1} \tag{6.54}$$

$$K = \frac{S_{11}^2 - S_{21}^2 + 1}{2S_{11}} \tag{6.55}$$

$$T = \frac{S_{11} + S_{21} - \Gamma}{1 - (S_{11} + S_{21})\Gamma} \tag{6.56}$$

$$\sqrt{\frac{\varepsilon}{\mu}} F_g = \frac{1-\Gamma}{1+\Gamma} \tag{6.57}$$

$$\sqrt{\varepsilon\mu}\, l = \frac{ic}{2\pi f} \ln(T) \tag{6.58}$$

In case of no mismatch, $F_g = 1$, $Z_p = Z_c$ the algorithm reduces to the classic NRW. The choice of the positive or negative sign in Eq. 6.54 is determined by the condition $|\Gamma| \leq 1$. Combining Eqs. 6.57 and 6.58 the complex permittivity and permeability can be obtained:

$$\varepsilon = \frac{ic\ln(T)}{2\pi f l} F_g \frac{1-\Gamma}{1+\Gamma} \tag{6.59}$$

$$\mu = \frac{icF_g \ln(T)}{2\pi f l} \frac{1+\Gamma}{1-\Gamma} \tag{6.60}$$

Boughriet Simplification

In the simpler case of non-magnetic materials ($\mu = 1$), the Boughriet method can be used to estimate the complex permittivity [29]:

$$\varepsilon = \left[\frac{ic\ln(T)}{2\pi f l}\right]^2 \tag{6.61}$$

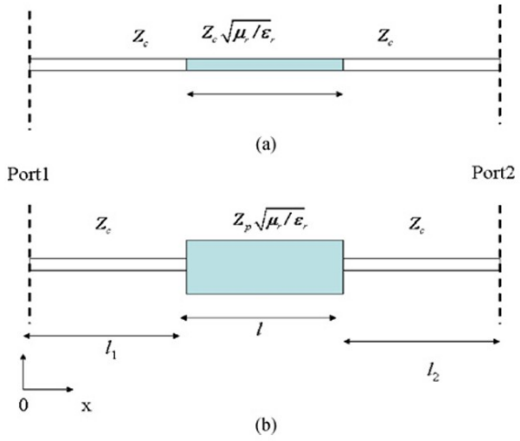

Figure 6.6: The upper panel (a) shows a uniform-air transmission line with no mismatch. The lower panel (b) shows the setup used in this work with different impedances between the probe and the connecting lines. In light blue, the transmission line of the probe has length l and impedance $Z_c\sqrt{\frac{\mu_r}{\varepsilon_r}}$ without the mismatch and $Z_c\sqrt{\frac{\mu_r}{\varepsilon_r}}$ in case of mismatch. Two cables (white transmission lines) of length l_1, l_2 and impedance Z_c connect the probe with the two port of the VNA (taken from [132]).

This formulation avoids divergence issues occurring in the NRW algorithm when $S_{11} \to 0$ and $S_{21} \to 1$ (Eq. 6.55) at specific frequencies:

$$f_n = \frac{nc}{2l\mathrm{Re}\{\sqrt{\varepsilon\mu}\}} \quad (n = 1, 2, 3, \ldots) \tag{6.62}$$

corresponding to half-wavelength resonances within the measurement cell.

6.4 Experimental Setup

Our measurement setup consists of the following (Fig. 6.7):

- Three measurement cells;
- Two-port Keysight E5071C Vector Network Analyzer;
- Polystyrene boxes;
- 50 Ω coaxial cables;
- Temperature sensors.

The used Vector Network Analyzer operates on the range 1 MHz to 3 GHz. The instrument connects to the measurement cell positioned inside the box via coaxial cables with N-type connectors. The instrumental sensitivity has been determined through characterization of reference materials with well-known EM properties ([31]):

$$\sigma_{limit} = 1.3 \times 10^{-5}\,\mathrm{S/m} \tag{6.63}$$

then in terms of f dependent imaginary permittivity:

$$\varepsilon''_{limit} = \frac{\sigma_{limit}}{2\pi\varepsilon_0 f} \tag{6.64}$$

6.4.1 Coaxial Probe Architecture

The measurement cells employ cage-coaxial configurations featuring eight outer conductors arranged in a circumference and a central conductor forming a cage, all 3.00 ± 0.03 mm diameter stainless steel rods to avoid chemical contamination of water samples. This multi-wire cage design is inserted in a teflon cell open at the top facilitating sample loading while minimizing interfacial polarization effects. Three probes (Fig. 6.8) with different dimensions accommodate diverse sample volumes. The three cells have the following dimensions: height = 60 mm, width = 50 mm, and length = 50 mm, 100 mm and 150 mm.

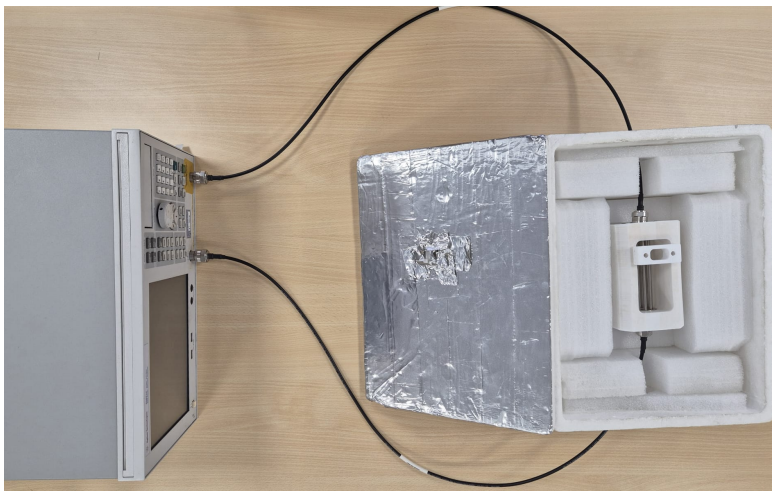

Figure 6.7: The picture shows the setup for the measurements. The cell containing the sample is placed inside the polystyrene box, which is then covered with the silver-colored coating on the side of the box in the picture. Two apertures located on the sides of the box allow the cell to be connected to the two coaxial cables interfacing with the VNA. Additionally, an opening on the lid of the box enables the temperature probe, inserted into the sample, to be routed outside.

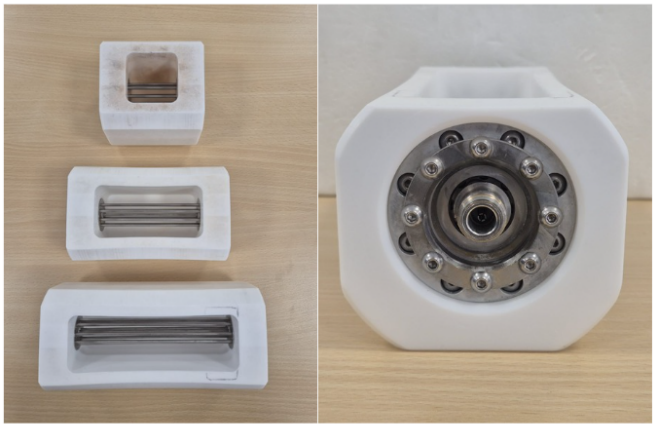

Figure 6.8: On the left, the three coaxial probe lines with different length (50 mm, 100 mm, or 150 mm going downward). On the right, one of the two N-type connectors on the profile of the cell where the cables have to be connected.

6.4.2 Calibration

The purpose of the calibration is to remove from the measured response all the contributions that do not originate from the intrinsic EM properties of the sample. The measurement structure comprises three transmission lines: input connector, sample cell, and output connector. Given this experimental configuration, the calibration procedure compensates for various extrinsic effects:

1. The influence of the two transmission lines corresponding to the coaxial cables;
2. Contributions introduced by the connectors located on both sides of the measurement cell (Fig. 6.8);
3. The electrical parameters (electrical length l and characteristic impedance Z_c) associated with the transmission line in the cell (the cage) responsible for the propagation of the signal inside the sample to determine its scattering parameters.

Cables

The VNA introduces two principal categories of measurement error: systematic and random errors. Random errors are often attributed to the intrinsic instrumental noise and can be limited by defining the lowest uncertainty threshold achievable with the instrument ($\sigma_{limit} =$

1.3×10^{-5} S/m in our case). Systematic errors, by contrast, can be mitigated through a full two-port calibration performed using the same coaxial cables employed during the actual measurements at the same environmental conditions. It is crucial to perform the calibration at the same temperature as the subsequent measurements, since even minor temperature variations between calibration and acquisition can introduce additional systematic deviations. The calibration procedure is carried out before every set of measurements for the two ports at the room temperature of 292 K (during the measurements the cables are at the room temperature), and consists of four steps called Short-Open-Load-Through (SOLT procedure):

- A measurement of an **Open** as a standard ideal total reflection of the generated signal;
- A measurement of a **Short** as a standard ideal total reflection of the generated signal with 180° phase shift;
- A measurement of a **Load** matched 50 Ω impedance to eliminate reflection.
- A measurement of the **Through**, i.e. a direct port-to-port connection representing ideal transmission between the two ports.

Connectors

The transmission matrix corresponding to our measurement setup is:

$$T_{meas} = T_{con} T_{mc} T_{con} \tag{6.65}$$

where: T_{con} is the two connectors transmission matrix;
T_{mc} is the measurement cell transmission matrix.
To eliminate the effects of the two connectors, a connector calibrator (identical to those present on the sides of the coaxial cells in Fig. 6.9) has been used. The quantification of the matrix T_{con} allows the analysis of cell parameters through T_{mc}.

Figure 6.9: The connector calibrator used to eliminate the effects of the connectors on the sides of the measurement cell

Measurement cells

The parameters of the probes are the electrical length l_e and characteristic impedance Z_c and exhibit frequency and temperature dependence. To determine their electrical parameters, measurements were performed with empty cells (air) and filled with glass beads, a soil simulant with well known permittivity and no electrical losses. While the air measurements suffer from poor field confinement at low frequencies, glass beads measurements provide superior field localization and parameter stability; therefore, they were used for the calibration (6.10). Temperature-dependent calibration has been performed in the range 200 - 290 K and allows corrections for both electrical parameters, ensuring accurate material characterization across the operational temperature range. The calibration of the cells has been validated employing ethanol standards (pure and 96% purity) across 200-290 K. The extracted relaxation frequencies are in a good agreement with literature values spanning 110-323 K, confirming measurement fidelity across the extended temperature domain ([31]).

6.5 Uncertainty Quantification

The uncertainties in scattering parameters, and consequently EM properties, have been computed following ISO Guide to the Expression of Uncertainty in Measurement principles ([88]). The total uncertainty comprises type A and type B contributions.

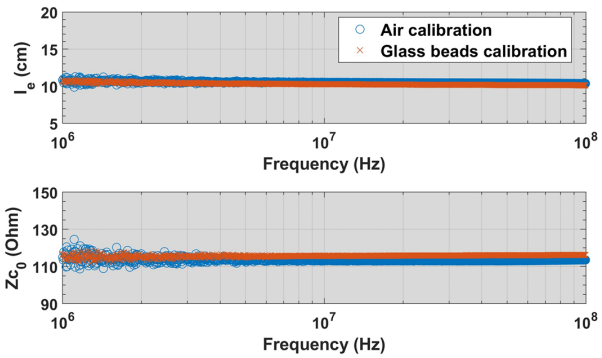

Figure 6.10: Air and glass beads calibration of the 100 mm probe, at room temperature, to estimate electrical parameters l_e and Z_c (taken from [31]).

Type A Uncertainty

Statistical uncertainty has been obtained from repeated measurements of reference materials (empty cell, glass beads, distilled water, ethanol). For 500 measurement replications at fixed temperature, the propagation through the parameter extraction algorithm, under the assumption that the uncertainties are independent and uncorrelated, yields the following:

$$u_A = \sqrt{\sum_i \left(\frac{\partial y}{\partial x_i} u_{x_i} \right)^2} \tag{6.66}$$

where u_{x_i} represent standard deviations of scattering parameters for the different materials.

Type B Uncertainty

The type-B uncertainties arise from imperfect calibration and inherent setup asymmetry that cause asymmetries in scattering parameter measurements. Indeed the estimation of EM properties differs depending whether one uses S_{11}, S_{12} or S_{22}, S_{21} scattering parameters. The type-B uncertainty is therefore evaluated as the standard deviation of a uniform probability distribution defined over the interval bounded by the permittivity (and permeability) values obtained from the two couples of scattering parameters. For the permittivity, for example, it is:

$$u_B = \frac{\varepsilon_{S_{11},S_{12}} - \varepsilon_{S_{22},S_{21}}}{\sqrt{12}} \tag{6.67}$$

The total uncertainty follows from the quadrature combination:

$$u_{total} = \sqrt{u_A^2 + u_B^2} \tag{6.68}$$

6.5.1 Measurement Procedures

In this thesis, we analyzed dielectric measurements of perchlorate solutions as analogs of the Martian subglacial lake ([152]) and performed simulations based on measurement data obtained from analogues of the icy crusts of Jupiter's moons ([32]). However, the aqueous salt solutions for the two different purposes were prepared following the same procedures described in this section. For the mixture of ice and powdered materials as analogues of the Ganymede crust the procedure is more complex and can be found in detail in [32] and [31]. In addition to the measurement setup previously presented, the following equipment was employed:

- A water purification system that produces double-distilled water;
- $NaCl$ provided by the SIGMA-ALDRICH, magnesium perchlorate hexahydrate $Mg(ClO_4)_2 \cdot 6H_2O$ provided by ALFA AESAR, calcium perchlorate tetrahydrate $Ca(ClO_4)_2 \cdot 4H_2O$ provided by ACROS ORGANICS;
- A hot-plate stirrer (Bibby B212);

- An ultra-freezer (NEXUS H Angelatoni Life) with a working temperature of 193 K.

The measurement procedure is composed by different phases:

1. Solutions were prepared in beakers by dissolving bidistilled water and the desired salt in the required concentration.
2. The mixture was homogenized using a magnetic stir bar on a hot-plate stirrer (Fig. 6.11). Once prepared, the solution's electrical conductivity was measured at room temperature to check if it remains constant before and after the measurement.
3. Meanwhile, the empty measurement cell was placed inside the polystyrene box (6.12), with the temperature sensor inserted, but leaving the lid open.
4. The box was positioned inside the ultra-freezer.
5. The solution was poured into the cell, and the box was sealed. An aperture in the lid allowed the temperature probe, connected externally to the freezer, to monitor the temperature decrease of the sample during the freezing process.
6. After a predetermined time interval, defined according to the requirements of the analysis, the box was removed from the ultra-freezer, connected to the VNA as previously shown in Fig. 6.7. The cell was further insulated with additional thermal material.
7. The dielectric properties of the sample were measured as its temperature increased from the ultra-freezer temperature of 193 K up to room temperature of 292 K .

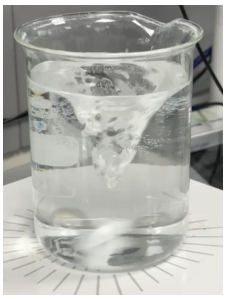

Figure 6.11: The mixing procedure of one perchlorate solution.

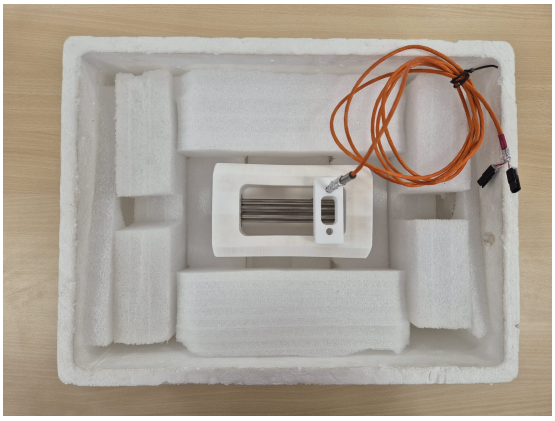

Figure 6.12: The setup of the box with the empty 100 mm cell before placing it in the ultra-freezer and then filling it with the sample. The temperature sensor (a pt 100 orange in the picture), consisting of a platinum thermoresistance, is inserted in the cell and will be connected to the instrument outside the ultra-freezer.

Chapter 7

Measurements

In this chapter, we present and discuss the results of dielectric measurements conducted for two main purposes. The first section focuses on the electromagnetic properties of analogues of potentially stable brines within the shallow Martian subsurface, with the aim of characterizing the putative subglacial lake detected by [152]. In the second part, we report both published and forthcoming results concerning analogues of the icy crusts of Jovian moons, which are subsequently employed in the next chapter for radar propagation and scattering simulations.
As previously discussed in Chapter 4, the electromagnetic properties of saline aqueous solutions are of particular relevance from a radar sounding perspective. On the one hand, dissolved salts enhance the imaginary component of the permittivity, thereby increasing signal attenuation and reducing radar penetration depth. On the other hand, by depressing the freezing point of water, saline solutions can produce strong dielectric contrasts that remain detectable even at temperatures below 273 K, allowing the identification of liquid or partially liquid phases in otherwise frozen environments. To introduce the results that will be discussed in the following sections, it is useful to examine an example of how the real part of the permittivity varies with temperature at a fixed frequency (radar sounder frequencies in this case), starting from the moment the sample is removed from the ultra-freezer ($\approx$ 195 K) until complete melting (above 273 K). From the permittivity, it is possible to identify the three phases, solid, mushy, and liquid, previously described. Fig. 7.1 shows two representative cases of saline solutions: one with sodium chloride and one with magnesium perchlorate. The measurements exhibit an initial plateau where the permittivity remains constant at values consistent with saline ice (equal to or slightly higher than that of pure ice, approximately 3.1). Once the eutectic temperature is exceeded, the more salt-enriched regions begin to melt, producing a rapid increase in permittivity. The subsequent rise in permittivity during the mushy phase depends on the fraction of brines that begins to melt within the volume of the sample probed by the measurement cage. Above 273 K, the sample is fully melted, and a further abrupt increase in permittivity is observed, approaching or exceeding that of pure water ($\varepsilon_{pure\,water} = 80$) due to effects introduced by the dissolved salts.

7.1 Martian Subglacial Brines

Given their ability to lower the freezing temperature of water to martian subsurface temperatures, perchlorates are critical for assessing the stability of brines even at shallow depths. Moreover, such brines may remain liquid due to their low eutectic temperatures or persist in metastable states below the eutectic point [118], staying in the mushy state at temperatures below the eutectic point. Calcium and magnesium perchlorates ($Ca(ClO_4)_2$, $Mg(ClO_4)_2$) have been both detected on the Martian surface ([168],[30]) and, are therefore strong candidates for the composition of possible Martian brines and for the characterization of the bright reflector detected by [152] and [118].
We measured the complex dielectric permittivity ε across a temperature range of 195 K to 292 K, including the eutectic temperatures of calcium and magnesium perchlorates (198 K [172] and 216 K [190] respectively) at different concentrations below the eutectic values (49.8% and 44% respectively) over a radar sounder frequency spectrum, from 1 MHz to 1 GHz. Beyond complex permittivity ε and conductivity σ, we computed the apparent permittivity ε_a (Eq. 7.1), which is indicative of the reflection coefficient Γ_{12} at an interface between two media characterized by distinct permittivities ε_1 and ε_2 ([133]). To reproduce MARSIS data consistent with the

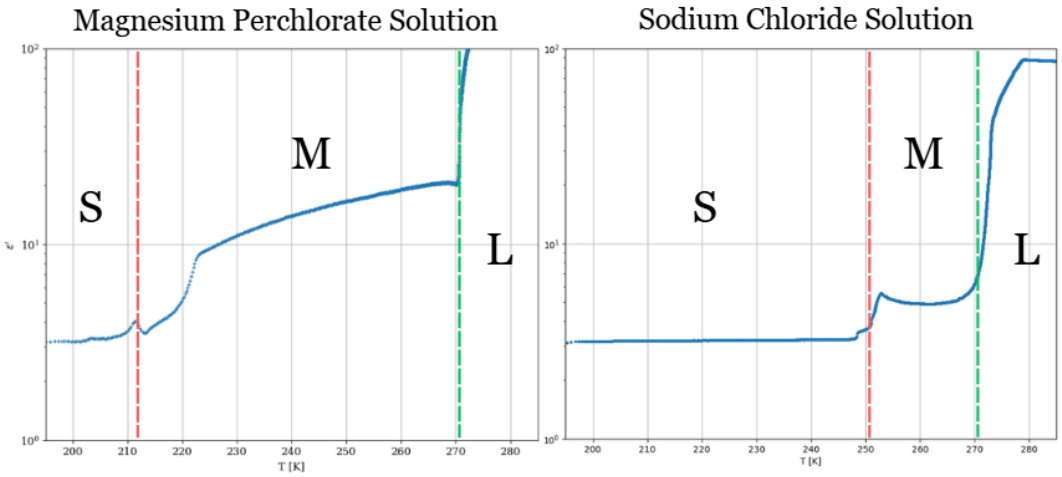

Figure 7.1: Real permittivity as a function of the temperature of a magnesium perchlorate solution (left) and sodium chloride solution (right) at radar frequencies. In the three regions corresponding to the different physical states of the sample (solid, mush, liquid), marked respectively by the capital letters S, M, and L and delimited by vertical dashed lines, the permittivity assumes distinctly different values: approximately 3.1 in the solid phase, above 80 in the fully liquid phase, and intermediate values within the mushy region. The transition zones exhibit abrupt changes in permittivity, associated first with the partial and then with the complete melting of the sample. Due to the two different eutectic temperatures the transitions between solid and mush happen at two different points.

observed subglacial water body, ε_a should exceed 33 [133]. It is important to note that the criteria used to assess the physical state of the sample (ε' around 3.1 indicates a fully frozen sample, ε' around or above 80 indicates a liquid state, and intermediate values corresponding to mushy phases) remain valid for ε_a as well.

$$\varepsilon_a = \varepsilon_1 \left[\frac{1+|\Gamma_{12}|}{1-|\Gamma_{12}|}\right]^2 = \varepsilon_1 \frac{\varepsilon_1 + |\varepsilon_2| + \sqrt{\varepsilon_1 + |\varepsilon_2| - 2\varepsilon_1\varepsilon_2'}}{\varepsilon_1 + |\varepsilon_2| - \sqrt{\varepsilon_1 + |\varepsilon_2| - 2\varepsilon_1\varepsilon_2'}} \tag{7.1}$$

7.1.1 Magnesium Perchlorate Solutions

Here we report Tab. 7.1 compiling all measurements acquired changing three parameters: the dimensions of the cell to investigate the influence of the volume on EM properties, the period inside the ultra-freezer to analyze the effects of the time, and the concentration of the solute to examine the dependence on the composition. Since the EM properties can change depending on the heating rate of the sample, it is important to verify that the heating times of all measurements are comparable. Fig. 7.2 shows the variations of temperature during each measurement. All results are mutually consistent, as all the curves overlap regardless of the salt concentration, the measurement cell used, or the residence time in the ultra-freezer. By considering the variations of the real part of the permittivity and the conductivity over the entire frequency range, i.e. the spectrum (Fig. 7.3), examined for a representative sample, three distinct behaviors can be identified at three different temperatures, corresponding to the solid, mush, and liquid phases previously described. The conductivity values remain fairly constant across the full frequency interval for both the mushy and liquid phases, particularly within the range of interest (1–10 MHz); the variations in the real part of the permittivity are also minimal. At low frequencies, the conductivity becomes noisy as it approaches the instrumental detection limit. At higher frequencies, between 10^8 Hz and 10^9 Hz, both quantities exhibit irregular behavior at all temperatures due to instrumental resonances (the same anomalies recur at the same frequencies in every measurement). However, this issue does not affect our analysis, which focuses exclusively on the MARSIS operating frequencies. The working frequencies of MARSIS are 3, 4, and 5 MHz. To assess how the different parameters influence the electromagnetic properties, we present the results as a function of temperature at 4 MHz. Fig. 7.4 shows all measurements in terms of real permittivity and conductivity. In the following paragraphs, we focus on the apparent permittivity (Fig. 7.5) and examine the effects of each of the three parameters while keeping the other two fixed, ensuring that any observed differences can be attributed specifically to the parameter under investigation. Since the results are very similar at high temperature (T > 240 K) and show irregularities during the phase transition between

Magnesium Perchlorate Solutions

Cell Length (mm)	Time (d)	Concentration (wt%)
50	4	10
100	1	10
100	1	10
100	1	15
100	2	15
100	2	15
100	4	5
100	4	10
150	1	10
150	4	5
150	4	10
150	4	10
150	4	12
150	4	15
150	4	15
150	4	20
150	15	10

Table 7.1: Overview of the magnesium perchlorate solutions measurements. The three columns represent the dimension of the cell (its length in mm, see 6), the time of residence in the ultra-freezer, and the percentage of the concentration.

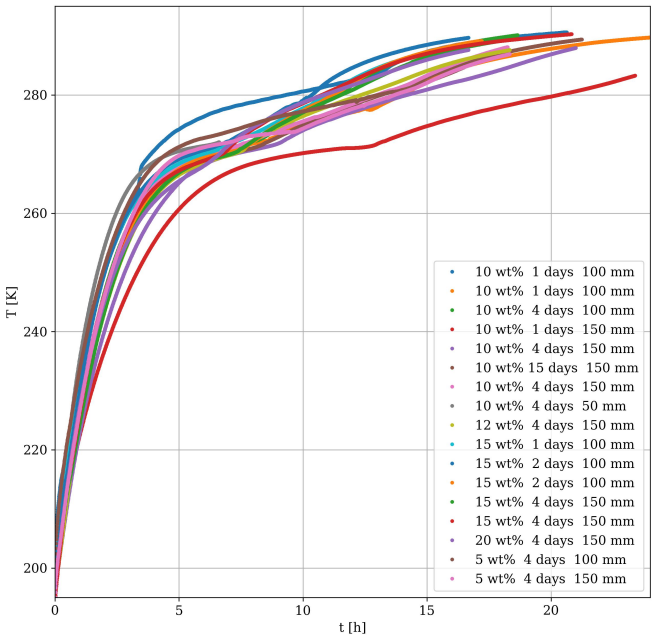

Figure 7.2: Variations of the temperature of magnesium perchlorate solutions in the heating phase in which the scattering parameters have been acquired. All the measurements show consistent heating rate, therefore the measurements are comparable consistently.

260 K and 280 K (temperature range not involved in our analysis) the following considerations concern the region where $T < 240$ K.

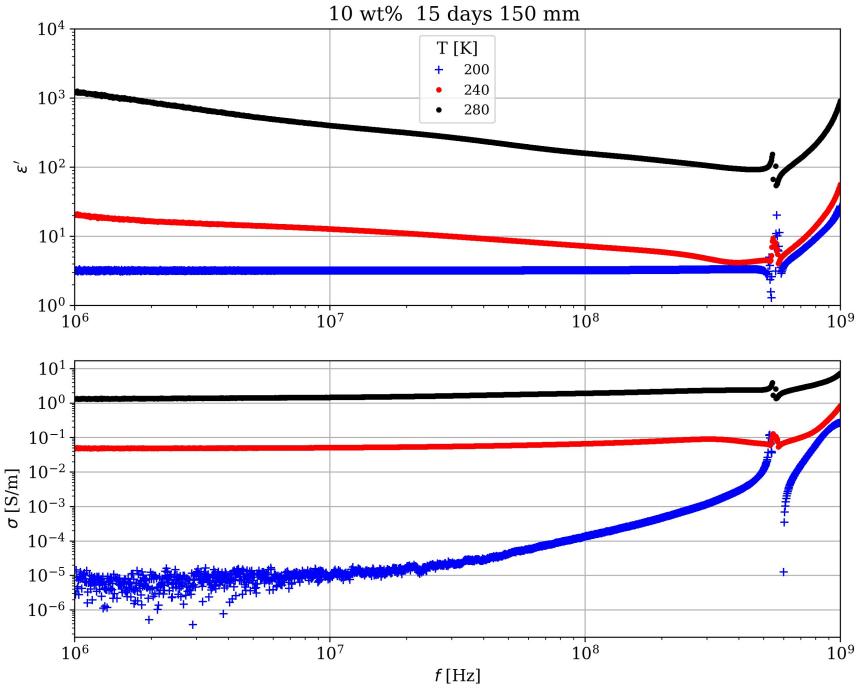

Figure 7.3: Spectra of real permittivity (upper panel) and conductivity (lower panel) of a magnesium perchlorate sample with salinity of 10% measured in the 150 *mm* cell after 15 days in the ultra-freezer, at three different temperatures, 200 K, 240 K, 280 K.

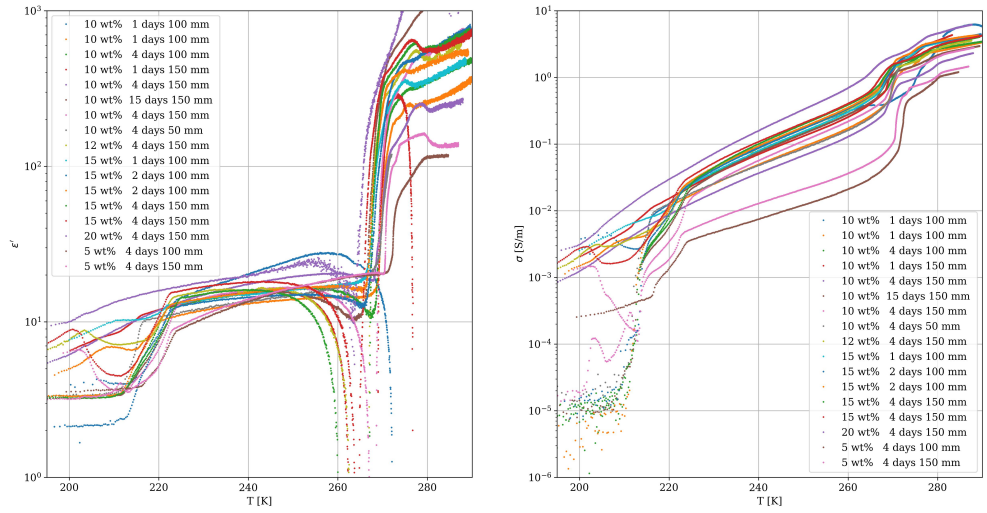

Figure 7.4: All the measurements of ε' and σ of magnesium perchlorate solutions at 4 MHz. The legend reports, in order, the perchlorate concentration in the solution, the residence time in the ultra-freezer, and the length of the measurement cell. At temperatures corresponding to the complete melting of the sample, some irregularities appear in the measurements: the real part of the permittivity exhibits a sudden decrease followed by an abrupt increasing. In this interval, the instrument is unable to capture the sharp increase occurring during the phase transition. However, this effect has no impact on our analysis, as we focus on lower temperatures compatible with Martian environmental conditions.

Cell Volume

To investigate the dependence on cell geometry, Fig. 7.6 presents measurements acquired at fixed ultra-freezer residence time (4 days) and constant perchlorate concentration (10 %). With increasing cell dimensions, the apparent permittivity behavior exhibits reduced regularity.

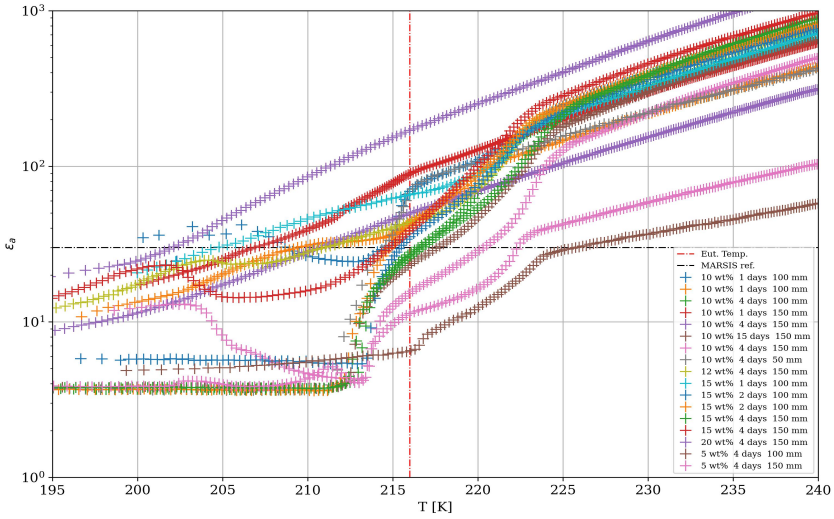

Figure 7.5: Apparent permittivity ε_a as a function of temperature in the range 195 K - 240 K of all the measurements of magnesium perchlorate solutions.

As these measurements were performed during warming cycles, and excluding the anomalous freezing behavior observed in one measurement (likely attributable to mechanical stress that we will discuss later), the data suggest incomplete freezing in larger cell configurations, as evidenced by permittivity values approximately equal to 10 even at temperatures lower than the eutectic point. For those samples that, at some point, froze reaching the value of 3 the abrupt increase of the permittivity around the eutectic happens less gradually in smaller cells. This behavior may be attributed to factors related either to the intrinsic response of the sample or to the measurement setup. On one hand, smaller samples could tend to melt more rapidly. On the other hand, in shorter measurement cells, the portions of the sample within the cage that begin to melt may represent a larger fraction of the total volume, leading to a greater increase in the average permittivity. In contrast, in longer cells, the melting regions constitute a smaller percentage of the sample inside the cage, resulting in a comparatively slower rise in the average permittivity.

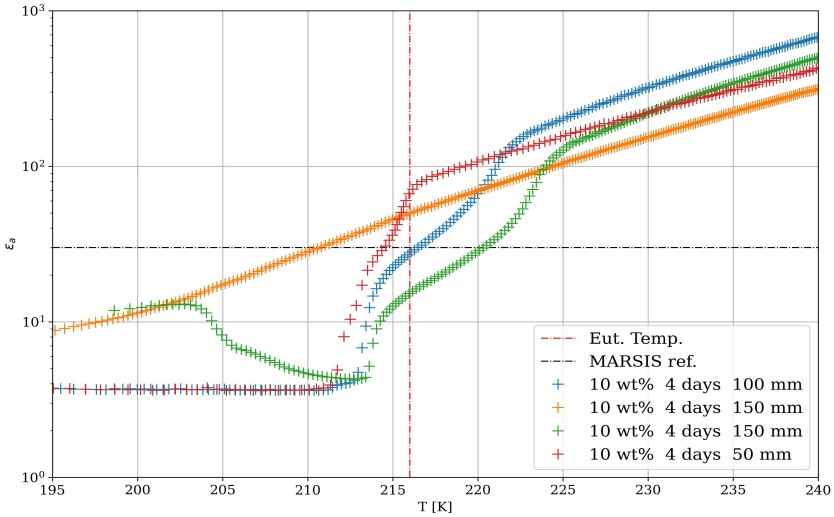

Figure 7.6: Apparent permittivity ε_a as a function of temperature in the range 195 K - 240 K of 4 different measurements with the same concentration (10%) and residence time in the ultra-freezer (4 days), but different cell length (50 mm, 100 mm, 150 mm).

Residence Time in the ultra-freezer

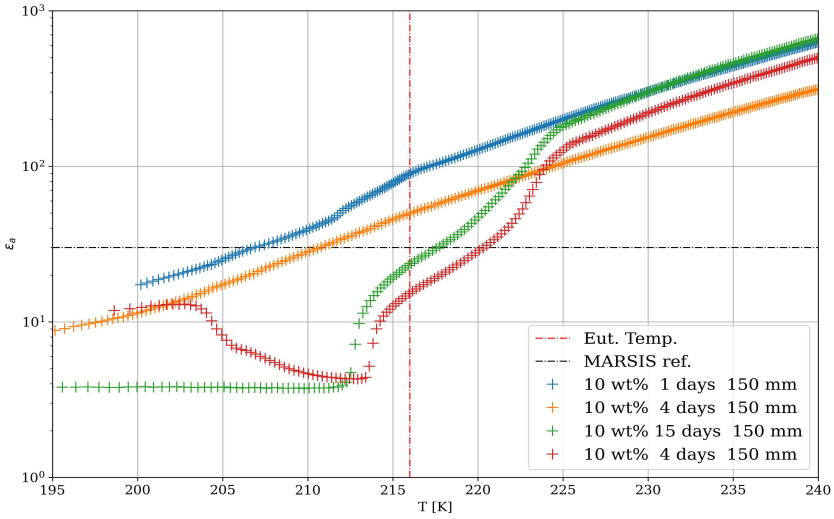

Figure 7.7: Apparent permittivity ε_a as a function of temperature in the range 195 K - 240 K of 4 different measurements with the same concentration (10 %) and same cell length (150 mm), but different residence time in the ultra-freezer (1-4-15 days).

To examine the effects of the residence time in the ultra-freezer Fig. 7.7 shows the apparent permittivity of samples with a fixed concentration (10%) and cell length (150 mm). The samples did not completely freeze in the short periods (1, 4 days), and the brine fraction appears higher for samples with shorter residence times. In the long-period (15 days) measurement, the sample is, instead, completely frozen. This behavior may indicate that a duration of 4 days is insufficient for the sample to reach full thermodynamic equilibrium. Despite the low temperatures, a longer residence time appears to be required for complete crystallization of the ice and full solidification of the solution. However, Fig. 7.6 shows that, for smaller sample volumes, a 4-days residence time is sufficient to achieve complete freezing. This observation indicates that the time required to reach thermodynamic equilibrium depends not only on temperature but also on sample volume. The resulting time-volume dependence is particularly relevant for Martian conditions, as it implies that the stability of potential subsurface brines may vary significantly with the spatial and temporal scale of the brine reservoirs. Further measurements will provide a more complete understanding of these effects.

Concentration

Perchlorate concentration has a substantial influence on the measured apparent permittivity, both in magnitude and in determining the physical state of the sample (Fig. 7.8). In this case we analyzed the 4-days, 150-mm measurements. With the exception of a single measurement at 15% concentration (red dataset), samples with perchlorate content exceeding 5% did not freeze completely within 4 days. Furthermore, the apparent permittivity approaches the MARSIS detection threshold at progressively lower temperatures with increasing perchlorate concentration. For instance, if the subglacial reservoir contains 20% magnesium perchlorate, the MARSIS observations could be reproduced at approximately 204 K. Above 230 K, all permittivity values increase monotonically and consistently with increasing concentration.
In summary, our results suggest that larger measurement cell volumes and high salt concentrations tend to inhibit sample freezing, whereas longer times in the ultra-freezer appear to favor solidification.

Metastability

We observe in the real part of the permittivity in Fig. 7.4 and the apparent permittivity in Fig. 7.5 that in several cases the samples did not freeze even at temperatures lower than eutectic. This metastability arises from the fact that, in many cases, the solutions did not form a sufficient number of nucleation seeds to trigger crystallization throughout the entire sample

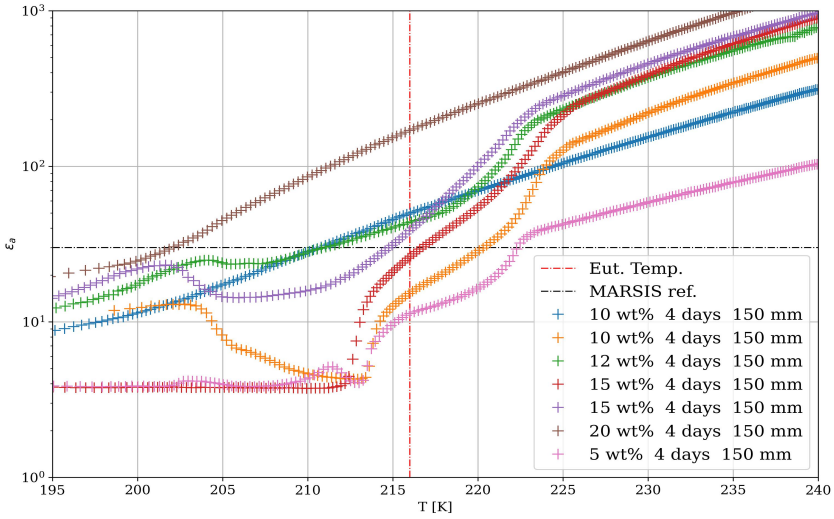

Figure 7.8: Apparent permittivity ε_a as a function of temperature in the range 195 K - 240 K of 4 different measurements with the same residence time in the ultra-freezer and same cell length (150 mm), but different concentration of magnesium perchlorate.

under the given experimental conditions and measurement configurations. Metastability may indeed play a key role in interpreting the MARSIS observations and the potential existence of brines under supercooled conditions ([118]). As discussed above, metastable states depend on sample volume, time, and salt concentration, in addition to temperature. Another factor that can influence metastability is mechanical stress. In this regard, it is useful to examine one specific measurement, both in terms of the recorded permittivity, and the picture of the sample itself. By documenting each measured sample, we observed that, immediately after extraction from the ultra-freezer, fully frozen samples are characterized by a whitish surface appearance. This appearance is likely due to perchlorate inclusions trapped within the ice matrix and the presence of air bubbles (which, however, do not affect the dielectric properties [10]). In contrast, samples that did not freeze completely and remained in a mushy state display a more transparent surface due to the liquid part still present in them (Fig. 7.9). Taking into

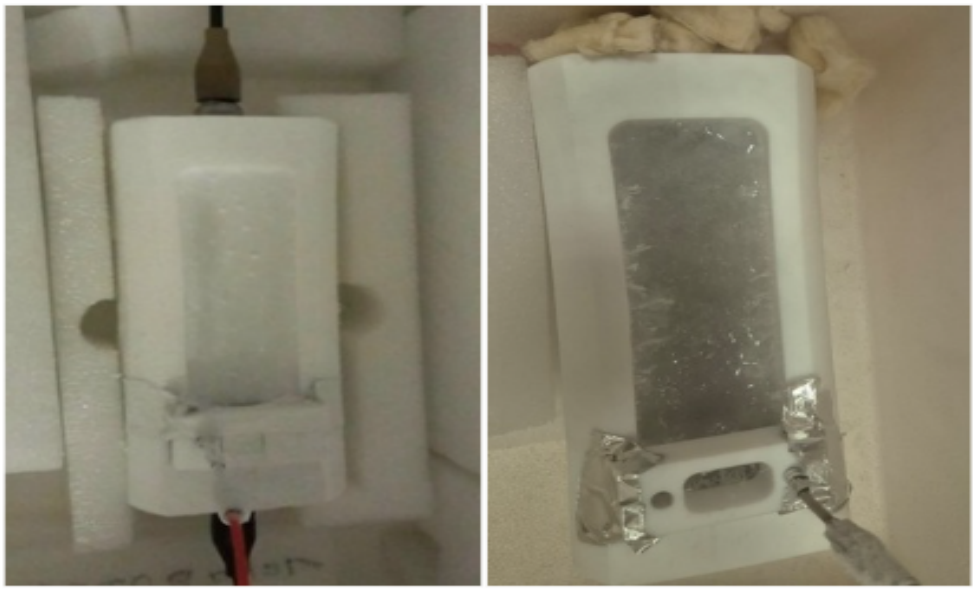

Figure 7.9: Pictures of two magnesium perchlorate solutions samples immediately after the extraction from the ultra-freezer. The picture on the left shows a fully frozen sample with an ε_a of approximately 3.1, while the picture on the right corresponds to a sample in the mushy state, characterized by an ε_a of about 10.

consideration the measurement with the configuration: cell length 150 mm, time in the ultra-

freezer 4 days, 10% of concentration, we can see a very different behavior of the permittivity in Fig. 7.10. The orange curve corresponds to a sample that was in a mushy state when extracted from the ultra-freezer but began to freeze as a result of mechanical stress applied during the cables connection, which, in this specific measurement, had been particularly difficult (the measurement was therefore started at a higher temperature because the setup required more time). This phenomenon was observed both through a visible change in the surface appearance (Fig. 7.11) and through a subsequent decrease in the measured permittivity (Fig. 7.10), despite the increasing temperature, down to values consistent with the frozen phase.

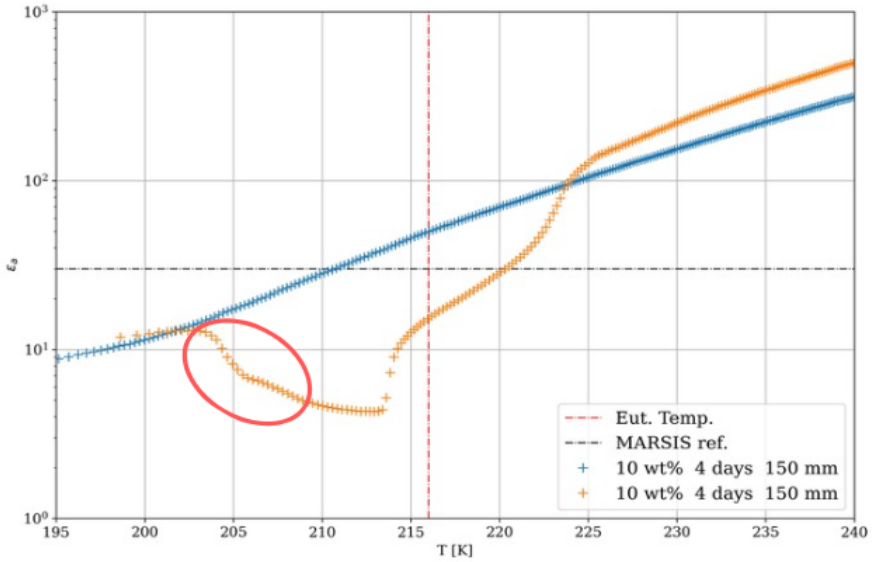

Figure 7.10: Permittivity values of two measurements with same configuration: cell length 150 mm, time in the ultra-freezer 4 days, 10% of concentration. Both were found in a mushy state, but the orange one, subjected to mechanical stress, underwent freezing and consequently exhibited decreasing permittivity highlighted by the red circle, reaching the characteristic of fully frozen material, even as the temperature increased.

7.1.2 Calcium Perchlorate Solutions

Calcium Perchlorate Solutions

Cell Length (mm)	Time (d)	Concentration (wt%)
150	4	5
150	4	5
150	4	10
150	4	10
150	4	10
150	4	15
150	4	15
150	13	5

Table 7.2: Overview of the calcium perchlorate solutions measurements. The three columns represent the dimension of the cell (its length in mm, see Chap.6), the time of residence in the ultra-freezer, and the percentage of the concentration.

Calcium perchlorate is characterized by a lower eutectic temperature (198 K) compared to magnesium perchlorate. Since our measurements start at 195 K, investigation of potential anomalies at temperatures substantially below the eutectic point, as observed for magnesium perchlorate, was not possible. All calcium perchlorate measurements were conducted using identical experimental configurations (150 *mm* cell length, 4 days ultra-freezer residence time, Tab. 7.2) while systematically varying perchlorate concentration to characterize the influence of impurity

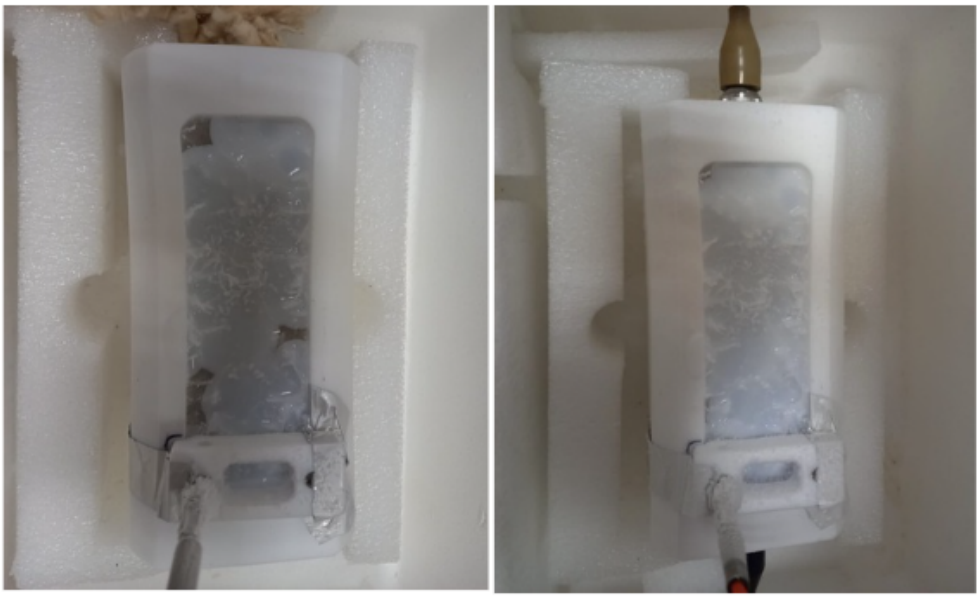

Figure 7.11: Pictures of the sample subjected to mechanical stress during cable tightening. Left picture shows its appearance immediately after removal from the ultra-freezer, with transparent regions indicative of the mushy state. After the cables were fully connected, however, the sample appears fully frozen, consistent with a mechanical-stress-induced crystallization observed also in the permittivity measurements.

content on the electromagnetic properties of ice. Notably, complete freezing was not observed in any measurement, even at temperatures below but proximate to the eutectic point, with all samples exhibiting apparent permittivity values above 5. An additional extended-duration measurement (13 days) was performed at the lowest concentration investigated; however, complete solidification was not observed even under these conditions. Analogously to the magnesium perchlorate case, we show the temperature increase during the measurement to verify that all experiments were conducted under comparable thermal conditions (Fig. 7.12), as well as the frequency spectra at three different temperatures (Fig. 7.13), even though the frozen phase is absent. From all measurements, we can also observe that the anomalies associated with the rapid rise in permittivity during complete melting are present in this case as well (Fig. 7.14).

The spectra (Fig. 7.13) have similar behavior to those of magnesium perchlorate showing the same features at high frequencies, due to instruments effects. However, for calcium perchlorate solutions, the conductivity is less noisy at low frequencies because it is significantly higher than the instrument limit. In this case, the only effects we can analyze are those related to concentration, which become more evident when focusing on temperatures well below those associated with complete melting (270 K). As in the previous case, we therefore restrict our analysis to temperatures below 240 K and to the apparent permittivity, in order to assess how these measurements relate to the Martian subglacial lake.

Concentration

The apparent permittivity curves (Fig. 7.15) are very consistent and show a similar trend that varies systematically with solute concentration. Even below the eutectic temperature, no abrupt decreases are observed: the samples appear to maintain highly regular metastable states in which the permittivity increases with increasing concentration. The long-period measurement is fully comparable to the others, confirming the stability of the dielectric behavior under the explored conditions. Additional measurements, performed at even lower temperatures or over longer time periods, may reveal whether any non-linear behavior or unexpected variations emerge. Because of the low eutectic point, the calcium perchlorate solutions reach higher permittivity values at low temperatures. The compatibility with the MARSIS data occurs below 200 K for the most concentrated samples, and up to about 210 K for the less concentrated ones. Calcium perchlorate solutions, therefore, appear to be a much more plausible candidate for describing brines in the Martian subsurface, as they remain partially liquid at temperatures much closer to the expected Martian basal conditions.

The pictures of the samples taken immediately after removal from the ultra-freezer (Fig. 7.16) are also very similar to one another. They show a transparent surface, indicating the presence

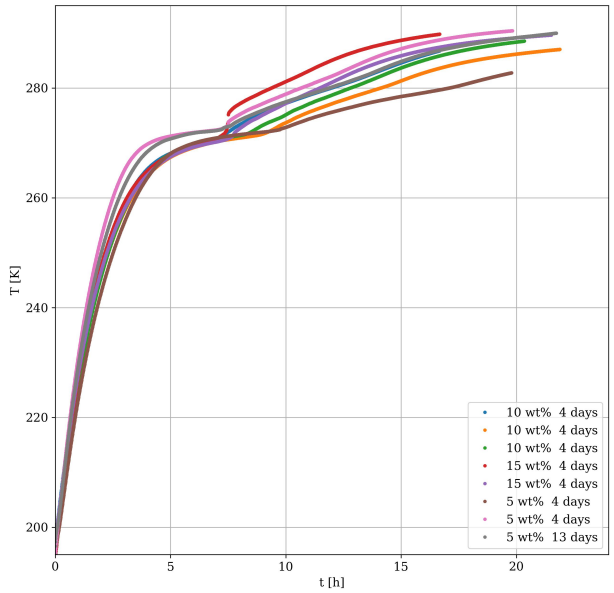

Figure 7.12: Variations of the temperature of calcium perchlorate solutions in the heating phase in which the scattering parameters have been acquired. All the measurements show consistent heating rate, therefore the measurements are comparable consistently.

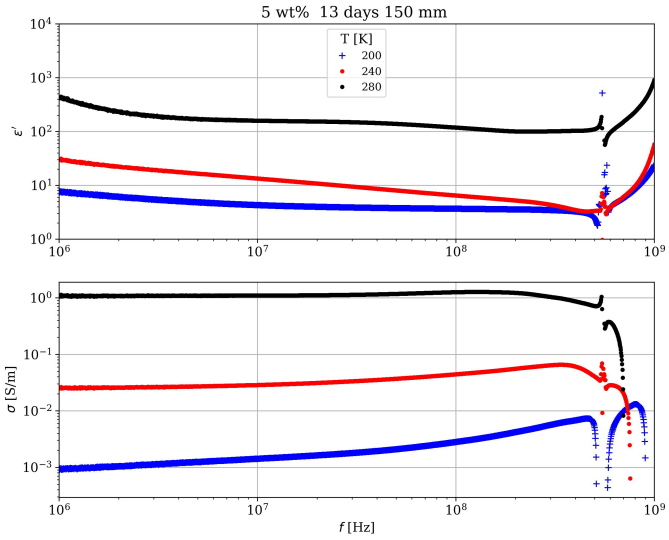

Figure 7.13: Spectra of real permittivity (upper panel) and conductivity (lower panel) of a calcium perchlorate sample with salinity of 5% measured in the 150 mm cell after 13 days in the ultra-freezer, at three different temperatures, 200 K, 240 K, 280 K.

of a liquid fraction inside, which is consistent with the measured permittivity values. Other studies have been made to characterize the subglacial lake in terms of perchlorate solutions and in the next paragraph we will report a comparison.

7.1.3 Previous Studies

Comparing our results with the literature, and in particular with [192], many differences emerge (Fig. 7.17). The computed ε_a values are higher, at lower temperatures, than our measurements. This substantial discrepancy can be attributed to differences in the experimental setup. The primary distinction between the measurements reported in [192] and our calcium perchlorate

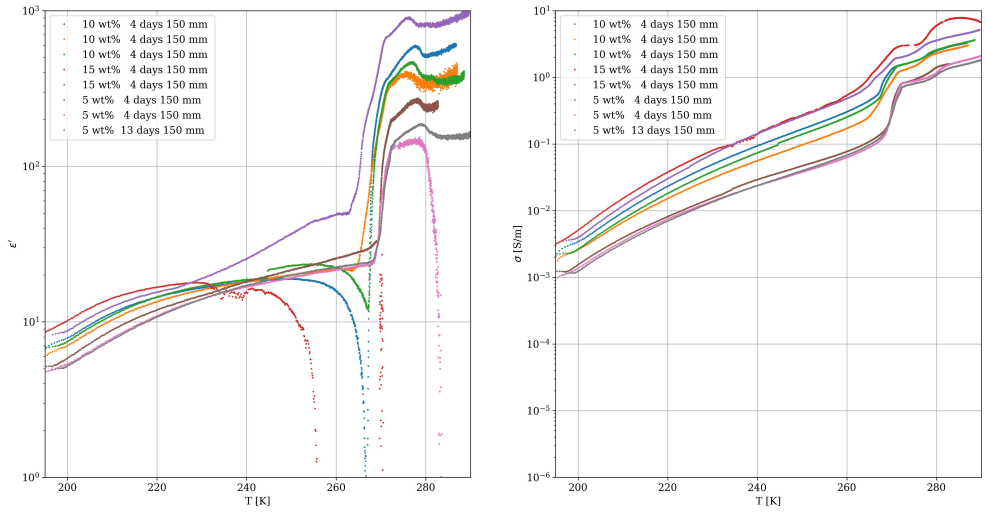

Figure 7.14: All the measurements of ε' and σ of calcium perchlorate solutions at 4 MHz. The legend reports, in order, the perchlorate concentration in the solution, the residence time in the ultra-freezer, and the length of the measurement cell. At temperatures corresponding to the complete melting of the sample, some irregularities appear in the measurements: the real part of the permittivity exhibits a sudden decrease followed by an abrupt increase. In this interval, the instrument is unable to capture the sharp increase occurring during the phase transition. However, this effect has no impact on our analysis, as we focus on lower temperatures compatible with Martian environmental conditions.

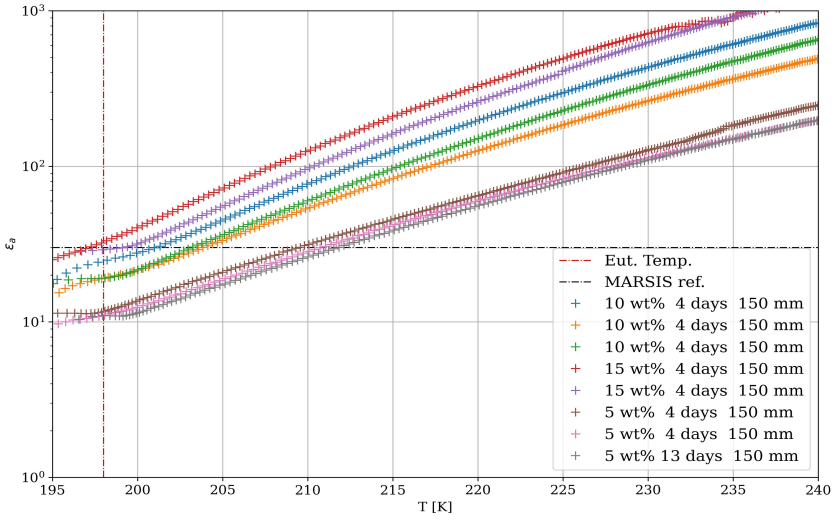

Figure 7.15: Apparent permittivity ε_a as a function of temperature in the range 195 K - 240 K of all the measurements of calcium perchlorate solutions.

results concerns both the experimental apparatus and measurement protocol. The study by [192] includes data acquired during the cooling phase, whereas all results presented here were obtained during warming cycles. Additionally, different measurement instrumentation was employed. To facilitate direct comparison, we conducted one measurement of a 5% calcium perchlorate solution in the ultra-freezer at 1 MHz using similar instrumentation (LCR meter with a square cell of approximately 30 cm^3 volume [31]) during the cooling phase. The observed behavior is consistent with [192], despite the different concentration, with elevated apparent permittivity values at lower temperatures (Fig. 7.18). The discrepancy between these results and our primary calcium perchlorate measurements (Fig. 7.15) may be attributed to differences in measurement instrumentation (significantly smaller cell volume in [192] and Fig. 7.18, with potential electrode polarization effects responsible for the higher permittivity) and experimental

Figure 7.16: Pictures of the calcium perchlorate solutions immediately after the removal from the ultra-freezer. The samples are of the three concentrations available, 15%, 10%, 5% from the left to the right. The three samples show transparent surface, indicating they are not completely frozen.

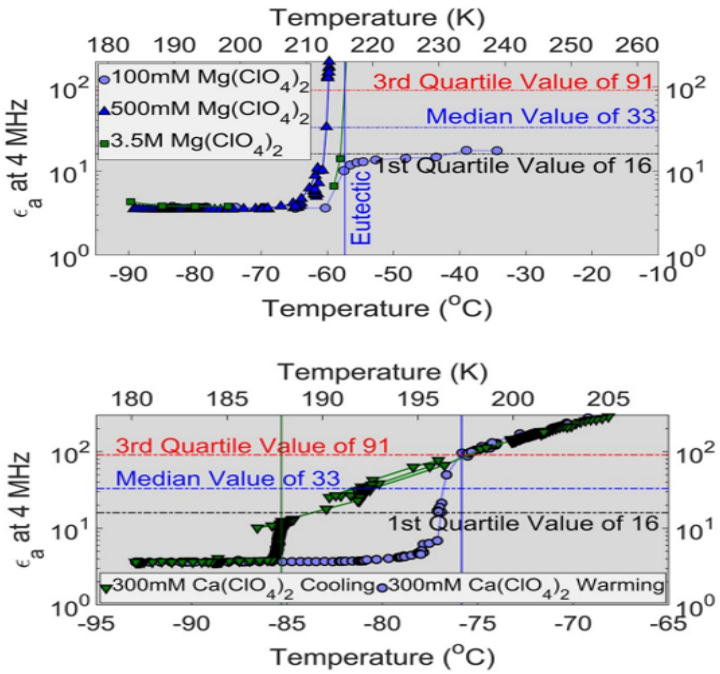

Figure 7.17: Perchlorate solution measurements from [192]. Upper panel: apparent permittivity of various $Mg(ClO_4)_2$ concentrations as a function of temperature. The concentrations are 100 mM(around 2.2 %), 500 mM(around 10%) and 3.5 M (44%). Lower panel: apparent permittivity of 300 mM(around 6.9 %) of $Ca(ClO_4)_2$ as a function of temperature during both cooling and warming cycles. ε_a decreases continuously with decreasing temperature below the eutectic point until complete freezing occurs at 187.9 K (vertical green line). Upon warming, complete thawing occurs at the eutectic temperature of 197.3 K (vertical blue line), recovering the same ε_a values observed during cooling. The horizontal lines refer to MARSIS data of the bright reflector in *Ultimi Scopuli* (modified form [192]).

protocols (cooling versus warming measurements, varying freezing durations). The frequency differences (1 MHz in Fig. 7.18 versus 4 MHz in Fig. 7.17) do not significantly affect the results.

In conclusion, the dielectric properties reported in the literature exhibit significant variability, likely attributable to the small measurement volumes employed in those studies. Our

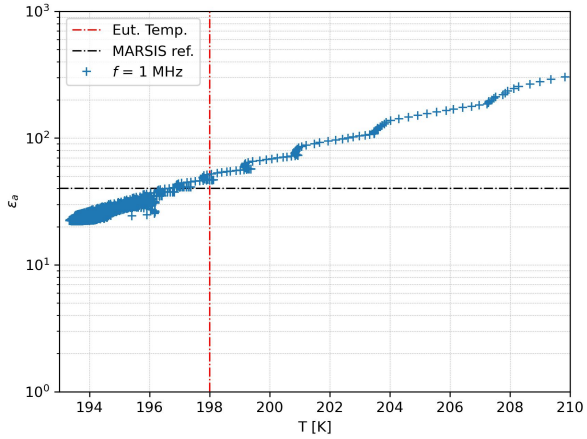

Figure 7.18: LCR meter measurements at 1 MHz of the apparent permittivity of a 5% calcium perchlorate solution inside the ultra-freezer in a 30 cm^3 square cell. These measurements enable direct comparison with the results reported in [192].

results, obtained using larger sample volumes, indicate that perchlorate solutions can persist in a mushy metastable state below the eutectic points, depending on solute concentration and volume, at temperatures comparable to those expected under Martian conditions. The MARSIS observations are more consistent with calcium perchlorate solutions, as magnesium-perchlorate brines, although they do not freeze under the relevant conditions, exhibit apparent permittivity values that are significantly lower than those inferred from radar measurements. Moreover, only a limited number of comparable measurements exist in the literature and no standardized procedures are currently available for the preparation of ice samples or perchlorate solutions. Nevertheless, the measurements obtained in this work exhibit a high degree of internal consistency, thereby strengthening robustness and reliability of the results. Most importantly, these findings highlight the capability of perchlorate solutions to produce bright radar reflections even at Martian temperatures, supporting their interpretation as a plausible explanation for the reflectors observed in the MARSIS data. Further measurements will be performed to provide a more complete description of perchlorate solutions, as analogues of possible brines in Martian subsurface.

7.2 Icy Moons

In this section, we present the measurements conducted to characterize analogues representative of the crusts of Jovian icy satellites, Europa, Ganymede, and Callisto. The measurements discussed here concern both saline ice and dirty ice, and they serve as the basis for the simulation work developed in the subsequent chapter. We therefore examine in greater detail the compositions and environmental conditions of the icy crusts of these moons, expanding upon the overview provided in Chapter 2.

7.2.1 Europa: Ice Doped with Sodium Chloride

As discussed previously, several compounds have been identified on Europa's surface, including two major salts: sodium chloride and magnesium sulfate. The presence of salts can induce two primary effects:

- The doping of the ice matrix enhancing its electrical conductivity and therefore the expected radar attenuation;
- There could be potential formation of liquid brines at temperatures below 273 K depending on the eutectic point of the solutions.

For the purposes of both our measurements and subsequent simulations, we focus on sodium chloride since prior studies have shown that the influence of magnesium sulfate on radar signal propagation is negligible ([162]) and consequently, a magnesium-sulfate-dominated icy crust would exhibit electromagnetic behavior broadly comparable to that of pure water ice.

The EM properties of sodium chloride solutions were measured in all the three regimes: the solid phase (195 – 252 K), which is potentially representative of the frozen upper crust, the brine phase (252 – 270 K), corresponding to partially melted regions that may constitute relevant radar targets, and the fully liquid phase (>270 K), which serves as an analogue for the subsurface ocean, at radar-sounder frequencies (1 MHz–1 GHz). Regarding the salinity of both the crust and the ocean, the literature reports a broad range of hypotheses. These include concentrations lower than those of Earth's oceans ([213]), values comparable to terrestrial seawater ([37]), and significantly higher concentrations ([44]). Moreover, the salinity within the crust is very likely non-uniform. Aside from transient processes such as potential ocean upwellings altering the salinity locally, theoretical models suggest the presence of a downward salinity gradient from the surface toward the ocean originated during crust formation and subsequent evolution. This aspect will be examined in greater detail in the following chapter, where we discuss the range of geophysical scenarios that the radar instrument may encounter. Therefore, we measured different concentrations of $NaCl$ solutions and investigated how the EM properties change depending on the amount of salt and the temperature to characterize the entire icy shell of Europa. Tab. 7.3 shows all the $NaCl$ concentrations of the initial solutions studied with the weight percentage of the salt inserted in the solution and the conductivity of the initial liquid solution from [31]. Fig. 7.19 reports the real part of the permittivity and the electrical

NaCl conc.(mM)	**Number of Measurements**	**NaCl wt%**	**Conductivity (mS/cm)**
10	2	0.06	1.06 ± 0.01, 0.97 ± 0.01
20	4	0.12	1.79 ± 0.01, 1.81 ± 0.01, 1.91 ± 0.01, 1.98 ± 0.01
30	1	0.17	3.01 ± 0.02
40	1	0.23	3.07 ± 0.02
50	1	0.29	5.14 ± 0.02
70	1	0.41	6.79 ± 0.02
80	2	0.47	8.95 ± 0.05
100	1	0.59	9.81 ± 0.05
171	2	1.00	16.37 ± 0.05, 21.44 ± 0.05
200	2	1.17	18.05 ± 0.05, 18.91 ± 0.05
300	1	1.8	27.30 ± 0.06
500	1	2.9	43.9 ± 0.1
700	1	4.1	64.1 ± 0.1
1000	2	5.8	83.7 ± 0.1, 82.1 ± 0.1
4000	1	23.3	216.9 ± 0.5

Table 7.3: The list of $NaCl$ concentrations of the solutions examined by [31] together with the number of measurements performed for each concentration. The salt weight percent and the conductivity of the initial liquid salty solution are reported. Conductivity measurements were performed with a conductivity meter GLP-31.

conductivity of the samples for all concentrations up to 500 mM, at the temperatures monitored during the melting phase. Measurements were acquired at 9 MHz, the operating frequency of the RIME and REASON radar sounders for probing the deeper regions of the icy crust, using the VNA. As in the previously presented measurements, the observed behavior varies significantly depending on the physical state of the sample. For the characterization of the icy shell and the radar signal penetration analysis, we focus primarily on the ice region. However, as evident from Fig. 7.19, our experimental setup did not allow measurements at temperatures below the ultra-freezer temperature. It is, therefore, necessary to model the behavior of the EM parameters in order to describe the uppermost layers of the crust (surface temperature 50 – 100 K) where there are no direct experimental data. In order to investigate the electromagnetic properties of the frozen regime (Fig. 7.20), we conducted measurements using an LCR meter in combination with liquid nitrogen cooling, enabling characterization down to 160 K. These measurements allowed us to fit the temperature and concentration dependent trends of both permittivity and conductivity across the relevant parameter space. Regarding the real part of the permittivity, it is evident from Fig. 7.20 that the trend is similar for different concentrations, increasing with the amount of salts. Moreover, the measurements obtained with the VNA and LCR meter are in agreement, despite being performed at different frequencies (9 MHz for the VNA and 1 MHz for the LCR meter), as the real component is nearly frequency-independent over this range (1-10 MHz). The resulting dataset was therefore fitted in temperature using a Gough-like

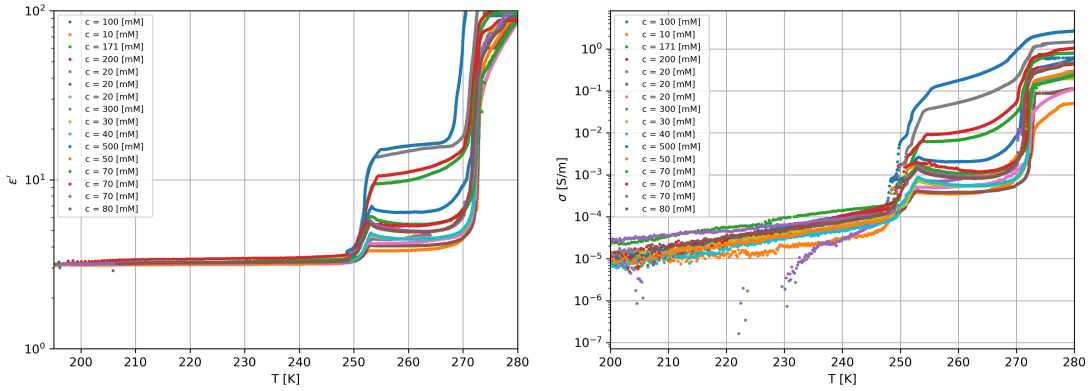

Figure 7.19: ε' (left panel) and σ (right panel) versus temperature of $NaCl$ solutions collected by [31] using the VNA. Data are shown at 9 MHz, up to 500 mM of concentration of the solute.

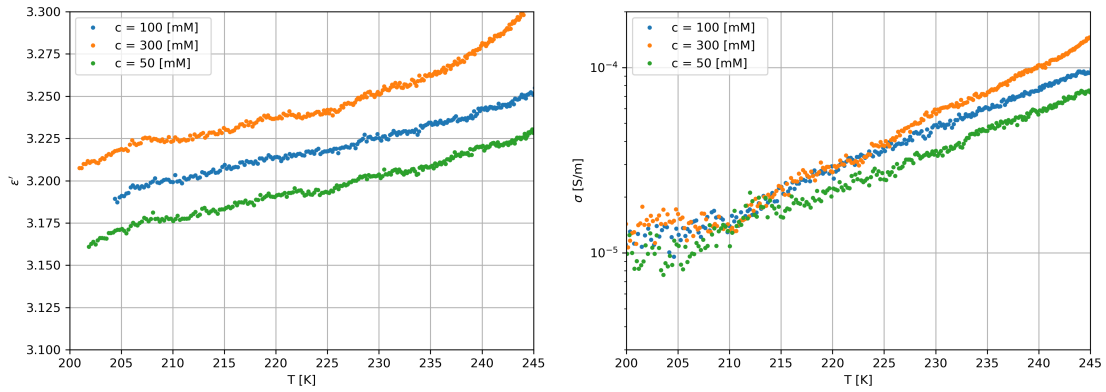

Figure 7.20: ε' (left panel) and σ (right panel) versus temperature in the frozen phase of $NaCl$ solutions collected by [31] using the VNA. Data are shown at 9 MHz, for three concentration 50, 100, 300 mM.

equation ([70]):

$$\varepsilon'(c,T) = \varepsilon'_0(c) - C(T - T_0) + D(T - T_0)^2 \tag{7.2}$$

in which:
c is the concentration in [mM];
T_0 is a reference temperature 240 K;
ε_0 is a value computed using mixing formulas;
C and D are parameters obtained through the fit, valid in the temperature interval 160 - 245 K.
The value of ε_0 is computed through some of the mixing formulas described in Chap. 4. In Fig. 7.21, the real permittivity values at a fixed temperature T_0 fitted for the concentration variations using three different mixing formulas, which yield nearly identical results at low concentrations. These fits were used to determine the value of ε_0 in Eq. 7.2. Regarding the parameters C and D, the values obtained from the temperature fit shown in Fig. 7.22 using LCR meter data are:
$C = (1.8 \pm 0.5) \times 10^{-3}$;
$D = (7.3 \pm 0.3) \times 10^{-6}$.
Below 160 K, the real permittivity at all concentrations converges toward the value of pure ice, and the influence of salt becomes nearly negligible for the concentrations investigated.
With respect to electrical conductivity, the behavior is more complex, and at 9 MHz it can be modeled as a function of temperature by introducing a threshold concentration, estimated to be around 100 mM. To fit the conductivity data, we employed an Arrhenius-type dependence of the following form:

$$\sigma(c,T) = \sigma_0(c) e^{-\frac{E_a(c)}{k_B}(\frac{1}{T} - \frac{1}{T_0})} \tag{7.3}$$

in which:
T_0 is the reference temperature of 240 K;

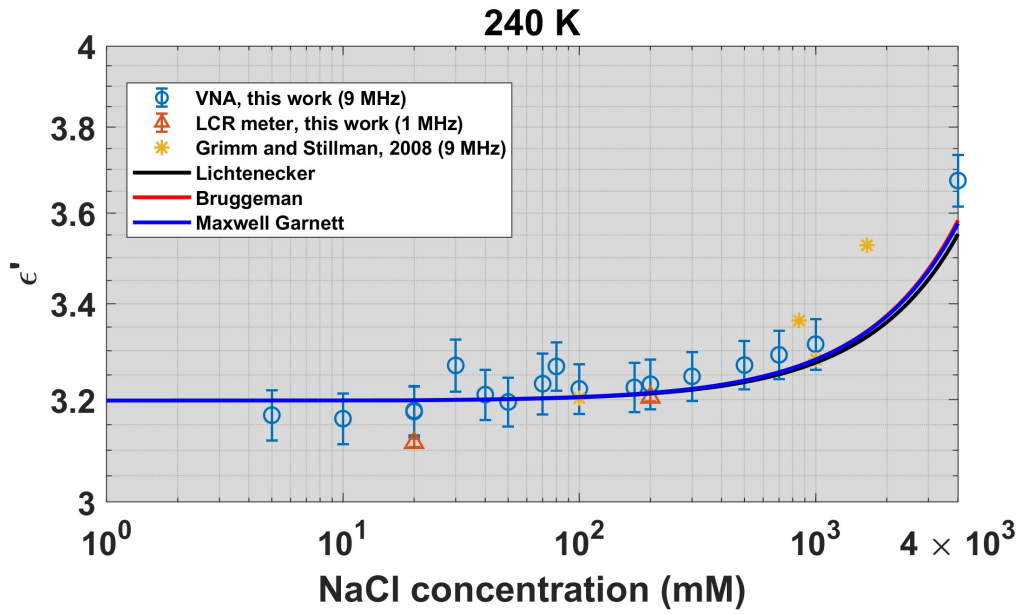

Figure 7.21: Real part of the permittivity at 240 K as a function of $NaCl$ concentration measure with the VNA, together with the three different mixing formulas employed for the fit. The orange carets markers are the measurements performed by means of the LCR meter at 1 MHz, whereas the yellow asterisks are data taken from [74] at 9 MHz (taken from [33]). This dataset also includes an additional measurement at a concentration of 5 mM, acquired subsequent to the original set of experiments presented in this work.

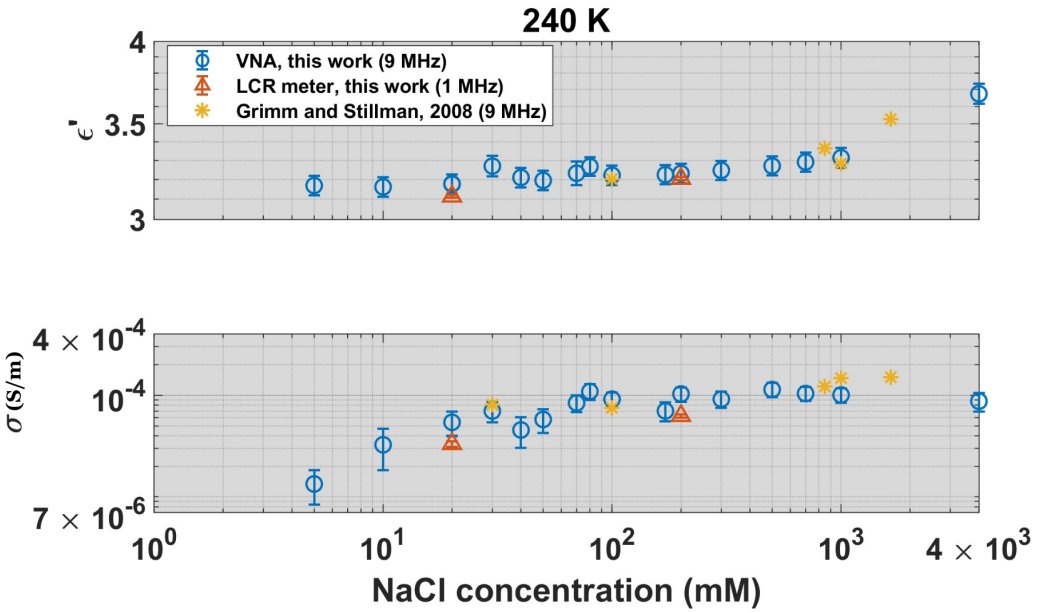

Figure 7.22: Real part of the permittivity of the 20 mM $NaCl$ doped ice sample as a function of temperature at 1 MHz. Data were acquired using the LCR meter, and the solid black line represents the fit according to Eq. 7.2 (taken from [33]).

$E_a(c)$ is the activation energy that depends on the concentration;
k_B is the Boltzmann constant;
$\sigma_0(c)$ is a concentration-dependent parameter computed at the reference temperature using Eq. 7.4 valid up to 100 mM to fit data in Fig. 7.23.

$$\sigma_0(c) = ac^b \tag{7.4}$$

the parameters a and b obtained with the fit are:
$a = (8.3 \pm 0.8) \times 10^{-6}$;
$b = (0.54 \pm 0.05)$;
above the value of 100 mM the value of σ_0 is constant.

The activation energy also exhibits a concentration dependence, with a threshold at 100 mM. In particular, by fitting the dataset, it is possible to distinguish two populations of activation energies for $T > 220K$ (Fig. 7.24). This behavior was already identified by [74] showing similar values.
In conclusion, the conductivity shows a complex behavior due to the different slopes in different temperature intervals. Beneath the threshold concentration ($c < 100\,mM$), there are three slope changes ($T < 180\,K$ and $180\,K < T < 220\,K$ and $T > 220\,K$) corresponding to different activation energies; above the threshold, instead, the conductivity shows two slopes changes ($T < 180\,K$ and $T > 180\,K$). The activation energies in the different intervals are shown in Tab. 7.4. Fig. 7.25 shows the conductivity of a 20 mM sample versus the temperature as an example of these different trends: the red part could be represented by the higher-E_a population and the blue parts could be reproduced by the lower-E_a population.

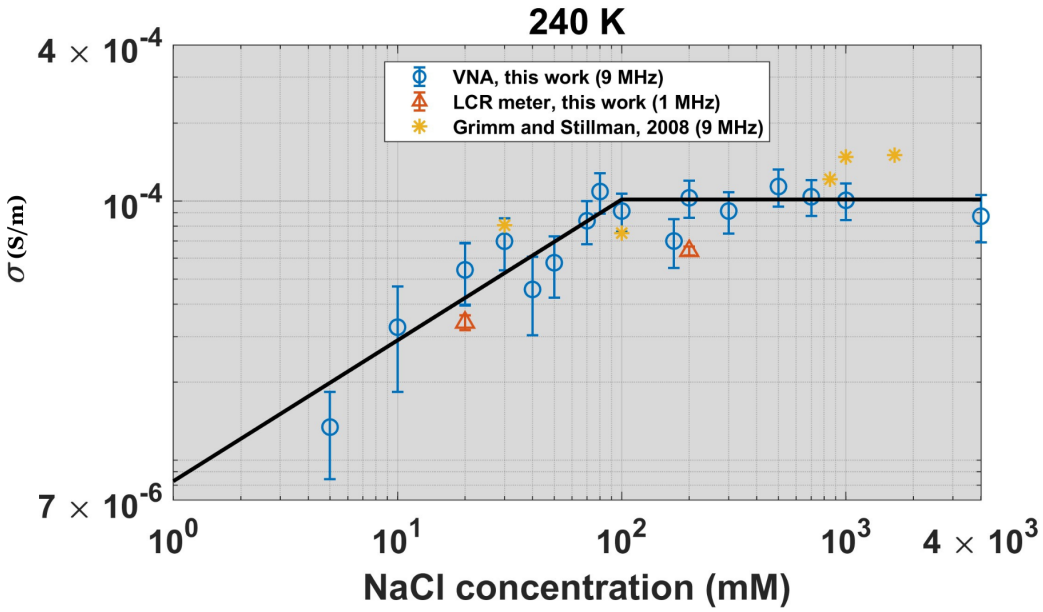

Figure 7.23: Conductivity at 240 K as a function of the concentration in a log-scale. The solid line is the power-law model (Eq. 7.4) valid up to 100 mM concentration (taken from [33]). The orange carets markers are the measurements performed by means of the LCR meter at 1 MHz, whereas the yellow asterisks are data taken from [74] at 9 MHz. This dataset also includes an additional measurement at a concentration of 5 mM, acquired subsequent to the original set of experiments presented in this work (taken from [33]).

	E_a for $T < 180K$	E_a for $180K < T < 220K$	E_a for $220K < T < 245K$
$c < 100mM$	$E_a = (0.22 \pm 0.04)eV$	$E_a = (0.30 \pm 0.04)eV$	$E_a = (0.22 \pm 0.04)eV$
$c > 100mM$	$E_a = (0.22 \pm 0.04)eV$	$E_a = (0.30 \pm 0.04)eV$	$E_a = (0.30 \pm 0.04)eV$

Table 7.4: Activation Energies for different concentrations and temperature intervals ([33]).

7.2.2 Ganymede and Callisto: Dirty Ice

As previously discussed, the surface of Ganymede, and thus its crust, is composed primarily of dirty ice, consisting of a mixture of pure water ice, salts, and a darkening agent whose composition may vary and it remains unclear. From a radar perspective, this darkening material is of particular interest, as its composition and spatial distribution are expected to play a dominant role in controlling signal attenuation and in governing the radar response of both the surface and the deeper subsurface layers. To date, literature proposes several possible compositions for this darkening agent and discusses whether it is of exogenous origin, and thus confined to the surface and the uppermost crustal layers, or of endogenous origin, and thus distributed throughout the entire crust. The darkening agent is not spatially homogeneous on the surface, being present mainly in darker older terrain. High-resolution spectral observations have identified silicates and carbonaceous materials as the primary darkening agents on Ganymede's surface ([141] [11]). These materials are consistent with meteoritic components, such as carbonaceous chondrites, whose origin within the icy moons remains under debate ([34]). Some

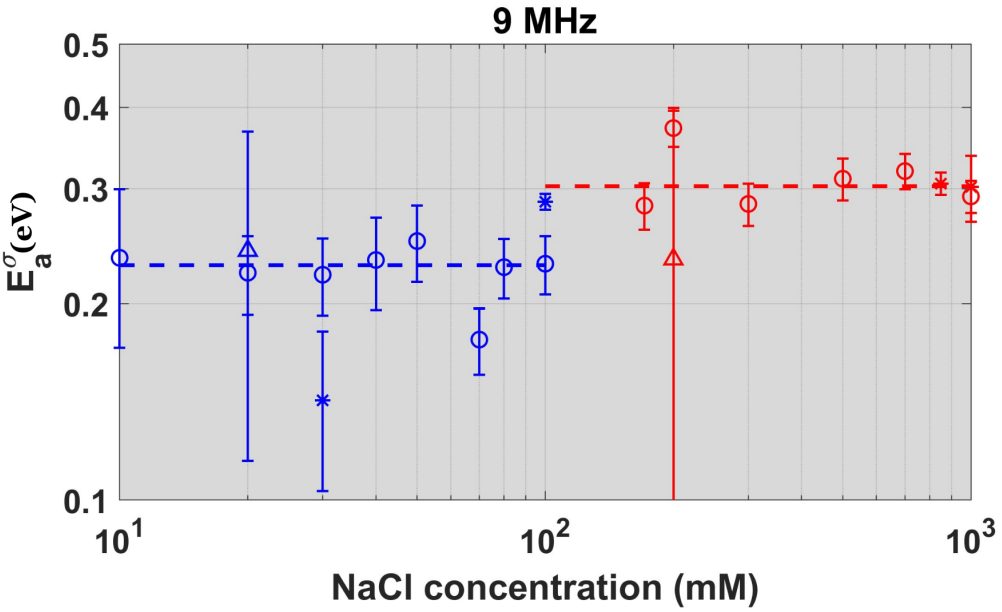

Figure 7.24: Activation energy in $[eV]$ as a function of $NaCl$ concentration at 9 MHz. The carets markers are the activation energies estimated from the measurements performed by means of the LCR meter at 1 MHz, whereas the asterisks are the ones retrieved from [74] data at 9 MHz. Two populations of activation energy were identified by [31] with a threshold value around 100 mM (taken from [33]).

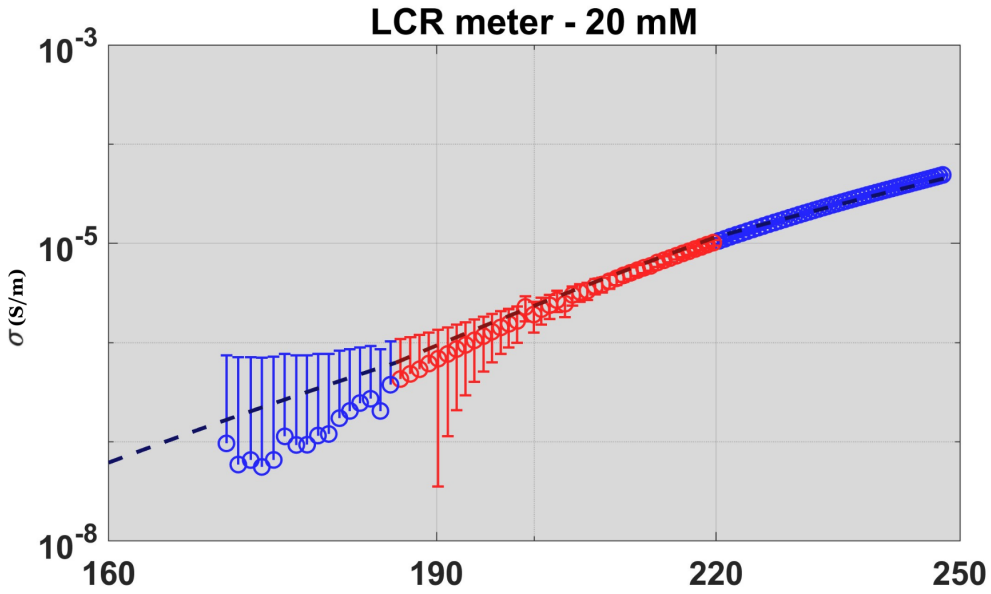

Figure 7.25: Conductivity of 20 mM doped ice sample as a function of temperature measured with the LCR meter. Dots represent the data and the dashed line the model (7.3) with the values showed in 7.4 (taken from [33]). The color represent the two populations of activation energies: as in Fig. 7.24 red is the high one and blue is the lower one.

internal-structure models of icy moons also predict the presence of silicate materials analogous to L/LL ordinary chondrites ([111]). In contrast, the origin of carbonaceous chondrites may be either exogenous or endogenous ([86]), implying that such material could be confined to the shallower surface layers or distributed throughout the entire icy crust. Regarding the possible presence of L/LL ordinary chondrites, [82] considers different vertical concentration gradients of silicate-rich inclusions within Ganymede's ice with a steeper decrease of impurities in dark terrains and a more gradual distribution in bright terrains. The laboratory measurements presented in this section are reported in [32] and constitute the basis for the attenuation and interference simulations discussed in the subsequent chapter. These measurements focus on the electromagnetic characterization of dirty ice samples composed of L5 ordinary chondrites or carbonaceous chondrite CI simulants mixed with pure water ice. These materials present

magnetic properties that could affect significantly radar performances (Chap. 8), therefore the measurements include permeability μ characterization. Additional contaminants, such as chlorate salts and ammonia-like or sulfate compounds, are also expected to be present; however, the effects of these compounds will be addressed in future experimental investigations.

Estimation of Permittivity and Permeability

In order to characterize dirty ice with these two contaminants, permittivity and permeability have been measured with the VNA for dry and saturated samples to understand which mixing formulas are more representative of these mixtures. The investigated samples consist of two-phase systems composed of a granular solid matrix of the analyzed materials and pore spaces either filled with air or fully saturated with ice. Fig. 7.26 and 7.27 show the behavior of dielectric permittivity of this two end-members. The permeability spectrum shown in Fig. 7.28 demonstrates that magnetic permeability is not negligible and has to be taken into account in radar analyses of these materials. Both the real and imaginary components of permittivity and permeability of the dry samples exhibit an almost temperature-independent behavior over the investigated range. The bulk dielectric permittivity is, therefore, modeled using classical two-phase electromagnetic mixing formulas, in which one phase is treated as the host medium and the other as inclusions. In the dry configuration, the bulk permittivity ε_b^{dry} is expressed as a function of the grain permittivity ε_g, the air permittivity $\varepsilon_{air} = 1$, and the volume fraction of pores ϕ. In the frozen saturated case, the air component is replaced by pure ice with permittivity ε_{ice}. The inversion of grain dielectric permittivity ε_g and magnetic permeability μ_g was performed using the probabilistic approach mentioned in [31], in which measured bulk electromagnetic properties and volume fractions ϕ were treated as probability density functions. This inversion was applied both at fixed porosity over varying temperatures and at fixed temperature for varying porosity in order to find the behavior of dirty ice mixture depending on these two parameters. A direct comparison between the retrieved ε_g values and reference measurements on solid samples demonstrates that the performance of mixing models strongly depends on the specific lithology: L5 ordinary chondrite inclusions are well represented by the Maxwell-Garnett random disks (see Chap. 4) while for CI carbonaceous chondrite simulant, the Lichtenecker formula (see Chap. 4) displays slightly better behavior at low temperatures, but none of the mixing models tested are in good agreement with data over the entire temperature range examined. The magnetic permeability retrieved from different models exhibits only minor variations between formulations confirming that, under weakly magnetic conditions, the choice of the mixing model has a limited impact on μ_g estimation. The reliability of the selected models was further validated through forward modeling of bulk permittivity for frozen saturated samples. For the L5–ice mixture, again the Maxwell-Garnett Random disks formulation provides the best agreement with experimental data. In the case of the CI-ice mixture, all models reproduce the real part within uncertainties, while none represents the temperature evolution of the imaginary part above approximately 210 K and this discrepancy is interpreted as the result of chemical and physical interactions between ice and clay-rich materials, which violate the assumptions underlying classical mixing models. As in the NaCl-doped-ice case, extrapolation procedures were required to extend the dielectric characterization to the temperatures of surface and shallow subsurface of Ganymede and Callisto. Additional measurements were performed with LCR at the frequency of 1 MHz to validate the reliability of the low-temperature extrapolations of the VNA measurements. The grain dielectric permittivity and magnetic permeability were therefore fitted as continuous functions of temperature down to 120 K at 9 MHz. The results obtained demonstrate that dielectric losses in icy mixtures are controlled by a complex interplay between ice and dust content, mineralogy, and temperature. Clay-rich materials exhibit strong deviations from classical electromagnetic mixing models at low temperatures.

The models for the ε_g with the corresponding best-fitting mixing formula obtained after these analyses, reported in Tab. 7.5, enable the calculation of the effective electromagnetic properties of a two-phase composite material as a function of temperature and volume fraction of the inclusion ϕ. The bulk permittivity of the two possible dirty icy crust analogues are then:

$$\varepsilon_{\text{bulk}}^{ice-CI} = \varepsilon_g^{\phi} \varepsilon_{ice}^{1-\phi} \tag{7.5}$$

for the carbonaceous chondrite CI in which:
ϕ is the fraction of impurities;
ε_g is the grain permittivity that changes in temperature according to the Tab. 7.5;

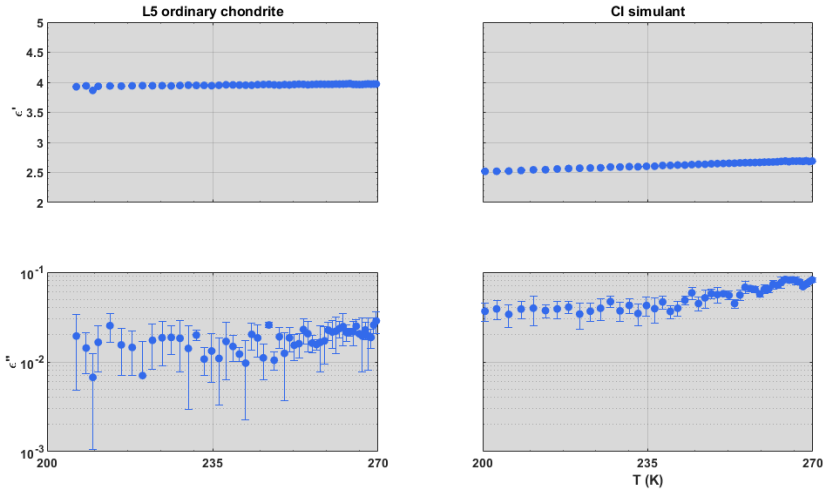

Figure 7.26: Powdered dry samples dielectric permittivity as a function of temperature at the fixed frequency of 9 MHz (modified from [32]).

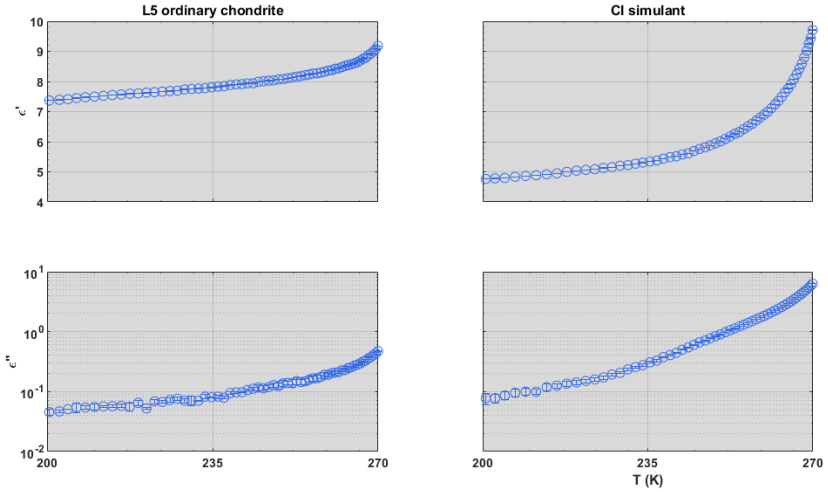

Figure 7.27: A powdered frozen saturated sample dielectric permittivity as a function of temperature at the fixed frequency of 9 MHz (modified from [32]).

ε_{ice} is the pure ice dielectric permittivity.
And

$$\varepsilon_{\text{bulk}}^{ice-L5} = \varepsilon_{ice} + \frac{\phi(\varepsilon_g - \varepsilon_{ice})(2\varepsilon_g + \varepsilon_{ice})}{(3-\phi)\varepsilon_g + \phi\varepsilon_{ice}} \tag{7.6}$$

for the L5 chondrite in which:
ϕ is the fraction of impurities;
ε_g is the grain permittivity that changes in temperature according to the Tab. 7.5;
ε_{ice} is the pure ice dielectric permittivity.
The same equations can be applied to compute the bulk magnetic permeability. Figs. 7.29 and 7.30 show maps of variations of real and imaginary part of dielectric permittivity of the dirty ices examined as a function of temperature and volume fraction of the inclusion, in which the lower limit is the pure ice ($\phi = 0$).

The imaginary component of the permittivity of these dirty ice samples, particularly in the presence of non-negligible contaminant fractions, is relatively high, and this consequently leads to strong radar signal attenuation. Radar signals are expected to penetrate only the coldest portion of the crust and our simulations will be focused specifically on this upper part using in particular dirty ice data at low temperatures. This approach allows us to investigate potential interference phenomena that could introduce ambiguities in the interpretation of surface radar observations.

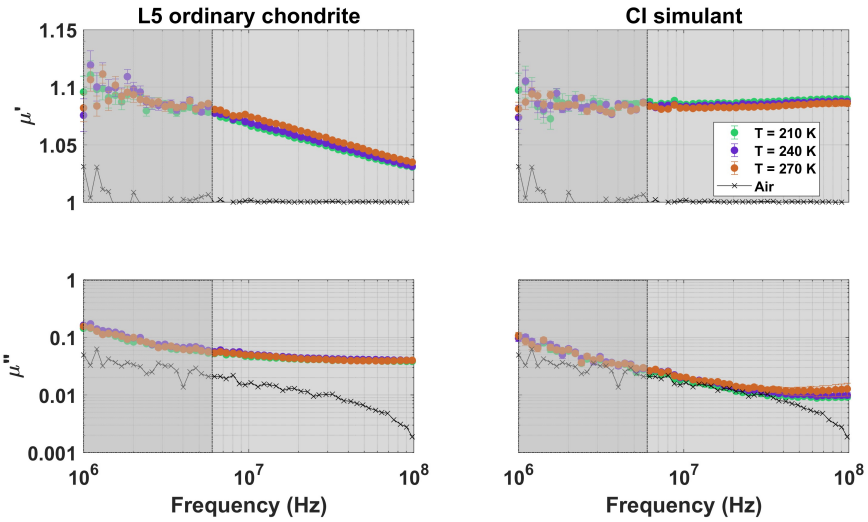

Figure 7.28: Magnetic permeability spectra of the three powdered dry samples at three different temperatures (210 K, 240 K, 270 K) in the frequency range 1–100 MHz. The shadow box indicates values that are not reliable because of the VNA instrumental limits. The porosities for the two dry samples are $\phi^{L5} = 0.37 \pm 0.01$, $\phi^{CI} = 0.60 \pm 0.01$ (taken from [32]).

Sample	T function (9 MHz)	Mixing formula
L5 Chondrite	$\varepsilon'_g(T) = 9.5 + 0.01T$ $\varepsilon''_g(T) = 0.01 + 0.02e^{0.017T}$ $\mu'_g = 1.1$ $\mu''_g(T) = 0.05 + 0.0001T$	Maxwell-Garnett Random Disks
CI Carbonaceous Chondrite Simulant	$\varepsilon'_g(T) = 5.9 + 0.02T$ $\varepsilon''_g(T) = 0.3 + 4 \times 10^{-6}e^{0.04T}$ $\mu'_g = 1.3$ $\mu''_g(T) < 0.07$	Lichtenecker

Table 7.5: Temperature fitting functions at 9 MHz for the EM properties of the grains of the L5 ordinary chondrite and CI carbonaceous chondrite simulant. For the imaginary part of the CI simulant magnetic permeability, only upper limits at 9 MHz have been reported due to the instrumental limits.

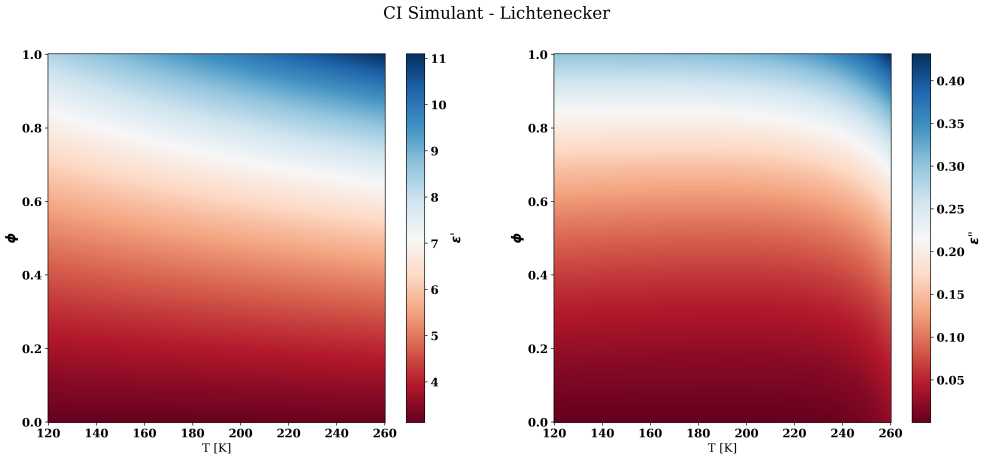

Figure 7.29: Real (left) and imaginary (right) components of the dielectric permittivity of dirty ice contaminated with CI carbonaceous chondrites, shown as functions of porosity and temperature. The EM properties were computed using the grain permittivity values derived from [32] and the Lichtenecker mixing formula, which provides the best agreement with the experimental data.

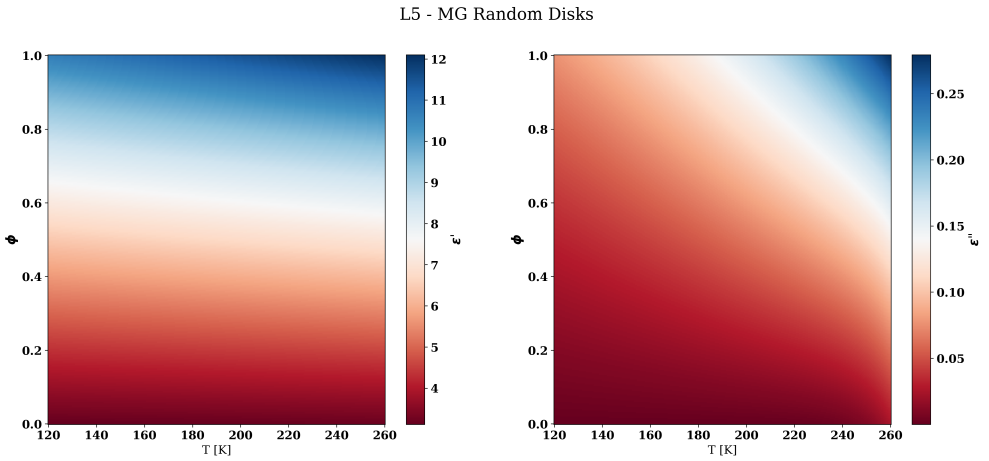

Figure 7.30: Real (left) and imaginary (right) components of the dielectric permittivity of dirty ice contaminated with L5 ordinary chondrites, shown as functions of porosity and temperature. The EM properties were computed using the grain permittivity values derived from [32] and the MG Random Disks mixing formula, which provides the best agreement with the experimental data.

Chapter 8

Simulations

This chapter presents the results of radar-signal propagation simulations performed using the models derived from the experimental data discussed in the previous one. We focus in particular on two environments:

- A first set of simulations focuses on evaluating the detectability of various types of subsurface targets beneath a layer of saline ice, representative primarily of Europa (and, by extension, of the other two Jovian icy moons if impurities are confined to the uppermost surface). Here, "saline ice" refers to ice doped with sodium chloride, as the presence of other salts hypothesized for Europa, such as magnesium sulfate ([162]), could be neglected for radar analysis purposes, because of their weak influence on signals propagation;
- A second set of simulations investigates how dirty ice layers of varying characteristics covering pure ice could cause interference phenomena on radar data. This phenomenon depends on thickness and composition of this layer. These conditions are particularly relevant for Ganymede and Callisto due to the presence of a darkening agent in their icy crust. For Ganymede, we additionally computed attenuation profiles similar to those reported in [32], accounting for different impurity distributions throughout the crust.

8.1 Simulations Framework

The simulations aim to approximate the analyses that will be performed by the RIME and REASON instruments onboard the JUICE and Europa Clipper missions respectively. We used a one-dimensional model that does not include surface topography, elevation variations, or clutter effects. The results therefore describe an idealized, flat, homogeneous region and do not account for the morphology of potential subsurface targets. All simulations employ a chirp signal centered at 9 MHz, the operating frequency of RIME and of the deepest penetrating band of REASON. To provide a complete description of the simulation methodology, we recall some elements of the transmission line theory (Sec. 6.1). The methodology employs the transmission matrix formalism to simulate the propagation through multilayered structures with arbitrary impedance profiles (Fig. 8.1) and consists of multiple steps.

1. The construction of the desired stratigraphy, defining the thickness of the i-th layer L_i (the same for each layer), the temperature T_i (determined by the temperature profile), the composition along the layers, and consequently their EM properties ε_i and μ_i. In our simulations the stratigraphy is formed by the first air layer, the layers of the crust with different characteristics (depending on the satellite, on the target, and on the phenomenon we are investigating), and the last layer, which is the ocean or a mushy layer.
2. The definition of the radar signal and its frequency-domain representation. This step leads to the production of a bandwidth-limited chirped signal centered at frequency f_0 with bandwidth B_{nd}.
3. The computation of the electromagnetic impedance Z_i and the complex wavenumber k_i of each layer from the relative permittivity profile using the following relations:

$$Z_i = \eta_0 \sqrt{\frac{\mu_{ri}}{\varepsilon_{ri}}} \tag{8.1}$$

$$k_i = \frac{2\pi f}{c}\sqrt{\mu_{ri}\varepsilon_{ri}} \tag{8.2}$$

where:
$\eta_0 = \sqrt{\mu_0/\varepsilon_0}$ is the intrinsic impedance of free space.
μ_{ri}, ε_{ri} are the relative permeability and permittivity of the i-th layer.

4. The implementation of the transmission matrix method for stratified media. This approach is particularly powerful for analyzing wave propagation through multilayered structures, as it systematically accounts for multiple reflections and transmissions at each interface. For each layer i the transmission matrix $\mathbf{B}_i$ relates the electromagnetic field amplitudes at the layer boundaries:

$$\mathbf{B}_i = \begin{bmatrix} \cos(k_i L_i) & jZ_i \sin(k_i L_i) \\ j\frac{1}{Z_i}\sin(k_i L_i) & \cos(k_i L_i) \end{bmatrix} \tag{8.3}$$

The cosine terms represent the propagating components, while the sine terms account for the standing wave patterns established by boundary reflections. j is the imaginary unit.

5. The computation of the total transmission matrix for the stratified structure formed by n layers through:

$$\mathbf{B}_t = \mathbf{B}_1 \times \mathbf{B}_2 \times \ldots \times \mathbf{B}_n \tag{8.4}$$

This operation accounts for all multiple scattering events within and between layers, making the method exact within the assumptions of one-dimensional stratified media theory.

6. The extraction of the frequency-dependent reflection coefficient $R(\omega)$ and transmission coefficient $T(\omega)$ using impedance matching conditions at the air-medium and medium-substrate interfaces:

$$T(\omega) = \frac{2Z_{fin}}{Z_{fin} \cdot B_{00} + B_{01} + Z_{fin} \cdot Z_{in} \cdot B_{10} + B_{11} \cdot Z_{in}} \tag{8.5}$$

$$R(\omega) = \frac{Z_{fin} \cdot B_{00} + B_{01} - Z_{fin} \cdot Z_{in} \cdot B_{10} - B_{11} \cdot Z_{in}}{Z_{fin} \cdot B_{00} + B_{01} + Z_{fin} \cdot Z_{in} \cdot B_{10} + B_{11} \cdot Z_{in}} \tag{8.6}$$

where Z_{in} and Z_{fin} are, respectively, the impedances of the upper and lower media with respect to a discontinuity, and B_{ij} denote the elements of the total transmission matrix and $\omega = 2\pi f$.

7. The derivation of the reflected signal in the frequency domain, obtained by multiplying the incident signal spectrum S_{in} with the reflection coefficient:

$$S_{ref}(\omega) = S_{in}(\omega) \cdot R(\omega) \tag{8.7}$$

This operation considers the complete frequency-dependent scattering behavior of the stratified structure. To convert signals to the time-domain, we applied the inverse Fourier transform.

The resulting time-domain signal $y(t)$ represents the temporal evolution of the reflected electromagnetic field as measured by the radar receiver (in terms of the reflection coefficient, R_c). Peaks in this signal correspond to reflections from impedance discontinuities (layer interfaces), with arrival times directly related to layer depths and electromagnetic velocities. The signal amplitude and shape contain information about the dielectric contrast and the frequency-dependent dispersion and attenuation characteristics of the stratified medium. We examine now the applications in the case of Jovian icy satellites.

8.2 Europa

As the most geologically active and dynamic of the Jovian icy moons, Europa's icy crust has been most extensively investigated in the literature. Furthermore, due to its ongoing resurfacing and interior–surface exchange processes it is also the one with the highest probability of identifying targets of diverse natures. Moreover, the apparent absence of a significant darkening agent allows radar signal penetration to greater depths because of the purer icy crust. Since

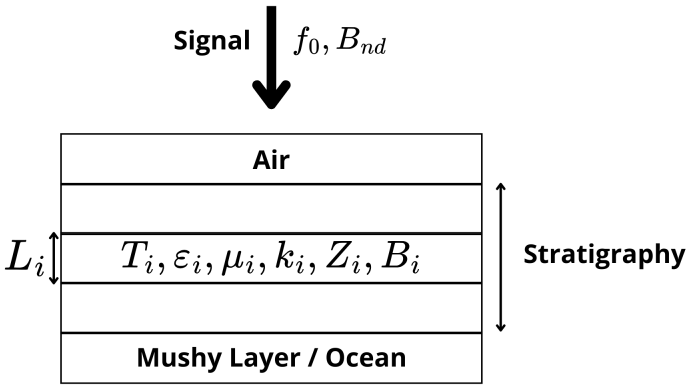

Figure 8.1: Scheme of the stratigraphy structure of the simulations.

radar penetration is governed by the dielectric permittivity, which depends on both composition and temperature, simulating radar performance requires modeling plausible thermal and compositional profiles of the crust. Additionally, the strength of reflections produced by potential subsurface targets depends on the permittivity contrast across interfaces; consequently, we have to model the dielectric properties of candidate targets within the crust.

8.2.1 Temperature Profiles

The temperature gradient throughout the crust depends on the thermal heating regime. The models typically consider either conductive or convective heat transport. Most studies converge on the idea that the shallower portion of the crust behaves as a conductive stagnant lid, whereas at greater depths approaching the mushy layer, where temperatures rise and partial melting begins, the conditions become more favorable for convection. This convective regime causes mixing of different compounds, a process that contributes to Europa's relevance for planetary habitability. In conclusion, the dominant heating transfer mechanism changes with depth and depends on the total thickness of the crust and on the model. A description of several possible crustal configurations as a function of the tidal strain has been provided by [140]. The author shows that the upper layers remain dominated anyway by conductive heat transfer and a deeper conductive layer may also develop gradually as illustrated in Fig. 8.2. Since the radar analysis focuses on the first kilometers of the crust, the thermal profiles used in our simulations are purely conductive. An overview of possible temperature variations is provided in the diagram in Fig. 8.3 from [46] and more recent studies generally adopt one of these four profiles. In particular, the three conductive models differ according to the value of the volumetric heat dissipation parameter due to the tidal heating of the ice layer q, and their temperature gradients, $T(z)$, are described by the following equations:

- Solid line (Fig. 8.3) for q that peaks in warmer ice:

$$T(z) = T_s \left(\frac{T_b}{T_s}\right)^{z/b} \tag{8.8}$$

- Dashed line (Fig. 8.3) for $q = 0$:

$$T(z) = T_s + (T_b - T_s)\frac{z}{b} \tag{8.9}$$

- Dotted line (Fig. 8.3) for q *constant*:

$$T(z) = T_s e^{\left[\left(2z - \frac{z^2}{b}\right)/b\, ln\left(\frac{T_b}{T_s}\right)\right]} \tag{8.10}$$

in which:
T_s is the surface temperature;
T_b is the temperature at the base of the conductive layer;
b is the thickness of the conductive shell;
In this work, for the simulations, we consider the power law (8.8) and the linear (8.9) temperature profiles, adopted even in more recent studies ([37],[44]).

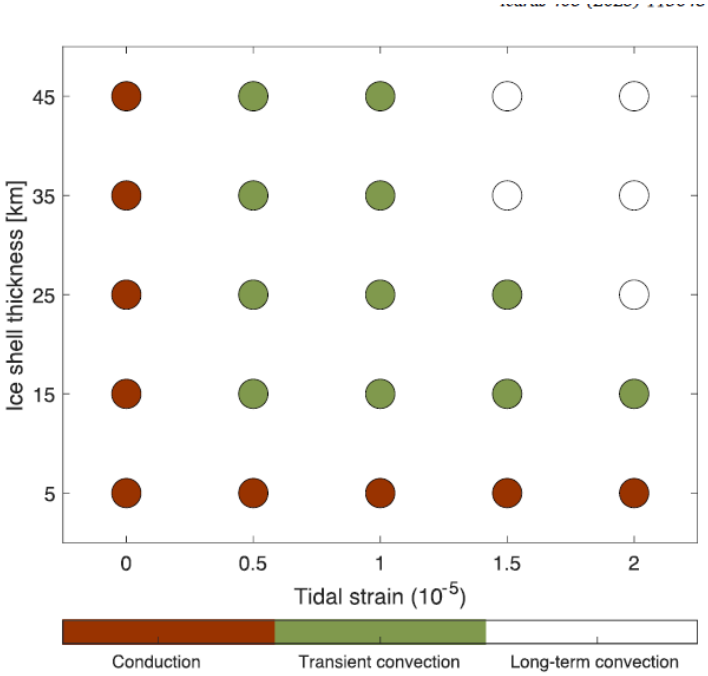

Figure 8.2: Numerical simulations of solid-state convection within Europa's ice shell, covering ice shell thicknesses from 5 to 45 km. For each numerical simulation indicated as a circle, the occurrence of conduction is indicated in red, transient-state convection in green, while long-term convection in white (taken from [140]).

8.2.2 Concentration Profiles

Regarding the distribution of salt within the ice shell, it is necessary to consider crust formation models and the associated timescales in order to understand how salts have been expelled or incorporated in the ice from the surface to the ocean. In our simulations, we apply the top-down solidification approach proposed by [37] and [44]. In this scenario, the uppermost layers freeze rapidly, leaving insufficient time for efficient brine rejection and thus forming relatively salt-rich ice. Deeper layers, closer to the ocean interface, become progressively less saline, approaching an asymptotic regime in which the ice shell contains very small amounts of salt. The detailed implementation of this model is generated using the SOlidification, Flow, and Thermodynamics in Binary ALLoys reactive porous media model, an open source code that simulates the phase evolution, heat transport, and mass transport in mushy layers (SOFTBALL, [156]) and can be found in [37]. The salt distribution depends on the initial concentration of the top-down solidification. Assuming as in [37] the same concentration of the sea on the Earth, 35 ppt, the obtained concentration profile is given by:

$$C(z) = a + \frac{b}{c - z}\left(1 - de^{-fz}\right) \tag{8.11}$$

in which:
C $[ppt]$ is the concentration;
z $[m]$ is the depth;
a, b, c, d, f are constants determined by the simulations of [37] with the values:
$a = 0.984$ $[ppt]$;
$b = -1014$ $[ppt \times m]$;
$c = -123.4$ $[m]$;
$d = -3.529$;
$f = 0.1529$ $[m^{-1}]$;
According to [37], the temperature profile most coherent with this model of the crust is the linear one (Eq. 8.9). Fig. 8.4 shows temperature and concentration profiles for a 10 km icy crust. For an ice shell characterized by the conditions shown in the Fig. 8.4, the complex permittivity of doped ice at 9 MHz computed following [33] measurements (in terms of its real part and electrical conductivity) is shown in the Fig. 8.5 as a function of depth. In particular, the real part shows very small variations: in the shallow, colder parts of the crust, where salt concentration is higher, it has slightly larger values, whereas at greater depths its increase is due to the increase in temperature that becomes the dominant factor controlling its magnitude. On

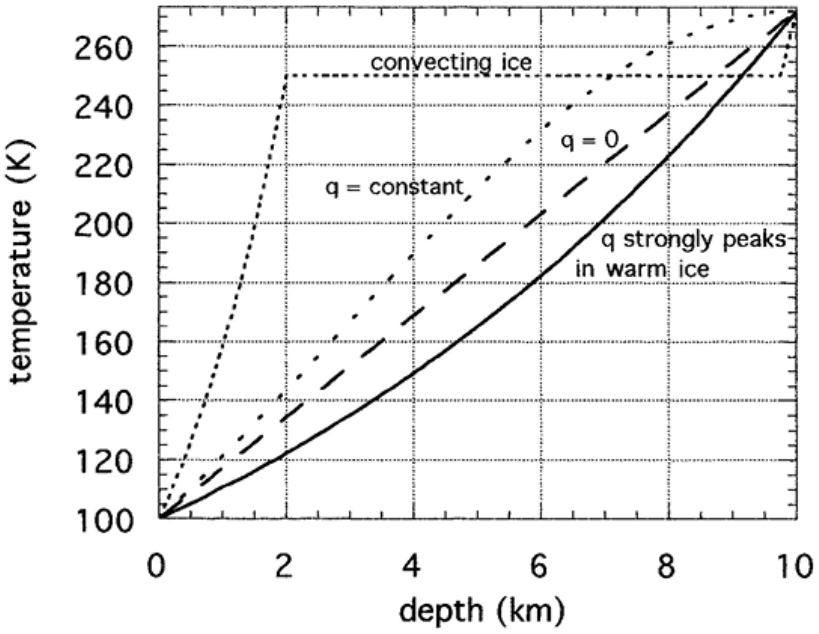

Figure 8.3: Representative diagram of different temperature profiles within Europa's ice shell, assuming a thickness of 10 km, as a function of the heating dissipation factor q. Three conductive profiles are shown, each corresponding to a different value of q: the solid line corresponding to a q value that peaks in warmer ice (Eq. 8.8), the dashed line corresponding to $q = 0$ (Eq. 8.9), and the dotted line corresponding to $q = constant$. The convective ice profile, instead assumes a conductive lithosphere of approximately 2 km, within which the temperature reaches 250 K; below this depth, the shell is modeled with a convective regime at that temperature (taken from [46]).

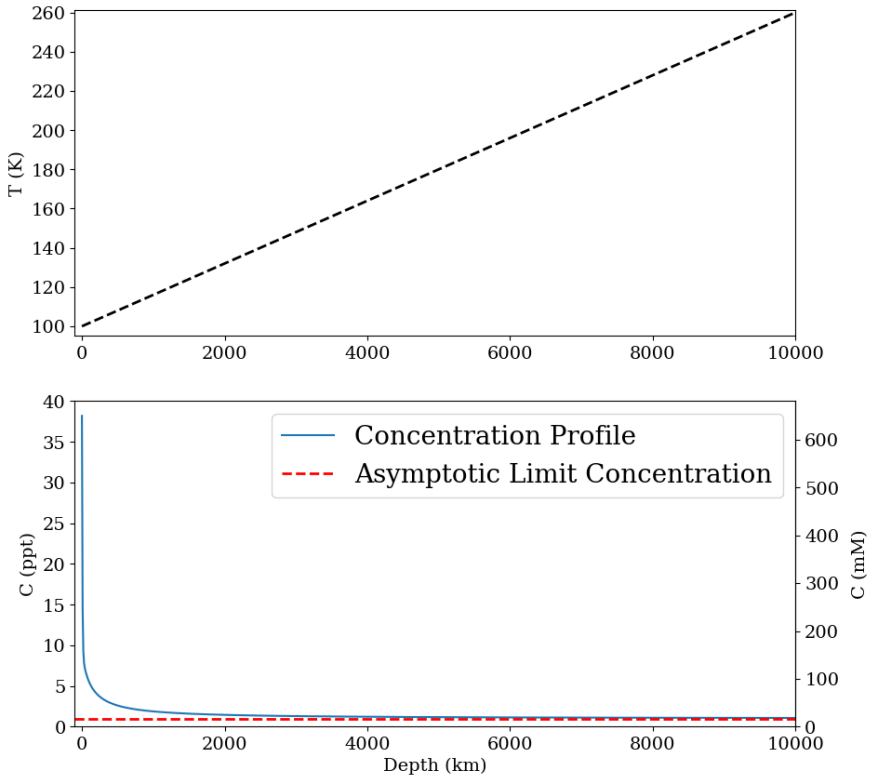

Figure 8.4: Temperature (upper panel) and salinity (lower panel) profiles according to top-down solidification proposed by [37] for a 10 km icy crust. The vertical axis shows the concentration of salt in ppt (left) and in mM (right). The asymptotic concentration is around 0.984 ppt, approximately 17 mM. The temperature and concentration profiles are given respectively by Eq. 8.9 and 8.11.

the other hand, the conductivity component is governed primarily by temperature throughout the entire crust.

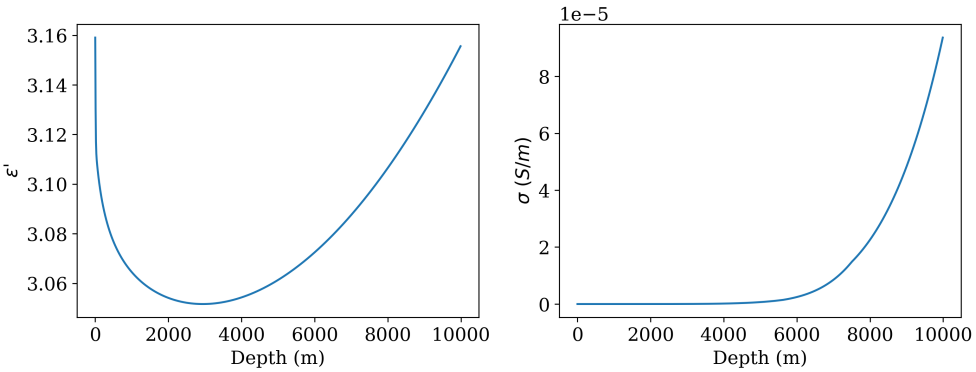

Figure 8.5: ε' (left) and σ (right) as a function of depth of an icy crust characterized by the parameters in Fig. 8.4 computed following [33].

8.2.3 Targets

Due to the shell's dynamic nature and the continuous exchange of material with the subsurface ocean, there are different potential targets within Europa's icy crust:

- The liquid water ocean interface and the transition between the icy crust and the mushy layer;
- Liquid brines of various morphologies and composition generated by different types of upwelling processes could remain stable for long periods under certain particular conditions ([44]);
- Since freezing timescales depend on local environmental conditions, some regions of the shell may have expelled salts very efficiently, leading to the formation of discrete salt layers of different thicknesses ([210]).
- Same dynamic processes could cause repeated injections of liquid material in vertical (dike-like) or horizontal (sill-like) directions that subsequently freeze ([51], [189]) leading to the formation of regions of ice with differing salt concentration.

An overview of these possible targets is shown in Fig. 8.6 ([160]). These possible targets repre-

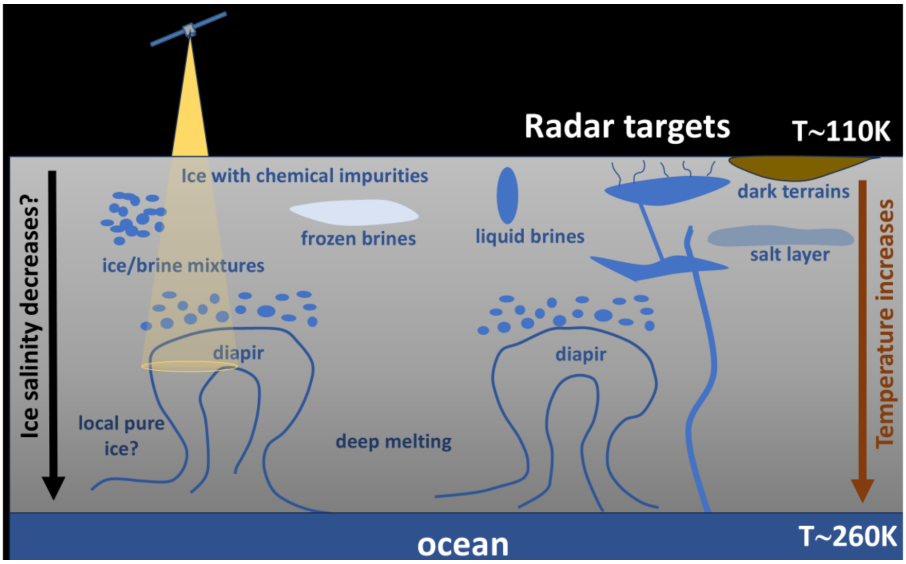

Figure 8.6: An overview of the possible radar targets in the icy crust of Europa, including all the features generated by liquid water injections from the inner ocean such as salty water of different shape (brines) or refrozen material (frozen brines). The picture is taken from [160].

sent discontinuities in the dielectric properties within the icy shell environment. The resulting contrasts are relatively small when caused by variations in ice salinity, become moderately larger in the presence of salt layers, and increase dramatically in cases involving liquid materials such

as mushy regions or brines (as previously shown in Chap. 7). Consequently, the reflected radar signals differ substantially depending on the type of discontinuity: larger dielectric contrasts lead to a higher detectability of a given target.

8.2.4 Results

The overall simulation framework consists of assessing the detectability of subsurface targets characterized by different dielectric permittivities by varying the target depth, the thickness of the icy shell, the temperature and salinity profiles (Fig. 8.7). Simulations have been performed considering:

1. A pure icy crust, the salinity profile described by [37] and a constant salinity icy shell of 20 mM (slightly above the asymptotic concentration of the profile).

2. Linear and power law temperature profiles (respectively dashed and solid lines in Fig. 8.3, taken from [46]). The surface temperature has been fixed at 100 K and the mushy layer temperature at 260 K. The thickness of the crust has been changed from a thin crust at 5 km to a thicker crust at 12 km.

The target's detectability is evaluated by computing the reflection coefficient, expressed in dB $R_c\,(dB)$, of the echo peak generated by the correspondent interface. For instance, Fig. 8.8 shows the reflections caused by a target with ε' of 80 (consistent with liquid water), at different depths in an icy shell characterized by the parameters of Fig. 8.4. The R_c of the interface between the icy crust and the target decreases with depth, because the signals are attenuated by the icy crust. Since the attenuation is very low in the first cold part of the crust, R_c remains almost constant (blue and orange peaks in Fig. 8.8). This region with very low attenuation is called in some literature ([210]) *pellucid region*

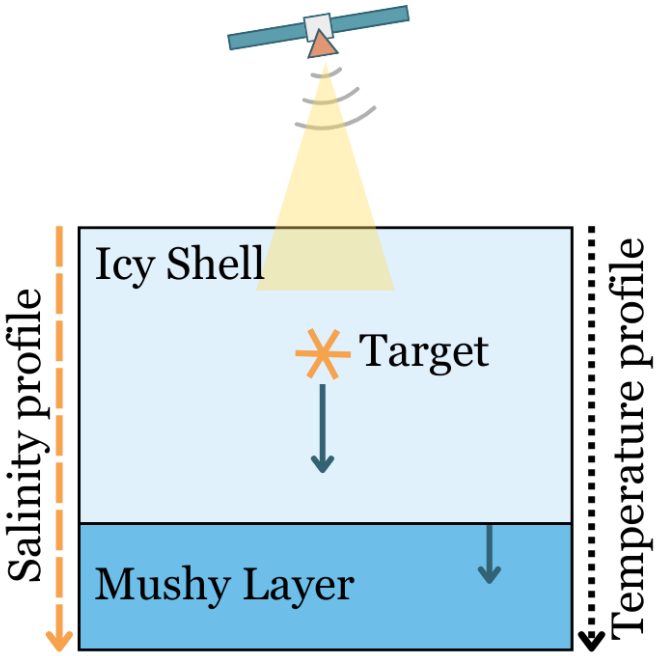

Figure 8.7: Simplified scheme of the simulations. The interfaces of the target and the mushy layer have been moved to assess the effect of a larger depth of the target and a larger thickness of the crust as indicated by the solid blue lines. The effects of the salinity and temperature profiles have been investigated using 2 concentration profiles and 2 temperature profiles.

Crust Composition

The most significant effects of crustal composition on the radar signal become evident when comparing an ice shell characterized by a salinity gradient with one composed of pure water ice. As an illustrative example, we consider the $R_c\,(dB)$ caused by a hypothetical mushy layer target

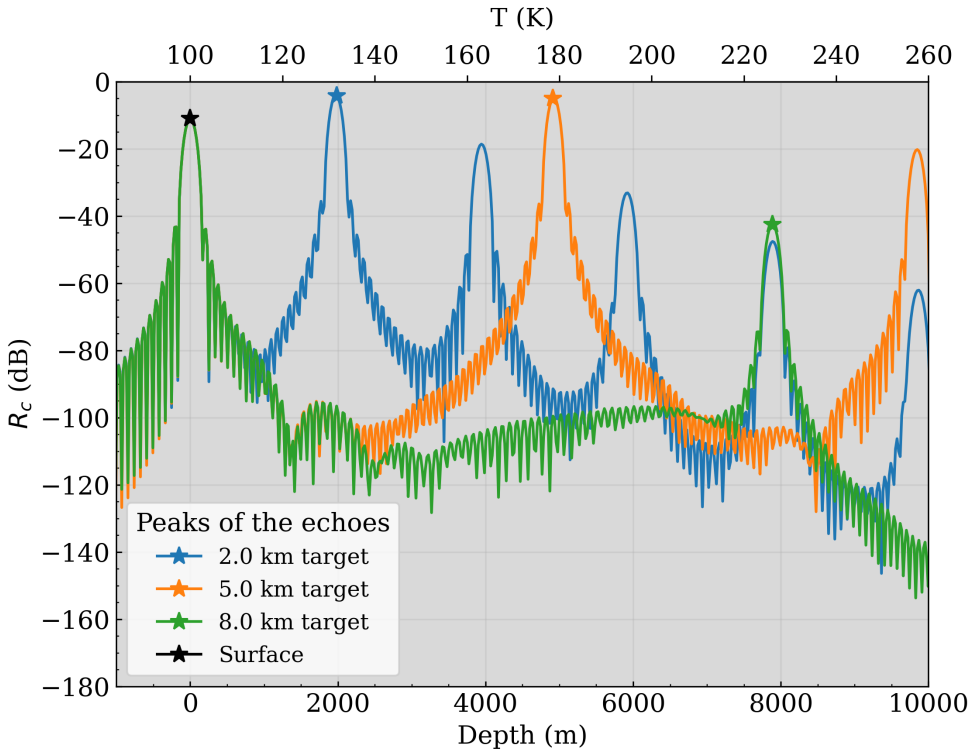

Figure 8.8: Reflection coefficient, as a function of depth (lower x axis) and temperature (upper x axis), caused by a target of liquid water ($\varepsilon' = 80$) at different depths (2 km, 5 km, 8 km) in an icy crust with the parameters of Fig. 8.4. In the simulations representing the three different scenarios, the first peak (black star) is the surface one and it is the same for the three scenarios (peaks are overlapped); the other peaks marked with a star represent the reflections coming from the targets. Other peaks are multiple reflections caused by repeated signal "bouncing" between the surface and target interfaces.

located at a depth of 3 km in both scenarios. As shown in Fig. 8.9, the reflection produced in the pure ice case is significantly stronger, due to the low attenuation of radar signals (a result of the low conductivity). The situation is markedly different for an icy shell with a salinity gradient, in which the reflection peak is significantly reduced.

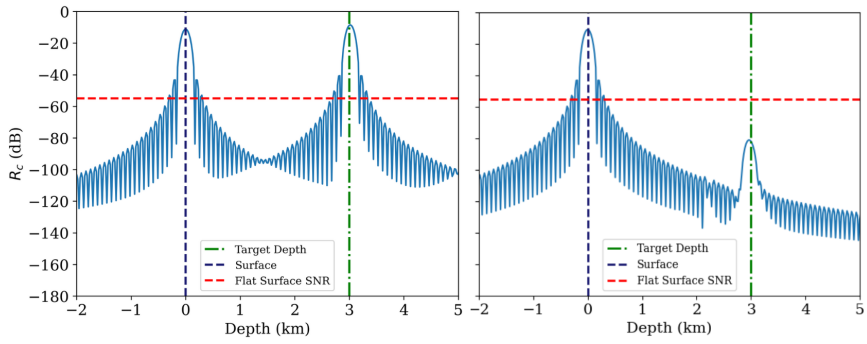

Figure 8.9: Reflection coefficient in the case of a 3 km icy crust, with a mushy layer as a target situated at the end of the crust. The left panel shows the peaks of surface and the mushy layer in a pure icy crust, while the right panel shows the case of a saline crust with the salinity profile proposed by [37]. The vertical lines represent the position of the surface and target interfaces. As a reference we report the flat surface SNR at 55 dB of RIME from the altitude of 200 km [128].

Target Permittivity and Depth

We now examine detectability as a function of depth for an icy shell in which the temperature increases linearly and has uniform salinity or a salinity gradient, by analyzing the peaks of the reflection coefficient for various targets with different values of real permittivity (Fig. 8.10). In particular, we consider the value of 5, representative of a layer of salt, 30 and 70, representative of mushy layers with different percentages of brines and 100, representative of a discontinuity of completely liquid salty water. In both cases, the detectability increases with increasing the real part of permittivity since the R_c is determined by the dielectric contrast between the icy shell and the target interfaces. In the colder shallower shell the detectability, in terms of R_c, remains almost constant until a temperature between 160 K - 180 K. In the case of a salinity gradient profile, target detectability does not appear to be significantly reduced. The presence of highly saline layers in the upper portions of the crust, therefore, does not strongly affect radar signal propagation, due to the low temperature.

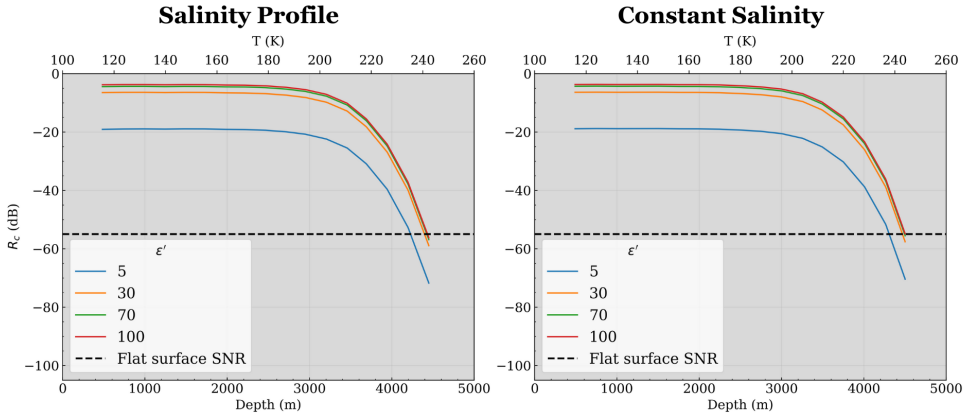

Figure 8.10: Reflection coefficient, expressed in dB, of target of different permittivities in a 5 km icy crust before the mushy layer with a linear temperature profile. In the left panel the amount of salt in the ice decreases following the model from [37], and in the right panel it is fixed at 20 mM, close to the asymptotic value of the gradient. As a reference we report the flat surface SNR at 55 dB of RIME from the altitude of 200 km [128].

Effects of the Thickness of the Shell

To investigate the dependence of detectability on the thickness of the conductive shell, we analyzed three ice shell thicknesses, 6 km, 9 km, and 12 km, assuming the same target real permittivities as in the previous section, the same salinity profile, and a linear temperature profile (Fig. 8.11). The simulations indicate that a deeper ocean interface allows radar signals to probe greater depths. This occurs because a thicker conductive layer leads to a more gradual increase in temperature, delaying the point at which the detectability is reduced (between 160 K and 180 K). Since the salinity profile influences detectability primarily in the uppermost portion of the crust, as it becomes nearly constant below the first kilometer according to [37], its influence is the same for both thin and thick shells. At equivalent temperatures, detectability is slightly lower in the thicker crust because the ice layer probed by the radar is thicker and the signal is more attenuated; however, this difference is not significant at colder temperatures, and the reflection coefficient remains nearly constant in all examined cases up to temperatures of approximately 170 K. At warmer temperatures the detectability decreases to lower values in deeper shells because the layers with high temperatures are thicker and cause a strong attenuation of the signal.

Effects of the Temperature Profile

By comparing the reflection coefficients for two different temperature profiles, the linear and the power-law (Fig. 8.12), under one of the previously considered conditions (a 6 km thick ice shell with a salinity gradient), we find that detectability is higher at greater depths in the power law

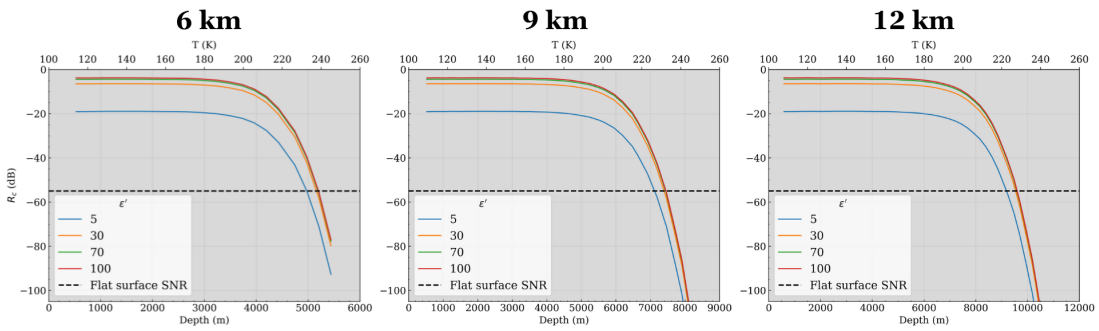

Figure 8.11: Reflection coefficient, expressed in dB, of target of 4 different permittivities in a 6 km, 9 km and 12 km conductive icy crust with the parameters of 8.4. As a reference we report the flat surface SNR at 55 dB of RIME from the altitude of 200 km [128].

case. As also evident from [46]'s temperature profiles, for a given depth, the power-law profile yields lower temperatures; consequently, electrical conductivity is reduced, leading to weaker radar signal attenuation. Target detectability is, therefore, favored if the temperature gradient follows a power law in which the detectability starts to decrease at temperatures above 200 K, 20 K more than the linear T profile case.

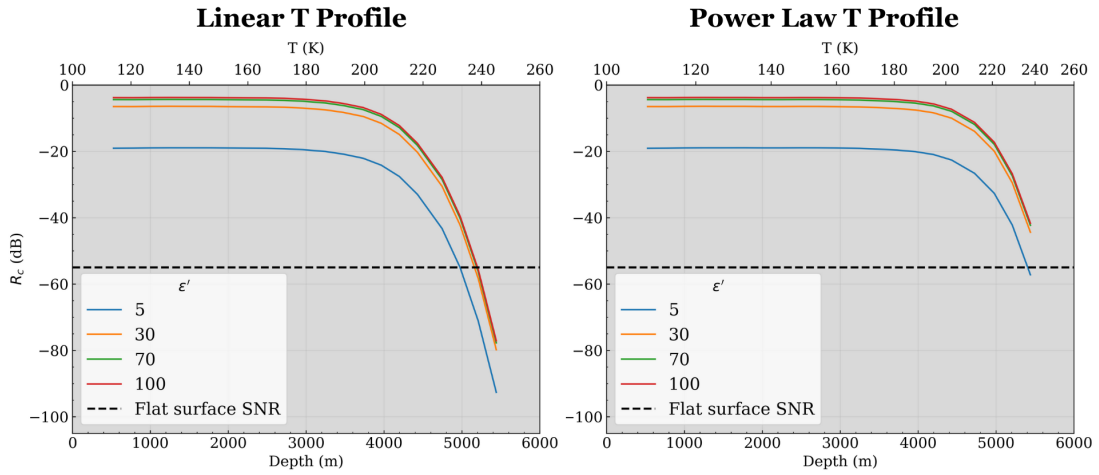

Figure 8.12: Reflection coefficient, expressed in dB, of target of different permittivities in a 6 km icy crust before the mushy layer with a linear temperature profile (left) and a power law temperature profile (right). As a reference we report the flat surface SNR at 55 dB of RIME from the altitude of 200 km [128].

In conclusion, for a saline ice shell, radar signal penetration is primarily controlled by low temperatures and only secondarily by the salt content of the ice. Even at relatively high salinity, detectability is enhanced if the temperature is low. However, the presence of high permittivity targets such as mushy layers requires elevated ambient temperatures and influences the temperature of the surrounding environment, otherwise, such partially liquid-solid states cannot be sustained. These thermal conditions directly affect their detectability. Depending on the size of the associated thermal anomalies and the extent to which they perturb the surrounding crust, the occurrence of mushy regions within the coldest portions of the ice shell is therefore unrealistic. This limitation does not apply, however, to solid salt layers.

8.3 Ganymede and Callisto

For Ganymede and Callisto, due to the presence of the darkening agent the situation is markedly different. Because of the high conductivity of the darkening agent and the possibility of a non-negligible magnetic permeability, the attenuation of radar signals is much higher and significantly limits the penetration with respect to Europa environment. Moreover, the large thickness of the icy crust (equal to or greater than 80 km according to [82]) makes the detection of high-permittivity targets associated with liquid water considerably less likely. Nevertheless, in regions where the ice is comparatively purer, the results discussed in the previous section could be applied. Given these considerations, we now examine a set of analyses distinct from those performed for Europa, focused on attenuation and interference phenomena.

8.3.1 Attenuation

The computation of the attenuation was previously investigated in [32] as a function of the percentage of the darkening agent in the icy crust (Fig. 8.13). However, even assuming the darkening agent as endogenous, the abundance of inclusions is expected to decrease with depth, progressively approaching a purer ice composition, as also suggested by [82]. We therefore analyze radar attenuation in the scenario illustrated in Fig. 8.14, in which the amount of impurities in the ice decreases linearly from different percentages at the surface to a small constant quantity around 5%. Because of the thickness of Ganymede's ice shell, the temperature gradient within the crust is relatively gradual. For this reason, all simulations for Ganymede were performed assuming a constant temperature of 120 K. Moreover, at such low temperatures the electromagnetic properties exhibit only weak temperature dependence for small thermal variations; therefore, this assumption does not significantly affect the simulation results. The results

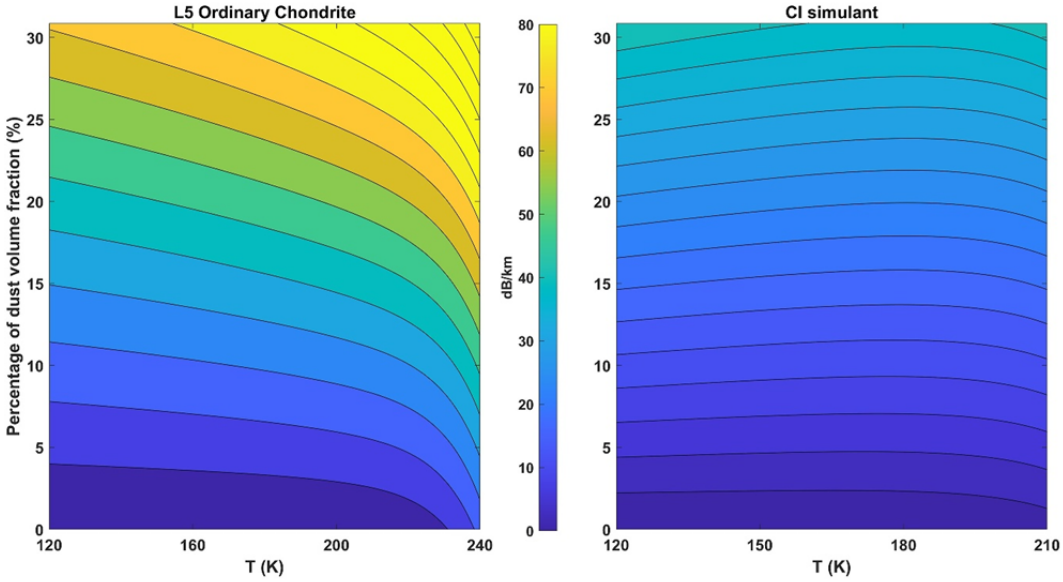

Figure 8.13: Maps of the parametric attenuation in a dirty ice layer with L5 ordinary chondrite (left panel) and CI simulant (right panel) as contaminant computed at 9 MHz. The attenuation is expressed in dB per kilometer (taken from [32]).

(Fig. 8.15) show that the attenuation increases significantly including magnetic properties, that would dramatically affect radar performance. A dirty icy crust with ordinary chondrites L5 as darkening agent would favor radar penetration with respect to carbonaceous chondrite CI. However, since magnetic permittivity data of the carbonaceous chondrite simulants are upper limits, the attenuation in that case could be overestimated. The identification of the characteristics of the darkening agents and the models of its distribution along the crust is crucial to interpret future radar data.

8.3.2 Interference Phenomena

The analysis of interference phenomena discussed in Chap. 5 in Sec. 5.6 may be particularly relevant for the interpretation of radar data from Ganymede and Callisto. Specifically, if the

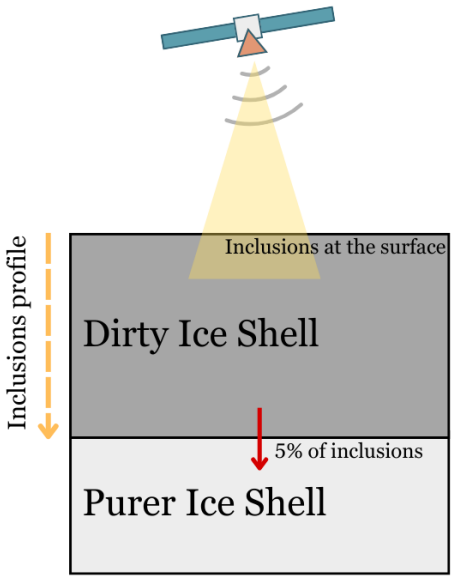

Figure 8.14: Illustration of the scenarios investigated by the simulations. The attenuation (dB) was computed in the first 5 km of the crust considering different percentage of inclusions at the surface until 50% that decreases following a linear gradient from the surface to a downward moving interface at the percentage of 5%.

darkening agents are of exogenous origin, it is plausible that radar signals encounter layers of dirty ice only a few tens to hundreds of meters thick overlying a purer ice crust. Under the conditions described previously, surface and subsurface echoes may combine constructively or destructively, resulting in a single composite signal that is difficult to interpret. In the following simulations, we consider the presence of dirty-ice layers with different CI simulants inclusion fractions, assumed to be of potential exogenous origin on the satellite's surface. The analysis focuses on the combined surface and subsurface reflection peak produced by interference effects. This investigation is carried out across several scenarios to examine different aspects:

- The distributions of the darkening agents;
- The effects of magnetic properties;
- The effects of the bandwidth of the radar.

The simulated scenarios were designed with progressively increasing complexity to systematically investigate electromagnetic interference phenomena. The baseline scenario consists of a dirty ice layer with variable carbonaceous chondrite (CI) inclusion percentages, where the layer thickness varies from 0 m (representing the absence of an intermediate layer) to 300 m. In the initial analysis, magnetic permeability effects were neglected, enabling direct derivation of the real component of the dielectric permittivity (8.16). The interference phenomenon is evident up to a depth of approximately 150 m. The initial value is independent of inclusion percentage and demonstrates consistency with the absence of an intermediate layer: the R_c ("power ratio") equals -11 dB and the derived permittivity approximates 3.1, corresponding to the established value for pure water ice. Beyond 150 m thickness, the intermediate layer becomes sufficiently substantial such that the underlying subsurface layer has negligible influence on the surface echo characteristics. In this regime, both the reflection coefficient and permittivity values align with those expected for dirty ice containing varying percentages of carbonaceous chondrite CI inclusions. In order to examine the phenomenon in detail, we focused our analysis on the thickness range where interference effects are most pronounced (0-50 m), as illustrated in Fig. 8.17. The results demonstrate that higher impurity concentrations, corresponding to larger permittivity contrasts between layers, produce both increased frequency and intensity of constructive and destructive interference patterns. Furthermore, the interference peak amplitudes are characterized by rapid attenuation when substantial permittivity contrasts exist between layers. Consequently, the interference phenomenon dissipates at shallower depths for higher percentages of impurities, and subsurface echoes become distinguishable at reduced penetration depths. Subsequently, we also incorporated magnetic properties into the simulation

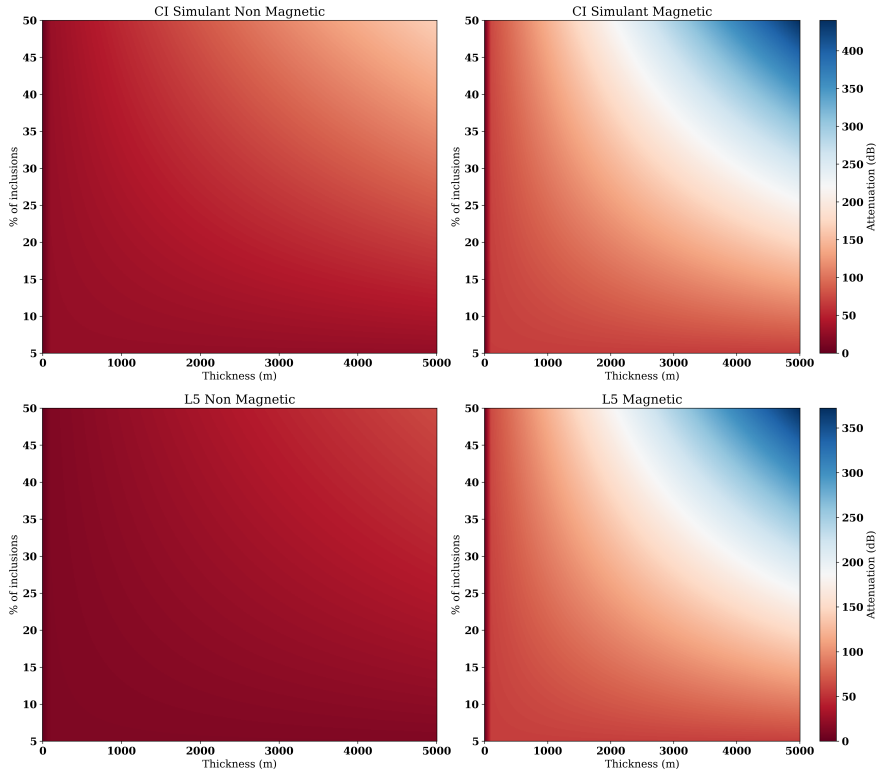

Figure 8.15: Results of simulations of the attenuation, expressed in decibels, corresponding to the scenario illustrated by 8.14. The y-axis indicates the surface percentage of inclusions. The upper panel refers to the CI simulants case, while the lower panel corresponds to the L5 case. The left panels show simulations in which magnetic properties are neglected, whereas the right panels include magnetic effects, for which the attenuation is significantly higher.

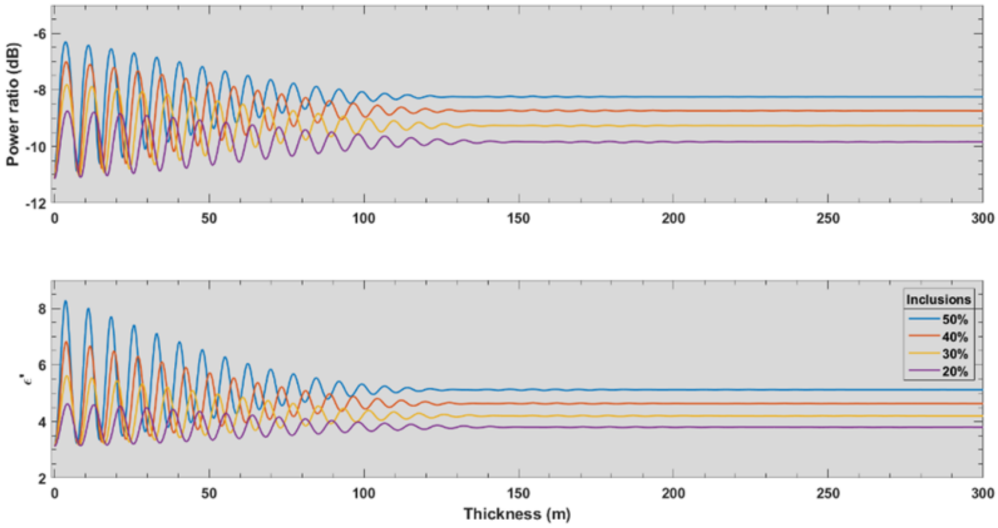

Figure 8.16: The upper panel shows the trend of the reflection coefficient, here indicated as "power ratio" of the surface discontinuity given by a dirty ice layer with carbonaceous chondrite CI inclusions in function of the layer thickness in the first 0 - 300 m for 4 different percentages of inclusions (20, 30, 40, 50). The lower panel shows the real part of the surface dielectric permittivity obtained by the upper panel data.

framework causing an additional difference in electromagnetic properties between dirty ice and pure ice (Fig. 8.18). The inclusion of magnetic permeability in the reflection-coefficient calculation has an opposing effect (Eq. 5.32), leading to a reduction in reflection coefficient intensity with respect to the previous case. Compared to the non-magnetic simulations, the interference peaks are systematically lower when magnetic effects are taken into account. In this case, the

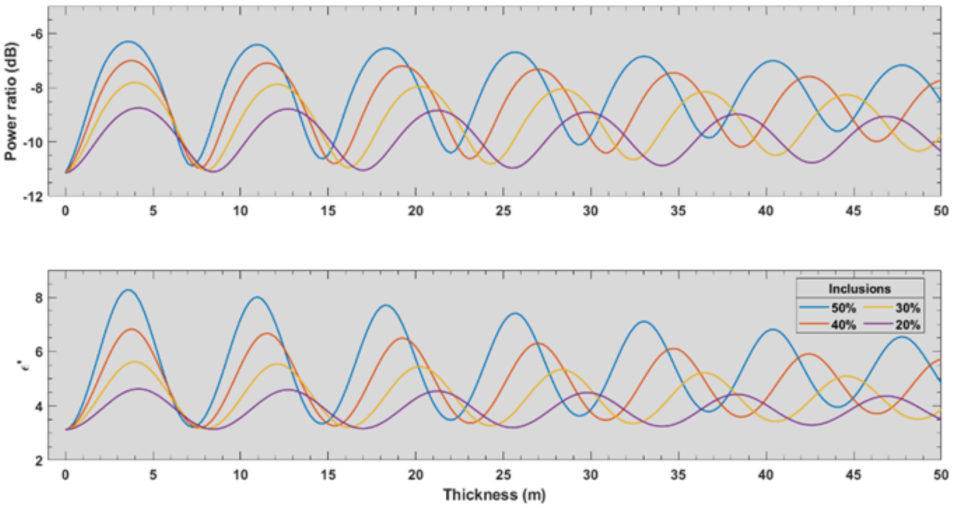

Figure 8.17: The upper panel shows the trend of the peaks of the reflection coefficient of the surface given by a dirty ice layer with carbonaceous chondrite CI inclusions of different percentage in function of the layer thickness. The lower panel shows the real part of the dielectric permittivity obtained by the upper panel data.

dielectric permittivity cannot be independently derived and instead has to be considered in combination with the magnetic permeability. In the previous analysis we consider a 1 MHz

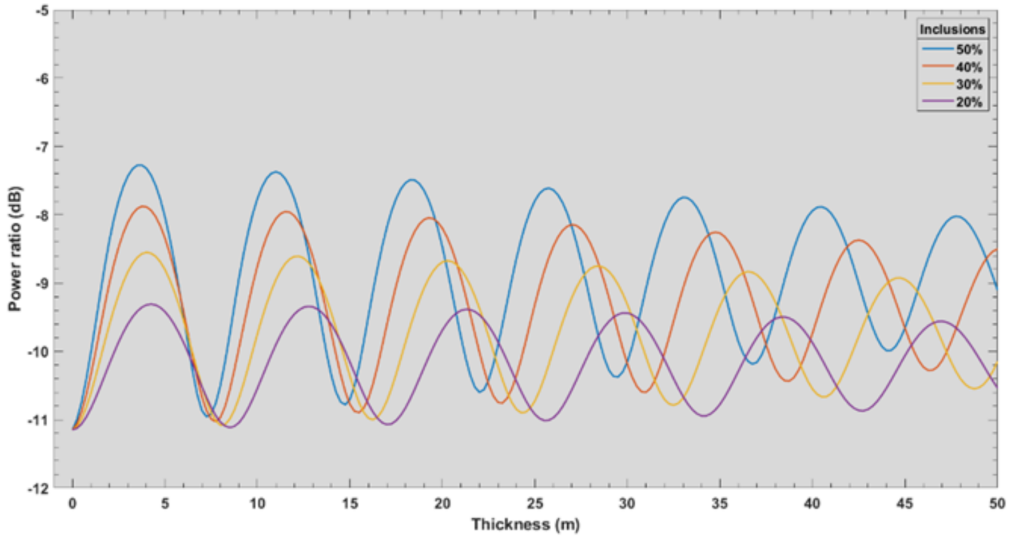

Figure 8.18: Reflection coefficient of a surface characterized by dirty ice layer with carbonaceous chondrites inclusions in function of the thickness of this layer, including the magnetic permeability in the simulation.

bandwidth signal since it was one of the RIME configurations. Let us now examine the other operating mode, the 3 MHz bandwidth signals, in the identical scenario of Fig. 8.18. In this case interference phenomena decay more rapidly and become negligible even at 40 m depth (Fig. 8.19) due to reduced temporal overlap of surface and subsurface signal returns. Therefore, the use of a broader bandwidth may represent an effective strategy for mitigating interference phenomena that could otherwise complicate radar data interpretation. In conclusion, Fig. 8.20 provides a comprehensive visualization of the reflection coefficient as a function of both surface layer thickness and inclusion percentage within the dirty ice, comparing results obtained using 1 MHz and 3 MHz bandwidth signals each with and without magnetic properties. The maximum R_c, as a measure of the ratio between emitted and receiver power of the radar, occurs at minimal thicknesses combined with high inclusion percentages, where interference effects

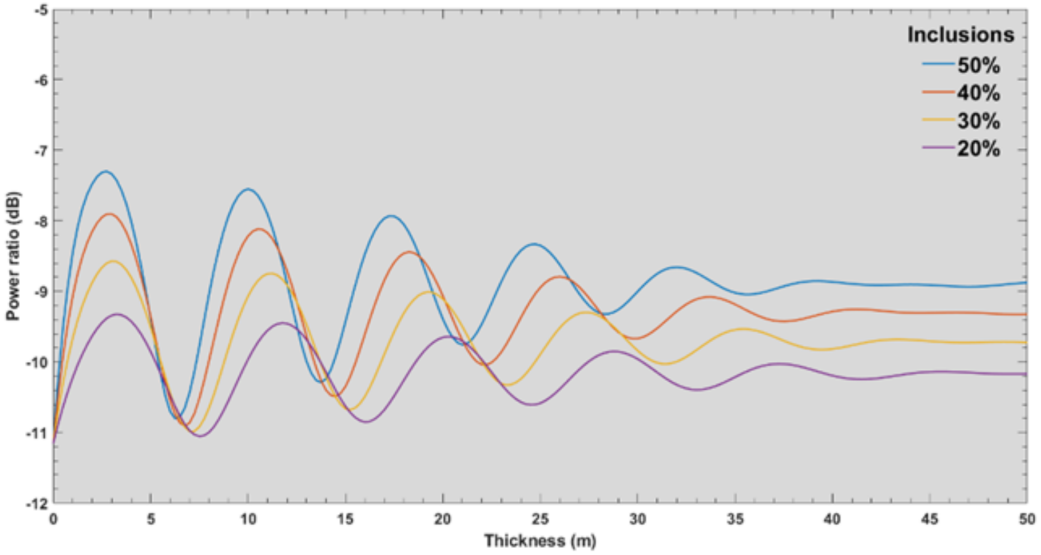

Figure 8.19: Reflection coefficient of a dirty ice surface with carbonaceous chondrites inclusions in function of the thickness of the upper layer, including the magnetic permeability in the simulation in the case of a 3 MHz emitted signal.

are most pronounced. The permittivity contrast directly governs the number of constructive and destructive interference patterns, the peak amplitude of R_c fluctuations, and the rate of interference decay. When the two layers exhibit similar permittivities (corresponding to low impurity concentrations), interference peaks manifest with reduced amplitude but demonstrate slower decay rates. In all scenarios examined, R_c intensity decreases with the incorporation of magnetic properties. As anticipated, the 3 MHz signal exhibits substantially weaker interference effects compared to the 1 MHz bandwidth case making it an efficient solution to prevent ambiguity in radar data. Previous results were obtained assuming uniform impurity concentration throughout the dirty ice layer. However, realistic conditions may deviate from this idealization. Considering the hypothesis of an exogenous material origin, a gradient in impurity concentration along the vertical profile of the ice shell represents a more physically plausible scenario with larger concentrations of the darkening agent at the surface. We performed simulations incorporating linearly decreasing inclusion profiles, ranging from various surface concentrations to 0% (pure ice) at depth within the icy crust layer (Fig. 8.21) in magnetic and non-magnetic cases. The interference effects under these conditions are remarkably weak. The amplitude between destructive and constructive interference peaks remains small and exhibits further reduction at lower surface impurity levels. The influence of magnetic permeability manifests similarly to the constant concentration cases examined previously and represents the most favorable case to avoid interference phenomena.

These analyses show that, in addition to the attenuation issue which remains central to the interpretation of radar data from Ganymede, interference effects may also play a significant role in the interpretation of surface echoes, depending on the distribution and nature of the materials that contaminate the surface ice.

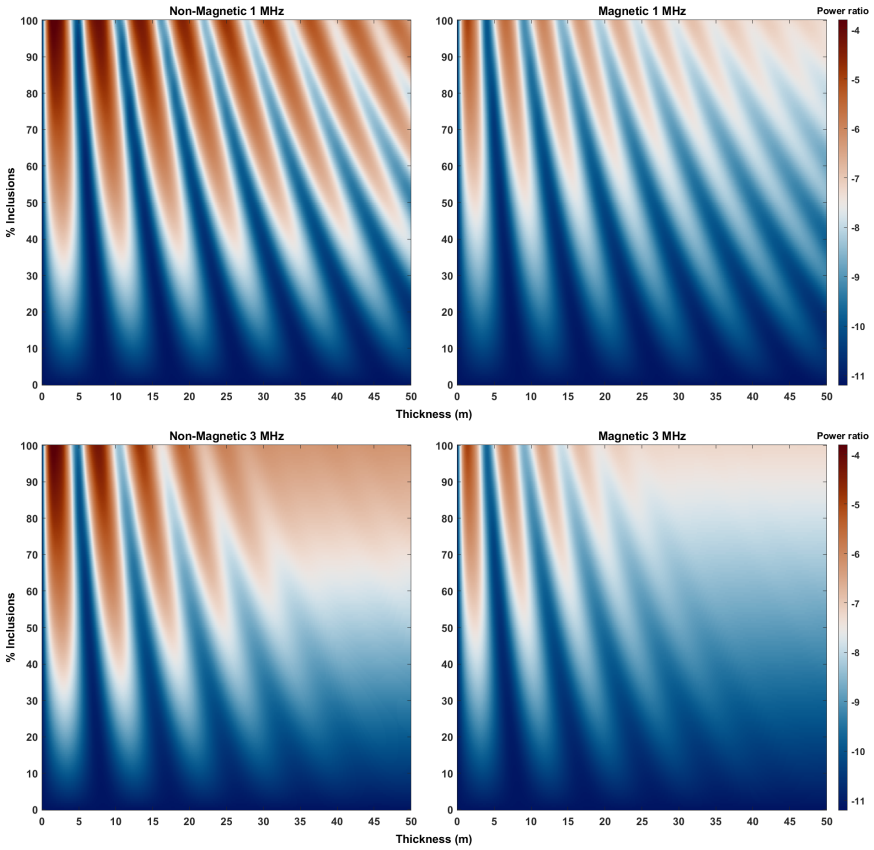

Figure 8.20: Maps of the reflection coefficient, expressed in dB, of the surface signal in case of dirty ice with carbonaceous chondrite CI simulants inclusions in function of the percentage of inclusions and the thickness of the intermediate layer, with (left) and without (right) considering the magnetic permeability. The upper panels refer to simulations performed with signals of 1 MHz bandwidth; the lower panels refer to 3 MHz simulations.

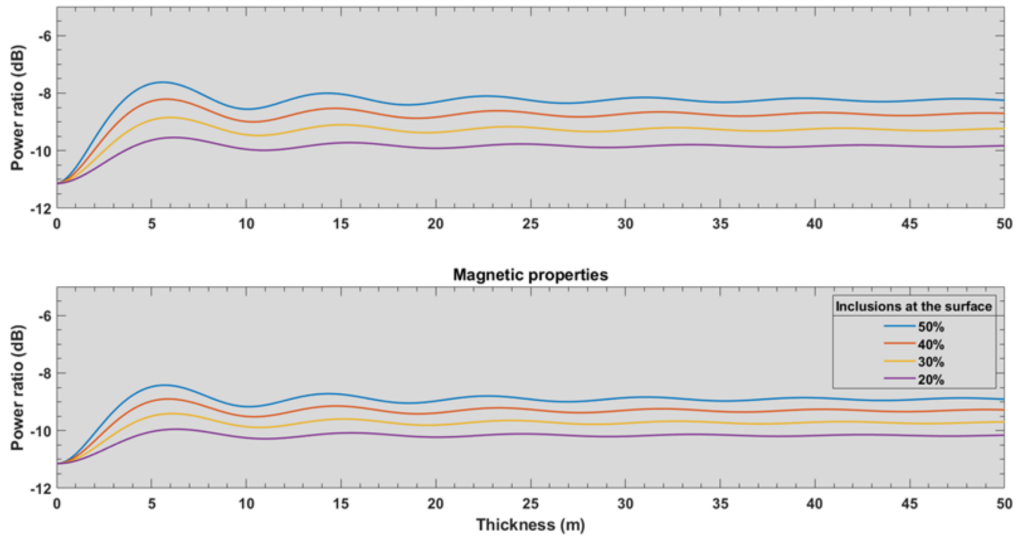

Figure 8.21: The upper panel shows the reflection coefficient of the surface discontinuity in the case of a gradient of inclusions with different percentage at the surface level with (lower panel) and without (upper panel) including the magnetic permeability.

Chapter 9

Conclusion

The search for liquid water and for habitable conditions in the Solar System using radar sounders is a relatively recent field of investigation. In fact, supporting laboratory measurements for these research methods remain limited. The electromagnetic behavior of ice and ice mixtures at radar sounder frequencies has not yet been fully understood, and this work aims at starting to fill this gap by exploiting experiments and models developed to improve the interpretation of radar observations.

In Chapter 7, structured in two parts, we showed how electromagnetic laboratory measurements can significantly improve our understanding of the dielectric behavior of liquid, mushy, and solid salty ices and how strong dielectric contrast can be generated at the interfaces between different materials and different phases. In particular, we identified under which temperature conditions the perchlorate solutions can remain liquid, or partially in a liquid state, below the Martian Polar Ice caps, specifically in the region of the bright reflector detected by MARSIS. Based on our results, calcium perchlorate solutions appear to be the most plausible candidates for explaining the strong basal echoes identified by the radar; in fact, such solutions tend to remain in a mushy state even at Martian temperatures, and better match the observed MARSIS data.
These results are relevant to the possible existence of brines in the Martian subsurface beyond the polar region, and at shallower depths where temperatures are comparatively higher. They may also prove useful in guiding the design and interpretation strategies of future radar instruments aimed at identifying liquid water bodies beneath the Martian South Pole. Further investigations of the electromagnetic properties of additional salt solutions, multi-salt mixtures, and salt-dust composites will provide new constraints for a deeper understanding of the Martian subsurface structure and geological history.
Moreover, this experimental work has revealed distinctive metastable behaviors in magnesium perchlorate solutions. At temperatures significantly lower than the eutectic point, the solution was found to be in a metastable state in some cases, while in others it was not. The factors that most influence the occurrence of metastable conditions will need to be investigated further through additional measurements. The experimental approach used here to understand radar data collected on Mars has been subsequently applied to the preparation of icy planetary analogues in the context of missions JUICE and Europa Clipper targeting Jupiter's icy satellites Europa, Ganymede, and Callisto. Based on the existing literature and the most recent observations, we investigated plausible analogues of the icy crusts, focusing on ice doped with sodium chloride for Europa and dirty ice for Ganymede and Callisto.

Our laboratory measurements have been fundamental to perform realistic simulations of the radar signal propagation in Chapter 8, exploring a range of potential subsurface scenarios for the crusts of Jovian icy moons, whose interiors are thought to be highly dynamic. The presence of liquid water in the shallower part of the crust, or within a pure icy crust, is relatively easy to detect using radar sounders. However, if the crust is composed of saline ice, or if the targets produce smaller dielectric contrasts - such as in the case of brines or salt layers -, the interpretation of radar data becomes significantly challenging. The simulations move towards this direction, aiming at identifying and characterizing the different reflections generated by various types of targets under different conditions. Although these results are necessarily simplified, as they are based on one-dimensional simulations that neglect surface topography effects, they provide meaningful insights. In particular, they show that the presence of salts can signifi-

cantly affect radar performance by limiting signal penetration. This effect, however, is partially counterbalanced by the temperature, since, in cold regions of the icy shell, the attenuation of the signals is very low - especially below approximately 180 K. In fact, our simulations showed that, in this temperature regime, even in the presence of relatively high salt concentrations, it remains possible to detect low dielectric-contrast targets - such as salt layers - in addition to more detectable features - such as brines. Since temperature is the dominant factor controlling electromagnetic properties, and thus radar signal propagation, the thermal profile of the icy shell is critical in determining the maximum probing depth. In the case of a power-law temperature profile, deeper subsurface targets can be detected. In addition to simulations of saline ice shells, we also investigated the behavior of crusts characterized by dirty ice, representative of certain regions on Ganymede and Callisto. We found that the presence of chondritic-type impurities has an even more pronounced impact on radar signals, further reducing signal penetration. This effect is even worse when the contaminant materials exhibit magnetic properties. Moreover, shallow layers of dirty ice covering the surface may generate interference effects in radar echoes, leading to ambiguities in the interpretation of the surface and near-subsurface composition. It is noted, however, that magnetic properties tend to suppress such interference effects. These interference effects are also mitigated when the impurity content decreases with depth within the ice shell. To address these phenomena, the use of broader-bandwidth radar signals represents a more effective strategy. For example, in the case of RIME, the employment of the 3 MHz bandwidth mode instead of the 1 MHz mode would reduce the risk of interference phenomena. These measurements and simulations, although approached from the perspective of the electromagnetic properties of the materials, provide important constraints on the conditions that the upcoming missions to the Jovian icy moons are likely to encounter. Combined with more complex three-dimensional analyses accounting for surface and subsurface topography, they have the potential to contribute to a more accurate and robust interpretation of future radar data.

In summary, this work has enabled the development and validation of laboratory methodologies for studying the electromagnetic properties of pure ice, saline ice and dirty ice across the radar-frequency range of interest. This effort represents a first step to develop a much broader project, and thus will continue within the framework of the ERC Advanced Grant project *Surfing Radio Waves to Detect Liquid Water in the Solar System* (SWIM), with the goal of achieving a comprehensive and systematic understanding of the electromagnetic properties of analogues representative of the icy crusts of Solar System bodies.

Acknowledgements

This work was partially supported by the PRIN project *ARES*, funded by the Italian Ministry of University and Research.

Bibliography

[1] John Rundle Addison. "Electrical properties of saline ice". In: *Journal of Applied Physics* 40.8 (1969), pp. 3105–3114.

[2] JD Anderson et al. "Gravitational constraints on the internal structure of Ganymede". In: *Nature* 384.6609 (1996), pp. 541–543.

[3] JD Anderson et al. "Europa's differentiated internal structure: Inferences from four Galileo encounters". In: *Science* 281.5385 (1998), pp. 2019–2022.

[4] AP Annan. "Ground-penetrating radar". In: (2005).

[5] Gustave E Archie et al. "The electrical resistivity log as an aid in determining some reservoir characteristics". In: *SPE reprint series* (2003), pp. 9–18.

[6] NS Arnold et al. "Surface topographic impact of subglacial water beneath the south polar ice cap of Mars". In: *Nature astronomy* 6.11 (2022), pp. 1256–1262.

[7] Vasily G Artemov. "A unified mechanism for ice and water electrical conductivity from direct current to terahertz". In: *Physical Chemistry Chemical Physics* 21.15 (2019), pp. 8067–8072.

[8] Yosef Ashkenazy. "The surface temperature of Europa". In: *Heliyon* 5.6 (2019).

[9] Yosef Ashkenazy and Eli Tziperman. "Dynamic Europa ocean shows transient Taylor columns and convection driven by ice melting and salinity". In: *Nature communications* 12.1 (2021), p. 6376.

[10] Robert P Auty and Robert H Cole. "Dielectric properties of ice and solid D2O". In: *The Journal of Chemical Physics* 20.8 (1952), pp. 1309–1314.

[11] Namitha Rose Baby et al. "Ray and Halo impact craters on Ganymede: Fingerprint for decoding Ganymede's crustal structure". In: *Earth and Space Science* 11.9 (2024), e2024EA003541.

[12] Victor R Baker. "Water and the Martian landscape". In: *Nature* 412.6843 (2001), pp. 228–236.

[13] Constantine A Balanis. *Advanced engineering electromagnetics*. John Wiley & Sons, 2012.

[14] W Bruce Banerdt et al. "Initial results from the InSight mission on Mars". In: *Nature Geoscience* 13.3 (2020), pp. 183–189.

[15] Jamaledin Baniamerian et al. *An experimental set-up for dielectric characterization of Venusian crust analogs at high temperatures*. Tech. rep. Copernicus Meetings, 2024.

[16] S Barabash et al. "The analyzer of space plasmas and energetic atoms (ASPERA-3) for the Mars Express mission". In: *Space Science Reviews* 126.1 (2006), pp. 113–164.

[17] S Barabash et al. "Particle environment package (PEP)". In: *European planetary science congress*. 2013, EPSC2013–709.

[18] John D Bernal, Ralph H Fowler, et al. "A theory of water and ionic solution, with particular reference to hydrogen and hydroxyl ions". In: *J. chem. Phys* 1.8 (1933), pp. 515–548.

[19] Jean-Loup Bertaux et al. "SPICAM on Mars Express: Observing modes and overview of UV spectrometer data and scientific results". In: *Journal of Geophysical Research: Planets* 111.E10 (2006).

[20] Rohit Bhartia et al. "Perseverance's scanning habitable environments with Raman and luminescence for organics and chemicals (SHERLOC) investigation". In: *Space Science Reviews* 217.4 (2021), p. 58.

[21] Jean-Pierre Bibring et al. “Global mineralogical and aqueous Mars history derived from OMEGA/Mars Express data”. In: *science* 312.5772 (2006), pp. 400–404.

[22] CJ Bierson et al. “Strong MARSIS radar reflections from the base of Martian south polar cap may be due to conductive ice or minerals”. In: *Geophysical Research Letters* 48.13 (2021), e2021GL093880.

[23] Sandra E Billings and Simon A Kattenhorn. “The great thickness debate: Ice shell thickness models for Europa and comparisons with estimates based on flexure at ridges”. In: *Icarus* 177.2 (2005), pp. 397–412.

[24] Niels Bjerrum. “Structure and properties of ice”. In: *Science* 115.2989 (1952), pp. 385–390.

[25] Diana L Blaney et al. “The mapping imaging spectrometer for Europa (MISE)”. In: *Space Science Reviews* 220.7 (2024), p. 80.

[26] Donald D Blankenship et al. “Radar for Europa assessment and sounding: ocean to near-surface (REASON)”. In: *Space science reviews* 220.5 (2024), p. 51.

[27] Dominique Bockelee-Morvan et al. “Composition and thermal properties of Ganymede’s surface from JWST/NIRSpec and MIRI observations”. In: *Astronomy & Astrophysics* 681 (2024), A27.

[28] Scott J Bolton et al. “The juno mission”. In: *Space Science Reviews* 213.1 (2017), pp. 5–37.

[29] A-H Boughriet, Christian Legrand, and Alain Chapoton. “Noniterative stable transmission/reflection method for low-loss material complex permittivity determination”. In: *IEEE Transactions on Microwave Theory and Techniques* 45.1 (1997), pp. 52–57.

[30] Ardith D Bravenec and David C Catling. “Effect of concentration, cooling, and warming rates on glass transition temperatures for NaClO4, Ca (ClO4) 2, and Mg (ClO4) 2 brines with relevance to Mars and other cold bodies”. In: *ACS Earth and Space Chemistry* 7.7 (2023), pp. 1433–1445.

[31] Alessandro Brin. “Electromagnetic Characterization of Dirty Ice and NaCl Doped Ice for Radar Investigations of Jupiter Icy Moons”. PhD thesis. Università degli studi Roma 3, 2024.

[32] Alessandro Brin et al. “Electromagnetic measurements and modeling of rocky and icy crust simulants to support planetary radar sounder exploration”. In: *Journal of Geophysical Research: Planets* 130.6 (2025), e2025JE008942.

[33] Alessandro Brin et al. “Electrical properties of NaCl doped ice in RIME frequency range”. In: (2026). In preparation.

[34] Shannon Brown et al. “Microwave observations of Ganymede’s sub-surface ice: I. Ice temperature and structure”. In: *Journal of Geophysical Research: Planets* 128.6 (2023), e2022JE007609.

[35] Von DAG Bruggeman. “Berechnung verschiedener physikalischer Konstanten von heterogenen Substanzen. I. Dielektrizitätskonstanten und Leitfähigkeiten der Mischkörper aus isotropen Substanzen”. In: *Annalen der physik* 416.7 (1935), pp. 636–664.

[36] Lorenzo Bruzzone et al. “RIME: Radar for icy moon exploration”. In: *2013 IEEE international geoscience and remote sensing symposium-IGARSS*. IEEE. 2013, pp. 3907–3910.

[37] JJ Buffo, CR Meyer, and JRG Parkinson. “Dynamics of a solidifying icy satellite shell”. In: *Journal of Geophysical Research: Planets* 126.5 (2021), e2020JE006741.

[38] Paolo Cappuccio et al. “Callisto and Europa gravity measurements from JUICE 3GM experiment simulation”. In: *The Planetary Science Journal* 3.8 (2022), p. 199.

[39] Shane R Carberry Mogan et al. “Callisto’s atmosphere: First evidence for H2 and constraints on H2O”. In: *Journal of Geophysical Research: Planets* 127.11 (2022), e2022JE007294.

[40] Michael H Carr. *Water on mars*. Oxford University Press, 1996.

[41] Richard J Cartwright et al. “Revealing Callisto’s carbon-rich surface and CO2 atmosphere with JWST”. In: *The Planetary Science Journal* 5.3 (2024), p. 60.

[42] Lin-Feng Chen et al. *Microwave electronics: measurement and materials characterization*. John Wiley & Sons, 2004.

[43] Augustin Chicarro, Patrick Martin, and R Trautner. "The Mars Express mission: an overview". In: *In: Mars Express: the scientific payload. Ed. by Andrew Wilson, scientific coordination: Agustin Chicarro. ESA SP-1240, Noordwijk, Netherlands: ESA Publications Division, ISBN 92-9092-556-6, 2004, p. 3-13* 1240 (2004), pp. 3–13.

[44] CJ Chivers, JJ Buffo, and BE Schmidt. "Stable brine layers beneath Europa's chaos". In: *The Planetary Science Journal* 4.9 (2023), p. 159.

[45] Philip R Christensen et al. "The Europa thermal emission imaging system (E-THEMIS) investigation for the Europa clipper mission". In: *Space Science Reviews* 220.4 (2024), p. 38.

[46] Christopher F Chyba, Steven J Ostro, and Bradley C Edwards. "Radar detectability of a subsurface ocean on Europa". In: *Icarus* 134.2 (1998), pp. 292–302.

[47] Corey J. Cochrane et al. "Stronger Evidence of a Subsurface Ocean Within Callisto From a Multifrequency Investigation of Its Induced Magnetic Field". In: *Agu Advances* (2025). DOI: 10.1029/2024av001237.

[48] Kenneth S Cole and Robert H Cole. "Dispersion and absorption in dielectrics I. Alternating current characteristics". In: *The Journal of chemical physics* 9.4 (1941), pp. 341–351.

[49] Barbara Cosciotti et al. "Laboratory investigation into the dielectric properties of a L-chondrite (NWA 12857)". In: *Icarus* 362 (2021), p. 114426.

[50] Barbara Cosciotti et al. "Can clay mimic the high reflectivity of briny water below the Martian SPLD?" In: *Journal of Geophysical Research: Planets* 128.3 (2023), e2022JE007513.

[51] Kathleen L Craft et al. "Fracturing and flow: Investigations on the formation of shallow water sills on Europa". In: *Icarus* 274 (2016), pp. 297–313.

[52] Mike Craven et al. "Properties of a marine ice layer under the Amery Ice Shelf, East Antarctica". In: *Journal of Glaciology* 55.192 (2009), pp. 717–728.

[53] Michael W Davis et al. "The JUICE ultraviolet spectrograph: a next-generation compact UVS for ESA's JUICE mission". In: *International Conference on Space Optics—ICSO 2020*. Vol. 11852. SPIE. 2021, pp. 919–929.

[54] Vincenzo Della Corte et al. "The JANUS camera onboard JUICE mission for Jupiter system optical imaging". In: *Space Telescopes and Instrumentation 2014: Optical, Infrared, and Millimeter Wave*. Vol. 9143. SPIE. 2014, pp. 1062–1073.

[55] Michael Dentith and Stephen T Mudge. *Geophysics for the mineral exploration geoscientist*. Cambridge University Press, 2014.

[56] Josselin Desmars et al. *Two new Europlanet/VESPA services about planetary moons*. Tech. rep. Copernicus Meetings, 2024.

[57] Myron C Dobson et al. "Microwave dielectric behavior of wet soil-Part II: Dielectric mixing models". In: *IEEE Transactions on geoscience and remote sensing* 1 (2007), pp. 35–46.

[58] Deborah L Domingue, Arthur L Lane, and Ross A Beyer. "IUE's detection of tenuous SO2 frost on Ganymede and its rapid time variability". In: *Geophysical research letters* 25.16 (1998), pp. 3117–3120.

[59] Michele Dougherty. "J-MAG: Magnetometer science on the JUICE mission". In: *EGU General Assembly Conference Abstracts*. 2014, p. 8791.

[60] DC Dube and R Parshad. "Study of Böttcher's formula for dielectric correlation between powder and bulk". In: *Journal of Physics D: Applied Physics* 3.5 (1970), p. 677.

[61] Bethany L Ehlmann et al. "Subsurface water and clay mineral formation during the early history of Mars". In: *Nature* 479.7371 (2011), pp. 53–60.

[62] Hajo Eicken, Manfred A Lange, and Peter Wadhams. "Characteristics and distribution patterns of snow and meteoric ice in the Weddell Sea and their contribution to the mass balance of sea ice". In: *Annales Geophysicae*. Vol. 12. 1. Springer. 1994, pp. 80–93.

[63] Keigo Enya et al. "The Ganymede Laser Altimeter (GALA) for the Jupiter Icy Moons Explorer (JUICE): Mission, science, and instrumentation of its receiver modules". In: *Advances in space research* 69.5 (2022), pp. 2283–2304.

[64] S Evans and BME Smith. "A radio echo equipment for depth sounding in polar ice sheets". In: *Journal of Physics E: Scientific Instruments* 2.2 (1969), p. 131.

[65] LS Farenzena et al. "Secondary ion emission from CO2–H2O ice irradiated by energetic heavy ions: Part I. Measurement of the mass spectra". In: *International Journal of Mass Spectrometry* 243.1 (2005), pp. 85–93.

[66] Anna A Fedorova et al. "Stormy water on Mars: The distribution and saturation of atmospheric water during the dusty season". In: *Science* 367.6475 (2020), pp. 297–300.

[67] Vittorio Formisano et al. "The planetary Fourier spectrometer (PFS) onboard the European Mars Express mission". In: *Planetary and Space Science* 53.10 (2005), pp. 963–974.

[68] Eric Gaidos and Giles Marion. "Geological and geochemical legacy of a cold early Mars". In: *Journal of Geophysical Research: Planets* 108.E6 (2003).

[69] Gabriella Gilli et al. "Increased hydrogen escape from Mars atmosphere during periods of high obliquity". In: *Nature Astronomy* (2025), pp. 1–9.

[70] SR Gough. "A low temperature dielectric cell and the permittivity of hexagonal ice to 2 K". In: *Canadian Journal of Chemistry* 50.18 (1972), pp. 3046–3051.

[71] Olivier Grasset et al. "JUpiter ICy moons Explorer (JUICE): An ESA mission to orbit Ganymede and to characterise the Jupiter system". In: *Planetary and Space Science* 78 (2013), pp. 1–21.

[72] C Grima et al. "The basal detectability of an ice-covered Mars by MARSIS". In: *Geophysical Research Letters* 49.2 (2022), e2021GL096518.

[73] C Grima et al. "Revising the basal permittivity of the south polar layered deposits of Mars with a surficial dust cover". In: *Geophysical Research Letters* 51.12 (2024), e2024GL109085.

[74] Robert E Grimm et al. "Low-frequency electrical properties of polycrystalline saline ice and salt hydrates". In: *The Journal of Physical Chemistry B* 112.48 (2008), pp. 15382–15390.

[75] Claus U Hammer. "Acidity of polar ice cores in relation to absolute dating, past volcanism, and radio–echoes". In: *Journal of Glaciology* 25.93 (1980), pp. 359–372.

[76] Candice J Hansen, Donald E Shemansky, and AR Hendrix. "Cassini UVIS observations of Europa's oxygen atmosphere and torus". In: *Icarus* 176.2 (2005), pp. 305–315.

[77] Paul Hartogh. "The Submillimeter Wave Instrument (SWI) on the JUpiter ICy moons Explorer (JUICE)". In: *AAS/Division for Planetary Sciences Meeting Abstracts# 55*. Vol. 55. 8. 2023, pp. 201–02.

[78] Zvi Hashin and Shmuel Shtrikman. "A variational approach to the theory of the effective magnetic permeability of multiphase materials". In: *Journal of applied Physics* 33.10 (1962), pp. 3125–3131.

[79] JB Hasted. "Dielectric properties". In: *Water in Crystalline Hydrates Aqueous Solutions of Simple Nonelectrolytes*. Springer, 1973, pp. 405–458.

[80] S Havriliak and S Negami. "A complex plane representation of dielectric and mechanical relaxation processes in some polymers". In: *Polymer* 8 (1967), pp. 161–210.

[81] Essam Heggy et al. "Radar properties of comets: Parametric dielectric modeling of Comet 67P/Churyumov–Gerasimenko". In: *Icarus* 221.2 (2012), pp. 925–939.

[82] Essam Heggy et al. "Radar probing of Jovian icy moons: Understanding subsurface water and structure detectability in the JUICE and Europa missions". In: *Icarus* 285 (2017), pp. 237–251.

[83] A Herique et al. "Dielectric properties of comet analog refractory materials". In: *Planetary and Space Science* 50.9 (2002), pp. 857–863.

[84] Alain Hérique et al. "Direct observations of asteroid interior and regolith structure: Science measurement requirements". In: *Advances in Space Research* 62.8 (2018), pp. 2141–2162.

[85] CA Hibbitts, TB McCord, and GB Hansen. "Distributions of CO2 and SO2 on the surface of Callisto". In: *Journal of Geophysical Research: Planets* 105.E9 (2000), pp. 22541–22557.

[86] Charles A Hibbitts. “Dark ray craters on Ganymede: Impactor or endogenous origin”. In: *Icarus* 394 (2023), p. 115400.

[87] Dylan Christian Hickson. “Characterizing the dielectric properties of geologic and asteroid regolith analogue material for improved planetary radar interpretation”. In: *yorkspace.library.yorku.ca* (2019).

[88] I ISO. and BIPM OIML. *Guide to the Expression of Uncertainty in Measurement*. Aenor Madrid, Spain, 1993.

[89] Claude Jaccard. “Étude théorique et expérimentale des propriétés électriques de la glace”. PhD thesis. ETH Zurich, 1959.

[90] Claude Jaccard. “Thermodynamics of irreversible processes applied to ice”. In: *Physik der kondensierten Materie* 3.2 (1964), pp. 99–118.

[91] H Donald Brooke Jenkins. *Chemical thermodynamics at a glance*. John Wiley & Sons, 2008.

[92] GP Johari and SJ Jones. “The orientation polarization in hexagonal ice parallel and perpendicular to the c-axis”. In: *Journal of Glaciology* 21.85 (1978), pp. 259–276.

[93] GP Johari and Edward Whalley. “The dielectric properties of ice Ih in the range 272–133 K”. In: *The Journal of Chemical Physics* 75.3 (1981), pp. 1333–1340.

[94] RE Johnson et al. “The production of oxidants in Europa’s surface”. In: *Astrobiology* 3.4 (2003), pp. 823–850.

[95] Torrance V Johnson, CM Yeates, and R Young. “Space science reviews volume on Galileo mission overview”. In: *Space Science Reviews* 60.1 (1992), pp. 3–21.

[96] Harry M Jol. *Ground penetrating radar theory and applications*. elsevier, 2008.

[97] R Jordan et al. “The Mars express MARSIS sounder instrument”. In: *Planetary and Space Science* 57.14-15 (2009), pp. 1975–1986.

[98] Kwan Chi Kao. *Dielectric phenomena in solids*. Elsevier, 2004.

[99] Syuji Kawada. “Dielectric anisotropy in ice Ih”. In: *Journal of the Physical Society of Japan* 44.6 (1978), pp. 1881–1886.

[100] Sascha Kempf. “The Surface Dust Analyzer (SUDA) on Europa Clipper”. In: *European Planetary Science Congress*. 2018, EPSC2018–462.

[101] W David Kennedy and David C Herrick. “Conductivity models for Archie rocks”. In: *Geophysics* 77.3 (2012), WA109–WA128.

[102] Aditya R Khuller and Jeffrey J Plaut. “Characteristics of the basal interface of the Martian south polar layered deposits”. In: *Geophysical Research Letters* 48.13 (2021), e2021GL093631.

[103] KK Khurana et al. “Induced magnetic fields as evidence for subsurface oceans in Europa and Callisto”. In: *Nature* 395.6704 (1998), pp. 777–780.

[104] Krishan K Khurana et al. “The origin of Ganymede’s polar caps”. In: *Icarus* 191.1 (2007), pp. 193–202.

[105] Oliver King and Leigh N Fletcher. “Global Modeling of Ganymede’s Surface Composition: Near-IR Mapping From VLT/SPHERE”. In: *Journal of Geophysical Research: Planets* 127.12 (2022), e2022JE007323.

[106] Margaret G Kivelson et al. “Galileo magnetometer measurements: A stronger case for a subsurface ocean at Europa”. In: *Science* 289.5483 (2000), pp. 1340–1343.

[107] Margaret G Kivelson et al. “The Europa clipper magnetometer”. In: *Space Science Reviews* 219.6 (2023), p. 48.

[108] MG Kivelson, KK Khurana, and M Volwerk. “The permanent and inductive magnetic moments of Ganymede”. In: *Icarus* 157.2 (2002), pp. 507–522.

[109] MG Kivelson et al. “Discovery of Ganymede’s magnetic field by the Galileo spacecraft”. In: *Nature* 384.6609 (1996), pp. 537–541.

[110] Lawrence Klein and C Swift. “An improved model for the dielectric constant of sea water at microwave frequencies”. In: *IEEE transactions on antennas and propagation* 25.1 (1977), pp. 104–111.

[111] VA Kronrod and OL Kuskov. "Chemical differentiation of the Galilean satellites of Jupiter: 4. Isochemical models for the compositions of Io, Europa, and Ganymede". In: *Geochemistry International* 44.6 (2006), pp. 529–546.

[112] OL Kuskov and VA Kronrod. "Models of the internal structure of Callisto". In: *Solar System Research* 39.4 (2005), pp. 283–301.

[113] Daniel E Lalich, Alexander G Hayes, and Valerio Poggiali. "Small variations in ice composition and layer thickness explain bright reflections below martian polar cap without liquid water". In: *Science Advances* 10.23 (2024), eadj9546.

[114] DE Lalich, AG Hayes, and V Poggiali. "Explaining bright radar reflections below the south pole of mars without liquid water". In: *Nature Astronomy* 6.10 (2022), pp. 1142–1146.

[115] Lev Davidovich Landau et al. *Electrodynamics of continuous media*. Vol. 8. elsevier, 2013.

[116] JA Lane and JA Saxton. "Dielectric dispersion in pure polar liquids at very high radio frequencies-III. The effect of electrolytes in solution". In: *Proceedings of the Royal Society of London. Series A. Mathematical and Physical Sciences* 214.1119 (1952), pp. 531–545.

[117] Sebastian E Lauro et al. "Using MARSIS signal attenuation to assess the presence of South Polar Layered Deposit subglacial brines". In: *Nature communications* 13.1 (2022), p. 5686.

[118] Sebastian Emanuel Lauro et al. "Multiple subglacial water bodies below the south pole of Mars unveiled by new MARSIS data". In: *Nature Astronomy* 5.1 (2021), pp. 63–70.

[119] Sebastian Emanuel Lauro et al. "Reply to the Matters Arising: Explaining Bright Radar Reflections Below the Martian South Polar Layered Deposits Without Liquid". In: *Nature Astronomy* (2023).

[120] Sebastina Lauro. *Note sulla teoria delle linee di trasmissioni e le misure delle proprietà elettromag netiche.*

[121] Mao-Chang Liang et al. "Atmosphere of Callisto". In: *Journal of Geophysical Research: Planets* 110.E2 (2005).

[122] Karl Lichtenecker. "Die dielektrizitatskonstante naturlicher und kunstlicher mischkorper". In: *Physikalische Zeitschrift* 27 (1926), pp. 115–158.

[123] Robert J Lillis et al. "Photochemical escape of oxygen from Mars: First results from MAVEN in situ data". In: *Journal of Geophysical Research: Space Physics* 122.3 (2017), pp. 3815–3836.

[124] Lucas Liuzzo et al. "The impact of Callisto's atmosphere on its plasma interaction with the Jovian magnetosphere". In: *Journal of Geophysical Research: Space Physics* 120.11 (2015), pp. 9401–9427.

[125] Lucas Liuzzo et al. "Magnetic signatures of plasma interaction and induction at Callisto: The Galileo C21, C22, C23, and C30 flybys". In: *Journal of Geophysical Research: Space Physics* 122.7 (2017), pp. 7364–7386.

[126] David Long and Fawwaz Ulaby. *Microwave radar and radiometric remote sensing*. Artech, 2015.

[127] H Looyenga. "Dielectric constants of heterogeneous mixtures". In: *Physica* 31.3 (1965), pp. 401–406.

[128] ASI Lorenzo Bruzzone Jeffrey J. Plaut. *JUICE-Radar for Icy Moon Exploration (RIME) Instrument Scientific and Technical Plan*. Tech. rep. Internal technical document. ESA, 2012.

[129] Nicolas Mangold et al. "Perseverance rover reveals an ancient delta-lake system and flood deposits at Jezero crater, Mars". In: *Science* 374.6568 (2021), pp. 711–717.

[130] Donald James Marshall and Theodore R Madden. "Induced polarization, a study of its causes". In: *Geophysics* 24.4 (1959), pp. 790–816.

[131] E Mattei et al. "Dielectric measurements and radar attenuation estimation of ice/basalt sand mixtures as martian Polar Caps analogues". In: *Icarus* 229 (2014), pp. 428–433.

[132] Elisabetta Mattei et al. "Coaxial-cage transmission line for electromagnetic parameters estimation". In: *IEEE Transactions on Instrumentation and Measurement* 62.11 (2013), pp. 2938–2942.

[133] Elisabetta Mattei et al. "Assessing the role of clay and salts on the origin of MARSIS basal bright reflections". In: *Earth and Planetary Science Letters* 579 (2022), p. 117370.

[134] Christian Mätzler. *Thermal microwave radiation: applications for remote sensing*. Vol. 52. Iet, 2006.

[135] James Clerk Maxwell. *A treatise on electricity and magnetism*. Vol. 1. Clarendon press, 1873.

[136] J Cl Maxwell-Garnett. "XII. Colours in metal glasses and in metallic films". In: *Philosophical Transactions of the Royal Society of London. Series A, Containing Papers of a Mathematical or Physical Character* 203.359-371 (1904), pp. 385–420.

[137] TB a McCord et al. "Organics and other molecules in the surfaces of Callisto and Ganymede". In: *Science* 278.5336 (1997), pp. 271–275.

[138] Melissa A McGrath et al. "Aurora on ganymede". In: *Journal of Geophysical Research: Space Physics* 118.5 (2013), pp. 2043–2054.

[139] William M Merrill et al. "Effective medium theories for artificial materials composed of multiple sizes of spherical inclusions in a host continuum". In: *IEEE Transactions on antennas and propagation* 47.1 (1999), pp. 142–148.

[140] Giuseppe Mitri. "Ice dynamic recrystallization within Europa's ice shell: Implications for solid-state convection". In: *Icarus* 403 (2023), p. 115648.

[141] PM Molyneux et al. "Ganymede's far-ultraviolet reflectance: Constraining impurities in the surface ice". In: *Journal of Geophysical Research: Planets* 125.9 (2020), e2020JE006476.

[142] John C Moore, Andrew P Reid, and Josef Kipfstuhl. "Microstructure and electrical properties of marine ice and its relationship to meteoric ice and sea ice". In: *Journal of Geophysical Research: Oceans* 99.C3 (1994), pp. 5171–5180.

[143] John C Moore et al. "Electrical response of the Summit-Greenland ice core to ammonium, sulphuric acid, and hydrochloric acid". In: *Geophysical Research Letters* 21.7 (1994), pp. 565–568.

[144] Ignacio Mosqueira and Paul R Estrada. "Formation of the regular satellites of giant planets in an extended gaseous nebula I: subnebula model and accretion of satellites". In: *Icarus* 163.1 (2003), pp. 198–231.

[145] A Mura et al. "Infrared observations of Ganymede from the Jovian InfraRed auroral mapper on Juno". In: *Journal of Geophysical Research: Planets* 125.12 (2020), e2020JE006508.

[146] Gerhard Neukum and Ralf Jaumann. "HRSC: The high resolution stereo camera of Mars Express". In: *In: Mars Express: the scientific payload. Ed. by Andrew Wilson, scientific coordination: Agustin Chicarro. ESA SP-1240, Noordwijk, Netherlands: ESA Publications Division, ISBN 92-9092-556-6, 2004, p. 17-35* 1240 (2004), pp. 17–35.

[147] AM Nicolson and GF Ross. "Measurement of the intrinsic properties of materials by time-domain techniques". In: *IEEE Transactions on instrumentation and measurement* 19.4 (2007), pp. 377–382.

[148] F Nimmo and Robert T Pappalardo. "Ocean worlds in the outer solar system". In: *Journal of Geophysical Research: Planets* 121.8 (2016), pp. 1378–1399.

[149] G R[UNK] Olhoeft and DW Strangway. "Dielectric properties of the first 100 meters of the Moon". In: *Earth and Planetary Science Letters* 24.3 (1975), pp. 394–404.

[150] Gary R Olhoeft et al. "Electrical properties of rocks". In: *Physical properties of rocks and minerals* 2 (1981), pp. 257–297.

[151] Thomas Ormston et al. "From Monitoring Camera to Mars Webcam-Producing Outreach from Ops". In: *SpaceOps 2008 Conference*. 2008, p. 3297.

[152] Roberto Orosei et al. "Radar evidence of subglacial liquid water on Mars". In: *Science* 361.6401 (2018), pp. 490–493.

[153] Roberto Orosei et al. "Numerical simulations of radar echoes rule out basal CO2 ice deposits at Ultimi Scopuli, Mars". In: *Icarus* 386 (2022), p. 115163.

[154] Robert T Pappalardo and Amy C Barr. "The origin of domes on Europa: The role of thermally induced compositional diapirism". In: *Geophysical Research Letters* 31.1 (2004).

[155] Robert T Pappalardo et al. "Science overview of the Europa clipper mission". In: *Space Science Reviews* 220.4 (2024), p. 40.

[156] James RG Parkinson et al. "Modelling binary alloy solidification with adaptive mesh refinement". In: *Journal of Computational Physics: X* 5 (2020), p. 100043.

[157] Martin Pätzold et al. "MaRS: Mars express orbiter radio science". In: *In: Mars Express: the scientific payload. Ed. by Andrew Wilson, scientific coordination: Agustin Chicarro. ESA SP-1240, Noordwijk, Netherlands: ESA Publications Division, ISBN 92-9092-556-6, 2004, p. 141-163* 1240 (2004), pp. 141–163.

[158] SJ Peale and Man Hoi Lee. "A primordial origin of the Laplace relation among the Galilean satellites". In: *Science* 298.5593 (2002), pp. 593–597.

[159] Victor F Petrenko and Robert W Whitworth. *Physics of ice*. OUP Oxford, 1999.

[160] Elena Pettinelli. *Surfing radio waves to detect liquid water in the solar system*. Presentation in the context of an ERC Interview. PowerPoint slides, personal communication. 2023.

[161] Elena Pettinelli et al. "Dielectric properties of Jovian satellite ice analogs for subsurface radar exploration: A review". In: *Reviews of Geophysics* 53.3 (2015), pp. 593–641.

[162] Elena Pettinelli et al. "Dielectric characterization of ice/MgSO4 11H2O mixtures as Jovian icy moon crust analogues". In: *Earth and Planetary Science Letters* 439 (2016), pp. 11–17.

[163] Gand Picardi et al. "MARSIS: Mars advanced radar for subsurface and ionosphere sounding". In: *In: Mars Express: the scientific payload. Ed. by Andrew Wilson, scientific coordination: Agustin Chicarro. ESA SP-1240, Noordwijk, Netherlands: ESA Publications Division, ISBN 92-9092-556-6, 2004, p. 51-69* 1240 (2004), pp. 51–69.

[164] Christina Plainaki et al. "Kinetic simulations of the Jovian energetic ion circulation around Ganymede". In: *The Astrophysical Journal* 900.1 (2020), p. 74.

[165] Carolyn C Porco et al. "Cassini imaging of Jupiter's atmosphere, satellites, and rings". In: *Science* 299.5612 (2003), pp. 1541–1547.

[166] F Poulet et al. "Moons and jupiter imaging spectrometer (MAJIS) on jupiter icy moons explorer (JUICE)". In: *Space Science Reviews* 220.3 (2024), p. 27.

[167] David M Pozar. *Microwave engineering: theory and techniques*. John wiley & sons, 2021.

[168] Richard C Quinn et al. "Perchlorate radiolysis on Mars and the origin of martian soil reactivity". In: *Astrobiology* 13.6 (2013), pp. 515–520.

[169] Robin Ramstad et al. "The Martian atmospheric ion escape rate dependence on solar wind and solar EUV conditions: 1. Seven years of Mars Express observations". In: *Journal of Geophysical Research: Planets* 120.7 (2015), pp. 1298–1309.

[170] KD Retherford et al. "Europa Ultraviolet Spectrograph (Europa-UVS)". In: *Space Science Reviews* 220.8 (2024), p. 89.

[171] Mark A Richards, James A Scheer, and William A Holm. *Principles of modern radar: basic principles*. IET, 2010.

[172] Edgard G Rivera-Valentín et al. "Distribution and habitability of (meta) stable brines on present-day Mars". In: *Nature astronomy* 4.8 (2020), pp. 756–761.

[173] Lorenz Roth et al. "Transient water vapor at Europa's south pole". In: *science* 343.6167 (2014), pp. 171–174.

[174] Lorenz Roth et al. "Europa's far ultraviolet oxygen aurora from a comprehensive set of HST observations". In: *Journal of Geophysical Research: Space Physics* 121.3 (2016), pp. 2143–2170.

[175] Lorenz Roth et al. "A sublimated water atmosphere on Ganymede detected from Hubble Space Telescope observations". In: *Nature Astronomy* 5.10 (2021), pp. 1043–1051.

[176] M Rubin et al. "Self-consistent multifluid MHD simulations of Europa's exospheric interaction with Jupiter's magnetosphere". In: *Journal of Geophysical Research: Space Physics* 120.5 (2015), pp. 3503–3524.

[177] Kaito Sasaki et al. "Dielectric relaxation time of ice-Ih with different preparation". In: *The Journal of Physical Chemistry B* 120.16 (2016), pp. 3950–3953.

[178] Joachim Saur et al. “The search for a subsurface ocean in Ganymede with Hubble Space Telescope observations of its auroral ovals”. In: *Journal of Geophysical Research: Space Physics* 120.3 (2015), pp. 1715–1737.

[179] EL Scheller et al. “Long-term drying of Mars by sequestration of ocean-scale volumes of water in the crust”. In: *Science* 372.6537 (2021), pp. 56–62.

[180] SK Sharma et al. *Standoff Raman spectroscopy for future Europa Lander missions*. 2020.

[181] Adam P Showman, Malhotra, and Renu. “The galilean satellites”. In: *Science* 286.5437 (1999), pp. 77–84.

[182] Anatolij M Shutko and EM Reutov. “Mixture formulas applied in estimation of dielectric and radiative characteristics of soils and grounds at microwave frequencies”. In: *IEEE Transactions on Geoscience and Remote Sensing* 1 (2007), pp. 29–32.

[183] Ari H Sihvola. *Electromagnetic mixing formulas and applications*. 47. Iet, 1999.

[184] Kelsi N Singer, William B McKinnon, and Paul M Schenk. “Pits, uplifts and small chaos features on Europa: Morphologic and morphometric evidence for intrusive upwelling and lower limits to ice shell thickness”. In: *Icarus* 364 (2021), p. 114465.

[185] Bradford A Smith et al. “The Jupiter system through the eyes of Voyager 1”. In: *Science* 204.4396 (1979), pp. 951–972.

[186] David E Smith et al. “Mars Orbiter Laser Altimeter: Experiment summary after the first year of global mapping of Mars”. In: *Journal of Geophysical Research: Planets* 106.E10 (2001), pp. 23689–23722.

[187] IB Smith et al. “A solid interpretation of bright radar reflectors under the Mars south polar ice”. In: *Geophysical Research Letters* 48.15 (2021), e2021GL093618.

[188] Michael M Sori and Ali M Bramson. “Water on Mars, with a grain of salt: Local heat anomalies are required for basal melting of ice at the south pole today”. In: *Geophysical Research Letters* 46.3 (2019), pp. 1222–1231.

[189] Christophe Sotin, James W Head III, and Gabriel Tobie. “Europa: Tidal heating of upwelling thermal plumes and the origin of lenticulae and chaos melting”. In: *Geophysical Research Letters* 29.8 (2002), pp. 74–1.

[190] David E Stillman and Robert E Grimm. “Dielectric signatures of adsorbed and salty liquid water at the Phoenix landing site, Mars”. In: *Journal of Geophysical Research: Planets* 116.E9 (2011).

[191] David E Stillman, Robert E Grimm, and Steven F Dec. “Low-frequency electrical properties of ice- silicate mixtures”. In: *The Journal of Physical Chemistry B* 114.18 (2010), pp. 6065–6073.

[192] David E Stillman et al. “Partially-Saturated brines within basal ice or sediments can explain the bright basal reflections in the south polar layered deposits”. In: *Journal of Geophysical Research: Planets* 127.10 (2022), e2022JE007398.

[193] A Stogryn. “Equations for calculating the dielectric constant of saline water (correspondence)”. In: *IEEE transactions on microwave theory and Techniques* 19.8 (1971), pp. 733–736.

[194] Weijia Sun et al. “Seismic evidence of liquid water at the base of Mars’ upper crust”. In: *National Science Review* 12.6 (2025), nwaf166.

[195] JR Szalay et al. “Oxygen production from dissociation of Europa’s water-ice surface”. In: *Nature Astronomy* 8.5 (2024), pp. 567–576.

[196] Federico Tosi et al. “Characterization of the surfaces and near-surface atmospheres of Ganymede, Europa and Callisto by JUICE”. In: *Space science reviews* 220.5 (2024), p. 59.

[197] Kevin T Trinh, Carver J Bierson, and Joseph G O’Rourke. “Slow evolution of Europa’s interior: metamorphic ocean origin, delayed metallic core formation, and limited seafloor volcanism”. In: *Science Advances* 9.24 (2023), eadf3955.

[198] Samantha K Trumbo and Michael E Brown. “The distribution of CO2 on Europa indicates an internal source of carbon”. In: *Science* 381.6664 (2023), pp. 1308–1311.

[199] Samantha K Trumbo, Michael E Brown, and Kevin P Hand. “Sodium chloride on the surface of Europa”. In: *Science advances* 5.6 (2019), eaaw7123.

[200] Samantha K Trumbo et al. “A new UV spectral feature on Europa: confirmation of NaCl in leading-hemisphere chaos terrain”. In: *The Planetary Science Journal* 3.2 (2022), p. 27.

[201] EP Turtle et al. “The Europa imaging system (EIS) investigation”. In: *Space Science Reviews* 220.8 (2024), p. 91.

[202] SD Vance, KP Hand, and RT Pappalardo. “Geophysical controls of chemical disequilibria in Europa”. In: *Geophysical Research Letters* 43.10 (2016), pp. 4871–4879.

[203] Steve Vance et al. “Ganymede’ s internal structure including thermodynamics of magnesium sulfate oceans in contact with ice”. In: *Planetary and Space Science* 96 (2014), pp. 62–70.

[204] Arthur R Von Hippel and SO Morgan. “Dielectric materials and applications”. In: *Journal of The Electrochemical Society* 102.3 (1955), 68Ca.

[205] J-E Wahlund et al. “The Radio & Plasma Wave Investigation (RPWI) for the JUpiter ICy moons Explorer (JUICE)”. In: *Space Science Reviews* 221.1 (2025), p. 1.

[206] JH Waite Jr et al. “MASPEX-Europa: the Europa Clipper neutral gas mass spectrometer investigation”. In: *Space Science Reviews* 220.3 (2024), p. 30.

[207] Shigeru Wakita et al. “Multiring basin formation constrains Europa’s ice shell thickness”. In: *Science Advances* 10.12 (2024), eadj8455.

[208] William B Weir. “Automatic measurement of complex dielectric constant and permeability at microwave frequencies”. In: *Proceedings of the IEEE* 62.1 (2005), pp. 33–36.

[209] Joseph H Westlake et al. “The Plasma Instrument for Magnetic Sounding (PIMS) on the Europa Clipper Mission”. In: *Space Science Reviews* 219.8 (2023), p. 62.

[210] NS Wolfenbarger et al. “Radar characterization of salt layers in Europa’s ice shell as a window into critical ice-ocean exchange processes”. In: *Geophysical Research Letters* 52.1 (2025), e2024GL109144.

[211] Tarik Zakri, Jean-Paul Laurent, and Michel Vauclin. “Theoretical evidence forLichtenecker’s mixture formulae’based on the effective medium theory”. In: *Journal of Physics D: Applied Physics* 31.13 (1998), p. 1589.

[212] Christophe Zimmer, Krishan K Khurana, and Margaret G Kivelson. “Subsurface oceans on Europa and Callisto: Constraints from Galileo magnetometer observations”. In: *Icarus* 147.2 (2000), pp. 329–347.

[213] Mikhail Y Zolotov and Everett L Shock. “Composition and stability of salts on the surface of Europa and their oceanic origin”. In: *Journal of Geophysical Research: Planets* 106.E12 (2001), pp. 32815–32827.